Optical Interferometry of Compact Objects: Testing General Relativity and the Extremes of Accretion

Idel Reis Waisberg

München 2019

Optical Interferometry of Compact Objects: Testing General Relativity and the Extremes of Accretion

Idel Reis Waisberg

Dissertation
an der Fakultät für Physik
der Ludwig–Maximilians–Universität
München

vorgelegt von
Idel Reis Waisberg
aus São Bernardo do Campo, SP, Brasilien

München, den 10.5.2019

Erstgutachter: Professor Reinhard Genzel
Zweitgutachter: Professor Joachim Puls
Tag der mündlichen Prüfung: 17.7.2019

Contents

List of Figures

List of Tables

Zusammenfassung

Das supermassive Schwarze Loch SgrA* im Zentrum der Milchstraße bietet die einzigartige Chance, die allgemeine Relativitätstheorie für extrem hohe Massen und Feldstärken zu testen. Möglich wird dies zum einen durch hochauflösende Beobachtungen von Sternen, die auf engen Bahnen und mit einem Abstand von nur wenigen Hundert bis einigen Tausend Gravitationsradien (R_g) um das schwarze Loch kreisen, zum anderen durch Beobachtungen von Flares des einströmenden Gases, die im Abstand von nur wenigen R_g aufleuchten. Diese Tests erfordern eine astrometrische Genauigkeit von nur wenigen zehn Mikrobogensekunden (μas) und waren Ziel und Motivation für den Bau des GRAVITY-Instruments für das Very Large Telescope Interferometer (VLTI).

Im zweiten Kapitel wird ein Modell zur Interpretation der interferometrischen Beobachtungen entwickelt, mit dem der Abstand zwischen S2 (der momentan am besten geeignete Stern zur Messung von relativistischen Effekten) und SgrA* gemessen werden kann. Dieses Modell berücksichtigt mehrere instrumentelle und physikalische Effekte, um die Position mit einer Genauigkeit von 10 bis 50 μas zu bestimmen. Diese Messungen werden mithilfe spektroskopischer Beobachtungen mit dem Instrument SINFONI kombiniert, um die gravitative Rotverschiebung im Licht des Sterns S2 während seines Periheldurchganges im Mai 2018 nachzuweisen. Die Detektion der Schwarzschild-Präzession im S2-Orbit wird Ende 2019 durch fortgesetzte GRAVITY-Beobachtungen erwartet. Darüber hinaus konnte während eines hellen Flares im nahen Infrarot (NIR) von SgrA* durch astrometrische Messungen mit GRAVITY die Bewegung des Gases auf einer Umlaufbahn von nur wenigen R_g aufgelöst werden. Diese Beobachtung ermöglicht die Vermessung der Raumzeit für extrem starke Gravitationsfelder und gibt Einblicke in die räumliche Struktur des Magnetfelds in der unmittelbaren Umgebung des schwarzen Loches.

Eine Detektion der viel schwächeren Lense-Thirring-Präzession, die vom Spin des schwarzes Loch verursacht wird, erfordert Sterne, die viel näher um SgrA* kreisen als S2. Die Stärke der Effekte durch den Spin nimmt mit kleinen Abständen deutlich zu, und newtonsche Störungen durch eventuell vorhandene dunkle Objekte im Umfeld von SgrA* können dann weitgehend ausgeschlossen werden.

Im dritten Kapitel werden die Anforderungen an die Umlaufbahn eines Sterns abgeleitet, damit innerhalb einer realistischen Beobachtungskampagne mit GRAVITY der Spin des schwarzen Loches gemessen werden kann. Da der Spin des schwarzen Loches und die Bahnparameter des Sternes gemeinsam gemessen werden, kommt der sorgfältigen Behandlung der Messunsicherheiten eine herausragende Rolle zu, um die weitgehende Entartung der Parameter zu durchbrechen. Dies geschieht durch Monte-Carlo-Simulation von relativistischen Sternbahnen und berücksichtigt das aktuelle Wissen zum Sternhaufen um SgrA*. Dadurch kann die Anzahl der Sterne abgeschätzt werden, die voraussichtlich mit GRAVITY beobachtet werden können und

die eine dynamische Messung des Spins von SgrA* erlauben könnten.

Die astrometrische Auflösung von GRAVITY ermöglicht darüber hinaus die Untersuchung von kompakten Doppelsternen und insbesondere der in diesen Systemen einfallenden und ausgestoßenen Materieströme. Der Schlüssel dazu sind Objekte mit starken Emissionslinien im NIR K-band (der Wellenlängenbereich in dem GRAVITY arbeitet). In diesen Fällen können eine hohe spektrale Auflösung, Interferometrie und differenzielle Methoden kombiniert werden, die Auflösung ist dann weit besser als eine Millibogensekunde.

Im vierten Kapitel werden hierzu GRAVITY-Beobachtungen des High-mass X-ray binary (HMXB) BP Cru präsentiert. Dieser Doppelstern besteht aus einem Neutronenstern und einem blauen Hyperriesen, von dem Materie auf den Neutronenstern überfließt. Die Beobachtungen zeigen einen ausgedehnten und asymmetrischen Sternwind. Damit können der Einfluss von Gravitations- und Strahlungsfeldern und der Strömgren-Sphäre des Röntgenpulsars auf das umgebende zirkumstellare Material untersucht werden. Hierfür wird unter anderem auch entwickelt, wie differenzielle interferometrische Größen verwendet werden können, um für sehr kompakte Objekte modellunabhängige Informationen (z. B. das erste und zweite Moment der Helligkeitsverteilung) zu erhalten.

Kapitel 5 und 6 widmen sich den interferometrischen und spektroskopischen Beobachtungen des galaktischen Mikroquasars SS 433, der für seine relativistischen (0.26c), präzessierenden, baryonischen Jets bekannt ist. SS 433 ist das einzige bekannte Objekt in der Milchstraße mit einer stets vorhandenen hyperkritischen Akkretionsscheibe und bietet damit auch die einzigartige Möglichkeit, eine solche Scheibe und ihre Super-Eddington-Ausflüsse im Detail zu untersuchen. Die geometrisch und optisch dicke Akkretionsscheibe absorbiert die Röntgenstrahlung und strahlt die absorbierte Energie wieder im ultravioletten (UV) und sichtbaren Wellenlängen ab, die dann interferometrisch mit höchster Winkelauflösung beobachtet werden.

In Kapitel 5 wird mit GRAVITY-Beobachtungen gezeigt, dass die stationäre Brγ Emissionslinie in SS 433 abwechselnd durch bipolare und äquatoriale Ausflüsse dominiert wird. Die äquatoriale Komponente zeigt dabei einen sehr hohen spezifischen Drehimpuls (Super-Keplerian). Diese Beobachtungen weisen darauf hin, dass durch Magnetfelder und Gezeitenkräfte induzierte Drehmomente – zusätzlich zum Strahlungsdruck – eine wichtige Rolle bei dem Antrieb der Ausflüsse in SS 433 spielen. Der Massen- und Drehimpulsverlust in der Umlaufscheibe ist für die Entwicklung des Doppelsternes von entscheidender Bedeutung.

Im sechsten Kapitel werden die Beobachtungen der optischen Jets von SS 433 mit GRAVITY und XSHOOTER präsentiert. Diese zeigen, dass die optischen Jets höchstwahrscheinlich durch kollimierte UV-Strahlung angetrieben werden. Dies deutet darauf hin, dass die Röntgenstrahlung und der Materieausfluss von der hyperkritischen Akkretionsscheibe im Fußpunkt des Jets kollimiert wird. Dort wird die Röntgenstrahlung absorbiert und im UV-Bereich wieder emittiert. Die Modellierung der Beobachtungen erlaubt die Bestimmung wichtiger Parameter der Jets, z. B. deren kinetische Leistung, Dichte und Füllfaktor. Die Modelle zeigen auch, dass signifikante, räumlich variable zirkumstellare Extinktion eine Rolle spielt.

Summary

The supermassive black hole SgrA* at the center of the Milky Way offers a unique opportunity to test the theory of General Relativity in unprecedented mass and field regimes through the motion of individually resolved stars in close orbits around it on scales of a few hundred to a few thousand gravitational radii (R_g), as well as gas on scales of a few R_g. Such tests require astrometric precision better than a few tens of microarcseconds (μas), beyond the reach of single diffraction-limited large telescopes, and have been the main driver for the construction of the GRAVITY instrument at the Very Large Telescope Interferometer (VLTI).

In Chapter 2, I describe a binary interferometric model that has been developed to do direct astrometry of S2 (the most suitable star among the currently known for detecting relativistic effects) relative to SgrA* from GRAVITY observations. This model takes into account several instrumental and physical effects to obtain a separation vector with precision $\sim 10 - 50\mu$as. These measurements, combined with spectroscopic observations with the instrument SINFONI, have been key to the detection of gravitational redshift in the light of S2 during its last periastron passage in May 2018, and are expected to provide the detection of Schwarzschild precession by the end of 2019. The GRAVITY astrometric measurements also revealed orbital motion of gas on the scale of a few R_g during bright near-infrared (NIR) flares of SgrA*, providing a probe of the spacetime in the strong field regime and the magnetic field structure in the innermost regions of the accretion flow.

A clean detection of the much more subtle effect of Lense-Thirring precession due to black hole spin will require the discovery and monitoring of stars with closer orbits within that of S2, not only because of the much smaller astrometric effect, but also because of Newtonian perturbations from a potential cluster of dark objects segregated around SgrA*, which would require closer stellar orbits to be overcome.

In Chapter 3, I investigate the conditions that a potential closer star would need to satisfy in terms of semi-major axis and eccentricity in order to allow the detection of black hole spin within a realistic observing campaign with GRAVITY. Because the star's orbital parameters need to be determined simultaneously with the black hole spin, the masking of relativistic effects by the uncertainty in these parameters needs to be taken into account. This is done through the simulation and fitting of relativistic stellar orbits. Furthermore, I combine the resulting constraints with the current knowledge about the stellar cluster around SgrA* in order to estimate the expected number of stars detectable by GRAVITY and which would allow a dynamical measurement of black hole spin.

The spatial resolution provided by GRAVITY also allows studies of close, compact Galactic binaries on the scale of the binary orbit, providing a new probe of their accretion-ejection spatial morphology. Key to this goal is to find objects with strong emission lines in the NIR K band (where GRAVITY operates) so that very robust quantities on a sub-beam (sub-milliarcsecond) scale can be obtained through spectral differential interferometry.

In Chapter 4, I present GRAVITY observations of the High-mass X-ray binary (HMXB) BP Cru, composed of a neutron star accreting from its blue hypergiant donor star. The observations reveal an extended and asymmetric stellar wind, and can probe the influence of the gravitational and radiation fields of the X-ray pulsar on the surrounding circumstellar environment through the formation of focused accretion streams and/or a Strömgrem sphere. This work also shows how differential interferometric quantities in the marginally resolved limit can be used to derive model-independent information (first and second-order moments) of the light intensity distribution.

Chapters 5 and 6 are dedicated to optical interferometric and spectroscopic observations of the unique Galactic microquasar SS 433, famous for its precessing, relativistic (0.26c), baryonic jets. As the only known manifestation of a steady hypercritical accretion disk in the Galaxy, it offers the opportunity to study a supercritical disk and its associated super-Eddington outflows in detail. The thermal downgrading of the X-ray luminosity into ultraviolet (UV) and optical wavelengths by the geometrically and optically thick accretion disk makes it into an ideal target for optical interferometry.

In Chapter 4, I show through high spectral resolution GRAVITY observations that the "stationary" Brγ emission line in SS 433 alternates between being dominated by a bipolar and an equatorial outflow, and that the latter carries a very high specific angular momentum ("super-Keplerian") which implies that magnetic and/or tidal torques (in addition to radiation pressure) play a major role in powering the outflows in this object. The significant mass and angular momentum loss in this dynamic circumbinary disk are crucial for the binary evolution of SS 433.

In Chapter 5, I show through spatially resolved observations of the optical jets with GRAVITY, as well as large wavelength coverage spectroscopy with XSHOOTER, that the optical jet emission in SS 433 is most likely powered by collimated UV radiation, which suggests that the hypercritical disk collimates but also downgrades the X-ray radiation to UV wavelengths also in the jet funnel. This work also constrains important properties of the jets such as their kinetic power, density and filling factor, and suggests significant and structured circumstellar extinction around the binary.

Chapter 1

Introduction

1.1 Testing General Relativity in the Galactic Center

First predicted by the theory of General Relativity (GR; Einstein, 1915) as objects with a boundary region from which not even light can escape (Schwarzschild, 1916), black holes are now known to be ubiquitous across a huge mass scale in the Universe. They have the potential to test GR in the most extreme gravitational potentials $\sim c^2$; nonetheless, isolated black holes are essentially invisible except for a feeble amount of radiation emitted as they evaporate on super-Hubble timescales due to quantum effects (Hawking, 1974). The presence of a black hole, however, can be inferred from the influence of its gravitational field on stars or gas circling around it, and associated phenomena such as tidal disruptions, rapid variability and superluminal motion that are produced as a consequence.

The existence of stellar mass black holes has been secured from mass measurements in X-ray binaries (Remillard and McClintock, 2006), as well as in black hole mergers producing gravitational waves (Abbott et al., 2016). On the other hand, the presence of supermassive black holes in the centers of galaxies has been inferred from the very high power density in quasars (Schmidt, 1963), the powerful emission from centers of galaxies in general (Lynden-Bell, 1969), spatially resolved ensemble motions of stars and gas (Kormendy and Richstone, 1995), and time resolved reverberation mapping of the Broad Line Region (Kaspi et al., 2000), which can now also be spatially resolved in a few objects (Gravity Collaboration et al., 2018c). The recent imaging of the black hole shadow in M87 by the Event Horizon Telescope (Event Horizon Telescope Collaboration et al., 2019a) provides another strong indication of a supermassive black hole in that galaxy.

Just the same, the Galactic Center still presents the strongest evidence for a supermassive black hole, known as SgrA* from its radio emission (Genzel et al., 2010). The monitoring of stellar orbits, in particular the star S2, proves that a total mass $\sim 4 \times 10^6 M_\odot$ must be concentrated within its periastron distance $\sim$ 16 light hours, and that no more than $\sim 1\%$ of this mass can be extended beyond a pure point mass (Gillessen et al., 2017). The detection of orbital motion of gas in the immediate vicinity of the black hole (Gravity Collaboration et al., 2018b) provides even stronger constraints, requiring such a mass to

be concentrated within mere ~ 3 light minutes. Beyond providing the best case for the existence of a supermassive black hole, these observations allow for tests of general relativity in both weak- and strong-field regimes, and in an unprecedented mass regime of millions of solar masses.

1.1.1 The S-star cluster

The Galactic Center is home to a dense cluster of stars in orbits around the central supermassive black hole up to its sphere of gravitational influence ~ 3 pc (Fig. 1(a)). The identification of individual stellar populations was enabled over the last decades through several key advancements in near-infrared (NIR) technology (the extreme extinction due to interstellar dust precluding optical and UV observations of the Galactic Center), such as large (8-10 m) ground-based telescopes, speckle imaging, adaptive optics, integral-field spectroscopy and efficient NIR detectors (for a review, see Genzel et al., 2010). The stellar population in the Galactic Center is extremely diverse and points to several episodes of star formation (e.g. Pfuhl et al., 2011). It includes (i) a population of bright late-type giants, which dominate on larger scales, with a central density profile that flattens within the central few 1" (e.g. Genzel et al., 2003b; Buchholz et al., 2009; Do et al., 2009; Bartko et al., 2010); (ii) a fainter population of late-type stars, which do appear to have a cusp density profile up to the central 1" (Gallego-Cano et al., 2018; Schödel et al., 2018; Habibi et al., 2019); (iii) a population of luminous O- and WR-type stars, concentrated in a clockwise disk (and in a less populated counterclockwise disk) extending from 1"-10" from the center (e.g. Paumard et al., 2006; Bartko et al., 2009; Lu et al., 2009); (iv) a less well characterized population of B stars on scales >1", both in the aforementioned disk and isotropic (e.g. Bartko et al., 2010); (v) a remarkable central cluster on scales < 1" (the S-star cluster, Fig. 1(b)), mostly comprised of young and massive B-dwarf stars on isotropic and eccentric orbits around the black hole, and whose origin is still a mystery (Ghez et al., 2003; Eisenhauer et al., 2005; Habibi et al., 2017).

1.1.2 GR tests with S2

The S-stars, with their close, short-period orbits around the black hole, hold the key for precise tests of GR in the Galactic Center. Their large proper motions (Eckart and Genzel, 1996; Genzel et al., 1997; Ghez et al., 1998), and in particular the close bound orbit of the star S2 (Schödel et al., 2002; Ghez et al., 2003), provided the first very convincing dynamical argument for the existence of a supermassive black hole in the Galactic Center. The astrometric and spectroscopy monitoring of the S-stars, which has been ongoing for more than two decades, has focused on S2 due to its unique properties: of the currently known stars, it has the shortest periastron distance ($\approx 2600 R_g$) and the second-shortest orbital period (≈ 16 years); its eccentricity $e = 0.87$, a parameter that plays a key role in GR effects, is significantly above the mean of the thermal eccentricity distribution of the S-stars (0.66); it is notoriously bright ($m_K \approx 14$) among the S-stars. This monitoring has provided very precise measurements of the mass and distance to the Galactic Center

black hole (Ghez et al., 2008; Gillessen et al., 2009; Boehle et al., 2016; Gillessen et al., 2017) and – since the advent of optical interferometry with VLTI/GRAVITY (Fig. 1(c)) – the detection of the gravitational redshift in the orbit of S2, the first precision test of GR near a supermassive black hole (Gravity Collaboration et al., 2018a; Amorim et al., 2019; Gravity Collaboration et al., 2019). In particular, the black hole mass M_0, distance R_0 and $f_{redshift}$ (a parameter characterizing the special relativistic Doppler effect and gravitational redshift, where $f_{redshift} = 0$ corresponds to a purely Keplerian orbit and $f_{redshift} = 1$ to the prediction of GR) are currently constrained to

$$M_0 = 4.154 \pm 0.014 \times 10^6 M_\odot \tag{1.1.1}$$

$$R_0 = 8178 \pm 26\text{pc} \tag{1.1.2}$$

$$f_{redshift} = 1.04 \pm 0.05 \tag{1.1.3}$$

(Gravity Collaboration et al., 2019). The detection of Schwarzschild precession in the orbit of S2 is predicted towards the end of 2019. However, higher-order GR effects, in particular due to the black hole spin, are much more difficult to detect with S2: not only is the required astrometric precision impossible to achieve with current or near-future facilities, but also the Newtonian perturbations caused by a putative cluster of dark objects segregated around the black hole would very likely corrupt the spin signature (e.g. Merritt et al., 2010; Zhang and Iorio, 2017). Therefore, the discovery of stars in even closer orbits than S2 is paramount to the measurement of spin through stellar orbits (Fig. 1(d,e)).

1.1.3 Measuring black hole spin

Together with their mass, black holes in GR can be entirely characterized by their spin (Kerr, 1963), under the reasonable assumption of charge neutrality. The spin is usually defined using the dimensionless parameter $a = \frac{cJ}{GM^2}$, where $|a| < 1$ is required by the cosmic censorship hypothesis (prohibition of naked singularities). The complete characterization of a black hole by its mass and spin is at the heart of the so-called no-hair theorem. The spin has a profound influence on the spacetime due to dragging of inertial frames: close enough to the black hole, test particles and even light are forced to co-rotate with it purely due to the spacetime curvature, without any applied force or torque. In this so-called ergosphere, extraction of the black hole's rotational energy is theoretically possible (Penrose and Floyd, 1971).

The black hole spin is a very important quantity not only as a test of the Kerr metric, but also because it carries important astrophysical significance. On the one hand, extraction of the rotational energy of a black hole through electromagnetic processes is one of the strongest candidates for the production of ultrarelativistic jets in both stellar mass and supermassive black holes (Blandford and Znajek, 1977). Such jets, extending to $\sim$ 100pc and $\sim$ many kpc scales respectively, can inject a significant amount of high-energy

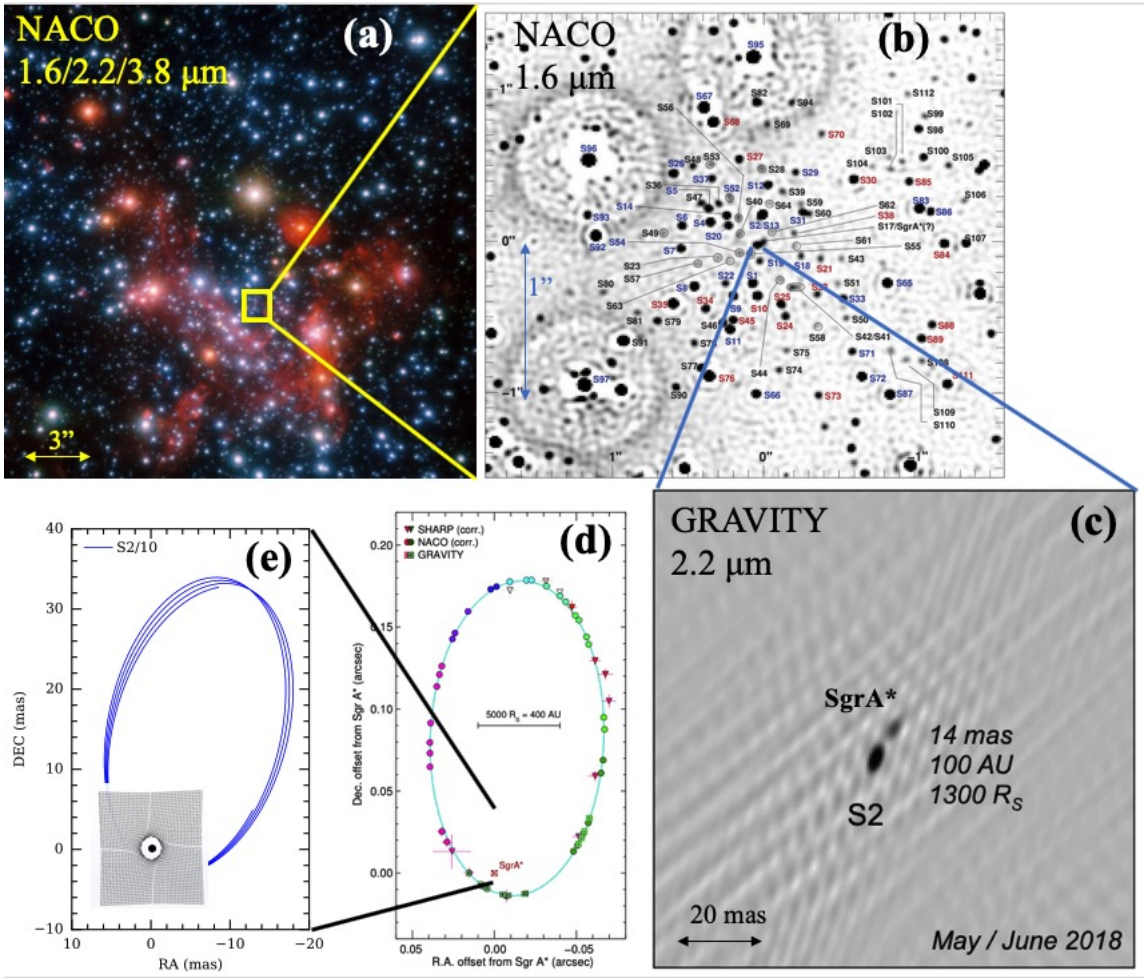

Figure 1.1: Zooming in on the Galactic Center. **(a)** The nuclear star cluster on $\sim$ 1 pc scale in a composite image in the NIR H, K and L bands, the former two tracing stars and the latter dust filaments. Image credit: ESO/Gillessen et al. **(b)** The S-star cluster in the central 1” mostly composed of young B stars (blue), but also with some late-type stars (red), in close orbits around SgrA*. Image credit: Gillessen et al. (2009). **(c)** Zoom in on the central 50 mas during periastron passage of the star S2 in 2018. The image was made with the GRAVITY instrument at unprecedented $\sim$ 1 mas spatial resolution, with both the star and the black hole visible. Image credit: Gravity Collaboration et al. (2018a). **(d)** The full orbit of the star S2 (orbital period $\approx$ 16 yrs) traced over almost 30 years. The drastic improvement in astrometric precision provided by GRAVITY since 2017 was paramount to the very significant detection of gravitational redshift. Image credit: Gravity Collaboration et al. (2018a). **(e)** The orbit of a putative faint star (orbital period 0.5 yrs) contained within the S2 orbit. The inset (image credit: Dexter and Agol (2009)) shows the spacetime in the immediate vicinity of the black hole, distorted by frame-dragging due to spin. At the scale of the star, it manifests as an additional (Lense-Thirring) precession on top of the zero-spin Schwarzschild precession.

particles and accretion products into their galactic neighborhood or the entire galaxy and surrounding circumgalactic medium, profoundly influencing their evolution. On the other hand, the spin of the black hole carries information about its origin and/or evolution. In the case of stellar objects, high or low spins in isolated objects may be correlated with a black hole or a neutron star as the supernova product, as the latter can be slowed down through magnetic breaking torques (Miller et al., 2011). For a supermassive black hole, the spin encodes information on its accretion history: coherent accretion produces $a \sim 1$, whereas chaotic accretion or growth by mergers tend to produce $a \sim 0$ (Volonteri et al., 2005; King and Pringle, 2006).

Contrary to mass, however, robust estimates of black hole spin have proven to be very elusive (Reynolds, 2019). One of the most important effects of a nonzero spin is to reduce the radius of the innermost stable circular orbit (ISCO) from $6R_g$ for $a = 0$ to $1R_g$ for $a = 1$. This leads to a shift in the inner edge of the accretion disk. Detection of the resulting increase in temperature and luminosity of the disk through thermal continuum fitting in the soft state of X-ray binaries allows estimates of the spin (Zhang et al., 1997), but they are not very robust due to degeneracies with distance and inclination (this technique is harder to apply to SMBHs because their disk emission peaks in the extreme UV and because the BH masses are significantly more uncertain, let alone the fact that thin disk spectra do not seem to describe AGNs at a very basic level (e.g. Koratkar and Blaes, 1999)). A more robust technique, applicable to X-ray binaries and SMBHs alike, uses the distorted line profile of the Fe Kα emission line, excited in the inner parts of the accretion disk by hard radiation from the surrounding corona, with a characteristic shape determined by relativistic effects (including gravitational redshift) which encode the black hole spin (Fabian et al., 1989; Tanaka et al., 1995). However, this method also suffers from significant systematic effects such as the shape of the underlying continuum as well as complexities in the accretion model such as disk winds and finite disk thickness (Reynolds, 2019).

New methods to measure black hole spin have come to light recently. Gravitational wave signals in BH binary mergers (currently limited to stellar mass BHs) encode spin information in a purely gravitational setup (i.e. without the complications of a plasma), but inferring precise individual black hole spins is challenging, as is constraining the final spin of the merger product during the very short ring-down phase, with the current sensitivity (Reynolds, 2019). On the other hand, EHT has the goal of imaging the size and shape of the black hole shadows in M87 and SgrA* (Falcke et al., 2000; Event Horizon Telescope Collaboration et al., 2019a), which carry information about the spacetime (including spin). In the case of M87, however, the uncertainty in the black hole mass (which translates into the shadow size) and the near face-on orientation (which leads to a $\lesssim 2\%$ variation of the shadow shape with spin) make a spin measurement difficult (Event Horizon Telescope Collaboration et al., 2019b). In the case of SgrA*, a very precise $\frac{M}{D}$ as measured from stellar orbits (Gravity Collaboration et al., 2019) together with an image of the black hole shadow could potentially allow a spin measurement, in case the size/shape of the shadow could be clearly isolated from the surrounding emission and enough precision could be achieved.

Even though the frame-dragging effects due to spin are strongest near the event horizon,

the considerations above show that a robust measurement of the spin of SgrA* (or in any other black hole) using the gas at such scales is difficult because of the many degrees of freedom introduced by the accretion flow model. On the other hand, the Galactic Center offers the opportunity to monitor individual stellar orbits on scales $\gtrsim 100-1000R_g$, which behave as ideal test particles for measuring general relativistic effects (Will, 2008; Merritt et al., 2010; Psaltis et al., 2013). At such scales, frame-dragging is not a dominant effect enforcing co-rotation, but instead causes small cyclic perturbations to the zero-spin orbit which introduce an additional precession on top of the Schwarzshild precession (Lense-Thirring precession) and which, if detectable, could provide a clean measurement of the spin (Fig.1(e)). A pulsar in an appropriately close orbit around the Galactic Center could also provide very precise measurements of spin and even the quadrupole moment through precise timing (e.g. Liu et al., 2012), but despite deep searches such an object has not been found, and it is currently unclear if because of technical or more exotic astrophysical reasons (Dexter and O'Leary, 2014). A cluster of stars, on the other hand, is known to exist around SgrA*, and closer stars than the currently known are in fact expected from the measured properties of the cluster (Genzel et al., 2003b). However, detecting such faint stars $m_K \gtrsim 17-18$ close to SgrA* requires new technology beyond single telescope AO to overcome confusion in the innermost regions of the S-star cluster.

1.2 The extremes of accretion

Conversion of gravitational energy into kinetic energy (followed by radiation) through accretion into objects with high compactness $\frac{M}{R}$ is one of the most efficient ways to produce large luminosities per unit volume: it is the driving process at the heart of quasars (Schmidt, 1963) and X-ray binaries (Shakura and Sunyaev, 1973), with an efficiency of rest mass energy conversion up to 42% for a maximally spinning black hole, roughly two orders of magnitudes higher than nuclear fusion. One of the most important parameters for the accretion process is the mass accretion rate in units of Eddington, $\dot{M_{Edd}}$, which corresponds to the accretion rate producing a luminosity which exactly counteracts gravity through radiation pressure

$$L_{Edd} = \frac{4\pi G M_* m_p c}{\sigma_T} \approx 10^{38} \frac{M_*}{M_\odot} \text{ erg/s} \tag{1.2.1}$$

$$\dot{M}_{Edd} = \frac{L_{Edd}}{\eta c^2} \tag{1.2.2}$$

under the assumption of spherical symmetry and free electron scattering as the dominant source of opacity (σ_T is the Thomson cross section), and where η is the efficiency of conversion of rest mass energy to radiation for the given accretor.

When the accretion rate is below but not too below Eddington ($1\%\dot{M}_{Edd} \lesssim \dot{M} \lesssim \dot{M}_{Edd}$), the accreted matter can thermalize and radiate efficiently (and the radiation can escape) in a geometrically thin and optically thick accretion disk (Shakura and Sunyaev, 1973).

1.2.1 Highly subcritical accretion flow in SgrA*

When the accretion rate is very low, however, the accretion flow is too rarefied so that the collision timescale between ions and electrons is longer than the viscous (inflow) timescale; as a result, the ions cannot cool and a two-temperature plasma (with $T_i >> T_e$) is formed. Most of the energy (carried by the ions) is advected, leading to an optically thin and geometrically thick radiatively inefficient accretion flow (RIAF) dominated by thermal gas pressure and prone to wind outflows (Yuan and Narayan, 2014). SgrA* is currently in an inactive state with extremely low luminosity ($\sim 5 \times 10^{35}$ erg/s $\sim 10^{-9} L_{Edd}$) and is thought to be in this regime (Narayan et al., 1995), fueled by a hot halo of gas and stellar winds. In this regime, the observed radiation from radio to NIR wavelengths is produced mostly by synchrotron emission from a hot population of thermal and non-thermal electrons in the inner parts of the accretion flow (Özel et al., 2000; Markoff et al., 2001; Yuan et al., 2003, 2004). Alternatively, it could be explained by a jet outflow, with synchrotron and synchrotron self-Compton producing the observed broadband emission (Falcke and Markoff, 2000). The observed linear polarization from radio to NIR confirm this synchrotron-dominated picture (e.g. Aitken et al., 2000; Trippe et al., 2007).

In addition to the low quiescent X-ray emission produced via bremsstrahlung from large scales up to the Bondi radius, SgrA* undergoes frequent X-ray flares above the quiescent limit by up to two orders of magnitude (Baganoff et al., 2001), which are always accompanied by NIR flares exceeding the quiescent emission by a smaller but substantial factor (up to one order of magnitude; Genzel et al., 2003a). Such flares are very likely produced by synchrotron emission from a highly relativistic electron population powered by magnetic energy density liberated in magnetic reconnection events (e.g. Ponti et al., 2017). In some context, therefore, the absence of a radiatively efficient accretion disk in SgrA* can be viewed as fortunate, as the localized emission from flare events can be more easily distinguished from the weak quiescent emission and used as a probe of the magnetic field structure and of the spacetime near the event horizon (Gravity Collaboration et al., 2018b).

1.2.2 The hypercritical disk in SS 433

When the accretion rate is very high, the large radiation pressure leads to a high aspect ratio $\frac{H}{R}$ inwards of the so-called spherization radius (the radius at which the integrated luminosity from the outer disk reaches the Eddington value), creating a disk which is geometrically thick in addition to optically thick due to the very high densities (Shakura and Sunyaev, 1973). This large radiation pressure leads to massive outflows, ejecting most of the incoming mass before it can be effectively accreted into the compact object, so that the total luminosity can only exceed Eddington logarithmically.

Super-Eddington luminosities are routinely observed in energetic transients such as gamma-ray bursts (Piran, 2005) and tidal disruption events (Komossa, 2015), but observing persistent supercritical accretion is more elusive. Just the same, it likely plays a crucial role in the early growth of supermassive black holes (Volonteri et al., 2015) and in the short-lived

but key stage of common envelope evolution in close binaries (Ivanova et al., 2013), one of the key processes in removing angular momentum to produce gravitational wave mergers within a Hubble time. Steady hypercritical accretors are important to answer critical questions regarding supercritical disks, such as the role of mass advection (Lipunova, 1999) or of magnetic fields in the production of collimated jets in a radiation-pressure dominated flow (Sądowski and Narayan, 2015). Ultraluminous X-ray sources (ULXs), off-nuclear point sources in nearby galaxies with X-ray luminosities in excess of 10^{39} erg/s, are now known to have a dominant population of supercritically accreting stellar compact objects (Kaaret et al., 2017); however, as extragalactic objects, their detailed study at multiple wavelengths is very limited. As the only known steady supercritical accretor in the Galaxy, the microquasar SS 433 then emerges as a key object for studying a hypercritical accretion flow in detail.

SS 433 was the first microquasar discovered through its relativistic (0.26c), baryonic and precessing optical jets, manifested as broad (FWHM $\sim$ 2000 km/s) emission lines of hydrogen and helium moving across its optical spectrum with large red and blueshifts (Margon et al., 1979). The jets also reveal themselves through emission lines of highly ionized metals in the X-ray spectrum, following the same precession model as the optical jets (Marshall et al., 2002), and as a larger scale corkscrew structure in the radio (Fig. 2(b), Blundell and Bowler, 2004). In addition to the baryonic jets, the spectrum also shows broad (FWHM $\gtrsim$ 2000 km/s) and complex "stationary" lines, formed in the super-Eddington outflows driven by the thick accretion disk. SS 433 sits at the center of the W50 supernova remnant, clearly distorted on large scales by the jets, estimated to have occurred $\lesssim 10^5$ yrs ago (Fig.2(a), Dubner et al., 1998). The nature of the compact object, neutron star or black hole, is still not securely determined, although the latter is preferred based on the collective information (Fabrika, 2004).

The uniqueness of SS 433 among other galactic X-ray binaries is thought to be due to the hypercritical accretion rate $\sim 500\dot{M}_{Edd}$ onto the compact object (Fabrika, 2004). As a result of the geometrically and optically thick disk, the X-ray luminosity from the inner disk is thermally reprocessed to UV and optical wavelengths except near the poles, so that edge-on observers (as earthlings happen to be) perceive it as a relatively faint X-ray object ($L_X \sim 10^{36}$ erg/s) but extremely bright in the UV-optical ($\sim 10^{39}$ erg/s). This property, unique among X-ray binaries in the Galaxy, makes SS 433 the ideal X-ray binary for optical interferometry. At a distance of 5.5 kpc, it is the most promising object for spatially resolving a supercritical disk and its outflows.

1.3 Optical Interferometry and Compact Objects

1.3.1 The need for interferometry

The Schwarzschild radius of SgrA* in angular units is $R_g = \frac{2GM_0}{c^2 R_0} \approx 10\mu$as, which is the spatial resolution required to image the gas close to its event horizon, or the astrometric

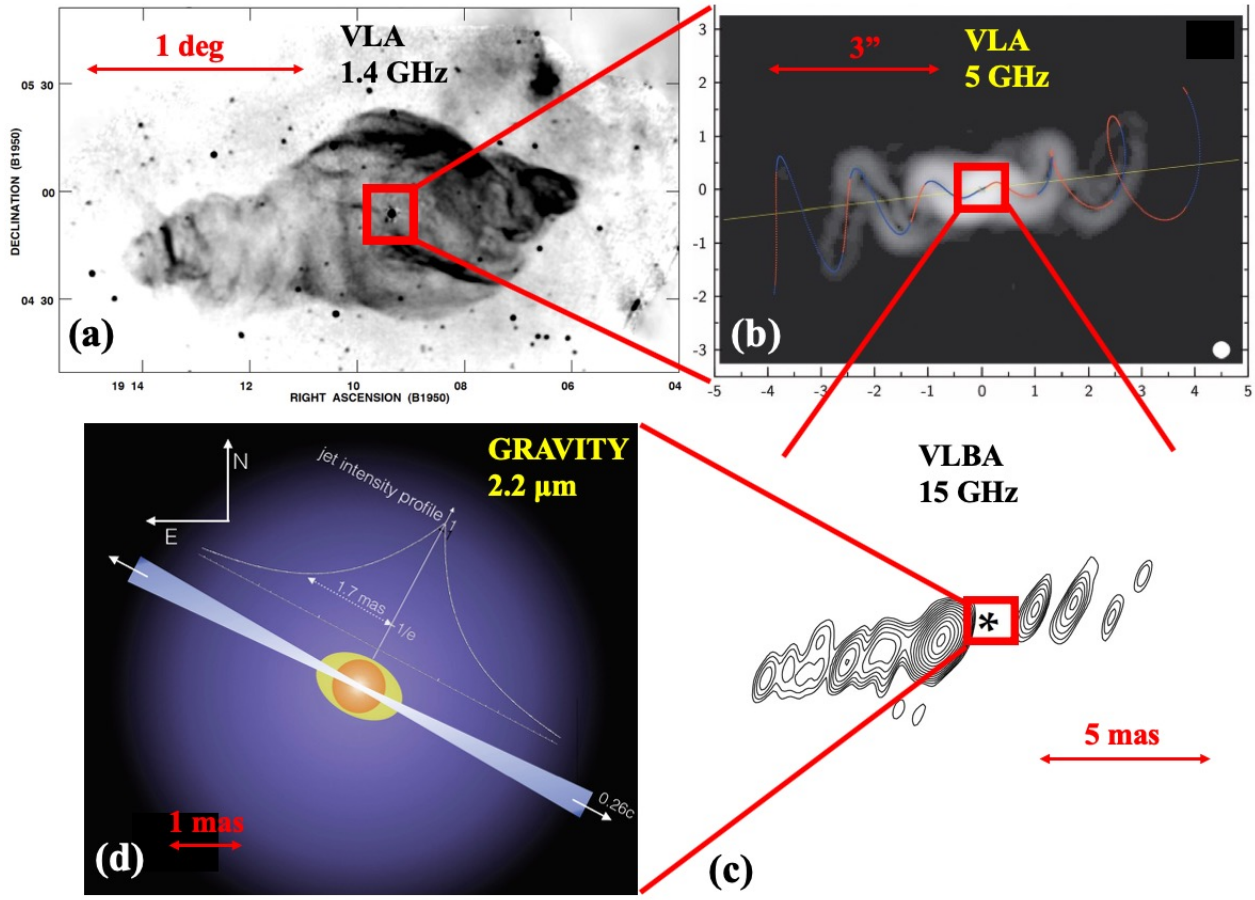

Figure 1.2: Zooming in on SS 433. **(a)** The W50 supernova remnant with SS 433 at its center. The remnant has been distorted by the microquasar jets, acquiring a seashell morphology. Image credit: Dubner et al. (1998). **(b)** The radio jets on arcsecond scales, with a corkscrew pattern formed by their $\approx$ 163-day period precession. Image credit: Blundell and Bowler (2004). **(c)** The highest resolution radio image of SS 433 to date, at a spatial resolution $\approx$ 1 mas. A gap due to synchrotron self-absorption and free-free absorption is clearly visible. Image credit: Paragi et al. (1999). **(d)** A schematic of SS 433 at sub-mas (1 mas = 5 AU) scales based on GRAVITY observations. The optical jets peak very close to the binary and decay exponentially on $\approx$ 2 mas scale, while the NIR continuum and the Brγ stationary line are more compact, with the latter tracing a bipolar outflow. Image credit: Gravity Collaboration et al. (2017).

precision required to track the motion of a compact emission region in its accretion flow. An astrometric precision of the order $10 - 50\mu$as also happens to be the one required to robustly detect Schwarzschild-like GR effects (such as periastron precession or light bending) in the orbit of the star S2, or Kerr-like GR effects (Lense-Thirring precession) in the orbit of a closer star. Therefore, a minimum precision of $\lesssim 50\mu$as is required to test GR in the Galactic Center. At the same time, this is also the spatial resolution required to directly resolve Galactic X-ray binaries with persistent accretion at a scale comparable to the binary orbit. For example, the semi-major axis of SS 433 is $a_{orb} = 70(\frac{M}{40M_\odot})^{1/3}\mu$as, where M is the total binary mass.

For a given light-collecting element of diameter D, diffraction limits the spatial extent of an imaged point source to a size $\approx 1.2\frac{\lambda}{D}$. The maximum spatial resolution at optical/NIR wavelengths with current single telescopes is therefore limited to ≈ 50 mas, achievable with adaptive optics at NIR wavelengths with $8 - 10$ m ground telescopes or at visual wavelengths with the Hubble Space Telescope. Interferometry, on the other hand, allows to increase the spatial resolution substantially by combining the light from two different telescopes: the resulting interference fringe encodes spatial information on scales of $\sim \frac{\lambda}{B}$, where B is the separation between the telescopes (baseline) projected on the part of the sky under study.

Interferometry is based on the van-Cittert-Zernike theorem, which relates the coherent flux $F(\boldsymbol{u})$ measured by the interferometer to the image $I(\boldsymbol{x})$ on the sky plane by a 2d Fourier transform (e.g., Glindemann, 2011):

$$F(\boldsymbol{u}) = \int I(\boldsymbol{x}) e^{-2\pi i \boldsymbol{x}\cdot\boldsymbol{u}} d\boldsymbol{x} \tag{1.3.1}$$

where $\boldsymbol{u} = \dfrac{\boldsymbol{B}}{\lambda}$ is the uv coordinate and $\boldsymbol{B}$ is the projected baseline on sky. The normalized coherent flux $V(\boldsymbol{u}) := \frac{F(\boldsymbol{u})}{F(\boldsymbol{0})}$ is defined as the complex visibility. Interferometry can then be seen as the collection of samples of 2d Fourier transforms of the image, which are sampled (i) as the Earth rotates and the projected baseline $\boldsymbol{B}$ changes and (ii) with different wavelength channels. A large enough uv sample may contain enough information for robust model-independent image reconstruction; otherwise, model fitting to the limited set of visibilities is required. The imaging resolution of the interferometric array can be roughly estimated as $\theta_{res} \sim \dfrac{\lambda}{|\boldsymbol{B}|_{max}}$, where $|\boldsymbol{B}|_{max}$ is the largest projected baseline, although the exact beam pattern (equivalent to a Point Spread Function) depends on the actual uv coverage.

1.3.2 The need for optical interferometry

Even though astronomical interferometry started at optical wavelengths (Michelson and Pease, 1921), it has flourished for many decades with radio arrays (Thompson et al., 2017). The dire need for interferometry in the radio comes from the longer wavelengths, which require large baselines to achieve meaningful spatial resolution. The technological and mathematical developments in heterodyne interferometry and aperture synthesis techniques, and

the science it enabled, were recognized with the 1974 Physics Nobel prize. Even though optical interferometry shares the exact same mathematical principles as radio interferometry, substantial technological differences and challenges have limited its widespread use as in the radio domain. The most fundamental difference stems from the fact that quantum noise prevents coherent amplification and the use of heterodyne techniques for wavelengths shorter than the mid-infrared. As a result, at optical/NIR wavelengths the light beams must be brought directly together to form fringes (homodyne interferometry), rather than being amplified and recorded separately and correlated later as in radio (Buscher and Longair, 2015). Furthermore, the impossibility of amplification means that the light from each telescope must be split to interfere with all others, leading to a severe limitation in the number of telescopes of the array. The much shorter coherence time has prevented the measurement of the fringe phase in optical interferometers (except when a nearby phase-reference source exists and is measured simultaneously – see below), so that significant phase information is lost. All these shortcomings severely limit the uv coverage achievable by optical interferometers, which is very often insufficient for model-independent image reconstruction. Finally, the much higher cost of an optical telescope compared to a radio antenna and the expensive and complex structure required for direct beam combination have also restricted the spread of optical interferometry as a standard technique.

Radio emission is usually due to synchrotron radiation by relativistic electrons spiraling around magnetic fields. As a result, radio interferometry has been historically used in high-resolution spatial studies of accreting black holes such as microquasars (Mirabel and Rodríguez, 1999) and supermassive black holes with jets. Continent-sized Very Long Baseline Interferometry (VLBI) sites such as the Very Large Baseline Array (VLBA) can achieve a spatial resolution $\gtrsim 1$ mas, and an Earth-sized array (EHT) has achieved $\sim 20\mu$as spatial resolution to image the black hole in M87 (Event Horizon Telescope Collaboration et al., 2019a) and to obtain spatial information on SgrA* (e.g. Krichbaum et al., 1998; Bower et al., 2006; Doeleman et al., 2008; Fish et al., 2016). However, there are crucial science cases which can only be achieved through optical interferometry. In the case of the Galactic Center:

1. the orbiting stars can only be detected in the NIR, and they can provide much cleaner (albeit in a weaker field regime) tests of GR than the accretion flow near horizon scales;

2. the fractional variability of SgrA* is inversely proportional to wavelength, being strongest ($\sim$100x) in the X-rays and NIR ($\sim$10x) and weak in the radio ($\sim 20\%$); therefore, optical interferometry can track intense localized emission moving in the accretion flow more easily than radio interferometry (but see e.g. Johnson et al., 2015).

In the case of X-ray binaries:

1. not all systems have strong radio emission; for instance, high-mass X-ray binaries (HMXBs) hosting a highly magnetic neutron star accreting from its companion's stellar wind typically do not produce jets;

2. even in systems that do have strong radio emission, it is very difficult to resolve the scale of the binary. As an example, Fig. 2(c) shows the highest resolution radio image of SS 433 to date, taken with VLBA at 15 GHz (Paragi et al., 1999). The binary system falls within the gap produced by self-synchrotron and free-free absorption; in order to resolve such inner regions, higher frequencies are required to overcome the latter and to increase the spatial resolution, but observations are progressively more challenging due to the reduced flux density at higher frequencies. Optical interferometry, on the other hand, can spatially resolve the system at sub-mas scales (Fig. 2(d));

3. radio non-thermal emission does not lead to emission lines; in contrast, systems with significant outflows can have strong emission lines in the NIR, which are paramount to obtaining sub-beam ($\lesssim 100\mu$as) resolution as well as velocity information through spectral differential optical interferometry.

1.3.3 The GRAVITY instrument

GRAVITY (Eisenhauer et al., 2011; Gravity Collaboration et al., 2017) is a second-generation beam combiner at the Very Large Telescope Interferometer (VLTI) in ESO Paranal, Chile (Fig. 3), operating in the NIR K band ($2 - 2.5\mu$m). It combines the light from either the four 8.2m Unit Telescopes (UT) or the four 1.8 m Auxiliary Telescope (AT) with baselines up to ≈ 130 m in order to achieve a spatial resolution of ≈ 3 mas. In order to overcome the short atmospheric coherence times at near-infrared wavelengths and allow longer integrations, GRAVITY makes use of a dual-field approach. Two independent single-mode fibers at each telescope point to the same or different objects within the field-of-view (2" for the UTs and 4" for the ATs). One of the fibers feeds the fringe tracker (FT), which measures the fringe phase at very high frequencies ≈ 1 kHz in order to track the atmospheric delays. The corresponding correction is applied in real-time to the optical path length of the other fiber, which feeds the science (SC) channel. This allows for long coherent integrations (up to 100 s) in the latter, necessary to measure visibilities for fainter (up to $K \lesssim 18$) objects or at high spectral resolution ($R = 4000$). With the UTs, GRAVITY can fringe track on sources as faint as $K \lesssim 11$.

The success of GRAVITY relies on the innovative characteristics of its many subsystems. (e.g. Pfuhl et al., 2014; Lippa et al., 2016; Scheithauer et al., 2016; Anugu et al., 2018; Perraut et al., 2018; Lacour et al., 2019). A pupil-guiding system, working in the NIR H band and based on laser beacons installed at the telescope spiders, stabilizes the field and images it to an acquisition camera. An integrated optics (IO) chip, created to work in the NIR K band especially for GRAVITY, realizes the splitting and interference of the beams through phase-shifting fringe sampling. A metrology system, based on laser beams which are sent back from the IO to the primary mirror of the telescope, controls the differential optical path difference between the FT and SC objects, allowing the measurement of the phase difference between them. Finally, GRAVITY makes use of adaptive optics (AO) in order to feed the light to the fibers (whose mode size FWHM ≈ 50 mas is matched to the

PSF of the UTs). It can use either the MACAO system (operating at visual wavelengths) or the CIAO system (operating at NIR wavelengths), which was developed for GRAVITY. The AO system consists of wavefront sensors (WFS) of Schack-Hartmann design which compute the wavefront corrections and send them to a deformable mirror.

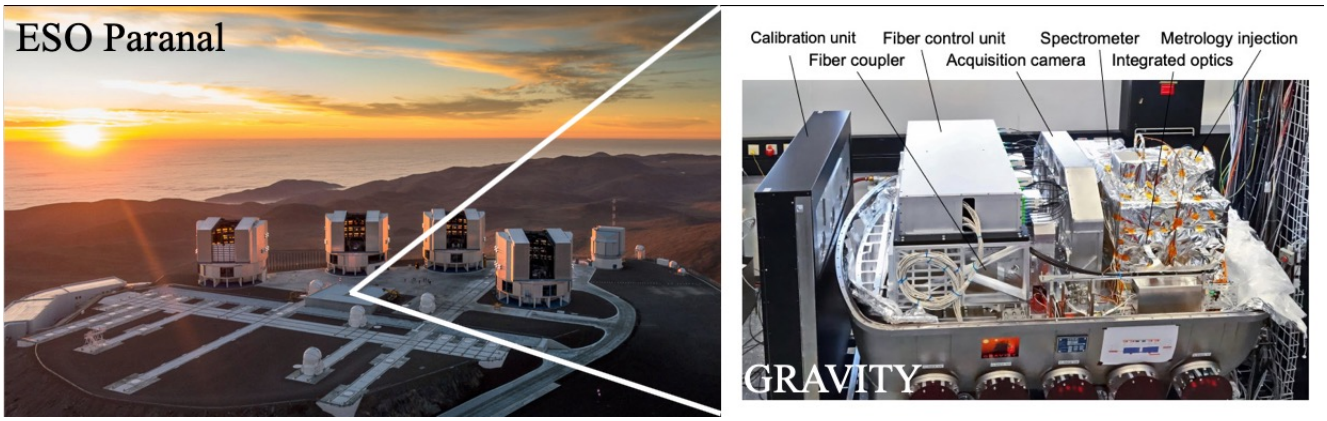

Figure 1.3: ESO Paranal observatory in Atacama, Chile. GRAVITY is located underground, and combines the light from either the four Unit Telescopes or the four Auxiliary Telescopes in order to perform optical interferometry. Image credit: http://www.atacamaphoto.com/search/index.php?/Themes/paranal/DSC4045.jpg and Gravity Collaboration et al. (2017).

GRAVITY can provide the following set of interferometric observables:

1. visibility amplitudes, corresponding to the amplitude of the interference fringe;
2. visibility phase of the SC object relative to the FT object (in dual field mode), which requires a nearby ($\lesssim 4$") source in the field;
3. closure phases, which correspond to the sum of the visibility phases across a closed triangle of baselines. This quantity is independent of telescope-based phase errors, such as the atmospheric phase disturbances which corrupt the visibility phases;
4. in case of high spectral resolution, differential visibility amplitudes and phases across emission or absorption lines. These quantities carry information about the image of the line relative to the continuum (e.g. their relative sizes and centroid offsets). The robustness of these measurements, resulting from their differential nature, provides spatial information on scales much smaller than the size of the beam, up to $\lesssim 10\mu$as.

This thesis is concerned with GRAVITY observations of the Galactic Center and of the X-ray binaries BP Cru and SS 433.

1. in the case of the Galactic Center, the observations were performed in dual-field mode, with the FT channel on a bright star (e.g. IRS16C or IRS13NE) and the SC channel on SgrA* or S2 at low spectral resolution ($R = 20$), using the CIAO system for AO. During the observations concerned in this thesis (2017-2018), S2 and SgrA* were close enough that both of their lights were fed into the SC fiber, so that an interferometric binary results. The SC channel provides visibility amplitudes and closure phases, which can be used for model fitting. With a well-controlled model and enough precision in the measured visibilities, a precision $\lesssim 50\mu$as in the separation between the two objects is typically achieved. In the future, when SgrA* and S2 are far enough apart, the differential phases between S2 and SgrA* will allow to measure their separation directly, with $\sim 10\mu$as astrometric precision per 1^o phase precision.

2. In the case of X-ray binaries, the observations were performed in single-field mode (i.e. the FT and the SC objects are the same) and at high spectral resolution ($R = 4000$), using the MACAO system for AO. The FT channel provides visibility amplitudes and closure phases for the NIR continuum, while the SC channel provides differential visibility amplitudes and phases across emission lines. This allows spatially and velocity resolved studies of their circumstellar environment and outflows.

1.4 This thesis

This thesis is centered on optical interferometric observations and data analysis related to the Galactic Center and X-ray binaries. In addition, it also includes simulations of relativistic stellar orbits and spectroscopic analysis of the baryonic jet in SS 433 with the X-shooter instrument.

1. Chapter 2 develops the interferometric binary model that has been used to fit the S2-SgrA* GRAVITY data. It includes physical and instrumental effects that must be included in order to achieve the required astrometric precision $\lesssim 10-50\mu$as necessary to detect GR effects and orbital motion of heated gas close to the black hole. These include bandwidth smearing due to the limited spectral resolution and large binary separation, wavelength-dependent flux ratios due to objects with different color, and telescope-dependent flux ratios due to different AO performance and fiber position accuracy between different telescopes.

2. Chapter 3 presents simulations of relativistic stellar orbits in a Kerr metric in order to investigate the prospects of measuring the spin of SgrA* through astrometric monitoring of a putative star on a close orbit within that of S2. For that we use a customized semi-analytic code to create a grid in semi-major axis and eccentricity, and proceed by fitting simulated orbits for a realistic $\lesssim 4-10$ years observing campaign in order to take into account the masking of GR effects by the unknown orbital parameters. We combine these results with the known properties of the nuclear star cluster in order to estimate the expected number of stars detectable by GRAVITY

that would allow a measurement of spin within this timescale, and conclude that for a give detected star there is a $\sim 10\%$ probability of success. We also investigate the impact of spectroscopic measurements with a precision ~ 50 km/s for the detection of spin effects.

3. Chapter 4 presents GRAVITY observations and data analysis of the HMXB BP Cru taken during commissioning of the instrument in 2016. We spatially resolve the wind emission lines from the blue hypergiant donor star through spectral differential interferometry, and show that they are both extended and distorted. We suggest that this is due to the effects of the gravitational and radiation fields of its companion accreting pulsar, which focuses the wind into a dense stream and ionizes its surrounding environment. In this chapter, we also show how differential visibility amplitudes and phases can be converted to model-independent information about the first and second moments of the image.

   Chapters 5 and 6 present a set of GRAVITY observations of SS 433 taken in 2017, after a first observation in 2016 during commissioning of the instrument (Gravity Collaboration et al., 2017).

4. Chapter 5 presents GRAVITY observations and data analysis of the NIR continuum and Brγ stationary line of the microquasar SS 433. The emission line is resolved into an extended (≈ 1 mas $= 5$ AU) equatorial (perpendicular to the jets) structure with a strong rotation component. By modeling the velocity and spatially resolved emission, we show that the structure cannot correspond to a stable disk in Keplerian rotation, because it would imply an unrealistically large enclosed mass $\sim 400 M_{\odot}$. Instead, we interpret it as a super-Keplerian equatorial outflow, implying that (i) the binary loses substantial mass and angular momentum through such outflow (ii) an efficient transfer of specific angular momentum between the binary and the disk must take place. In addition, we resolve an additional very extended ≈ 6 mas $= 30$ AU spherical line emission envelope which engulfs the binary.

5. Chapter 6 presents GRAVITY observations and data analysis of the optical baryonic jets in SS 433. We detect the change in spatial morphology of the jets over consecutive nights for the first time, and suggest that the smooth, extended profiles of the jets are indicative of photoionization by collimated radiation as the heating mechanism. We then use complementary X-shooter spectroscopic observations that contain up to twenty hydrogen and helium emission lines from the baryonic jets to model their properties as well as those of the ionizing radiation with the spectral synthesis code `Cloudy`. We conclude that there is indeed collimated UV radiation in SS 433 (not just thermal downgrading at low latitudes), with an inferred luminosity of $\sim 10^{41}$ erg/s for an observer looking through the jets. We also constrain the extinction in SS 433, and suggest there is substantial and structured circumstellar extinction around it.

Chapter 2

Interferometric Binary SgrA*-S2 Model

In this chapter, we describe and illustrate the interferometric binary model that has been used to measure the separation between SgrA* and S2 in GRAVITY 2017-2019 data.

2.1 Motivation

The motivation for measuring the most accurate possible S2-SgrA* separation is twofold:

1. On the one hand, it allows for the detection of general relativistic effects. As an example, the superior astrometry provided by GRAVITY has been key to the very significant detection of gravitational redshift in the orbit of S2 (Gravity Collaboration et al., 2018a, 2019). Although a purely spectroscopic effect ($\approx$ 200 km/s redshift during periastron passage), the constraining power of the astrometry was crucial to overcome the masking of the relativistic effect by degeneracies with the orbital parameters, which must be simultaneously fit. A detection of the general relativistic Schwarzschild precession effect, which directly impacts the astrometry, is expected by the end of 2019.

2. A very precise differential (and therefore more robust to systematic errors) astrometry $\lesssim 20\mu$as between S2 and SgrA* can be obtained during NIR flares, which last $\sim 30-60$ min. This technique allowed the detection of clockwise looped motion of the centroid emission of SgrA* on scales $\sim 3R_S$ during bright flares, close to the expected location of the innermost stable circular orbit (ISCO) of a Schwarzschild black hole (Gravity Collaboration et al., 2018b). The detection of relativistic rotation at these scales constrains the scale of concentration of a mass $\approx 4 \times 10^6 M_\odot$ from $\sim 1000R_S$ (derived from the orbit of S2 e.g. Gillessen et al., 2017) to $\sim 3R_S$, strengthening the case of a supermassive black hole in the Galactic Center. When combined with polarization information, we can use the astrometry of the flares to map out the magnetic field structure close to the black hole.

2.2 Single-field vs Dual-field

With a semi-major axis $a \approx 125$ mas and eccentricity $e \approx 0.88$, the projected distance between S2 and SgrA* varies from ≈ 10 mas to ≈ 180 mas along its ≈ 16 yr orbit. This leads to two possible techniques to measure the separation S2-SgrA* with GRAVITY, depending on how the current separation compares with the FWHM of the GRAVITY single-mode fiber of ≈ 50 mas:

1. dual-field approach: if the separation is $\gtrsim 75$ mas, each source can be observed independently and, ideally, would look like a point source. In this case, the differential visibility phase $\Delta\phi$ between the two can be directly converted to a separation on sky $\boldsymbol{\Delta x}$:

$$\Delta\phi = -2\pi \boldsymbol{u} \cdot \boldsymbol{\Delta x} \tag{2.2.1}$$

   where $\boldsymbol{u} = \frac{\boldsymbol{B}}{\lambda}$ and $\boldsymbol{B}$ is the projected baseline. Therefore, a minimum of two baselines already provides the separation. For $|\boldsymbol{B}| \sim 100$ m and $\lambda \sim 2\mu$m, an error $\delta(\Delta\phi) \sim 1^o$ leads to an astrometric error $\delta(\Delta x) \approx 10\mu$as. This is the envisioned mode to measure the separation relative to the FT reference source.

2. single-field approach: if the separation is $\lesssim 75$ mas, both sources will be included in the interferometric field-of-view, so that an interferometric binary results. In this case, a separation can be measured directly from the more canonical interferometric observables, namely the visibility amplitudes and closure phases. It turned out that SgrA* is almost always detected with GRAVITY ($\sim 90\%$ of the time) during these initial years, so that single-field techniques are not only useful but also required.

When GRAVITY first started observing the Galactic Center in 2016, the separation was transitioning from regime 1 to 2. During 2017-2019, it fell under regime 2. This chapter describes the binary interferometric model that has been used to obtain the separation SgrA*-S2 during these first years.

2.3 Basic interferometric binary model

The binary model is one of the canonical models in interferometry. For given components a (SgrA*) and b (S2), the coherent flux is simply

$$\mathscr{F}(\boldsymbol{u}) = \mathscr{F}_a(\boldsymbol{u}) + \mathscr{F}_b(\boldsymbol{u}) = F_a + F_b e^{-2\pi i s/\lambda} \tag{2.3.1}$$

where F_a and F_b are the fluxes, $s = \boldsymbol{B} \cdot \boldsymbol{\Delta x}$ is the OPD in microns, $\boldsymbol{B}$ is the projected baseline in meters and $\boldsymbol{\Delta x}$ is the separation vector in angular units. The visibility is therefore:

$$V(\boldsymbol{u}) = \frac{\mathscr{F}(\boldsymbol{u})}{\mathscr{F}(\boldsymbol{0})} = \frac{1 + f e^{-2\pi i s/\lambda}}{1 + f} \tag{2.3.2}$$

where $f = \frac{F_b}{F_a}$ is the flux ratio. Although very simple in principle, there are a number of additional instrumental and physical effects that must be introduced in order to obtain accurate modeling in the special case of the Galactic Center.

2.4 Additional effects

In the following, we describe the additional effects included in the binary model. To illustrate the impact of each effect on the data, we show a comparison of the visibility amplitudes and closure phases with the effect turned on and off, for a given mock observation. For that we adopt the following parameters:

1. a uv coverage as taken from an observation file
2. a spectral resolution $R = \frac{\lambda}{\Delta\lambda} = 20$
3. a separation S2-SgrA* of (-50,40) mas
4. a flux ratio S2/SgrA* at 2.2μm $f = 2.0$
5. a color of SgrA* $\nu F_\nu \propto \nu^\alpha$ with $\alpha = 1$
6. a flux ratio of background to SgrA* $f_{bg} = 0$

Fig. 2.1 shows the baselines projected on the sky plane, with their projected sizes indicated, as well as the positions of SgrA* and S2 for this mock observation.

2.4.1 Bandwidth Smearing

The low spectral resolution ($R = 20$) and the large separation (especially in 2017) lead to attenuation of the coherent flux from S2 due to bandwidth smearing (e.g. Thompson et al., 2017). This arises due to the integration of the coherent flux over a large wavelength range. To get an idea of the importance of the effect, we can assume the flux density F_ν is constant over the bandpass:

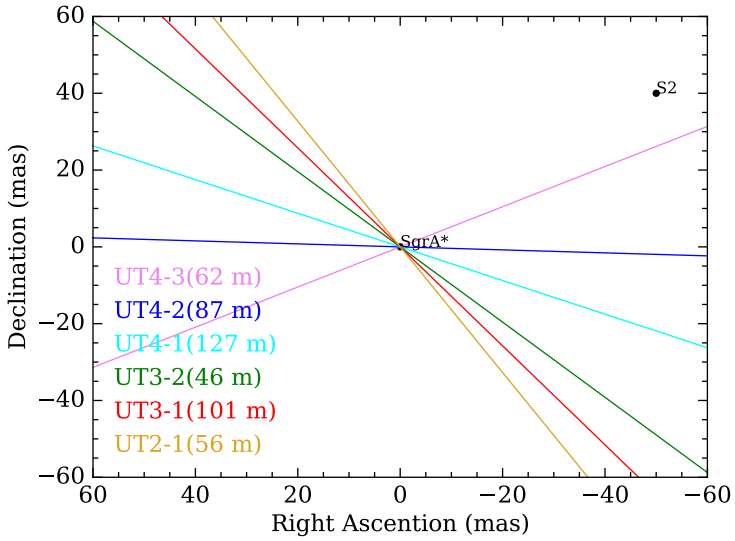

Figure 2.1: Baselines projected on the sky plane (with projected lengths indicated) for the mock observation.

$$\int_{\nu_0-\frac{\Delta\nu}{2}}^{\nu_0+\frac{\Delta\nu}{2}} F_\nu e^{-2\pi i s\frac{\nu}{c}} d\nu \tag{2.4.1}$$

$$\approx F_\nu \int_{\nu_0-\frac{\Delta\nu}{2}}^{\nu_0+\frac{\Delta\nu}{2}} e^{-2\pi i s\frac{\nu}{c}} d\nu \tag{2.4.2}$$

$$= F_\nu \Delta\nu \,\mathrm{sinc}\left(\frac{s\Delta\nu}{c}\right) e^{-2\pi i s\frac{\nu_0}{c}} \tag{2.4.3}$$

$$= F_\lambda \Delta\lambda \,\mathrm{sinc}\left(\frac{s\Delta\lambda}{\lambda_0^2}\right) e^{-2\pi i s/\lambda_0} \tag{2.4.4}$$

$$= F_\lambda \Delta\lambda \,\mathrm{sinc}\left(\frac{s}{\lambda_0 R}\right) e^{-2\pi i s/\lambda_0} \tag{2.4.5}$$

where $F_\lambda = F_\nu \frac{c}{\lambda_0^2}$, $\Delta\lambda = \Delta\nu \frac{c}{\lambda_0^2}$ and $R = \frac{\lambda_0}{\Delta\lambda}$. The quantity $0.6\frac{\lambda_0 R}{B}$ defines the so-called "interferometric field-of-view" i.e. the projected separation for which the visibility is reduced by 50%. For $B \sim 100$ m, $\lambda_0 \sim 2\mu$m and $R = 20$, this corresponds to ≈ 50 mas.

For a flux density $F_\lambda \propto \lambda^\gamma$, the integral above becomes

$$\int_{\lambda_0-\frac{\Delta\lambda}{2}}^{\lambda_0+\frac{\Delta\lambda}{2}} F_\lambda e^{-2\pi i\frac{s}{\lambda}} d\lambda \tag{2.4.6}$$

$$\propto (2\pi)^{1+\gamma}\left(\frac{is}{\lambda}\right)^{1+\gamma} \lambda^{1+\gamma}\mathrm{Gamma}\left(-1-\gamma, \frac{2\pi i s}{\lambda}\right)\Big|_{\lambda_0-\frac{\Delta\lambda}{2}}^{\lambda_0+\frac{\Delta\lambda}{2}} \tag{2.4.7}$$

where Gamma is the incomplete gamma function.

Fig. 2.2 shows a comparison of visibility amplitudes and closure phases for the model with (full lines) and without (dashed lines) bandwidth smearing. Note that the effect is strongest for baselines for which the projected separation S2-SgrA* is large i.e. the baselines which are the best for measuring the separation, and that it also affects the closure phases.

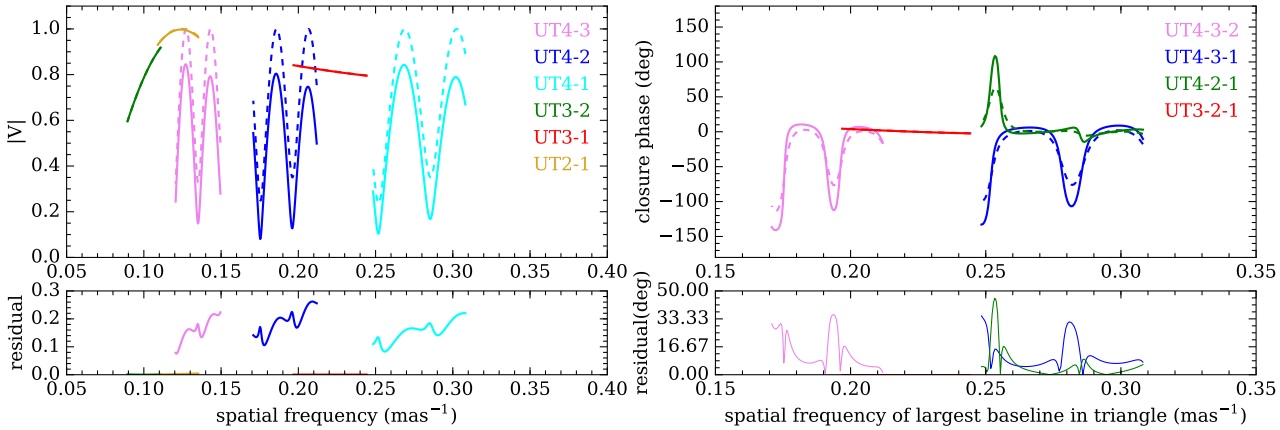

Figure 2.2: Comparison of visibility amplitudes and closures phases for a model with (full lines) and without (dashed lines) bandwidth smearing. The bottom panels show the residuals.

2.4.2 Bandpass shape

The different wavelength channels for each baseline can have slightly different bandpass shapes, which will affect the model. These shapes have been measured by inverse Fourier transform of the coherence loss for a point source calibrator as a function of OPD, and approximated as a tophat bandpass with a given spectral resolution. Fig. 2.3 shows a comparison of visibility amplitudes and closures phases for a model with a uniform spectral resolution ($R = 20$) for all wavelength channels (full lines) and with variable spectral resolutions per wavelength channel and per baseline as measured in the instrument (dashed lines). Note that the effect can be especially important for the closure phases.

2.4.3 Completely resolved background

A completely resolved background is added to the fit because, empirically, the visibility amplitudes do not reach unity. This background could have either

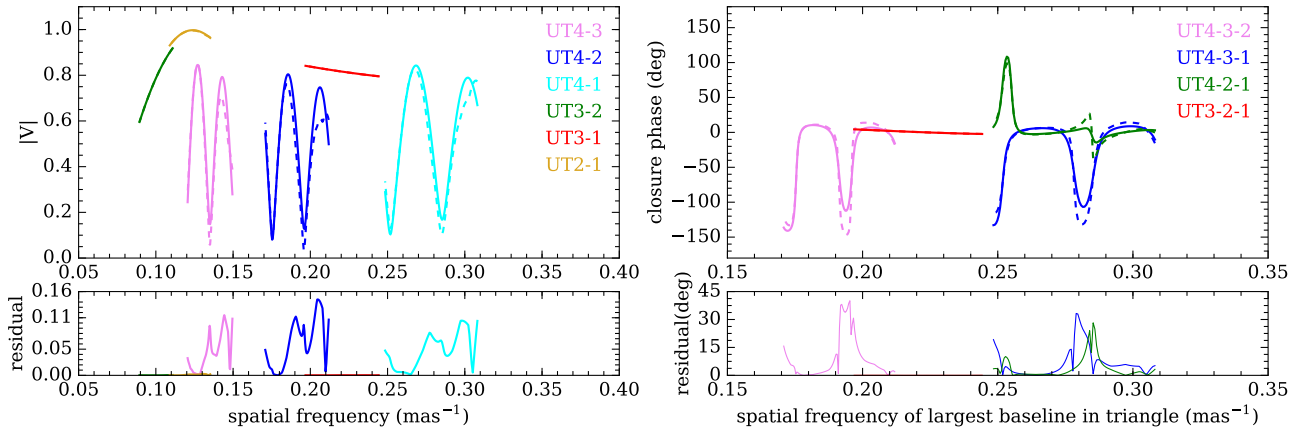

Figure 2.3: Comparison of visibility amplitudes and closures phases for a model with a uniform spectral resolution ($R = 20$) for all wavelength channels (full lines) and with variable spectral resolutions per wavelength channel and per baseline as measured in the instrument (dashed lines). The bottom panels show the residuals.

1. a real origin, such as diffuse gas or a population of many faint sources;
2. a systematic error origin, such as residual from sky subtraction or other forms of coherence loss.

With such a background, the visibility becomes

$$V(\boldsymbol{u}) = \frac{\mathscr{F}(\boldsymbol{u})}{\mathscr{F}(\boldsymbol{0})} = \frac{1 + f e^{-2\pi i s/\lambda}}{1 + f + f_{bg}} \tag{2.4.8}$$

where $f_{bg} = \frac{F_{bg}}{F_a}$. The background contributes to the total but not the correlated flux and so leads to a uniform reduction of the visibility amplitude at all baselines. It has no effect on the closure phases. Fig. 2.4 shows a comparison of visibility amplitudes and closures phases for a model without (full lines) and with a completely resolved background (dashed lines) with $f_{bg} = 0.5$. The very small difference in closure phases is due to numerical errors.

2.4.4 Color of SgrA*

Because S2 and SgrA* have different colors, the flux ratio between them is wavelength-dependent. S2 is a hot star so that in the NIR its flux density

$$\nu F_\nu \propto \nu^3 \Rightarrow F_\lambda \propto \lambda^{-4} \tag{2.4.9}$$

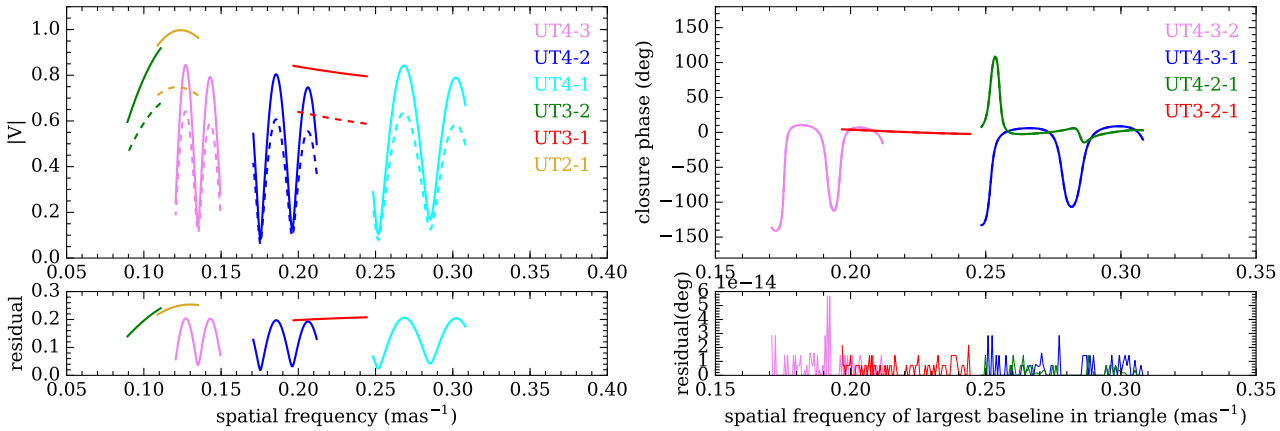

Figure 2.4: Comparison of visibility amplitudes and closures phases for a model without (full lines) and with a completely resolved background (dashed lines). The bottom panels show the residuals.

SgrA* is redder than S2 but has a variable color. We parametrize it as

$$\nu F_\nu \propto \nu^\alpha \Rightarrow F_\lambda \propto \lambda^{-1-\alpha} \tag{2.4.10}$$

with α varying from ~ -4 to 1, converging towards ~ 0.5 for bright flares (Eisenhauer et al., 2005; Hornstein et al., 2007). For the most extreme case, the flux ratio may therefore vary by up to $\sim \left(\frac{2.5}{2.0}\right)^7 \sim 5$ over the K band.

Fig. 2.5 shows a comparison of visibility amplitudes and closures phases for a model with $\alpha = 1$ (full lines) and with $\alpha = -3$ (dashed lines). Although the effect is minor on the visibility amplitudes, it can be very important for the closure phases, because they flip signs when the brightest component changes. Therefore, if such a flip occurs within the K band, it should manifest clearly in the closure phase.

2.4.5 Variable flux ratios per telescope

Because of the large separation, the amount of flux from each source that is coupled into the fiber is sensitive to the fiber position as well as to the shape of the PSF away from the center. Therefore, if the fiber position for a given telescope(s) is offset, or if the AO correction is different for different telescopes, the flux ratio between S2 and SgrA* will be different for each telescope. In order to include this effect, one has to go back and re-derive the coherent flux from first principles.

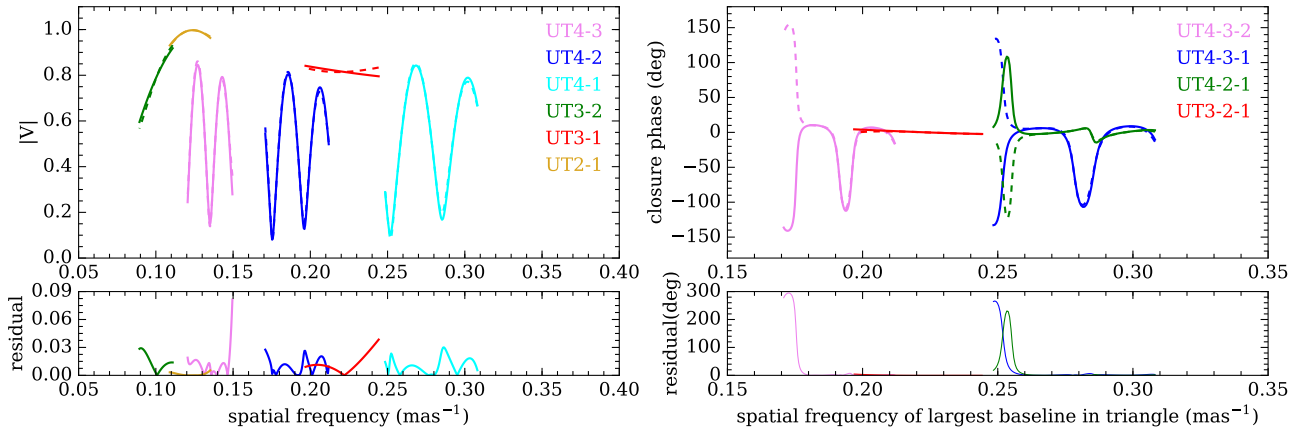

Figure 2.5: Comparison of visibility amplitudes and closures phases for a model with $\alpha = 1$ (full lines) and with $\alpha = -3$ (dashed lines), where α is the color of SgrA*. The bottom panels show the residuals.

We denote $F_{1,a}$ for the flux of object a at telescope 1. Consider a baseline formed by telescopes 1 and 2. A single star a will produce the following interference pattern on the "detector":

$$i(x) = F_{1,a} + F_{2,a} + 2\sqrt{F_{1,a}F_{2,a}}\,\mathrm{Re}[e^{-2\pi i \boldsymbol{\sigma_a}\cdot\boldsymbol{u}} e^{2\pi i p x}] \tag{2.4.11}$$

where $\boldsymbol{\sigma_a}$ is the separation of star a from the phase center, $\boldsymbol{u}$ is the (u,v) coordinate, x is position on the "detector" and p is the (purely instrumental) fringe frequency on the "detector".

Light from two stars is incoherent so if we add star b the pattern is simply:

$$i(x) = F_{1,a} + F_{2,a} + 2\sqrt{F_{1,a}F_{2,a}}\,\mathrm{Re}[e^{-2\pi i \boldsymbol{\sigma_a}\cdot\boldsymbol{u}} e^{2\pi i p x}] + \tag{2.4.12}$$

$$F_{1,b} + F_{2,b} + 2\sqrt{F_{1,b}F_{2,b}}\,\mathrm{Re}[e^{-2\pi i \boldsymbol{\sigma_b}\cdot\boldsymbol{u}} e^{2\pi i p x}] \tag{2.4.13}$$

From this, we can compute the normalized visibility in the following way:

$$V(\boldsymbol{u}) = \frac{2\sqrt{F_{1,a}F_{2,a}}e^{-2\pi i \boldsymbol{\sigma_a}\cdot\boldsymbol{u}} + 2\sqrt{F_{1,b}F_{2,b}}e^{-2\pi i \boldsymbol{\sigma_b}\cdot\boldsymbol{u}}}{2\sqrt{F_{1,a}+F_{1,b}}\sqrt{F_{2,a}+F_{2,b}}} \tag{2.4.14}$$

See the appendix for the explanation for the form of the denominator. Essentially, it comes from using the individual telescope fluxes (which can be measured from the "DC" part of the flux) and corrects for flux imbalance between the telescopes.

It is easy to check that one recovers the usual binary expression when $F_{1,a} = F_{2,a}$ and $F_{1,b} = F_{2,b}$. Note also that if $\frac{F_{1,b}}{F_{1,a}} = \frac{F_{2,b}}{F_{2,a}} = f$ i.e. the images on the two telescopes are

the same but each telescope might have a different injection, one again recovers the usual binary expression:

$$V(\boldsymbol{u}) = \frac{e^{-2\pi i \boldsymbol{\sigma_a}\cdot\boldsymbol{u}} + f e^{-2\pi i \boldsymbol{\sigma_b}\cdot\boldsymbol{u}}}{1+f} \tag{2.4.15}$$

Back to the full expression 2.4.14, $V(\boldsymbol{u})$ should not depend on any absolute flux, so we should be able to express the result in terms of flux ratios. Let's call a SgrA* and b S2. We define:

1. $f_a = \frac{F_{2,a}}{F_{1,a}}$ i.e. the ratio of SgrA* flux between the two telescopes
2. $f_{1,b} = \frac{F_{1,b}}{F_{1,a}}$ i.e. the flux ratio S2/SgrA* for telescope 1
3. $f_{2,b} = \frac{F_{2,b}}{F_{2,a}} = \frac{F_{2,b}}{F_{1,a}}\frac{1}{f_a}$ i.e. the flux ratio S2/SgrA* for telescope 2

Then it follows that

$$\boxed{V(\boldsymbol{u}) = \frac{e^{-2\pi i \boldsymbol{\sigma_a}\cdot\boldsymbol{u}} + \sqrt{f_{1,b} f_{2,b}} e^{-2\pi i \boldsymbol{\sigma_b}\cdot\boldsymbol{u}}}{\sqrt{1+f_{1,b}}\sqrt{1+f_{2,b}}}} \tag{2.4.16}$$

Note that f_a drops out (essentially, there is an extra constraint from being able to measure individual telescope fluxes) and that $|V(\mathbf{0})| \neq 1$ if $f_{1,b} \neq f_{2,b}$. Note also that variable flux ratios will affect both the visibility amplitude as well as the phase.

Fig. 2.6 shows a comparison of visibility amplitudes and closures phases for a model where the flux ratios S2/SgrA* per telescope are uniform (full lines) and one where the flux ratio was increased and decreased by 50% for UT2 and UT4, respectively. The effect is stronger on the closure phases.

2.5 Full binary model

We now derive the full form of the binary model taking into account all the effects above. We start with the expression for the complex visibility in the case of variable flux ratios per telescope for a binary model:

$$V(\boldsymbol{u}) = V(u,\lambda) = \frac{\sqrt{F_{1,a}F_{2,a}} e^{-2\pi i \boldsymbol{\sigma_a}\cdot\boldsymbol{u}} + \sqrt{F_{1,b}F_{2,b}} e^{-2\pi i \boldsymbol{\sigma_b}\cdot\boldsymbol{u}}}{\sqrt{F_{1,a}+F_{1,b}}\sqrt{F_{2,a}+F_{2,b}}} \tag{2.5.1}$$

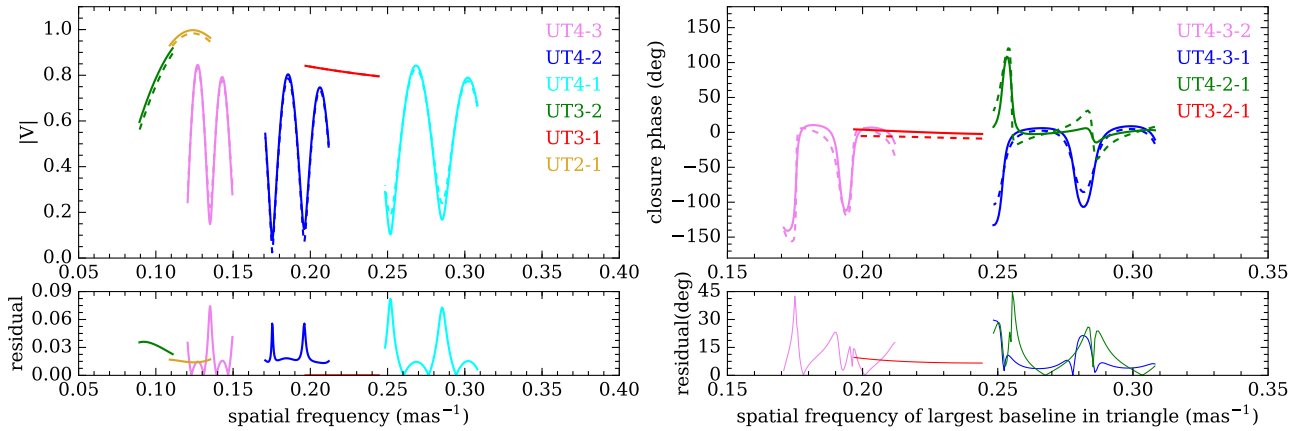

Figure 2.6: Comparison of visibility amplitudes and closures phases for a model where the flux ratios S2/SgrA* per telescope are uniform (full lines) and one where the flux ratio was increased and decreased by 50% for UT2 and UT4, respectively. The bottom panels show the residuals.

(2.4.14 above). From now on, a will refer to SgrA* and b will refer to S2. F refers to the flux, $\boldsymbol{\sigma_i}$ is the separation of component i from the phase center (in mas), and $\boldsymbol{u} = \frac{\boldsymbol{B}}{\lambda}$ is the uv-coordinate (in 1/mas) of the given baseline at the given wavelength.

We will expand this expression to include a completely resolved background flux. The background flux does not affect the coherent flux (numerator) so it will simply add to the total flux in the denominator:

$$V(\boldsymbol{u}) = V(u,\lambda) = \frac{\sqrt{F_{1,a}F_{2,a}}e^{-2\pi i\boldsymbol{\sigma_a}\cdot\boldsymbol{u}} + \sqrt{F_{1,b}F_{2,b}}e^{-2\pi i\boldsymbol{\sigma_b}\cdot\boldsymbol{u}}}{\sqrt{F_{1,a}+F_{1,b}+F_{1,bg}}\sqrt{F_{2,a}+F_{2,b}+F_{2,bg}}} \tag{2.5.2}$$

We will now write the complex visibility as a function of $\boldsymbol{B}$ (the baseline vector, in meters) for a given bandpass shape, $P = P(\lambda)$. Because we are integrating over wavelength, the F will now refer to the flux density i.e. $F_{i,j} = F_{i,j}(\lambda)$. Therefore we have:

$$V(\boldsymbol{B},P) = \frac{\int P(\lambda)\left(\sqrt{F_{1,a}(\lambda)F_{2,a}(\lambda)}e^{-2\pi i\boldsymbol{\sigma_a}\cdot\boldsymbol{B}/\lambda} + \sqrt{F_{1,b}(\lambda)F_{2,b}(\lambda)}e^{-2\pi i\boldsymbol{\sigma_b}\cdot\boldsymbol{B}/\lambda}\right)d\lambda}{\sqrt{\int P(\lambda)(F_{1,a}(\lambda)+F_{1,b}(\lambda)+F_{1,bg}(\lambda))d\lambda}\sqrt{\int P(\lambda)(F_{2,a}(\lambda)+F_{2,b}(\lambda)+F_{2,bg}(\lambda))d\lambda}} \tag{2.5.3}$$

where the integrations over wavelength are from $-\infty$ to $+\infty$. We parametrize the flux densities

$$\nu F_\nu \propto \nu^\alpha \Rightarrow F_\lambda \propto \lambda^{-1-\alpha} \tag{2.5.4}$$

for all three sources (S2, SgrA* and background). We adopt the flux at 2.2μm as the reference:

$$F_{i,j}(\lambda) = F_{i,j}(2.2\mu m)\left(\frac{\lambda}{2.2\mu m}\right)^{-1-\alpha_j} = F_{i,j}(2.2\mu m)\lambda_{2.2\mu m}^{-1-\alpha_j} \tag{2.5.5}$$

The flux ratio S2/SgrA* for a telescope i is therefore

$$\frac{F_{i,b}(\lambda)}{F_{i,a}(\lambda)} = f_i \lambda_{2.2\mu m}^{-\alpha_b+\alpha_a} \tag{2.5.6}$$

where f_i is defined as the flux ratio at 2.2μm.

Similarly, the flux ratio background/SgrA* for a telescope i is therefore

$$\frac{F_{i,bg}(\lambda)}{F_{i,a}(\lambda)} = f_{bg,i}\lambda_{2.2\mu m}^{-\alpha_{bg}+\alpha_a} = f_{bg}\lambda_{2.2\mu m}^{-\alpha_{bg}+\alpha_a} \tag{2.5.7}$$

where again $f_{bg,i}$ is the value at 2.2μm. We assume that the flux ratio background/SgrA* does not depend on telescope.

We will now simply substitute these flux densities and flux ratio expressions to the main visibility expression.

The terms in the denominator are

$$\sqrt{\int P(\lambda)(F_{i,a}(\lambda) + F_{i,b}(\lambda) + F_{i,bg}(\lambda))d\lambda} \tag{2.5.8}$$

$$= \sqrt{\int P(\lambda)(F_{i,a} + F_{i,a}f_i\lambda_{2.2\mu m}^{-\alpha_b+\alpha_a} + F_{i,a}f_{bg}\lambda_{2.2\mu m}^{-\alpha_{bg}+\alpha_a})d\lambda} \tag{2.5.9}$$

$$= \sqrt{\int P(\lambda)F_{i,a}(1 + f_i\lambda_{2.2\mu m}^{-\alpha_b+\alpha_a} + f_{bg}\lambda_{2.2\mu m}^{-\alpha_{bg}+\alpha_a}))d\lambda} \tag{2.5.10}$$

$$= \sqrt{F_{i,a}(2.2\mu m)}\sqrt{\int P(\lambda)\lambda_{2.2\mu m}^{-1-\alpha_a}(1 + f_i\lambda_{2.2\mu m}^{-\alpha_b+\alpha_a} + f_{bg}\lambda_{2.2\mu m}^{-\alpha_{bg}+\alpha_a}))d\lambda} \tag{2.5.11}$$

The first term in the numerator is

$$\int P(\lambda)\sqrt{F_{1,a}(\lambda)F_{2,a}(\lambda)}e^{-2\pi i\boldsymbol{\sigma_a}\cdot\boldsymbol{B}/\lambda}d\lambda \tag{2.5.12}$$

$$= \sqrt{F_{1,a}(2.2\mu m)}\sqrt{F_{2,a}(2.2\mu m)}\int P(\lambda)\lambda_{2.2\mu m}^{-1-\alpha_a}e^{-2\pi i\boldsymbol{\sigma_a}\cdot\boldsymbol{B}/\lambda}d\lambda \tag{2.5.13}$$

The second term in the numerator is

$$\int P(\lambda)\sqrt{F_{1,b}(\lambda)F_{2,b}(\lambda)}e^{-2\pi i\boldsymbol{\sigma}\cdot\boldsymbol{B}/\lambda}d\lambda = \int P(\lambda)\sqrt{F_{1,a}f_1F_{2,a}f_2}\lambda_{2.2\mu m}^{-\alpha_b+\alpha_a}e^{-2\pi i\boldsymbol{\sigma}\cdot\boldsymbol{B}/\lambda}d\lambda \tag{2.5.14}$$

$$= \sqrt{F_{1,a}(2.2\mu m)}\sqrt{F_{2,a}(2.2\mu m)}\sqrt{f_1f_2}\int P(\lambda)\lambda_{2.2\mu m}^{-1-\alpha_a}\lambda_{2.2\mu m}^{-\alpha_b+\alpha_a}e^{-2\pi i\boldsymbol{\sigma}\cdot\boldsymbol{B}/\lambda}d\lambda \tag{2.5.15}$$

$$= \sqrt{F_{1,a}(2.2\mu m)}\sqrt{F_{2,a}(2.2\mu m)}\sqrt{f_1f_2}\int P(\lambda)\lambda_{2.2\mu m}^{-1-\alpha_b}e^{-2\pi i\boldsymbol{\sigma}\cdot\boldsymbol{B}/\lambda}d\lambda \tag{2.5.16}$$

We can cancel the factors of $\sqrt{F_{1,a}(2.2\mu m)}\sqrt{F_{2,a}(2.2\mu m)}$ (as we should be able to, since V should not depend on the absolute flux) to get

$$\boxed{V(\boldsymbol{B},P) = \frac{\langle\lambda_{2.2\mu m}^{-1-\alpha_a}e^{-2\pi i\boldsymbol{\sigma_a}\cdot\boldsymbol{B}/\lambda}\rangle + \sqrt{f_1f_2}\langle\lambda_{2.2\mu m}^{-1-\alpha_b}e^{-2\pi i\boldsymbol{\sigma}\cdot\boldsymbol{B}/\lambda}\rangle}{\sqrt{\langle\lambda_{2.2\mu m}^{-1-\alpha_a}(1+f_1\lambda_{2.2\mu m}^{-\alpha_b+\alpha_a}+f_{bg}\lambda_{2.2\mu m}^{-\alpha_{bg}+\alpha_a})\rangle}\sqrt{\langle\lambda_{2.2\mu m}^{-1-\alpha_a}(1+f_2\lambda_{2.2\mu m}^{-\alpha_b+\alpha_a}+f_{bg}\lambda_{2.2\mu m}^{-\alpha_{bg}+\alpha_a})\rangle}}} \tag{2.5.17}$$

where $\langle x\rangle := \int P(\lambda)xd\lambda$. It is useful to note that there are two types of integrals in the expression above. If we assume a tophat bandpass, they have (semi-)analytical forms:

$$\int_{\lambda_0-\frac{\Delta\lambda}{2}}^{\lambda_0+\frac{\Delta\lambda}{2}}\lambda_{2.2\mu m}^{\gamma}d\lambda = (2.2\mu m)^{-\gamma}\frac{\lambda^{1+\gamma}}{1+\gamma}\Big|_{\lambda_0-\frac{\Delta\lambda}{2}}^{\lambda_0+\frac{\Delta\lambda}{2}} \tag{2.5.18}$$

$$\int_{\lambda_0-\frac{\Delta\lambda}{2}}^{\lambda_0+\frac{\Delta\lambda}{2}}\lambda_{2.2\mu m}^{\gamma}e^{-2\pi i\frac{s}{\lambda}}d\lambda = (2.2\mu m)^{-\gamma}(2\pi)^{1+\gamma}\left(\frac{is}{\lambda}\right)^{1+\gamma}\lambda^{1+\gamma}\mathrm{Gamma}\left(-1-\gamma,\frac{2\pi is}{\lambda}\right)\Big|_{\lambda_0-\frac{\Delta\lambda}{2}}^{\lambda_0+\frac{\Delta\lambda}{2}} \tag{2.5.19}$$

where Gamma is the incomplete gamma function. For the case $\alpha_b = 3$ as appropriate for S2, the integral becomes

$$(2.2\mu m)^4\frac{1}{4s^3\pi^3\lambda^2}e^{-2\pi is/\lambda}(-2is^2\pi^2-2s\pi\lambda+i\lambda^2)\Big|_{\lambda_0-\frac{\Delta\lambda}{2}}^{\lambda_0+\frac{\Delta\lambda}{2}} \tag{2.5.20}$$

2.6 Examples

In the following, we show a few examples of the binary fit to real GRAVITY data. The fit is implemented in a Bayesian framework using Markov-chain Monte Carlo (MCMC) technique to estimate the errors, using the python module `emcee` (Foreman-Mackey et al., 2013). The files have a total exposure time of 5 min (30 collections of 10s coherent integrations).

2.6.1 Large separation in 2017

Fig. 2.7 shows the visibility amplitudes and closure phases for GRAVITY data and the corresponding best-fit binary model for file 2018-08-07T01:31. The separation $(-51.319, 17.823) \pm (0.010, 0.017)$ mas is measured to $\lesssim 20\mu$as precision (the scatter between different files throughout the night, however, shows that systematic errors $\sim 100\mu$as are dominant in the final measurement). The flux ratios are ~ 1 in the fiber; however, the true flux ratio is much larger because S2 is very attenuated due to the large separation. The strong effect of bandwidth smearing due to the latter is clearly visible in the visibility amplitude data. The flux ratios per telescope show variation; in particular, the flux ratio of telescope 1 is $\sim 3\times$ lower than the others, suggesting a fiber displacement in the opposite direction of S2 or a better AO correction than the other telescopes. Fig. 2.8 shows the full contour plots for this fit.

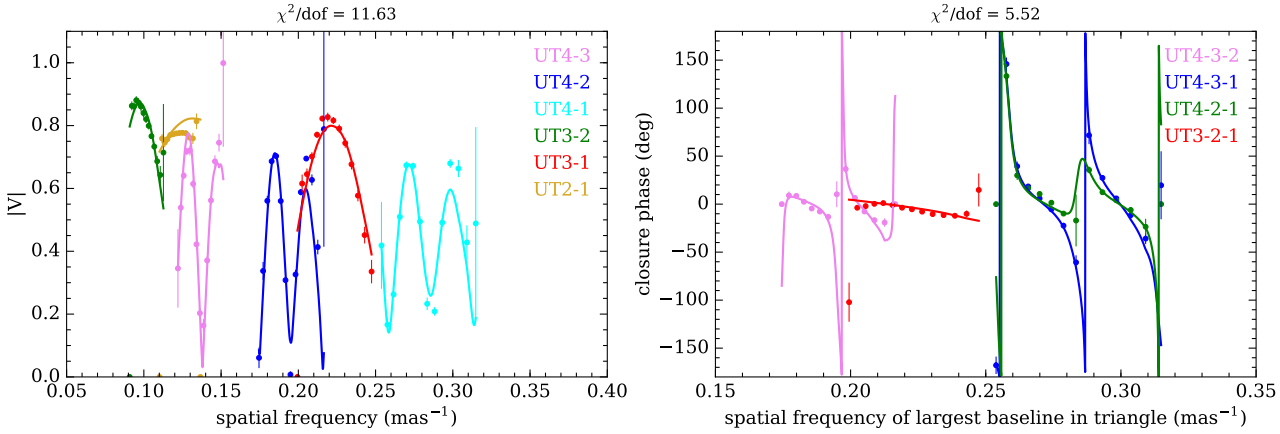

Figure 2.7: Visibility amplitudes and closure phases for GRAVITY data and best-fit S2-SgrA* binary model for the 2018-08-07T01:31 file.

2.6.2 Bright SgrA* in 2018

Fig. 2.9 shows the visibility amplitudes and closure phases for GRAVITY data and the corresponding best-fit binary model for file 2018-04-01T06:13. The separation $(-18.175, 12.699) \pm (0.018, 0.008)$ mas is measured to $\lesssim 20\mu$as precision. The separation is well within the fiber FWHM so that bandwidth smearing is not an important effect. The flux ratios per telescope are very similar, as expected when the two sources are very close. The flux of SgrA* is $\sim 40\%$ of S2 (corresponding to $m_K \approx 15$). Fig. 2.10 shows the full contour plots for this fit.

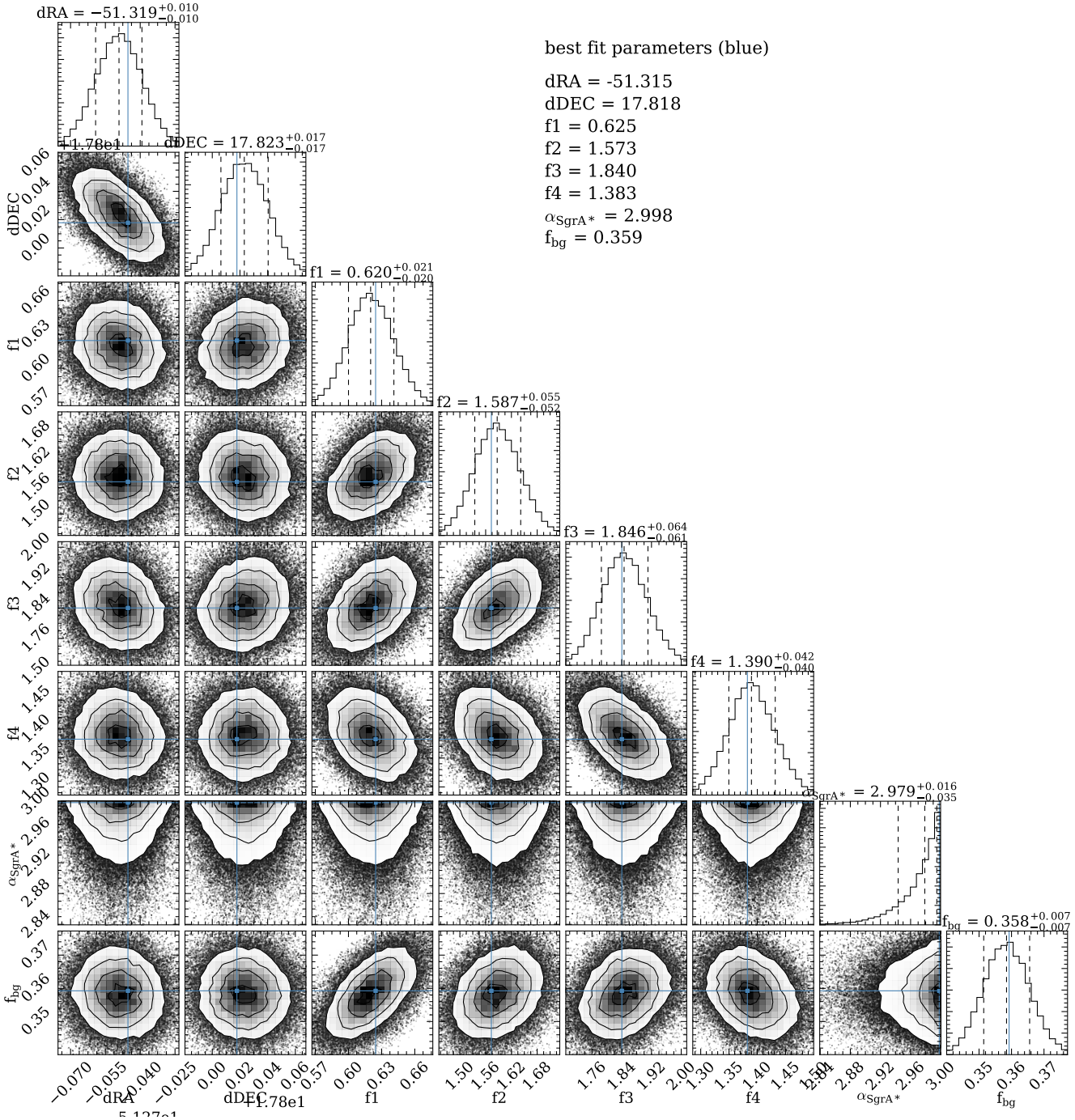

Figure 2.8: Visibility amplitudes and closure phases for GRAVITY data and best-fit S2-SgrA* binary model for the 2018-08-07T01:31 file.

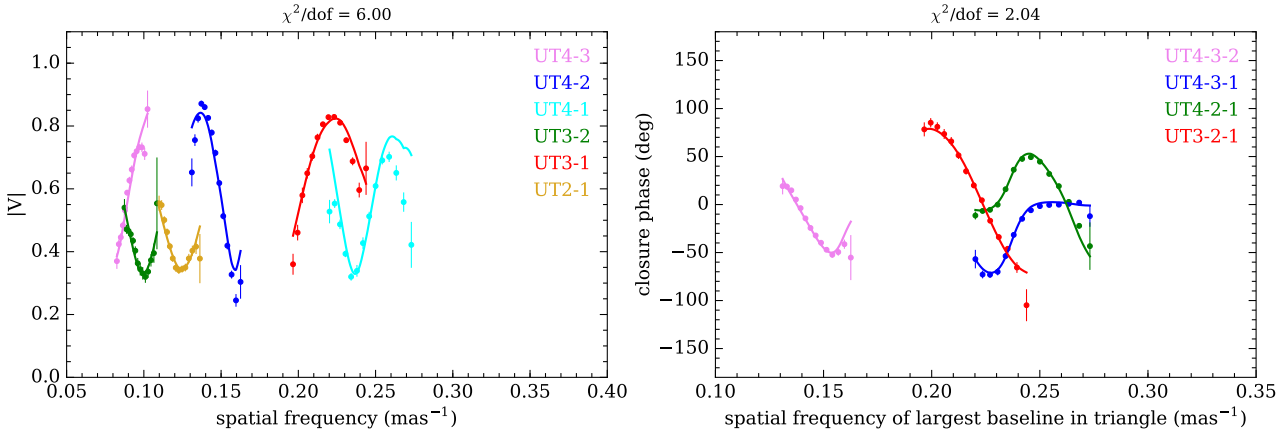

Figure 2.9: Visibility amplitudes and closure phases for GRAVITY data and best-fit S2-SgrA* binary model for the 2018-04-01T06:13 file.

2.6.3 Flaring SgrA* in 2018

Fig. 2.11 shows the visibility amplitudes and closure phases for GRAVITY data and the corresponding best-fit binary model for file 2018-07-23T00:12. This corresponds to one of the brightest flares observed in GRAVITY observations, with an intrinsic flux ratio ~ 1 (because of the small separation, attenuation effects are negligible). The separation $(22.934, 9.744) \pm (0.006, 0.005)$ mas is measured to an astounding $\lesssim 10\mu$as precision (again, the true error based on the scatter throughout the night is larger); however, the small fit error allows for unprecedented differential astrometry within close observations, which have allowed the detection of orbital motion in the centroid emission of SgrA* (Gravity Collaboration et al., 2018b). Fig. 2.12 shows the full contour plots for this fit.

Illustration of applications

Fig. 2.13 shows examples of the binary fitting results. The top left panel shows the S2 positions during periastron passage as derived from the GRAVITY data through binary fits. We note that these positions are the result of different implementations of binary fitting codes by different groups, which is important to estimate the true systematic-dominated

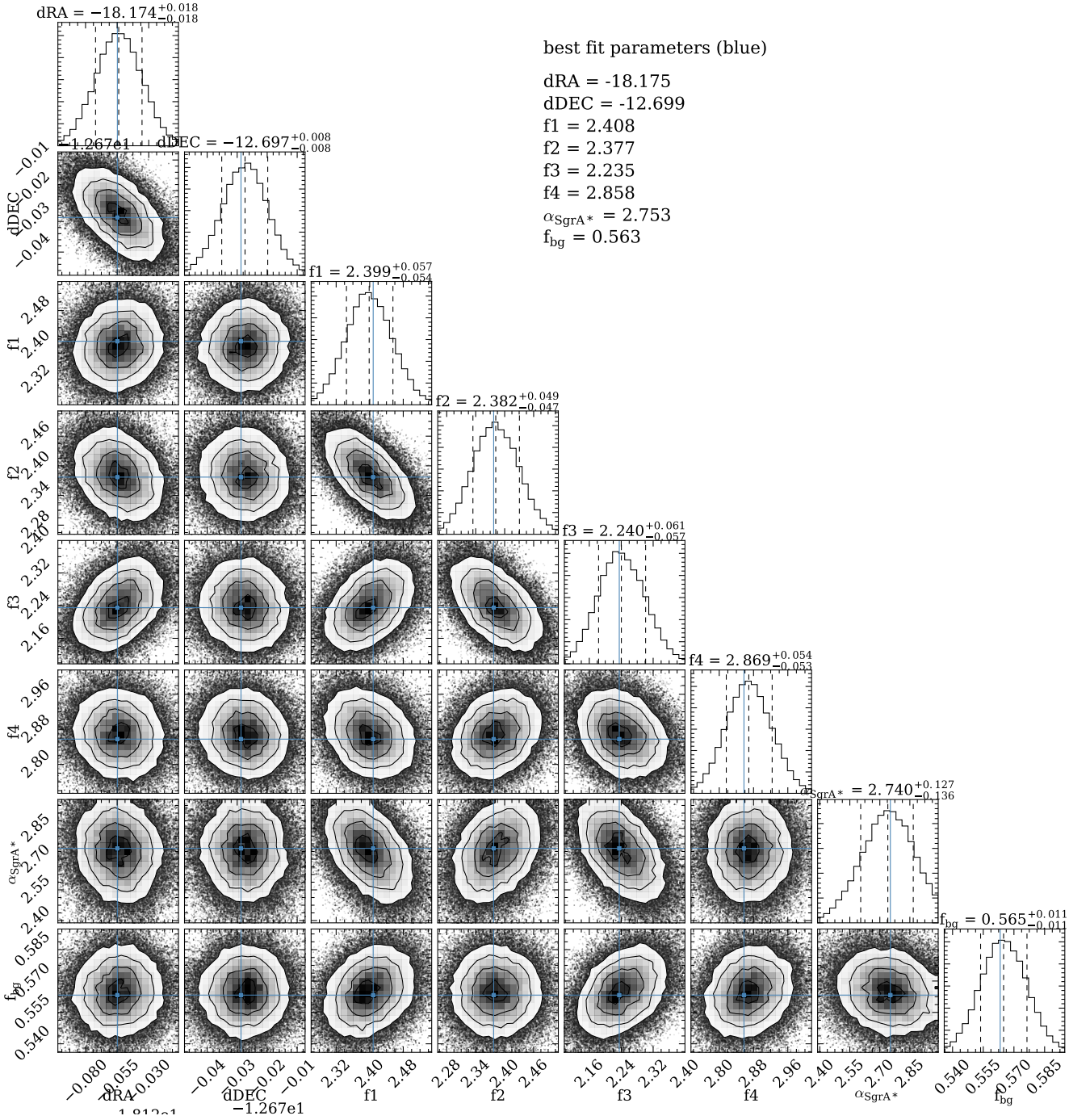

Figure 2.10: Visibility amplitudes and closure phases for GRAVITY data and best-fit S2-SgrA* binary model for the 2018-04-01T06:13 file.

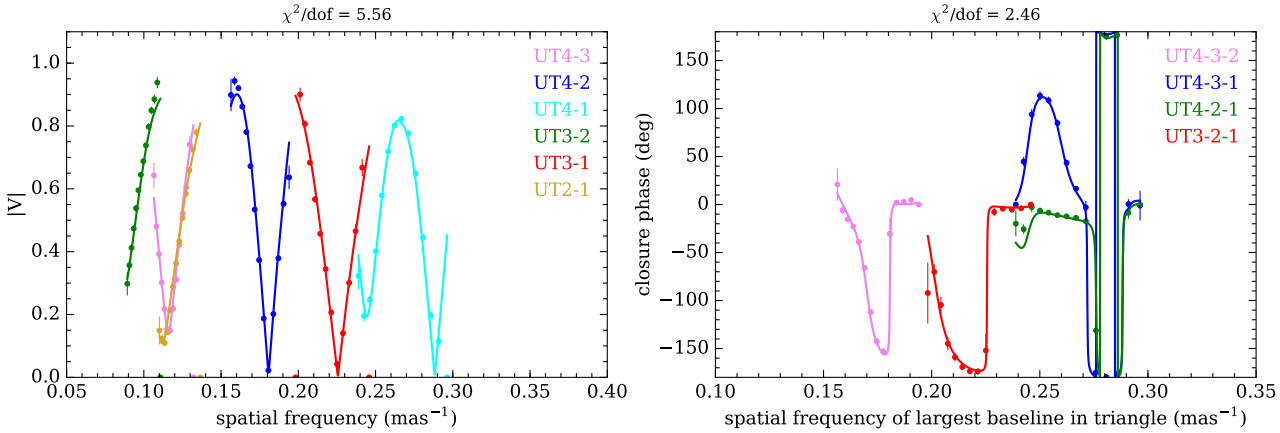

Figure 2.11: Visibility amplitudes and closure phases for GRAVITY data and best-fit S2-SgrA* binary model for the 2018-07-23T00:12 file.

errors. The constraining power of the GRAVITY astrometry was key for the early and significant detection of the gravitational redshift in the light of S2 with the instrument SINFONI, shown in the top right panel (Gravity Collaboration et al., 2018a, 2019). The $\approx$ 200 km/s effect peaking at periastron passage is a combination of such gravitational redshift and the relativistic Doppler effect at equal weights. The data points show the data residuals for the best-fit Keplerian orbit including SINFONI data up to 2016, with the red line showing the expected GR contribution for that orbit. Clearly, the post-2016 data points clearly prefer the GR solution rather than the pure Keplerian one. Because the GRAVITY data include the periastron passage, these accurate positions are essential for all work on the S2 orbit to come, including the expected detection of Schwarzschild precession by the end of 2019.

The bottom panels show the centroid motion of SgrA* relative to S2 (with the latter's orbital motion subtracted) during a $\sim$ 30 min NIR flare. The left panel shows the RA and DEC as a function of time, whereas the right panel shows the motion on the sky plane. In both panels, clockwise looped motion on the scales of the ISCO is clearly detected. These positions were measured with the binary code presented in this chapter, and agree with alternative codes by different groups. The red point shows the expected position of the dark mass based on the full orbit of S2 (Gravity Collaboration et al., 2018b). The differential nature of the relative motion during the flare allows to obtain an astrometric precision $\lesssim 20\mu$as.

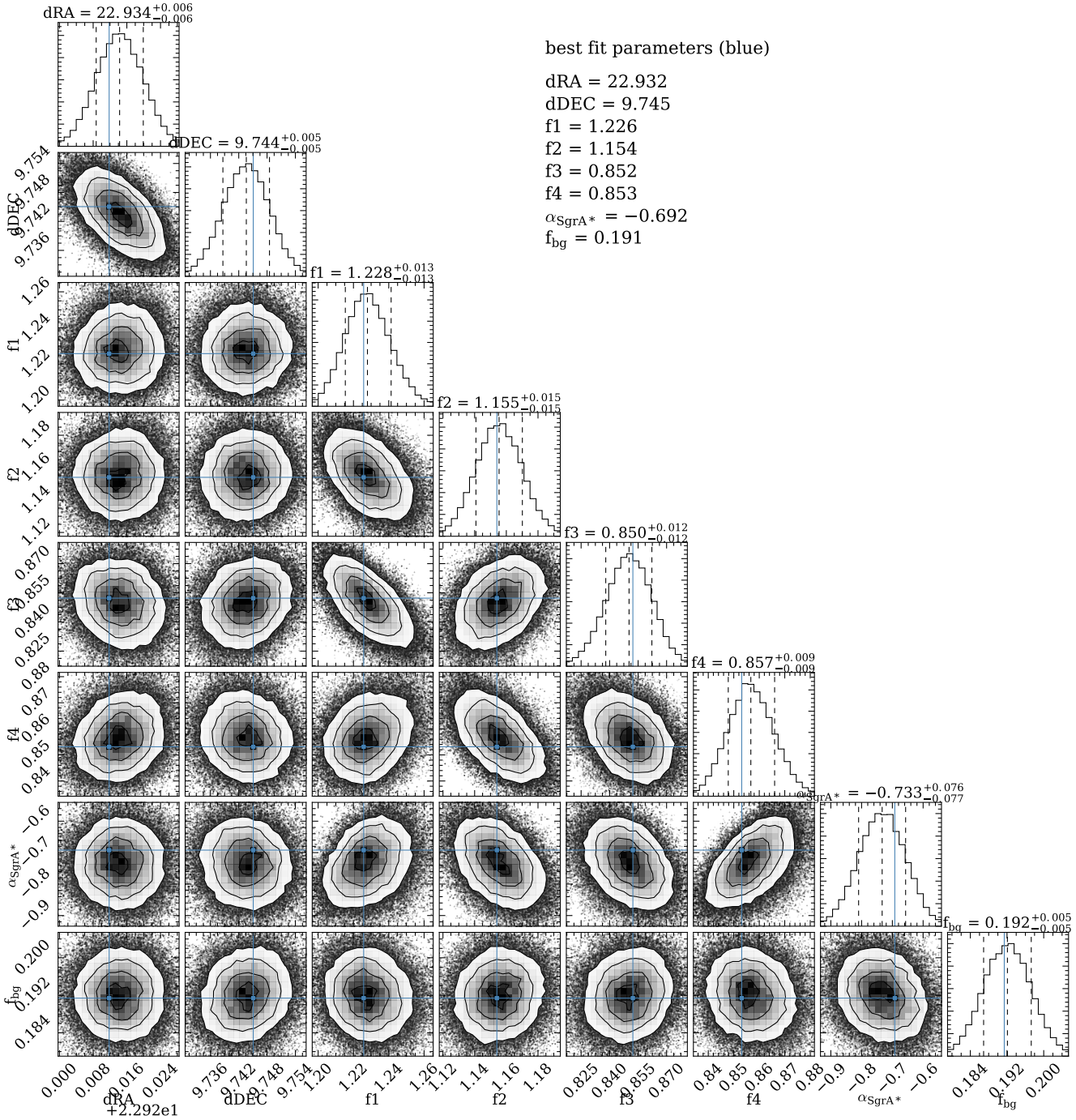

Figure 2.12: Visibility amplitudes and closure phases for GRAVITY data and best-fit S2-SgrA* binary model for the 2018-07-23T00:12 file.

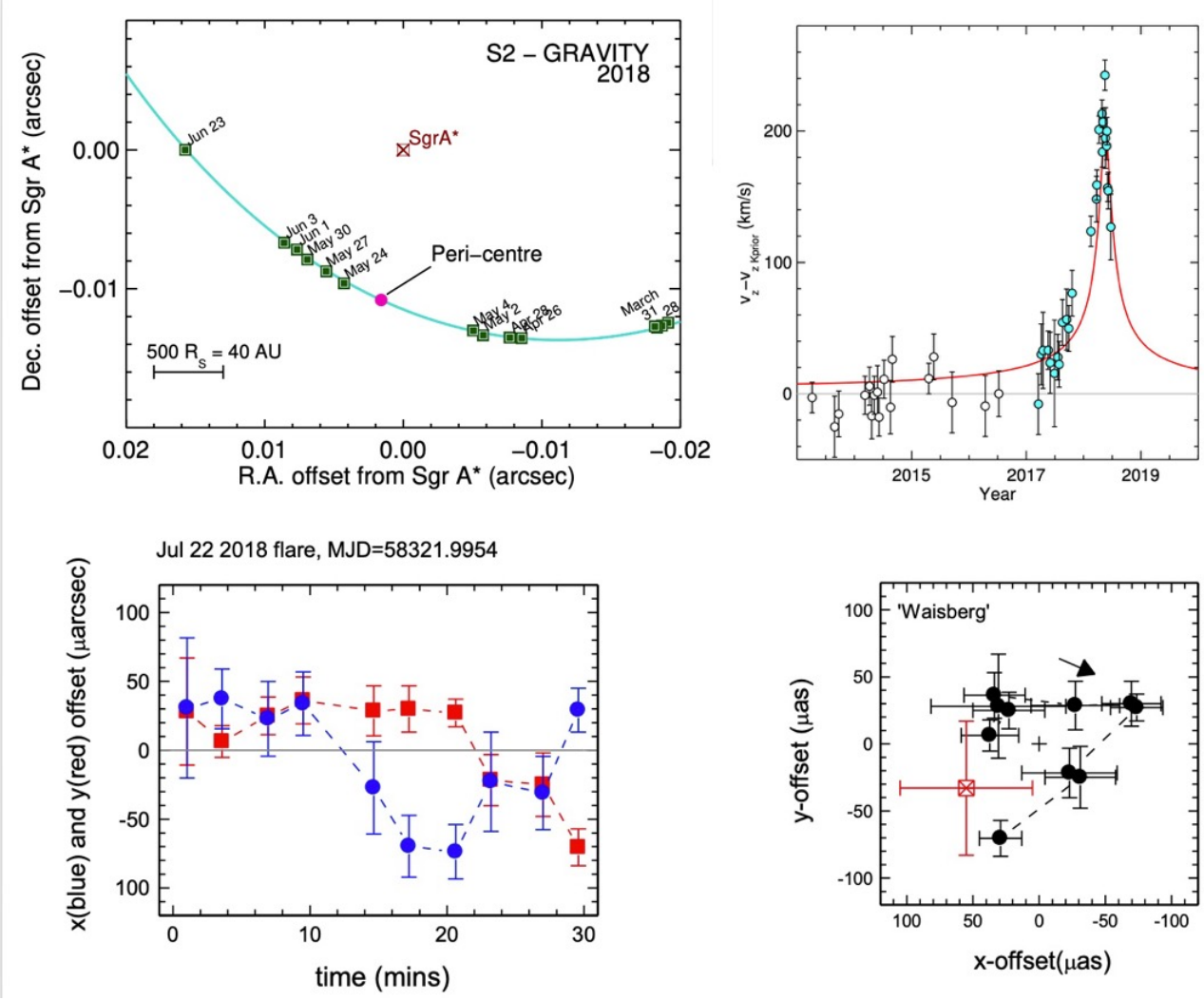

Figure 2.13: Examples of application of the binary fitting code described in this chapter. The top line shows the precisely measured S2 positions relative to the SgrA* during periastron passage from GRAVITY data (left), which have been key for the detection of the gravitational redshift of S2 through radial velocities measured with the instrument SINFONI (right). The bottom line shows the motion of the emission centroid of SgrA* during a NIR flare, as a function of time (left) and in the sky plane (right), and which clearly point to clockwise, looped motion at the scales of the ISCO of the black hole. Image credits: Gravity Collaboration et al. (2018a,b).

Appendix

Correction for Flux Imbalance

When the two telescopes of a given baseline have different fluxes, the intensity for a general image distribution $I(\boldsymbol{\sigma})$ is:

$$i(x) = \int\int (I_1(\boldsymbol{\sigma}) + I_2(\boldsymbol{\sigma}) + 2\sqrt{I_1(\boldsymbol{\sigma})I_2(\boldsymbol{\sigma})}\,\mathrm{Re}[e^{-2\pi i\boldsymbol{\sigma}\cdot\boldsymbol{u}}e^{2\pi isx}])d\boldsymbol{\sigma} \tag{2.6.1}$$

$$= \int\int (I_1(\boldsymbol{\sigma}) + I_2(\boldsymbol{\sigma}))d\boldsymbol{\sigma} + \mathrm{Re}[e^{2\pi isx}\int\int 2\sqrt{I_1(\boldsymbol{\sigma})I_2(\boldsymbol{\sigma})}e^{-2\pi i\boldsymbol{\sigma}\cdot\boldsymbol{u}})d\boldsymbol{\sigma}] \tag{2.6.2}$$

We measure the fringe amplitude $|\int\int 2\sqrt{I_1(\boldsymbol{\sigma})I_2(\boldsymbol{\sigma})}e^{-2\pi i\boldsymbol{\sigma}\cdot\boldsymbol{u}})d\boldsymbol{\sigma}|$. To compute a visibility amplitude, we would need $|\int\int 2\sqrt{I_1(\boldsymbol{\sigma})I_2(\boldsymbol{\sigma})}d\boldsymbol{\sigma}|$.

Because we have four telescopes/six baselines, we can actually solve for the individual telescope fluxes $\int\int I_1(\boldsymbol{\sigma})d\boldsymbol{\sigma}$ and $\int\int I_2(\boldsymbol{\sigma})d\boldsymbol{\sigma}$ from the "DC" part of $i(x)$ above $\int\int(I_1(\boldsymbol{\sigma})+I_2(\boldsymbol{\sigma}))d\boldsymbol{\sigma}$ using multiple baselines.

Finally, the pipeline data reduction assumes

$$\int\int 2\sqrt{I_1(\boldsymbol{\sigma})I_2(\boldsymbol{\sigma})}d\boldsymbol{\sigma} = 2\sqrt{\int\int I_1(\boldsymbol{\sigma})d\boldsymbol{\sigma}}\sqrt{\int\int I_2(\boldsymbol{\sigma})d\boldsymbol{\sigma}} \tag{2.6.3}$$

It is easy to show that this holds if the image is the same in the two telescopes i.e. $I_2(\boldsymbol{\sigma}) = \alpha I_1(\boldsymbol{\sigma})$, α =constant. However, this does not necessarily hold if the images of the two telescopes are not the same (due to e.g. varying flux ratios), in which case this flux-imbalance correction will not produce $|V(\mathbf{0})| = 1$.

Chapter 3

Measuring the spin of the Galactic Center black hole with stellar orbits

Original publication: I. Waisberg, J. Dexter, S. Gillessen, O. Pfuhl, F. Eisenhauer, P. Plewa, M. Bauböck, A. Jimenez-Rosales, M. Habibi, T. Ott, S. von Fellenberg, F. Gao, F. Widmann & R. Genzel, 2018, MNRAS, 476, 3600, *What stellar orbit is needed to measure the spin of the Galactic center black hole from astrometric data?*, DOI: 10.1093/mnras/sty476

Abstract: Astrometric and spectroscopic monitoring of individual stars orbiting the supermassive black hole in the Galactic Center offer a promising way to detect general relativistic effects. While low-order effects are expected to be detected following the periastron passage of S2 in Spring 2018, detecting higher-order effects due to black hole spin will require the discovery of closer stars. In this paper, we set out to determine the requirements such a star would have to satisfy to allow the detection of black hole spin. We focus on the instrument GRAVITY, which saw first light in 2016 and which is expected to achieve astrometric accuracies $10 - 100\mu$as. For an observing campaign with duration T years, N_{obs} total observations, astrometric precision σ_x and normalized black hole spin χ, we find that $a_{orb}(1-e^2)^{3/4} \lesssim 300 R_S \sqrt{\frac{T}{4\text{years}}} \left(\frac{N_{obs}}{120}\right)^{0.25} \sqrt{\frac{10\mu as}{\sigma_x}} \sqrt{\frac{\chi}{0.9}}$ is needed. For $\chi = 0.9$ and a potential observing campaign with $\sigma_x = 10\mu$as, 30 observations/year and duration 4-10 years, we expect ~ 0.1 star with $K < 19$ satisfying this constraint based on the current knowledge about the stellar population in the central 1". We also propose a method through which GRAVITY could potentially measure radial velocities with precision ~ 50 km/s. If the astrometric precision can be maintained, adding radial velocity information increases the expected number of stars by roughly a factor of two. While we focus on GRAVITY, the results can also be scaled to parameters relevant for future extremely large telescopes.

3.1 Introduction

The orbits of short period stars in the central 1" (S-stars) of the Milky Way Galaxy provide the best current evidence for the existence of supermassive black holes. Currently ≈ 40 orbits are known (Gillessen et al., 2017), including that of the star S2, reaching $R \approx 1300 R_S$ from the black hole, where $R_S = 2GM/c^2$. Such orbital monitoring has led to strong constraints on the black hole mass and distance to the Galactic center (Ghez et al., 2008; Gillessen et al., 2009; Boehle et al., 2016; Gillessen et al., 2017).

The orbits are all currently compatible with Newtonian gravity. Lower order effects such as periastron advance and gravitational redshift are expected to be probed with the star S2 (Jaroszynski, 1998; Fragile and Mathews, 2000; Rubilar and Eckart, 2001; Weinberg et al., 2005; Zucker et al., 2006; Angélil and Saha, 2010; Hees et al., 2017; Parsa et al., 2017; Grould et al., 2017) during or following its next closest approach in Spring 2018. However, Newtonian perturbations from a distribution of stars or remnants in the central region are very likely to dominate over higher order relativistic effects related to black hole spin for the currently known stars (e.g. Merritt et al., 2010; Zhang and Iorio, 2017). Detection of black hole spin from Lense-Thirring precession therefore requires the discovery and monitoring of closer stars.

Several works have pointed to the possibility of using astrometric measurements of closer stars to constrain the black hole spin (e.g. Kraniotis, 2007; Will, 2008; Merritt et al., 2010; Sadeghian and Will, 2011; Psaltis et al., 2016), but the technology to find such stars and achieve the required precision was lacking. This, however, has changed with the first light of the instrument GRAVITY at the Very Large Telescope Interferometer (VLTI, Gravity Collaboration et al., 2017), one of whose main goals is to resolve the inner region around SgrA* at few mas resolution in search for closer stars, and to achieve $\sim 10-100\mu$as astrometric precision in the monitoring of stellar orbits (Eisenhauer et al., 2011).

Recent investigations have explored possible constraints on the black hole spin of SgrA* using closer stars (Zhang et al., 2015; Yu et al., 2016) assuming a combination of astrometric $1-30\mu$as and redshift $0.1-10$ km/s precisions. Although the latter could allow a spin constraint (Kannan and Saha, 2009; Angélil et al., 2010), it is not achievable with current instruments, which are currently limited to ~ 30 km/s even for a star as bright as S2 (Gillessen et al., 2017).

Here we extend these studies by providing an expression for the detectability of a non-zero black hole spin as a function of stellar orbital parameters for a realistic GRAVITY observing campaign (duration, number of observations, achievable errors in astrometry and radial velocity). We use a semi-analytic geodesics code (§3.2) to rapidly simulate and fit relativistic orbits and show that it can reproduce past work on the star S2 (§3.3). We then simulate GRAVITY campaigns for closer in stars using astrometric data to determine the necessary conditions for a spin detection (§3.4). From the current knowledge on the stellar distribution, we estimate the expected number of detectable stars satisfying these conditions (§3.4.3). We study improvements in the prospects of spin detection from combining astrometry with radial velocity measurements at a precision of ~ 50 km/s (§3.5), more in line with what potentially could be reached with GRAVITY (Appendix A). Discussion

and conclusions are presented in §3.6.

3.2 Methods

We approximate the potential near the black hole as a Kerr spacetime and stars as test particles. This is appropriate in the range $100R_S \lesssim a \lesssim 5000R_S$, where the lower and upper limits are set by the tidal disruption radius and Newtonian perturbations from the underlying stellar/remnant distribution, respectively (Psaltis et al., 2013; Merritt et al., 2010; Zhang and Iorio, 2017). We can then use geodesic ray tracing to follow the orbits of stars. We note that the upper limit could be much more constraining depending on the properties of the stellar/remnant distribution (see §3.6).

3.2.1 Stellar orbits as timelike geodesics

We use the public YNOGKM code (Yang and Wang, 2014) to trace timelike geodesics in the Kerr metric. This code semi-analytically solves the geodesic equations in the Kerr metric by inverting the integral equation relating the r and θ coordinates that results from separating the Hamilton-Jacobi equation (Carter, 1968). The ϕ and t coordinates are then given as elliptic integrals involving functions of r and θ (Rauch and Blandford, 1994). The calculation of the many resulting elliptic integrals is sped up using the form developed by Carlson (Carlson, 1992; Dexter and Agol, 2009). The main difficulty with extending the method to timelike geodesics is accounting for the arbitrarily large number of r turning points along the orbit. Yang and Wang (2013, 2014) alleviate this problem by using a different independent variable, p, which monotonically increases from 0 to a maximum value along the geodesic.

To calculate the position of a star at coordinate time t from an initial coordinate position and velocity (see below), we choose an initial guess of p which is either equal to half of the maximum value along the geodesic (first point), or to the value used at the previous time (subsequent points). From the initial guess, a coordinate time is calculated, and the solution is then iterated until the observed time is found to the desired accuracy. Typically convergence to $10^{-6}GM/c^3$ is reached in $\lesssim 10$ iterations.

The YNOGKM code takes input initial position (r_0, θ_0) in the coordinate frame, and the locally non-rotating frame (Bardeen et al., 1972) three-velocity, $v^{(i)}$. For comparison of our orbits with known and expected stars in the GC, it is most convenient to parameterize in terms of the Keplerian orbital elements $(a_{orb}, e, i_{orb}, \omega, \Omega, T_p)$. We calculate approximate coordinate positions and velocities corresponding to the orbit by assuming that the star is non-relativistic near apocenter. The orbital elements are specified relative to the sky plane, while the input position and velocity to YNOGKM are relative to the black hole coordinate frame. We rotate the sky coordinates of the star to allow for arbitrary position angle and inclination of the black hole spin axis. With the convention that sky coordinates (x, y, z) point along the RA, DEC and line of sight (away from the observer) directions, we define the black hole spin angles i_{spin} ($[0, \pi]$) and ϵ_{spin} ($[0, 2\pi]$) as the angle between the

spin axis and z and between the projection of the spin axis onto the sky plane and $-x$, respectively.

This semi-analytic geodesic method is particularly efficient here. Each sample of a stellar orbit is independent, and so sampling at irregular, sparse observing epochs does not require integrating the orbit over many periods. This is the limit where analytic codes can be significantly faster than numerical integration while maintaining machine precision (Dexter and Agol, 2009).

3.2.2 Redshift Calculation

The redshift of the received starlight is

$$Z \equiv \frac{E_* - E_0}{E_0} = \frac{E_*}{E_0} - 1 = \frac{\boldsymbol{p}_* \cdot \boldsymbol{u}_*}{\boldsymbol{p}_0 \cdot \boldsymbol{u}_0} - 1 \tag{3.2.1}$$

where E_* and E_0 are the photon energies measured by an observer co-moving with the star and at infinity, $\boldsymbol{u}_*$ and $\boldsymbol{p}_*$ are the star's four-velocity and the photon's four-momentum at photon emission, and $\boldsymbol{u}_0 = (1, 0, 0, 0)$ and $\boldsymbol{p}_0$ are the four-velocity of the observer at infinity and the photon's four momentum at photon reception.

The four-velocity $\boldsymbol{u}_*$ is computed from the stellar orbits code, while $\boldsymbol{p}_*$ can be computed from the impact parameters of the photon (Cunningham and Bardeen, 1973).

3.2.3 The photon orbit

Light bending of photons affects both the measured position of the star as well as the redshift. Since the impact parameters of the photon are not known a priori, an exact calculation is costly and requires an iterative approach, in which e.g. the photon is propagated back from the observer until it passes close enough to the star (e.g. Zhang et al., 2015). We can simplify the problem considerably by noting that the effect of black hole spin on the photon orbit for the stars of interest in this paper ($a_{orb} \gtrsim 100 R_S$) is $\ll 1\mu$as (Bozza and Mancini, 2012; Zhang et al., 2015) and < 3 km/s (Angélil et al., 2010; Zhang et al., 2015), corresponding to $\lesssim 0.1\%$ and $\lesssim 10\%$ of the spin effects on the stellar orbit (Zhang et al., 2015). Therefore, for the purposes of this paper, we can compute the photon orbit in the Schwarzschild metric.

Furthermore, the weak-field approximation is valid for the orbits considered here, except for stars with extremely high inclinations as they pass behind the black hole. An upper limit to the closest approach distance of the photon to the black hole can be estimated as $d \sim R_p \cos(i_{orb})$, where $R_p = a_{orb}(1 - e)$ is the periastron distance. For $R_p = 100 R_S$, the photon could pass closer than $20 R_S$ from the black hole for inclination $i_{orb} \gtrsim 78°$. For randomly oriented orbits, the probability of such high inclinations is very small at $1 - \cos(90° - 78°) \sim 2\%$. It is interesting to note, however, that if such a star is indeed found, light bending effects on astrometry and redshift during its passage behind the black hole could be quite significant and could potentially allow probing the black hole spin (Bozza and Mancini, 2012).

For the Schwarzschild metric, it is possible to obtain a second-order differential equation relating r and ϕ (photon coordinates in star-black hole-observer plane) which is independent of the photon's impact parameter:

$$\frac{d^2u}{d\phi^2} + u = 3GMu^2 \tag{3.2.2}$$

where $u = \frac{1}{r}$ (Moore, 2012). In the weak-field limit, an analytic perturbative solution can be derived:

$$u(\phi) = A\sin(\phi + \phi_0) + \frac{3GMA^2}{2} + \frac{GMA^2}{2}\cos(2(\phi + \phi_0)) \tag{3.2.3}$$

where A and ϕ_0 are integration constants. Given the initial (r_*, ϕ_*) and final $(r_0, \phi_0) = (\infty, 0)$ positions of the photon, this nonlinear equation can be solved numerically for (A, ϕ_0) and the impact parameter determined from

$$\lim_{r->\infty} r\sin\phi = \frac{1}{A\cos(\phi_0) - GMA^2\sin(2\phi_0)}, \tag{3.2.4}$$

The impact parameters on the sky plane then give the measured astrometric position and redshift.

3.3 Code Validation with the Star S2

Of the currently known S-stars, S2 is the one with the closest approach to the black hole ($R_p \approx 1300R_S$), and the potential to detect relativistic effects through the monitoring of its orbit has been the subject of numerous works as mentioned in Section 3.1. It therefore offers an opportunity to validate our code by comparing the measured relativistic effects with results from previous work. In all of the following, we adopt the mass of the black hole $M_{BH} = 4.3 \times 10^6 M_\odot$, the distance to the Galactic Center $R_0 = 8.3$ kpc and the following orbital parameters for S2: semi-major axis $a_{orb} = 111.1$mas, eccentricity $e = 0.881$, inclination $i_{orb} = 131.9°$, argument of periastron $\omega = 65.4°$, longitude of ascending node $\Omega = 225.0°$ and time of periastron passage $T_p = 2002.33$ years (Gillessen et al., 2009, 2017). We will also consider a hypothetical star with the same orbital parameters as S2 but a ten times smaller semi-major axis ("S2/10").

3.3.1 Low-order Relativistic Effects

We checked that the orbit and redshift curves we obtain for S2 match the observed ones (Gillessen et al., 2017). For a zero spin orbit, we checked that the periastron shift for S2 and S2/10 match the expected values $\delta\omega\Big|_{orbit} \approx 0.22°$ and $2.2°$ respectively.

Fig. 3.1 shows an example of successive periastron shifts for S2/10 over a period of five years. Fig. 3.2 shows the effect of periastron shift compared to a purely Keplerian

orbit for S2 as a function of time near periastron passage, with the characteristic "kink" during periastron followed by the continuous increase of the effect over the following years. These curves are simply the difference between the relativistic and the Keplerian orbits for the same initial parameters. Similarly, we also tested the effects of transverse Doppler shift and gravitational redshift on the orbit of S2 during periastron, which amount to a maximum deviation of $\approx$ 100 km/s each. These effects are all consistent with previous work (e.g. Weinberg et al., 2005; Zucker et al., 2006; Angélil et al., 2010; Grould et al., 2017).

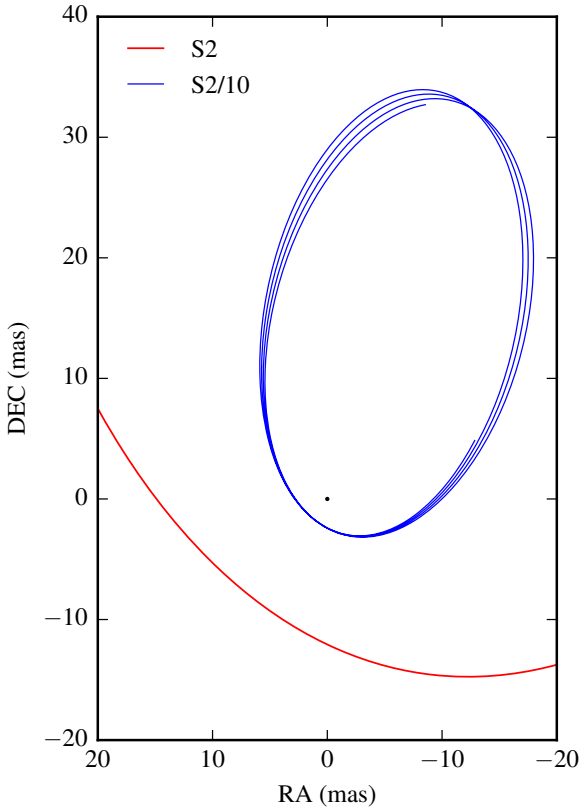

Figure 3.1: Example of Schwarzschild precession for the hypothetical star "S2/10" during 5 years. A portion of the S2 orbit is also shown.

3.3.2 Photon Orbit

In order to test the implementation of our solution for the photon orbit, we computed the effect of light bending on the astrometric position of the star S2. This is done by computing the difference $|\sqrt{\mathrm{RA}^2 + \mathrm{DEC}^2}|$ as a function of time between bent and non-bent photon orbits. As shown in Figure 3.2, the effect amounts to a deviation of $\approx 20\mu$as during periastron passage. This is consistent with previous results (Bozza and Mancini, 2012;

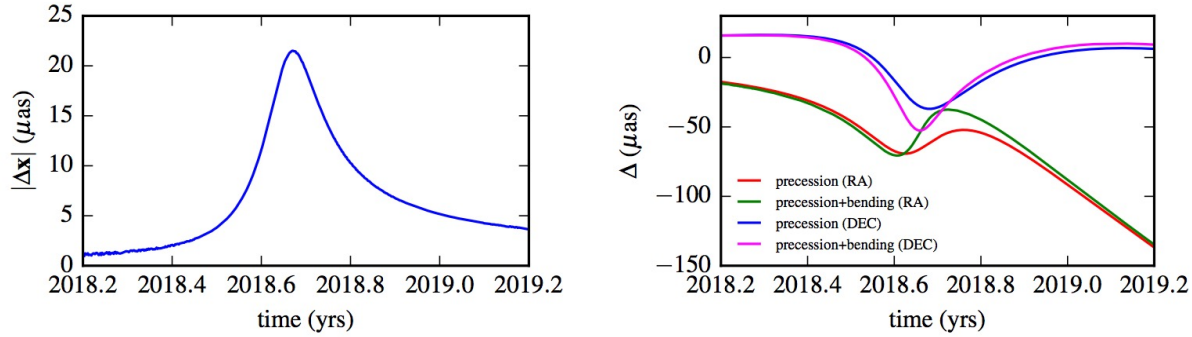

Figure 3.2: **Left**: The effect of light bending during periastron passage of S2 peaks at $\approx 20\mu$as 12 days after periastron. This is the difference between an orbit with and without light bending. **Right**: Effect of periastron shift alone and with light bending around periastron passage of S2. Light bending enhances the periastron "kink" and could help in the early detection of the combined effect, before having to wait for the continuous growth in the years following periastron passage. In both cases, the curves are the difference between the relativistic (without or with light bending) and the Keplerian orbits.

Grould et al., 2017). In Fig. 3.2, we also show the superimposed effects of periastron shift and light bending; the latter amplifies the former during the periastron "kink", enhancing the chances of an early detection of the combined effect.

3.3.3 Spin Effect

As mentioned above, for S2 the time scale associated with Newtonian perturbations due to an underlying stellar/remnant distribution is still shorter than the one associated with Lense-Thirring precession (Merritt et al., 2010; Zhang and Iorio, 2017). Nevertheless, several works have estimated the astrometric effect of frame-dragging on the orbit of S2 (e.g. Zhang et al., 2015; Yu et al., 2016; Grould et al., 2017). In particular, Yu et al. (2016) computed the shift in the apocenter position of S2 after one full orbit as a function of the two spin angles, as the effect can vary by more than an order of magnitude depending on the latter. We carried out a similar simulation by computing the maximum position difference $|\Delta\boldsymbol{x}|$ between an orbit of S2 with $\chi = 0$ and one with $\chi = 0.99$ after one full period, where $\chi \in (0, 1)$ is the normalized black hole spin. The resulting angle dependence and position difference $(1 - 15\mu$as) are in agreement with Yu et al. (2016). Finally, we note that the deviation averaged over the spin angles, defined as

$$\frac{1}{4\pi}\int_0^{2\pi}\int_0^{\pi} |\Delta\boldsymbol{x}|(i_{spin}, \epsilon_{spin}) \sin i_{spin} di_{spin} d\epsilon_{spin} \tag{3.3.1}$$

is $\approx 8.5\mu$as. For S2/10, the maximum astrometric shift over one full orbit as computed with the code is $\approx 3 - 48\mu$as, with average over spin angles $\approx 27.5\mu$as.

We also computed the equivalent spin effects on the redshift. Again, the spin-angle dependence and size of the effects ($0.01 - 0.3$ km/s and $3 - 30$ km/s per orbit for S2 and S2/10, respectively) are consistent with Yu et al. (2016).

3.4 Required Orbital Parameters for a Black Hole Spin Measurement

Using closer stars to measure black hole spin overcomes the dominance of Newtonian perturbations over the frame-dragging precession time scale. The significance σ of a spin detection through astrometry for an observing campaign of length T years, total number of observations N_{obs} and astrometric precision σ_x scales as

$$\sigma \propto \frac{\delta x\Big|_T}{\sqrt{N_{obs}}\sigma_x} \tag{3.4.1}$$

where $\delta x\Big|_T$ is the total astrometric shift due to Lense-Thirring precession. The Keplerian elements which experience nonzero average changes due to black hole spin over a full orbit are all angles (ω, Ω and i_{orb}) and the changes scale as

$$\delta\omega, \delta\Omega, \delta i_{orb}\Big|_{orbit} \propto \chi \left(\frac{1}{a_{orb}(1-e^2)}\right)^{3/2} \tag{3.4.2}$$

(for full expressions, including dependence on spin angles, see for e.g. Iorio, 2011). The *astrometric* change scales with the size of the orbit a_{orb}

$$\delta x\Big|_{orbit} \propto \chi \frac{1}{a_{orb}^{1/2}(1-e^2)^{3/2}} \tag{3.4.3}$$

The effect per orbit is therefore not strongly dependent on a_{orb}. The main benefit of using closer stars is their shorter periods, which, combined with the fact that precession is a cumulative effect, lead to a more significant astrometric deviation over a fixed period of time. Since the orbital period $P_{orb} \propto a_{orb}^{3/2}$, the astrometric deviation over a fixed time T scales as

$$\delta x\Big|_T \propto \frac{T}{P_{orb}} \chi \frac{1}{a_{orb}^{1/2}(1-e^2)^{3/2}} \propto \chi T \frac{1}{a_{orb}^2(1-e^2)^{3/2}} \tag{3.4.4}$$

We therefore have

$$\sigma \propto \frac{\chi T}{\sqrt{N_{obs}}\sigma_x} a_{orb}^2 (1-e^2)^{3/2} \tag{3.4.5}$$

A similar expression is used in Weinberg et al. (2005) but parametrized in terms of number of orbits covered instead of observing campaign duration. Our goal is to determine the

properties of a star (a_{orb}, e) that would allow a measurement of black hole spin with a realistic campaign with duration $\lesssim 10$ years, and subsequently infer the expected number of stars satisfying such constraints based on what is currently known about the stellar distribution in the innermost arcseconds of the Galaxy. We therefore expect σ contours to have the form

$$a_{orb}(1-e^2)^{3/4} = R \tag{3.4.6}$$

where R depends not only on the spin and observing campaign parameters but also on effects such as the masking of spin-related effects by fitting of the remaining parameters. We use simulated stellar orbits in order to estimate such unknown normalization factors.

3.4.1 Simulated Stellar Orbits

The astrometric deviations due to spin cited above were calculated as the difference between models with zero and maximum black hole spin when keeping all other parameters (initial positions and velocities of the star, BH mass and distance) constant. In practice, such parameters are not exactly known and have to be fit together with the black hole spin, which leads to masking of the spin-related effects.

We simulate stellar orbits across a grid of (a_{orb}, e), with $a_{orb} \in (200R_S, 5000R_S)$ and $e \in (0.1, 0.9)$. The other Keplerian parameters (ω, Ω, i_{orb}) are taken to be the same as for S2. They only matter in relation to the black hole spin angles as far as spin-related effects are concerned. We choose $i_{spin} = \epsilon_{spin} = 0°$, which give astrometric shifts close to the average over the spin angles (specifically, 9.6 and 31.7μas/orbit for S2 and S2/10, respectively, compared to the averages of 8.5 and 27.5μas referred above). We use $\chi = 0.9$ and the canonical M_{BH} and R_0 as above. The observing campaign is set to a total duration of $T = 4$ years, with observations taken in 3 consecutive months per year over a period of 10 consecutive days per month, for a total of $N_{orb} = 120$ observations. Gaussian errors with $\sigma_x = 10\mu$as and 100μas are added representing canonical astrometric accuracies that could be achieved with GRAVITY.

Given the simulated measurements with errors, one approach that could be used to estimate the spin error is to perform a Bayesian fit to the data using e.g. Markov chain Monte Carlo approaches (Zhang et al., 2015; Yu et al., 2016). However, we have found that ensuring the convergence of the spin parameters with such an approach is very challenging as the orbit is much more sensitive to other non-spin parameters, which must be simultaneously fit and which can also mask the effects of spin. We instead use a null hypothesis test in order to estimate the significance of spin, which entails in finding the best-fit zero-spin orbit to the simulated data and assessing the probability that the data were generated by such a model based on the residuals. For this, we follow the usual approach of converting the χ^2 of the best-fit solution to a p-value, and that into a significance σ:

$$\sigma = \sqrt{2}\,\mathrm{erfinv}(1 - \text{p-value}) \tag{3.4.7}$$

In order to find the best-fit zero-spin solution, we used a downhill simplex algorithm (Nelder and Mead, 1965) which does not require numerical derivatives (as opposed to gradient methods such as Levenberg-Marquardt) and was found to be more stable and less sensitive to local minima. The method is based on constructing simplexes (polytopes of $n+1$ vertices in n dimensions) and updating the vertices with operations (reflection, expansion, contraction, shrinkage) which result in successively better solutions. Because the method is not completely immune to local minima, we used 10 initial simplexes distributed around the initial parameters for each fit. This number was found to be sufficient in order to avoid local minima. We also note that no priors were used for M_{BH} and R_0. Even though they are constrained by the currently known S-stars, the best fit zero-spin solution is always within a few percent of the initial value and therefore the currently known bounds would not lead to a change in significance.

3.4.2 Results

Fig. 3.3 (top row) shows the resulting significance contours $\sigma(a_{orb}, e)$ for $\sigma_x = 10\mu$as. The graininess arises due to different error instantiations between simulated orbits. There is a region of low spin significance ($\sigma \lesssim 2$) and of high spin significance ($\sigma \gtrsim 5$) separated by a relatively narrow transition region. The white contour lines show analytic estimates for the shape of this region based on Eq. (3.4.6).

The left panel shows the significance before fitting i.e. using the initial parameters but setting $\chi = 0$, whereas the right panel shows the significance after finding the best fit zero-spin solution. The pure size of the effect would suggest a star with $a_{orb}(1-e^2)^{3/4} \lesssim 900R_S$ is needed to detect spin at high significance, but in practice when fitting for all parameters a star with $a_{orb}(1-e^2)^{3/4} \lesssim 300R_S$ (i.e. $\sim 3\times$ closer in) is required.

Following Eq.(3.4.5), we can then write the requirement on (a_{orb}, e) of the star as a function of the observing campaign length T in years, total number of observations N_{obs}, astrometric error σ_x in μas and normalized spin magnitude χ as

$$a_{orb}(1-e^2)^{3/4} \lesssim 300R_S \sqrt{\frac{T}{4\text{years}}} \left(\frac{N_{obs}}{120}\right)^{0.25} \sqrt{\frac{10\mu as}{\sigma_x}} \sqrt{\frac{\chi}{0.9}} \tag{3.4.8}$$

We have repeated the same experiment using $\sigma_x = 100\mu$as. In accordance with the expression above, we found $a_{orb}(1-e^2)^{3/4} \lesssim 100R_S$ is needed for a high significance spin detection.

3.4.3 Expected Number of Stars

In order to translate the constraint on orbital parameters from the previous section into an expected number of stars for which GRAVITY would be able to detect black hole spin, it is necessary to estimate the probability densities of semi-major axis, $n(a_{orb})$, and eccentricity, $n(e)$, and the K-band Luminosity Function (KLF, $\frac{d\log N(K)}{dK} = \beta$) in the central 1"/0.04pc.

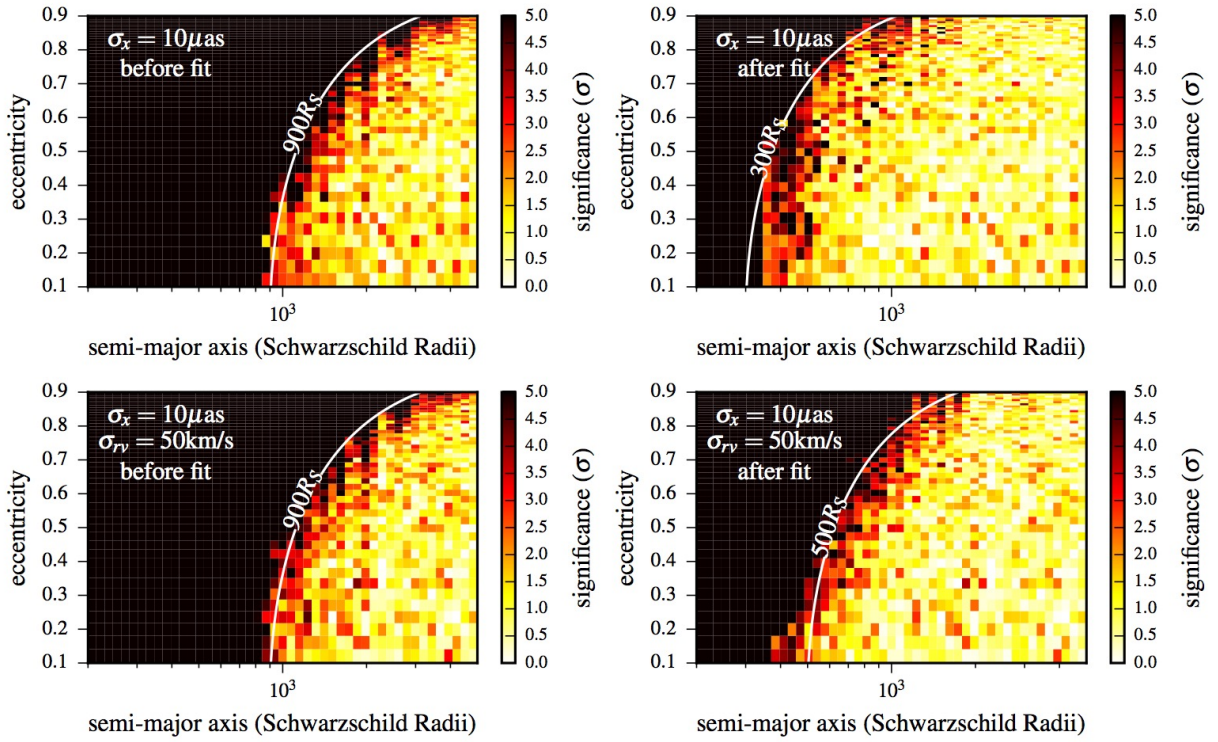

Figure 3.3: Contour plots for the significance σ of a black hole spin detection through monitoring of stellar orbits as a function of (a_{orb}, e) for an observing campaign of 4 years with a total of $N = 120$ observations. The black hole normalized spin is $\chi = 0.9$ and spin angle parameters that lead to an average astrometric deviation are assumed. The white lines show the expected contour for astrometric deviations due to spin effects, $a_{orb}(1 - e^2)^{3/4} =$ constant, which separates the regions of low and high significance. The left panels show σ before finding the best fit zero-spin solution i.e. simply setting $\chi = 0$, whereas the right panels show σ after fitting for the best zero-spin solution. The upper panels are for a purely astrometric campaign with precision $\sigma_x = 10\mu$as, while the lower panels contain additional radial velocity measurements with precision $\sigma_{rv} = 50$ km/s. Having to fit all parameters leads to masking of the spin-related relativistic effects and leads to more stringent limits on the required star for a spin detection. The additional radial velocity measurements do not lead to an increase in significance before fitting, but help with constraining the non-spin parameters during the fit, ameliorating their masking of the spin effects.

The latter has been estimated by several works with the consistent result $\beta \approx 0.20$ (Genzel et al., 2003b; Buchholz et al., 2009; Sabha et al., 2012). The most recent analysis of the S-stars orbits is consistent with a "thermal" eccentricity distribution (Gillessen et al., 2017); we therefore adopt $n(e)de = 2ede$. For such a distribution, if the energy distribution function follows a power-law, $f(\epsilon) \propto \epsilon^p$, then the space density distribution $n(r) \propto r^{-\gamma}$ and $n(a_{orb}) \propto a_{orb}^{-\gamma+2}$ (Schödel et al., 2003). Estimates of γ from stellar counts in the region $r \lesssim 10$" consistently find $\gamma \approx 1.2 - 1.4$ (Genzel et al., 2003b; Schödel et al., 2007; Do et al., 2009). We therefore adopt $n(a_{orb})da_{orb} \propto a_{orb}^{0.7}da_{orb}$, which is also in accord with the estimated semi-major axis distribution directly from the orbits of S-stars (Gillessen et al., 2009).

We generate a mock field of $N = 10^7$ stars with Keplerian orbits with a and e following the distributions above, using inverse transform sampling on the respective Cumulative Distribution Functions (CDFs):

$$N_E(e) = e^2 \tag{3.4.9}$$

$$N_A(a_{orb}) = \left(\frac{a_{orb}}{a_{max}}\right)^{1.7} \tag{3.4.10}$$

a_{max} is set to 10" ($n(a_{orb}) = 0$ for $a_{orb} > a_{max}$), which is justified below. The time of periastron is set randomly between 0 and 10^6 years, which is larger than the largest possible period ($\approx 12,000$ years). Consistently with the current known S-stars, the orbital orientations are drawn isotropically i.e. ω and Ω have uniform distributions and $n(i_{orb})di_{orb} = \frac{1}{2}\cos(i_{orb})di_{orb}$. We exclude stars that would undergo tidal disruption i.e. for which $R_p = a_{orb}(1-e) < R_t = R_* \left(\frac{M_{BH}}{M_*}\right)^{1/3} \sim 30R_S$. The effective number of stars is then normalized by the number of stars within a radius $r < 1$", which is known to be ≈ 56 for $K \lesssim 17$ (Genzel et al., 2003b). The final expected number for a given magnitude limit is then estimated using the KLF.

As mentioned, we set $a_{max} = 10$" since $n(a_{orb})$ would otherwise diverge. There is evidence from stellar counts that $\gamma \sim 2$ for $r > 10$" (Genzel et al., 2003b; Schödel et al., 2007; Fritz et al., 2016), so that $n(a_{orb}) =$ constant for $r > 10$". Furthermore, beyond the radius of influence of the black hole ∼75" (Alexander, 2005, we also note the direct measurements of a half-light radius of the nuclear star cluster ∼ 100"/178" by Schödel et al. (2014) and Fritz et al. (2016)), the orbits are significantly perturbed and not dominated by the gravitational potential of the black hole anymore. To check whether the chosen a_{max} leads to a bias, we simulate the contribution from stars with $10" < a_{orb} < 75"$ to the region $r < 1$", which is found to be $\lesssim 1\%$, since stars that do have the potential to reach $r < 1$" due to their higher eccentricities spend a very small portion of their orbital periods in this region.

We choose $K < 19$ as the upper limit on a star which could be detected with GRAVITY (Eisenhauer et al., 2011). The simulation predicts ~ 1 such star within a radius $r < 50$ mas ($\sim$ FOV of GRAVITY), in agreement with previous estimates (Genzel et al., 2003b).

The median (a_{orb}, e) of such a star from the simulations is ≈(80 mas, 0.8). Because we have included the eccentricity distribution, we can also predict the expected number of stars that satisfy the contours for measuring spin derived in the previous section. We include an additional cut-off in a_{orb} in order to ensure that at least one orbit is covered by the observing campaign ($a_{orb} < 5000 R_S$ for $T = 4$ years).

Table 3.1 shows the expected number of stars which would allow a detection of spin. The masking of the relativistic effects by other parameters ("Fit" vs "No Fit") leads to a significant reduction in the expected number of stars. For our canonical observing campaign of $T = 4$ years, $N_{obs} = 30 \times 4 = 120$ and $\sigma_x = 10\mu$as, we expect 0.035 star that would allow a significant detection of black hole spin. The median (a_{orb}, e) of such stars is $\approx (1200 R_S, 0.95)$.

We note that more recent papers have studied the faint population of stars in the Galactic Center in more detail, both using stellar counts going down to fainter limits (Gallego-Cano et al., 2018) as well as the faint diffuse light (Schödel et al., 2018). It is important to compare the estimated numbers above (which used assumptions on the stellar population based on brighter stars) to the ones based on the faint population alone. They found $\sigma_0 = 20$ stars arcsec^{-2} and $\sigma_0 \sim 72$ stars arcsec^{-2} at $R_0 = 0.25$" for stars with $17.5 \leq K \leq 18.5$ and $18.5 \leq K \leq 19.5$, respectively, and a surface density exponent $\Gamma \sim -0.4$. From that we estimate ≈ 0.5 and ≈ 2 stars within 50 mas in the two magnitude ranges above, compared to the ≈ 1 star with $K < 19$ we found before. In this case, it is possible that our numbers above are pessimistic to within a factor of ~ 2. We also note that Schödel et al. (2018) and Gallego-Cano et al. (2018) conclude that the population of faint stars is likely to be dominated by the old star population, and in that case a possible faint star found by GRAVITY is more likely to be part of the old cusp rather than a faint, typically young S-star of type A.

One of the consequences of Eq.(3.4.5) is that increasing T and N_{obs} or decreasing σ_x does not strongly increase the limit on $a_{orb}(1-e^2)^{3/4}$ (and therefore the number of stars). If we instead consider an observing campaign of 10 years with $N_{obs} = 30 \times 10 = 300$ total observations, then using Eq.(3.4.5) (and requiring $a_{orb} < 9000 R_S$ so that at least one orbital period is covered), the expected number of stars for measuring black hole spin increases to 0.12, with the median (a_{orb}, e) of such stars $\approx (2400 R_S, 0.96)$. The fraction of such stars with $a_{orb} > 5000 R_S$ (for which a spin measurement would very likely start to suffer from Newtonian perturbations) is $\approx 25\%$.

We can also use these scalings to estimate the potential of future extremely large telescopes for measuring black hole spin from stellar orbits. The main advantage is the large increase in sensitivity. Assuming a limit $K < 22$, the numbers above should be multiplied by a factor of 4 based on the KLF. However, if the astrometric precision cannot reach the 10μas level, the number of stars would be reduced accordingly. Also, if such telescopes could reach radial velocity precisions $\sim 1 - 10$ km/s on faint stars, those could also be used to probe the black hole spin. Because the radial velocity changes are strongest near periastron (as opposed to apastron for the astrometric changes), they should be more robust to Newtonian perturbations (e.g. Psaltis et al., 2016). Finally, in the case of a large FOV there is the possibility of measuring relativistic effects from the collective motions of

Table 3.1: Expected number of stars with $K < 19$ within given contour regions for measuring black hole spin for an observing campaign of duration T with 30 observations/year, $\chi = 0.9$ and spin angle parameters that lead to an average astrometric deviation.

	No Fit T=4 years	Fit T=4 years	Fit T=10 years
$\sigma_x = 10\mu$as no rv	0.15	0.035	0.12
$\sigma_x = 10\mu$as $\sigma_{rv} = 50$km/s	0.15	0.07	0.23

many further out stars (e.g. Do et al., 2017), but such an approach may be a challenge for measuring spin due to Newtonian perturbations.

We note that these estimates should be taken with caution since they are based on an extrapolation to the very inner region around the black hole which has been beyond the resolution limits of any instrument before GRAVITY. A cusp of massive stars in the immediate vicinity of the black hole (Alexander and Hopman, 2009), precursors of stellar-mass black holes, for example could increase the expected number. Alternatively, a break in the KLF from bursts of star formation history (Pfuhl et al., 2011) could decrease it.

3.5 Effect of Radial Velocities

In the above analysis for detecting black hole spin, we have not so far considered radial velocity measurements, which could potentially be made by measuring the redshifts of spectral lines as is traditionally done for S-stars in the Galactic Center (Gillessen et al., 2009). In order to probe redshift effects on a stellar orbit due to spin, however, a very high redshift precision would be needed. As mentioned above, the maximum redshift difference (assuming the most optimistic spin angles) over a full orbit between models with $\chi = 0$ and $\chi = 0.99$ is ≈ 0.3 km/s and 30 km/s for S2 and S2/10, respectively. The effect is also extremely sharped around periastron passage, and would require very targeted observing campaigns in order to be detected.

Previous work (Zhang et al., 2015; Yu et al., 2016) assumed redshift errors $1 - 10$ km/s combined with astrometry when estimating spin errors. Such precision allows redshift probes of spin for potential stars in close orbits around SgrA*, but could only be achieved with future facilities such as E-ELT or TMT (Do et al., 2017). Current redshift measurements for the star S2 (significantly brighter than any potential close star, Gravity Collaboration et al., 2017) have uncertainties ~ 30 km/s. Therefore, a natural question to ask is the extent to which potential radial velocity measurements with errors $\sigma_v > 30$ km/s could help in detecting spin. Although such precision would likely not be enough to measure spin by itself, it should help in better constraining the other parameters and therefore prevent the masking of spin effects to some extent, alleviating the constraints on the required stellar orbits.

Besides direct spectroscopy, we suggest a potential method to measure radial velocities of close orbit stars directly with GRAVITY using spectral differential interferometry in medium resolution. The method is outlined in Appendix 4.8 and we estimate a radial velocity precision $\sigma_v \sim 50$ km/s. In order to test the effect of adding the radial velocity measurements, we selected two example orbits near the transition region in Fig. 3.3, $(a_{orb}, e) = (500R_S, 0.3)$ and $(1600R_S, 0.9)$, corresponding to $a(1-e^2)^{3/4} \approx 460R_S$, and ran a series of 240 fits using (i) only astrometric measurements with $\sigma_x = 10\mu$as; (ii) astrometric and radial velocity measurements with $\sigma_x = 10\mu$as and $\sigma_v = 50$ km/s; and (iii) same as previous but with $\sigma_x = 50\mu$as. The latter covers the case of radial velocity measurements at the expense of astrometric precision. Figure 3.4 shows the histograms for the significance σ of spin detection for each case. The spread in σ (related to the graininess of the contour plots shown before) is natural due to the different error instantiations. A clear trend is observed, in the sense that adding the radial velocities increases the significance of a spin detection only if the astrometric precision can be maintained. Otherwise, if the astrometric precision is degraded by a factor of a few, the significance is severely lessened as the radial velocities themselves do not probe spin effects, but rather lead to a better constraint on the other parameters. Moreover, the increase in significance when adding radial velocities is stronger for the more eccentric orbit.

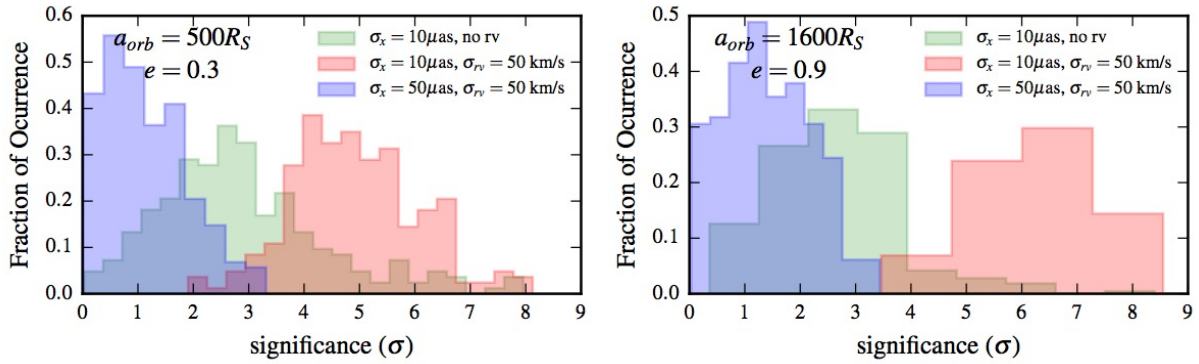

Figure 3.4: Effect of radial velocity measurements on the significance σ of black hole spin. We used the canonical observing campaign discussed previously, selected two orbits near the contour line $(a(1-e^2)^{3/4} \approx 460R_S)$ of the upper right plot of Figure 3.3, and ran 240 simulations to determine the significance after finding the best fit zero-spin solution. This was repeated for three cases: only astrometry with $\sigma_x = 10\mu$as (i), and including radial velocity measurements with $\sigma_{rv} = 50$ km/s with (ii) and without (iii) degradation of the astrometric precision to $\sigma_x = 50\mu$as. The spread in σ for each case is due to the different error instantiations. Adding radial velocity measurements increases the significance by better constraining the orbital parameters, as long as the astrometric precision can be maintained. Notice also that the increase in σ due to radial velocities is more pronounced for the eccentric orbit.

In order to estimate how the required number of stars changes when including radial

velocities, we created (a_{orb}, e) contour plots with the same parameters as before but with additional redshift measurement $\sigma_{rv} = 50$ km/s at each observation. The result is shown in Fig. 3.3 (lower row) and Table 3.1. Whereas the contour line does not change before fitting for the zero-spin solution (since radial velocities with this precision are not probing spin effects), it does move outwards after performing the zero-spin solution fit, consistent with the behavior observed in the two specific examples above. For the canonical observing campaign we use, this means $a_{orb}(1-e^2)^{3/4} \lesssim 500R_S$, with the expected number of stars increasing by a factor of two to 0.07. Increasing the observing campaign to $T = 10$ years increases the number of stars to 0.23.

3.6 Discussion and Conclusion

In this paper, the main goal was to determine the requirements that a hypothetical star would need to satisfy in order to allow a detection of black hole spin through the astrometric monitoring of its orbit around the supermassive black hole in the Galactic Center. In order to do this, we made use of a semi-analytical Kerr geodesics code to calculate stellar orbits close to Sgr A*. Given the sparse sampling of the orbits and the large number of simulations needed, avoiding the numerical integration of the orbits leads to a significant improvement in computational time. For the photon orbit, because the spin effects on both astrometry and redshift are negligible compared to realistic precisions, we have used a weak-field Schwarzschild approximation.

We tested the validity of our code by checking it reproduces the expected relativistic effects on the star S2 and a hypothetical star S2/10. In particular, we noticed that the light bending when S2 passes behind the black hole during periastron passage enhances the signature from periastron advance and could lead to an early detection of the combined effect.

In order to detect black hole spin, closer stars are needed to overcome gravitational perturbations from other stars/remnants (Merritt et al., 2010; Zhang and Iorio, 2017). For average black hole spin angle parameters, we found that the hypothetical star would have to satisfy

$$a_{orb}(1-e^2)^{3/4} \lesssim 300R_S\sqrt{\frac{T}{4\text{years}}}\left(\frac{N_{obs}}{120}\right)^{0.25}\sqrt{\frac{10\mu as}{\sigma_x}}\sqrt{\frac{\chi}{0.9}} \tag{3.6.1}$$

in order to allow detection of black hole spin. The left hand side was derived analytically (Eq. 3.4.6). By fitting simulated relativistic orbits with errors and determining the significance of the deviation from the best-fit zero-spin solution, we verified this expectation and calculated the normalization of the right hand side. In particular, we found that having to fit for all parameters simultaneously leads to a requirement which is about a factor of three more stringent than what would have been predicted directly from the size of the relativistic effect. Using the current distributions of eccentricities and semi-major axis in the inner region of the GC, we have estimated that the number of stars satisfying this con-

ditions is ~ 0.035 and ~ 0.12 for a 4-year and 10-year observing campaign, respectively, with 30 observations/year and 10μas errors in both cases.

We have also shown the effect that radial velocities with precision ~ 50 km/s would have in the detection of spin. Although such redshift precision does not allow to probe spin directly, it helps by providing stronger constraints on the other parameters. The number of expected stars increases by a factor of two if radial velocities at this precision are also available. It is therefore important to consider the possibility of radial velocity measurements in parallel to astrometry, and we give an example of a potential method to do this with GRAVITY.

In the above analysis, we have assumed that the black hole always lies at the origin. In practice, fitting S-star orbits requires the inclusion of offset and linear drift parameters of the black hole (Boehle et al., 2016; Gillessen et al., 2017). In the case of GRAVITY, astrometric measurements are taken relative to a reference star that is used to fringe track (Eisenhauer et al., 2011). Detecting relativistic effects would then require measuring its orbital parameters. However, Gravity Collaboration et al. (2017) showed that it may be possible to reference stellar positions directly to Sgr A*, removing the need for reference frame parameters as long as the near-infrared emission originates close to the black hole. In the case of upcoming extremely large telescopes, the results obtained here still apply except that the reference frame parameters should be included.

We have assumed a pure Kerr metric for the spacetime around Sgr A*, corresponding to the most optimistic case. In practice, a distribution of stars/remnants introduces perturbations that could mask the precession due to black hole spin. Even though these two effects could potentially be separated (e.g. astrometric deviations due to spin are maximum at apastron whereas Newtonian perturbations peak during periastron, Zhang and Iorio, 2017), disentangling them with limited observations and without prior knowledge on the perturbers would be very challenging. From the diffuse light background from faint stars that cannot be currently resolved, Schödel et al. (2018) estimated a total enclosed stellar mass of $\sim 180 M_\odot$ within 250 mas. Using their measured 3D power-law density profile $\gamma \approx 1.1$, this translates to only $\sim 2 M_\odot$ within 25 mas. From Fig.1 of Merritt et al. (2010), this would put an upper limit on $a_{orb} \sim 10,000 R_S$ for frame dragging dominating over Newtonian perturbations, which the stellar orbits considered in this paper are well within . However, both theoretical considerations as well as simulations predict an accumulation of stellar-mass black holes ($\sim 10 M_\odot$) in a steep cusp ($\gamma \approx 1.75 - 2.0$) close to SgrA* through mass segregation (Freitag et al., 2006; Hopman and Alexander, 2006; Alexander and Hopman, 2009; Preto and Amaro-Seoane, 2010; Amaro-Seoane and Preto, 2011). Current upper limits on the total mass within 25 mas ($1.3 \times 10^5 M_\odot$, Boehle et al., 2016) or 13 mas ($4 \times 10^4 M_\odot$, Gillessen et al., 2017) from fitting of stellar orbits cannot exclude the presence of a more massive dark cusp, and therefore it is important to consider its potential disturbance for the measurement of black hole spin with a closer star.

Both Merritt et al. (2010) and Zhang and Iorio (2017) consider a variety of stellar/remnant distributions with different perturber masses, total masses and density profiles to compare the effect of Newtonian perturbations to black hole precession. While Merritt et al. (2010) used N-body simulations to study the overall evolution of an entire cluster,

Zhang and Iorio (2017) studied the detailed evolution of a test star in response to the perturbers. We can use their results to assess how much a black hole spin measurement for our two example stars in §3.5 with $(a_{orb}, e) = (500R_S, 0.3)$ and $(1600R_S, 0.9)$ would suffer from Newtonian perturbations for different cluster properties. Considering stars with $e = 0.88$ and $e = 0.3$ with $\chi = 1$ and spin angles such that the spin-induced astrometric changes are average (as we consider here), Zhang and Iorio (2017) find that the critical semi-major axes are $1440 - 2040R_S$ and $1200 - 1560R_S$ for a cluster of $10M_\odot$ black hole perturbers with density profile $\gamma = 1.75$ and total mass of 30 and 100 $M_\odot$ within 25 mas, respectively. Therefore, the more eccentric star would start to suffer from Newtonian perturbations for cluster masses $\gtrsim 100M_\odot$. Since Zhang and Iorio (2017) found that the effect of Newtonian perturbations is much less dependent on eccentricity than frame dragging, the advantage of a more eccentric star in terms of allowing for a larger semi-major axis is balanced by a higher sensitivity to Newtonian perturbations. Alternatively, from Fig. 3 of Merritt et al. (2010), for a cusp of $10M_\odot$ black holes with $\gamma = 2$ and a total mass $\lesssim 100M_\odot$ within 25 mas and $\chi = 1$, the critical radius is $\gtrsim 5000R_S$, assuming the most optimistic black hole spin angles. Although the exact value depends on the black hole spin parameters, these results show that a steep cusp of black holes with total mass $\gtrsim 100M_\odot$ within 25 mas could start to compromise the measurement of black hole spin with a potential closer star.

Other methods could also be used to detect the black hole spin of SgrA*. Pulsar timing could reach much higher precision (e.g. Liu et al., 2012; Psaltis et al., 2016; Zhang and Saha, 2017), but the lack of ordinary pulsar detections in deep surveys of the central parsec (Johnston et al., 1995; Macquart et al., 2010; Wharton et al., 2012; Dexter and O'Leary, 2014) poses a significant challenge to this approach. Direct imaging of emission surrounding the "black hole shadow" of Sgr A* with radio VLBI (Doeleman et al., 2009) could also potentially constrain spin, but so far suffers from complicated model-dependence (e.g. Broderick et al., 2009; Dexter et al., 2009). Finally, depending on the mechanism behind the NIR flares of SgrA*, astrometric monitoring of e.g. an orbiting hot spot could also allow a measurement of spin (e.g. Broderick and Loeb, 2006; Hamaus et al., 2009; Vincent et al., 2011). All these methods are complementary. Although each is challenging, their combination could probe the spacetime around Sgr A* on scales ranging from $\sim 1 - 3000$ Schwarzschild radii.

Acknowledgements

JD thanks Yang and Wang (2014) for making the YNOGKM code public and D. Psaltis and J. Stone for useful discussions. This work was supported in part by a Sofja Kovalevskaja Award from the Alexander von Humboldt Foundation of Germany.

Appendix

A. Measuring Radial Velocities of a Faint Star with GRAVITY

Here, we explore the possibility of measuring radial velocities of a faint star with GRAVITY using differential visibility signatures across spectral lines. This would require the use of medium resolution ($R \approx 500$). Although low resolution ($R \approx 22$) has been the envisioned mode of operation in the Galactic Center due to SNR considerations, a bright flare state ($K \sim 15$) or partial coupling of S2 ($K \approx 14$) into the GRAVITY fiber (Gravity Collaboration et al., 2017) could provide the necessary SNR for medium resolution, together with long integration times.

A possible faint star is expected to have absorption lines in its spectrum. The faintest early-type stars observed spectroscopically in the Galactic Center ($K \lesssim 17.5$) are compatible with a A0/B9V classification and contain a Brγ absorption line (Pfuhl et al., 2011). For a fast moving star with $v_r \sim 10,000$ km/s, such a line would be significantly displaced from its rest wavelength; therefore, discovering differential visibility signatures at unexpected wavelengths could allow to identify such stars and measure their radial velocity. We focus on an early-type star since they dominate the current spectroscopically identified stars in the S-star cluster (Eisenhauer et al., 2005; Habibi et al., 2017); however, we note that late-type giants are also a possibility for faint stars (Pfuhl et al., 2011), and could very well dominate the population of faint stars close to the center (Schödel et al., 2018; Gallego-Cano et al., 2018). In the latter case, the series of sharp CO bands could provide even more convincing differential visibility signatures.

In order to simulate the expected size of the differential visibility signatures and the precision of the resultant radial velocity measurement, we consider a binary system consisting of a brighter source (either a flare or the star S2 displaced from the center of the GRAVITY fiber PSF) and a fainter source corresponding to the fast-moving star. The complex visibility of a binary system is

$$V(\boldsymbol{u}\cdot\boldsymbol{\sigma}, f) = \frac{1 + f e^{-2\pi i \boldsymbol{u}\cdot\boldsymbol{\sigma}}}{1+f} \tag{3.6.2}$$

where f is the flux ratio, $\boldsymbol{\sigma}$ the separation vector and $\boldsymbol{u} = \frac{\boldsymbol{B}}{\lambda}$ the spatial frequency, and has unit period in $\boldsymbol{u}\cdot\boldsymbol{\sigma}$. Figure 3.5 shows the maximum differential visibility amplitude and phase signals that could be obtained at a spectral line with depth $x = 0.85$ (as is the case for the Brγ line of an A0V star above) as a function of the flux ratio, defined as

$$\max_{0\leq \boldsymbol{u}\cdot\boldsymbol{\sigma}\leq 1} ||V(\boldsymbol{u}\cdot\boldsymbol{\sigma}, f)| - |V(\boldsymbol{u}\cdot\boldsymbol{\sigma}, xf)|| \tag{3.6.3}$$

and

$$\max_{0\leq \boldsymbol{u}\cdot\boldsymbol{\sigma}\leq 1} |\arg(V(\boldsymbol{u}\cdot\boldsymbol{\sigma}, f)) - \arg(V(\boldsymbol{u}\cdot\boldsymbol{\sigma}, xf))| \tag{3.6.4}$$

While the maximum differential visibility amplitude is $\approx 8\%$, the differential visibility

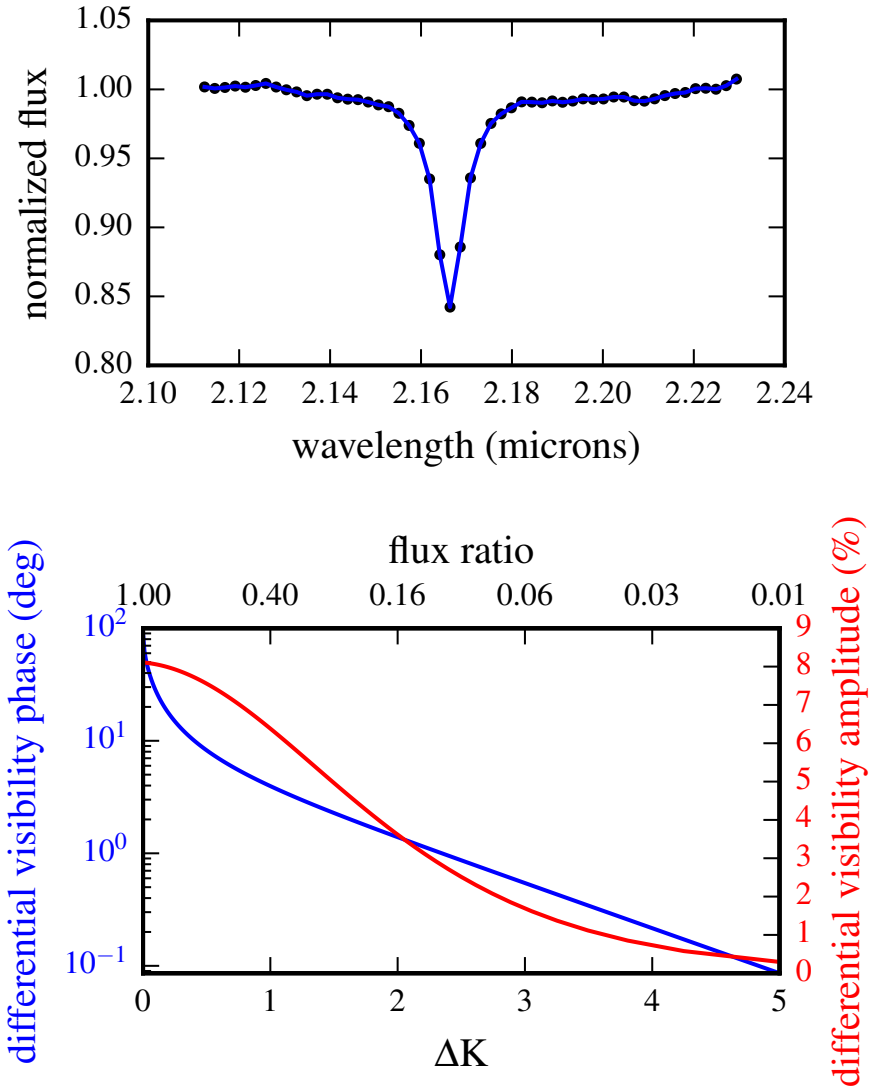

Figure 3.5: **Top:** Brγ line of an A0V star (Wallace and Hinkle, 1997) with sampling appropriate to GRAVITY's medium resolution ($R = 500$) mode. **Bottom:** Maximum differential visibility phase and amplitude across a spectral line for a binary as a function of the flux ratio or near infrared K band magnitude difference. We assume a line depth 0.85 of the continuum corresponding to the spectrum above.

phase is strongly nonlinear and could be $> 80°$ for an equal-brightness binary. Such a large signature could be used, for example, to test whether the quiescent emission from SgrA* has a contribution from a stellar component.

Here, we consider the case $\Delta K = 2$ ($f = 16\%$), which could correspond for e.g. to a faint star $K = 18$ with a brighter component (flare or S2). We set the binary separation $\sigma = (10, 10)$ mas and onsider again the above case for the Brγ line with depth 0.85. Figure 3.6 shows the differential visibility amplitude and phase as a function of $\boldsymbol{u} \cdot \boldsymbol{\sigma}$, as well as the points sampled by the six VLTI UT baselines, simulated assuming $LST = 18\,\mathrm{h}$ as appropriate for observing the Galactic Center. The maximum differential phase and amplitude signals are $\approx 1.5°$ and 4%, respectively. GRAVITY has already achieved a differential precision $0.2°/0.4\%$ and $0.5°/1\%$ on $K \approx 6$ and $K \approx 10$ sources with short integration times $\sim 1\,\mathrm{h}$, respectively (Gravity Collaboration et al., 2017).

In order to estimate the radial velocity precision that could be potentially achieved with such a method, we simulate differential signals on the six baselines assuming precisions $\sigma_\phi = 0.3°$ and $\sigma_{amp} = 0.6\%$, and fit all baselines simultaneously with Lorentzian profiles for the differential signatures. The resulting statistical error in redshift is $\sigma_{rv} \approx 30\,\mathrm{km/s}$. Considering additional systematic errors of comparable order, we adopt $\sigma_{rv} = 50\,\mathrm{km/s}$ for our simulations.

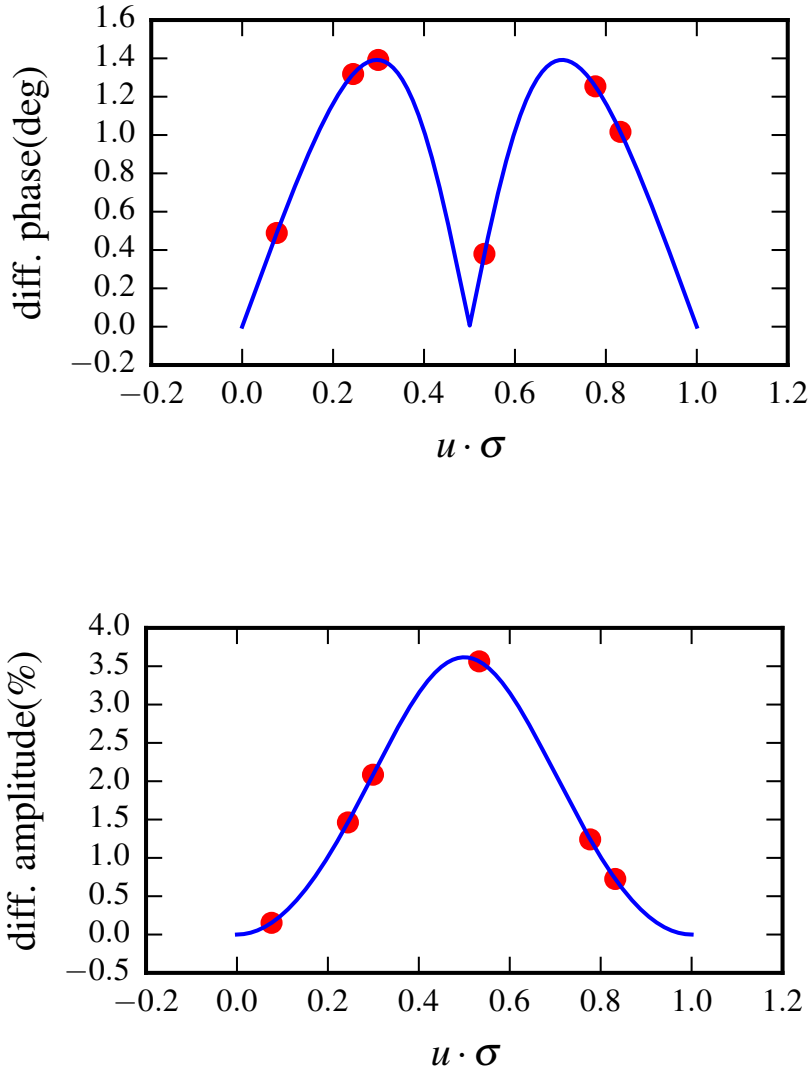

Figure 3.6: Differential visibility phase and amplitude across the Brγ spectral line as a function of $\boldsymbol{u} \cdot \boldsymbol{\sigma}$ for the case $\Delta K = 2$. The six red points show a possible sampling with the VLTI UT baselines with binary separation vector $\sigma = (10, 10)$ mas.

Chapter 4

Submilliarcsecond Optical Interferometry of the High-mass X-Ray Binary BP Cru with VLTI/GRAVITY

Original publication: GRAVITY Collaboration: I. Waisberg, J. Dexter, O. Pfuhl, R. Abuter, A. Amorim, N. Anugu, J. P. Berger, N. Blind, H. Bonnet, W. Brandner, A. Buron, Y. Clénet, W. de Wit, C. Deen, F. Delplanck-Ströbele, R. Dembet, G. Duvert, A. Eckart, F. Eisenhauer, P. Fédou, G. Finger, P. Garcia, R. Garcia Lopez, E. Gendron, R. Genzel, S. Gillessen, X. Haubois, M. Haug, F. Haussman, Th. Henning, S. Hippler, M. Horrobin, Z. Hubert, L. Jochum, L. Jocou, P. Kervella, Y. Kok, M. Kulas, S. Lacour, V. Lapeyrère, J.-B. Le Bouquin, P. Léna, M. Lippa, A. Mérand, E. Müller, T. Ott, L. Pallanca, J. Panduro, T. Paumard, K. Perraut, G. Perrin, S. Rabien, A. Ramírez, J. Ramos, C. Rau, R.-R. Rohloff, G. Rousset, J. Sanchez-Bermudez, S. Scheithauer, M. Schöller, C. Straubmeier, E. Sturm, F. Vincent, I. Wank, E. Wieprecht, M. Wiest, E. Wiezorrek, M. Wittkowski, J. Woillez & S. Yazici, 2017, ApJ, 844, 72, *Submilliarcsecond Optical Interferometry of the High-mass X-Ray Binary BP Cru with VLTI/GRAVITY*, DOI: 10.3847/1538-4357/aa79f1

Abstract: We observe the HMXB BP Cru using interferometry in the near-infrared K band with VLTI/GRAVITY. Continuum visibilities are at most partially resolved, consistent with the predicted size of the hypergiant. Differential visibility amplitude ($\Delta|V| \sim 5\%$) and phase ($\Delta\phi \sim 2^\circ$) signatures are observed across the HeI 2.059μm and Brγ lines, the latter seen strongly in emission, unusual for the donor star's spectral type. For a baseline $B \sim 100\,\mathrm{m}$, the differential phase RMS $\sim 0.2^\circ$ corresponds to an astrometric precision of $\sim 2\mu$as. We generalize expressions for image centroid displacements and variances in the marginally resolved limit of interferometry to spectrally resolved data, and use them to derive model-independent properties of the emission such as its asymmetry, extension and strong wavelength dependence. We propose geometric models based on an extended

and distorted wind and/or a high density gas stream, which has long been predicted to be present in this system. The observations show that optical interferometry is now able to resolve HMXBs at the spatial scale at which accretion takes place, and therefore probe the effects of the gravitational and radiation fields of the compact object on its environment.

4.1 INTRODUCTION

X-ray binaries are usually divided into two classes: high-mass (HMXB), in which the compact object is fed by a strong wind/disk from a massive OB/Be companion, and low-mass (LMXB), in which accretion happens through Roche lobe overflow from a low-mass star, leading to the formation of an accretion disk around the compact object. In both cases, the compact object can be a white dwarf, neutron star or a black hole.

The small scale of such systems, typically with semi-major axis $a < 1\,\mathrm{mas}$, means that they are below the imaging resolution even of the largest optical/near-infrared interferometers. Therefore, information about the accretion process in these systems and the interaction between the compact object's X-ray output and the stellar environment have so far been restricted to X-ray or optical photometry and spectroscopy, from which spatial information are then inferred (for recent reviews on HMXBs in particular, see for e.g. Charles and Coe, 2006; Chaty, 2011; Walter et al., 2015).

Spectral differential interferometry can provide direct spatial information on scales as small as $\sim 1-10\ \mu$as, depending on the differential visibility precision that can be achieved. However, optical interferometry requires a bright enough object for fringe tracking due to the very short atmospheric coherence time that degrades the interferometric signals. For the typical optical/near-infrared interferometers working in the V, K or H band, this means that nearly all LMXBs and the great majority of HMXBs cannot be observed interferometrically with the current facilities.

GRAVITY (Eisenhauer et al., 2011; GRAVITY Collaboration et al., 2017), the four-telescope beam combiner working at the Very Large Telescope Interferometer (VLTI) and which operates in the K band, has made it possible to observe fainter objects and to achieve very small differential visibility errors, mainly driven by an improved fringe tracking system, which allows for longer coherent integration times, as well as the overall stability of the instrument contributed by its many subsystems. In the case of GRAVITY, fringe tracking limits are $K \lesssim 7$ and $K \lesssim 10$ for the Auxiliary Telescopes (ATs) and Unit Telescopes (UTs), respectively, which means that there are only a handful of Galactic targets that are doable (Liu et al., 2006). We note that dual-field interferometers such as GRAVITY could potentially improve such magnitude limits, provided that a bright enough reference star exists within the FOV ($2-4$ arcseconds for GRAVITY).

The only published past observations of a HMXB with an optical interferometer were of Vela X-1 (Choquet et al., 2014) and CI Cam (Thureau et al., 2009, and references therein). The former was observed with VLTI/AMBER in the K band and VLTI/PIONIER in the

H band. It contains a supergiant O star emitting a strong stellar wind and a massive slowly rotating pulsar. Resolved structures of radius $\sim 8 \pm 3 R_*$ and $\sim 2 \pm 1 R_*$ were inferred from K and H band continuum visibilities, respectively. Two different interpretations were proposed: the resolved structure could be a stellar wind with a strong temperature gradient that deviates significantly from a black body at thermal equilibrium, or the resolved structure in the K band was a diffuse shell not present at the time of the H band observations, which would then correspond to either the stellar wind or the photosphere. Even though spectral lines from HI and HeI were observed in the high resolution K band spectrum, no differential visibility signatures were detected beyond the noise level, and therefore the application of differential spectral interferometry was not possible. CI Cam was observed with PTI in the K band and with IOTA in the K and H bands. The system is a B(e) X-ray binary and the nature of the compact object is unknown. The interferometric observations were able to resolve extended, hot emission from a ring-shaped circumstellar dust envelope of major axis ~ 8 mas. However, no clear evidence for the compact companion was found and the low resolution did not allow the usage of differential spectral interferometry.

BP Cru is among the brightest HMXBs in the K band ($K = 5.7$). It is also one of the canonical wind-accreting supergiant HMXBs (Walter et al., 2015); it has, however, several unique properties, some of which are listed in Table 4.1. It contains a massive and slow-spinning pulsar (GX 301-2) with a typical magnetic field strength of a young neutron star. The donor star, Wray 977, is a rare hypergiant of B1Ia+ classification (Kaper et al., 1995). There are only a handful others in the Galaxy (Clark et al., 2012), and it is the only one known to be in a binary system. Furthermore, it has one of the most eccentric orbits among HMXBs (Liu et al., 2006). t is therefore a promising candidate for studying the wind and outflow properties of the massive donor star in a HMXB (Martínez-Núñez et al., 2017) through optical interferometry. With the goal of studying the inner regions of this system, we have conducted interferometric observations of BP Cru during the commissioning stage of VLTI/GRAVITY in May 2016. This paper reports on these observations.

We summarize the relevant background about this system that will guide us in the interpretation of the interferometric results (Section 4.2). Section 4.3 summarizes the observations and the most important aspects of the data reduction. Section 4.4 presents the analysis of the K band spectrum. Section 4.5 presents the interferometric results, which are then discussed and fit to physically inspired geometrical models in Section 4.6. Section 4.7 presents complementary data that hints at the future work for this project. Finally, Section 4.8 summarizes the main results.

4.2 The Effects of the Compact Object on the Surrounding Stellar Environment

In this section, we summarize relevant information known about BP Cru that will guide the interpretation of the interferometric results. In BP Cru, the pulsar is embedded in the dense stellar wind of Wray 977 and its gravitational and radiation fields are expected to influence

Table 4.1: Properties of BP Cru / Wray 977 / GX 301-2

Parameter	Symbol/ Unit	Value	Reference
	BP Cru		
distance	d (kpc)	≈ 3	(1)
orbital period	P_{orb} (days)	41.498 ($\pm$0.002)	(2)
eccentricity	e	0.462 ($\pm$0.014)	(2)
binary inclination	i (deg)	60 ($\pm$10)	(1)
mean X-ray luminosity	$\langle L_X \rangle$(ergs/s)	7×10^{36}	(1)
maximum X-ray luminosity	L_X^{max}(ergs/s)	4×10^{37}	(1)
	Wray 977 (B1Ia+)		
mass	$M_*(M_\odot)$	$39 - 68$	(1)
radius	$R_*(R_\odot)$	62[a]	(1)
photosphere radius	$R_{2/3}(R_\odot)$	70[b]	(1)
bolometric luminosity	$L_*(L_\odot)$	5×10^5	(1)
effective temperature	$T_{eff}(K)$	18100[b] ($\pm$500)	(1)
mass-loss rate	$\dot{M}(M_\odot/\mathrm{yr})$	10^{-5}	(1)
wind terminal velocity	v_∞(km/s)	305	(1)
speed below sonic point	$v_{2/3}$(km/s)	4.40	(1)
volume filling factor	f	1.0	(1)
rotational velocity	$v \sin i$ (km/s)	50 ± 10	(1)
radial velocity amplitude	K_* (km/s)	10 ± 3	(1)
	GX 301-2		
projected semi-major axis	$a_X \sin i$ (lt-s)	368.3 ± 3.7	(2)
radial velocity amplitude	K_X (km/s)	218.3 ± 3.3	(2)
mass (lower limit)	$M(M_\odot)$	1.85 ± 0.6	(1)
spin period	$P_{spin}(s)$	696	(3)
surface magnetic field	$B(G)$	4×10^{12}	(3)

[a] At Rosseland optical depth $\tau \sim 30$.
[b] At Rosseland optical depth $\tau = 2/3$.
References: (1) Kaper et al. (2006) (2) Koh et al. (1997) (3) Kreykenbohm et al. (2004)

the surrounding stellar environment. We note that at the orbital phase of observation ($\phi \sim 0.21$ using orbital parameters from Koh et al., 1997), the compact object was at a distance $\sim 210 R_\odot$ from the donor star's center (the minimum distance at periastron is $\sim 100 R_\odot$).

4.2.1 The Accretion Mechanism and the Gravitational Influence of the Pulsar

The X-ray emission in wind-accreting HMXBs is explained through the capture of the strong stellar wind of the supergiant companion by the compact object (Bondi and Hoyle, 1944; Davidson and Ostriker, 1973). X-ray light curves and column densities for many of these systems, on the other hand, have found evidence of more complex mechanisms, with a spherically symmetric wind accretion model unable to explain the data successfully.

Stevens (1988) studied the gravitational effects of a compact object on an eccentric orbit in a HMXB system, and found that the wind mass-loss rate is substantially enhanced within a small angle around the line-of-centers, resulting in a higher accretion rate that could explain X-ray outburst intensities better than a spherically symmetric wind accretion model. This inspired accretion models which included, in addition to the spherical wind, a tidal stream of gas of enhanced density that trails the compact object along its orbit and is responsible for most of the accretion rate. In the case of BP Cru, such models better explain its X-ray emission and column density as a function of orbital phase than purely spherical wind models (Haberl, 1991; Leahy, 1991, 2002). In particular, the presence of a strong X-ray outburst slightly before periastron, as well as a smaller peak near apastron, could be explained by the pulsar moving through the dense gas stream two times per orbital period. Studies of the X-ray hardness ratio along the orbit are also in rough agreement with such a model (Evangelista et al., 2010). Moreover, an increase in column density during superior conjunction points to a stream of enhanced density trailing the X-ray source. The most recent analysis by Leahy and Kostka (2008) found a density enhancement in the stream of $\sim 20\times$ compared to the wind, resulting in a mass loss rate in the stream $\sim 2.5\times$ higher than the wind. In this scenario, such a gas stream would then dominate not only the accretion process, but also the mass loss itself. For BP Cru in particular, the high eccentricity, which implies that the pulsar's distance from the massive star varies by a factor of $\frac{1+e}{1-e} \sim 2.7$ (the same holding for its speed), can lead to complex stream shapes. Kaper et al. (2006) notes that tidal interaction is expected during periastron passage, and also finds evidence for variations in the emission and absorption parts of the optical P-Cygni lines Hβ and HeI $5876A$; in particular, a blue-shifted absorption component is seen at all orbital phases, which could be evidence for the presence of a large scale gas stream in the system, both in the orbital plane as well as in the direction perpendicular to it.

Models invoking a circumstellar disk around the supergiant star and inclined with respect to the binary plane have also been proposed as an accretion mechanism (Pravdo et al., 1995). However, they have found less success than the stream models to explain the X-ray light curve (Leahy, 2002). Furthermore, there is no evidence of a circumstellar disk

in the optical spectrum (Kaper et al., 2006).

We note that the X-ray light curve of BP Cru is quite stable, with no clear distinction between low/hard and high/soft states typical of systems containing accretion disks. However, Koh et al. (1997) reports on two rapid spin-up episodes of the pulsar lasting for about 30 days, and suggests that this may point to the formation of transient accretion disks following a period of increased accretion rate. Furthermore, the recent, first radio detection from BP Cru suggests a variable component in addition to a baseline component arising from Wray 977's wind, and possibly associated with a weak and transient jet (Pestalozzi et al., 2009).

4.2.2 The Radiation Influence of the Pulsar

The X-ray emission of the pulsar is expected to influence the surrounding stellar environment, mainly through radiation pressure, X-ray heating and photoionization. In hot stars, the wind is accelerated by scattering from photons absorbed in line transitions (CAK model, Castor et al., 1975). The ionization of the wind results in a cut off in the wind acceleration, leading to an increase in the wind density that has been evoked to explain the increase in accretion rates in systems that undergo transient behavior. At very high X-ray illumination that suppresses radiative cooling, X-ray heating can lead to thermally-driven winds (Blondin, 1994).

Haberl (1991) and Islam and Paul (2014) found evidence for X-ray ionization of the wind when BP Cru was in outburst near periastron from a low energy excess $\lesssim 3$ keV in the X-ray spectrum. Variations in the X-ray mean brightness between different orbital periods could also point to X-ray irradiation effects (Leahy and Kostka, 2008). Finally, we note that recently, about two months before the observations reported in this paper, an unusual and extremely bright X-ray outburst was reported with *Swift* with evidence for strong ionization of the surrounding environment (Fuerst et al., 2016).

In summary, there is ample evidence that the pulsar is closely interacting with the stellar environment in BP Cru. Recent 3D hydrodynamical simulations to study simultaneously the gravitational and radiation effects of the compact object on the stellar wind of HMXBs support that these interactions should play an important role in such systems (Walder et al., 2014; Čechura and Hadrava, 2015).

4.3 OBSERVATIONS AND DATA REDUCTION

4.3.1 Instrument Setup and Observations

We have observed BP Cru with VLTI/GRAVITY on the night of 2016-05-18 with the UTs. The observations were carried out in high resolution ($R = 4,000$) and in combined (i.e. no split polarization) mode. Table 4.2 summarizes the observations. Figure 4.1 shows the corresponding uv coverage.

Table 4.2: Summary of Observations

Date Time(UTC)	Mode	Integration Time/file	Total Integration Time	Seeing (")
2016-05-18 00:56-02:14	HR COMBINED	DIT=30s NDIT=10	35min	0.4-0.6

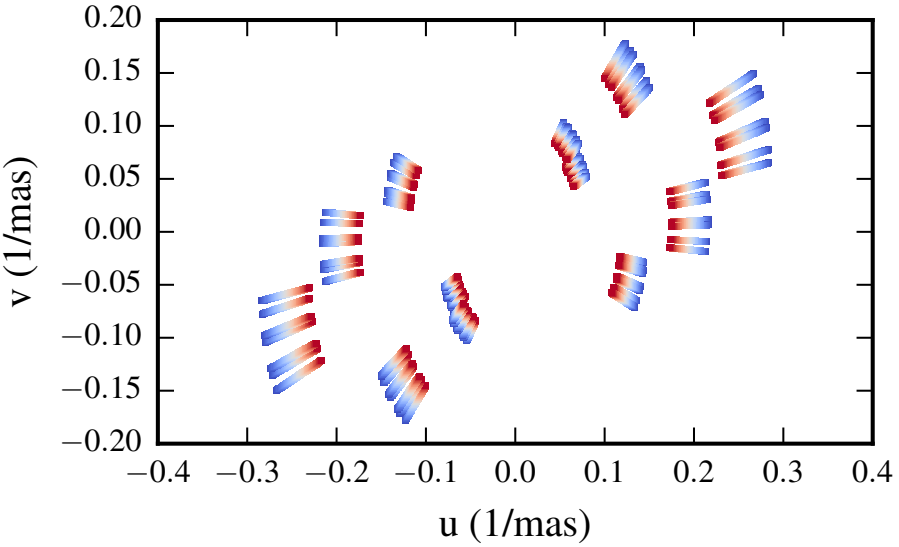

Figure 4.1: The uv-coverage of our GRAVITY BP Cru observations. The colors represent the different wavelength channels across the K band, from blue (1.99μm) to red (2.45μm).

The baseline directions on the sky plane are shown in Figure 4.2, together with the predicted binary image at the time of observation. Because there is no astrometric information on the binary system, the exact position of the pulsar on the sky plane is not known. However, we show that we can narrow down its position to the four possibilities shown (see Appendix A).

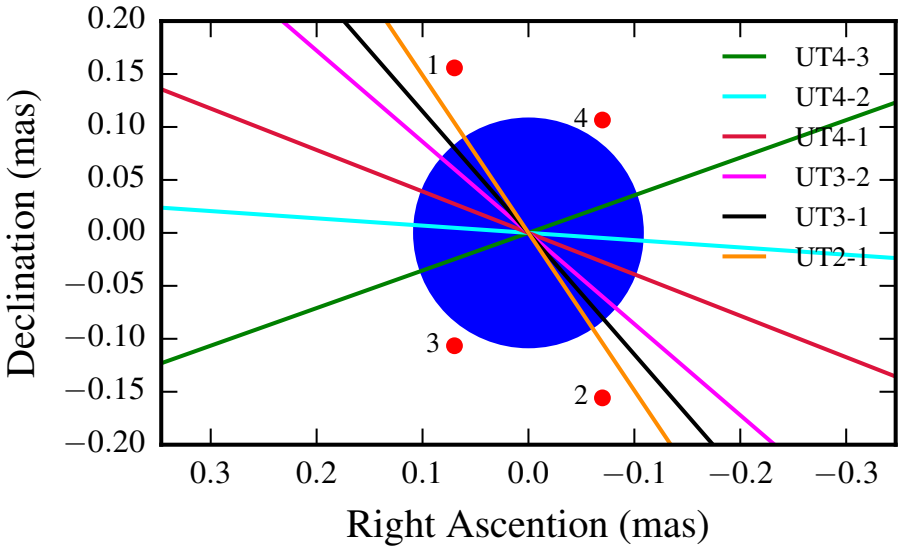

Figure 4.2: Baseline directions on the sky plane. Also shown are the donor star (photospheric radius $\sim 70 R_\odot$) and the predicted four possible positions of the pulsar (red) on the sky plane at the time of observation. For details see Appendix A.

4.3.2 Data Reduction

The data were reduced with the standard GRAVITY pipeline (version 0.9.6, Lapeyrere et al., 2014), which is based on the principle of the Pixel to Visibility Matrix (P2VM, Tatulli et al., 2007). An internal artificial light source is used to characterize the transition from pixel intensities to complex visibilities for each baseline in each of the two detectors (science and fringe tracker), which is then applied to the scientific observations (after appropriate sky subtraction). The wavelength calibration in this case (high resolution) is performed with an Argon lamp. Absolute visibilities are calibrated by means of computing a transfer function using calibrator stars of known diameter, which is also used to calibrate the visibility and closure phases. The default values in the pipeline were used. In particular, we use the so-called VFACTOR to estimate the loss of coherence of the science channel using the fringe tracker data (which measures the phase deviations at a faster rate than the applied corrections), and rescale the science absolute visibilities accordingly.

The interferometric calibrators used are listed in Table 4.3. These stars were also used as telluric calibrators for the spectrum. As cool supergiants, they are expected to contain

very weak absorption lines of hydrogen. In particular, by dividing by an approximate telluric spectrum[1], we checked that there was no remaining Brγ or HeI line to be removed within the noise level of the spectrum. Unfortunately, the calibrator stars contain CO absorption bands in the red part of the spectrum, which is also affected by telluric lines. Therefore, we do not show wavelengths $\gtrsim 2.20\mu$m. This region shows neither discernible spectral lines nor interferometric signatures above the noise level.

Table 4.3: Interferometric Calibrators

Name	Spectral Type	Diameter (mas)	Reference
HD 97550	G8II/III	0.828 ± 0.008	(a)
HD 110532	G8Ib/II	0.804 ± 0.008	(a)

[a] Merand et al. (2005)

The pipeline reports a wavelength calibration with absolute accuracy of ~ 1 spectral resolution element (40 km/s). Since we can achieve statistical errors that are smaller than that when fitting strong emission lines, we cross-correlated (IRAF, XCSAO package) the uncorrected spectra with the model telluric spectrum in order to reduce the systematic uncertainty in the wavelength calibration. We found a global shift $\sim -60 \pm 5$ km/s consistent for both calibrators and science spectra, and applied the correction.

4.4 SPECTROSCOPIC ANALYSIS

4.4.1 Results

Currently the most valid spectral classification of Wray 977 is an early blue hypergiant, B1Ia+, based on high-resolution optical spectra (Kaper et al., 2006). Figure 4.3 shows the K band spectrum obtained with GRAVITY, and comparison spectra of ζ^1 Sco, HD 169454 and HD190603, isolated stars of similar spectral type (Hanson et al., 1996). The most striking differences of Wray 977 are its stronger emission in HeI 2.059μm and Brγ in emission rather than absorption. The spectrum in Figure 4.3 has been degraded to a worse resolution for a better comparison with the other stars. The spectrum at the original resolution is shown in Figure 4.18.

Table 4.4 shows the identified lines and their measured radial velocities from Gaussian fits (all wavelengths referred are in vacuum). The HeI absorption doublet lines were fit jointly with separate Gaussians for each line and the HeI emission line was fit jointly with a P-Cygni absorption component. The errors shown combine the statistical errors from the fit with the estimated 5 km/s error on the wavelength calibration. In practice, the error is dominated by systematic effects caused by the limited spectral resolution and imperfect telluric correction. The velocities were converted to the heliocentric frame.

[1] taken from ESO Spectroscopic Standards webpage.

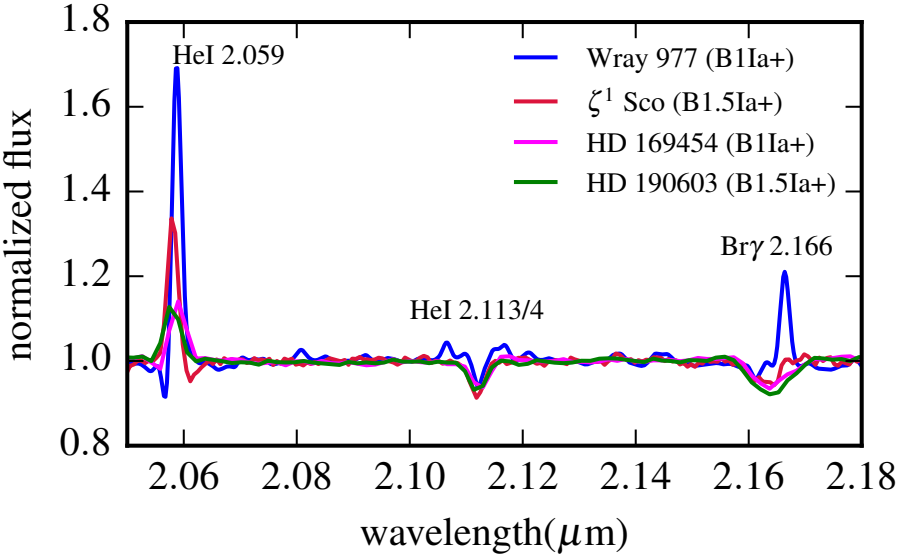

Figure 4.3: Comparison of Wray 977's GRAVITY spectrum with isolated stars of similar spectral type (Hanson et al., 1996). The GRAVITY spectrum has been degraded to the resolution of the ζ^1 Sco spectrum ($R \sim 1,500$). The other two spectra have slightly lower resolution, $R \sim 800$. Note the more prominent HeI 2.059μm emission and the Brγ line in emission for Wray 977. The stars have different wind properties, with Wray 977 having the densest wind.

Table 4.4: Spectral Lines Identified

Line (Rest Wavelength in Vacuum)	Measured Velocity (km/s)
HeI 2.0587μm	$+29 \pm 6$ km/s
HeI 2.1126μm	-43 ± 10 km/s
HeI 2.1138μm	$+2 \pm 15$ km/s
Brγ 2.16612μm	$+55 \pm 7$ km/s

The double HeI 2.113μm, 2.114μm absorption lines do not show any interferometric signature relative to the continuum above the noise level, which could mean that they are photospheric. If this were true, they would trace the systemic velocity of the system as well as the radial velocity of the hypergiant (which is very small, $|v| < 10$ km/s, Kaper et al., 2006). We obtain inconsistent results for the radial velocity of the two lines, which could be due to wind contamination. If that is the case, the lack of discernible interferometric signatures is not surprising as the lines are very weak.

4.4.2 Discussion

The HeI 2.059μm line has an unsaturated P-Cygni profile, which suggests an optically thin wind. This line is highly sensitive to temperature and wind properties and becomes very active in OB supergiants, acting as a tracer of extended atmospheres (Hanson et al., 1996). Wray 977 has an estimated mass-loss rate $\sim 5 - 10\times$ higher than the comparison stars shown, which is consistent with the stronger emission.

The Brγ in emission in Wray 977 is a clear deviation from the isolated comparison stars. One explanation could be that its denser wind drives the line into emission. Unfortunately, these are the only currently known galactic early-B hypergiants of subtype earlier than 2 (Clark et al., 2012), so this hypothesis cannot be tested observationally. Using detailed stellar atmosphere codes to test this hypothesis is beyond the scope of this paper. Preliminary results (F. Martins, private communication) and previous work (Clark et al., 2003) suggest that this could indeed be the case.

Another possibility is that the Brγ emission could be caused by denser accretion structures present in the system. As a recombination line, Brγ emission is usually very sensitive to density (Kudritzki and Puls, 2000). There are many reports in the literature of Brγ emission lines in X-ray binary systems originating from the accretion disk and its wind. Shahbaz et al. (1999) reports on a double-peaked Brγ emission line for the LMXB V616 Mon, in which the donor star is a K-type dwarf that should not show such an emission line. Bandyopadhyay et al. (1999) reports on Brγ lines with P-Cygni shape from the LMXB systems Sco X-1 and GX13+1. In the latter, the donor star is a K-type giant that is not expected to have emission in Brγ, whereas in the former the wind terminal velocity is too high to be associated with the O-type donor star wind. In both cases, an accretion disk wind is evoked to explain the emission. Perez M. and Blundell (2009) report on a spectroscopic campaign to decompose the Brγ emission line of the HMXB and microquasar SS433, and are able to find several emission components, including a double-peaked accretion disk component. Also in this case, the A-type donor star supergiant is not expected to show such emission line. In several of these cases, HeI lines in the K band, most notably HeI 2.059μm, are also in emission.

In HMXBs such as BP Cru, where a stable accretion disk is not expected, associating Brγ or HeI line emission with an accretion structure is less obvious. However, this possibility should not be excluded in the case of BP Cru, since a gas stream of enhanced density that could be dominating the mass-loss rate is expected to be present.

4.5 INTERFEROMETRIC RESULTS

Here we focus on the main results from the interferometric data. We divide this section in two parts: continuum visibilities and spectral differential visibilities. For the purposes of data analysis, the seven files were averaged, with the corresponding (u, v) coordinates averaged linearly, as appropriate given the short time interval ($\sim$1h20min) spanned by the files. Such interval is also negligible compared to the orbital period and X-ray variability timescale.

4.5.1 Continuum Size and Asymmetry

Here we estimate an upper limit on the continuum size from the continuum visibility amplitudes. The most reliable visibility amplitude estimator is the squared visibility modulus of the fringe tracker (FT), since it measures the fringe visibility within the coherence time of the atmosphere. The FT operates at low resolution ($R \sim 20$, or 5 spectral channels across the K band), which makes it useful for measuring continuum interferometric observables. As will be shown later, the emission lines are only marginally resolved (Figure 4.18), and therefore their effect on the visibilities of the FT spectral channels can be neglected.

We note that the continuum closure phases are zero to within the noise limit (RMS $< 1^\circ$) on all baselines. The closure phase is much more robust to systematic errors than the visibility amplitudes, and therefore there is strong indication for a symmetrical continuum emission. Since, in addition, the source is very close to unresolved, there is no big difference between using a disk, Gaussian or any similar model for the continuum $|V|$. We choose a uniform disk model with the angular diameter as the only parameter.

Figure 4.4 shows the squared visibility modulus measured by the FT, averaged over the five spectral channels for each baseline. The error bars include the measurement errors from the science object, as well as from the calibrator object and the calibrator diameter's systematic uncertainty $\sim 1\%$. Disk models with the indicated angular diameters are also plotted for comparison.

The data is most consistent with an unresolved continuum of size $\theta_d \lesssim 0.2$ mas. Because the continuum size is in the very challenging limit that is well below the interferometer canonical resolution $\theta \ll \frac{\lambda}{|\boldsymbol{B}|} \sim 3$ mas, the measurements are very sensitive to systematic errors between baselines. We therefore restrain from a formal fit, and restrict to providing a very conservative upper limit to the continuum size $\theta_d \lesssim 0.4$ mas. Structures larger than this are clearly inconsistent with the data, as shown in Figure 4.4.

4.5.2 Differential Visibilities and Phases

For treating the differential visibility signatures, we averaged the seven files after normalizing the visibility amplitudes to an unresolved continuum. The visibility phases are output from the pipeline already mean and slope subtracted i.e. as differential quantities.

Figure 4.5 shows the differential visibility amplitudes across the Brγ line for the six baselines at hand. The photospheric-corrected flux ratio (see Appendix B) between the

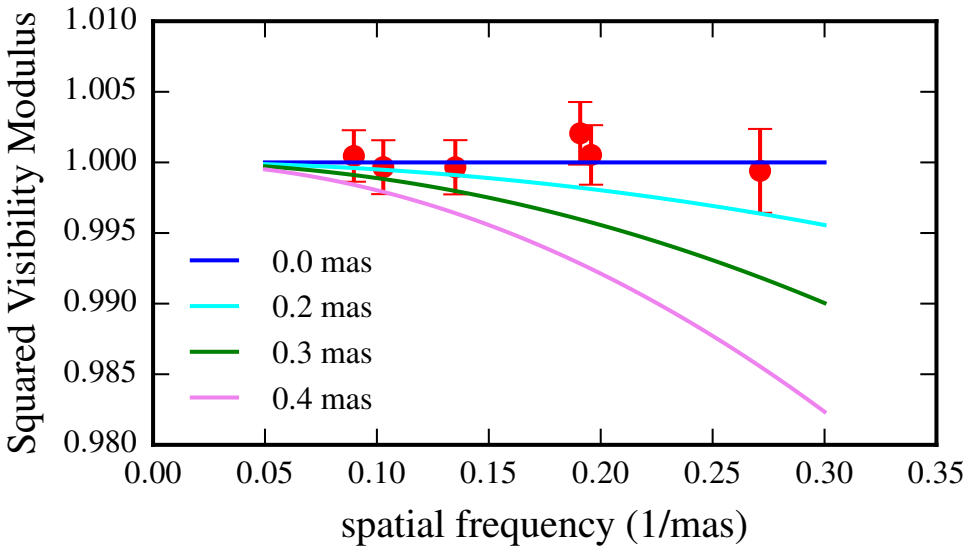

Figure 4.4: Continuum visibility amplitudes (spectrum average) measured by the fringe tracker. Disk models with varying angular diameters are shown for comparison.

continuum and the line emission is also shown for comparison. In general, the visibility amplitudes show, for some baselines, a decrease at the lines relative to the continuum, which is indicative of extended or multi-component emission. However, the peak of the $|V|$ drop does not happen at the center of the line, but rather it is displaced to the blue side. Figure 4.6 shows the differential visibility phases. They show larger, negative values on the blue side of the line and, for some baselines, smaller, positive values on the red side of the line. Such "S-shaped" differential visibility signatures across a line are typical interferometric tracers of rotation (e.g., they are often observed in Be stars, in which they are attributed to extended equatorial disks, but in these systems the blue and red phase signatures are roughly symmetric, Meilland et al., 2012). The black lines in the plots are model-independent fits to the data and will be discussed in the following section.

Figure 4.18 shows the differential visibilities across the spectrum. Similar interferometric features to Brγ in both differential visibility amplitudes and phases are also found across the HeI 2.059μm emission line. However, this region of the spectrum suffers from a particularly high level of noise due to the GRAVITY metrology laser and the large telluric absorption. For instance, the RMS in the visibility amplitude, estimated from the scatter in the continuum region around the lines, is 0.4% and 1.2% for Brγ and HeI, respectively. Similarly, the corresponding values for differential visibility phases are 0.2° and 0.6°. That, in addition to the more complicated (P-Cygni) shape of the line, led us to focus our analysis on the Brγ line. We show in Figure 4.7 the visibility signatures across the HeI 2.059μm line for some representative baselines.

Several factors point to the credibility of such features. The wavelength alignment between the extracted spectrum for each telescope agrees to $< \frac{1}{2}$ of a resolution element.

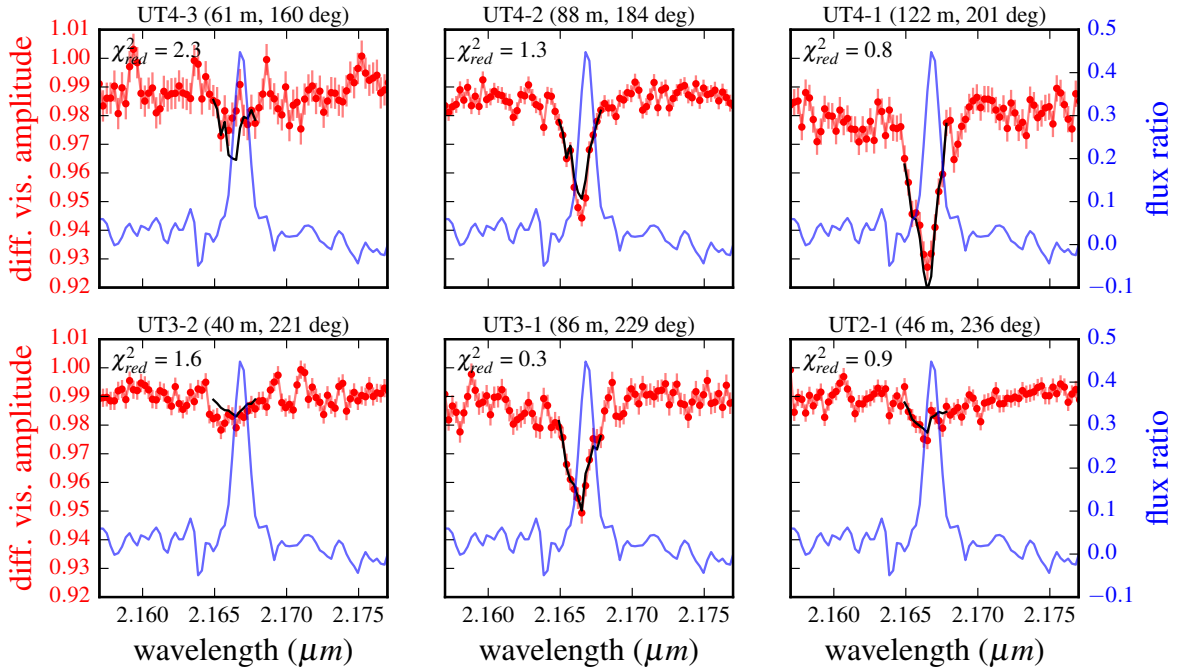

Figure 4.5: Differential visibility amplitudes at Brγ line (red) and the normalized photospheric-corrected flux ratio (blue). For each baseline, the projected baseline length and the position angle are also shown. In black, we show model-independent fits to the visibility amplitudes (see text for details).

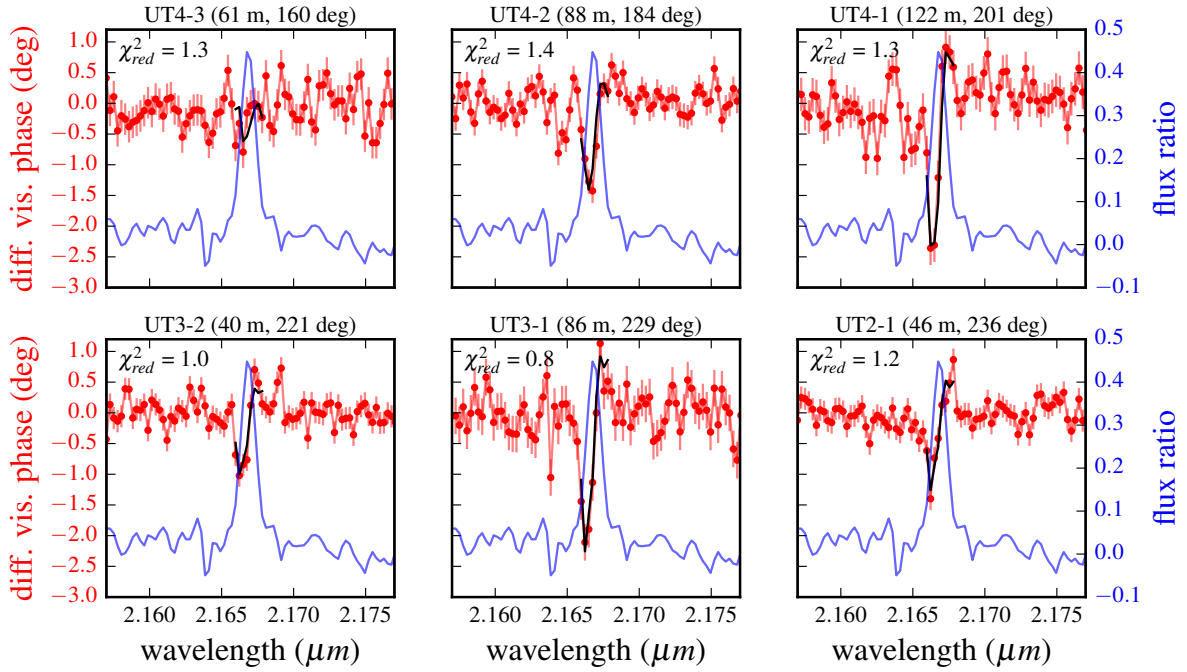

Figure 4.6: Differential visibility phases at Brγ line (red) and normalized photospheric-corrected flux ratio (blue). For each baseline, the projected baseline length and the position angle are also shown. In black, we show model-independent fits to the visibility phases (see text for details).

Similar features are not found at other lines in the spectrum, either related to the science object (e.g. HeI 2.113/4μm) or telluric. Moreover, they show up with different strengths for different baselines (as expected for any reasonable interferometric model) and are consistent between the two emission lines. Finally, for the differential visibility amplitudes, the features are strongest in three baselines which encompass all of the four telescopes, whereas for the differential visibility phases a signature is detectable in five of the six baselines.

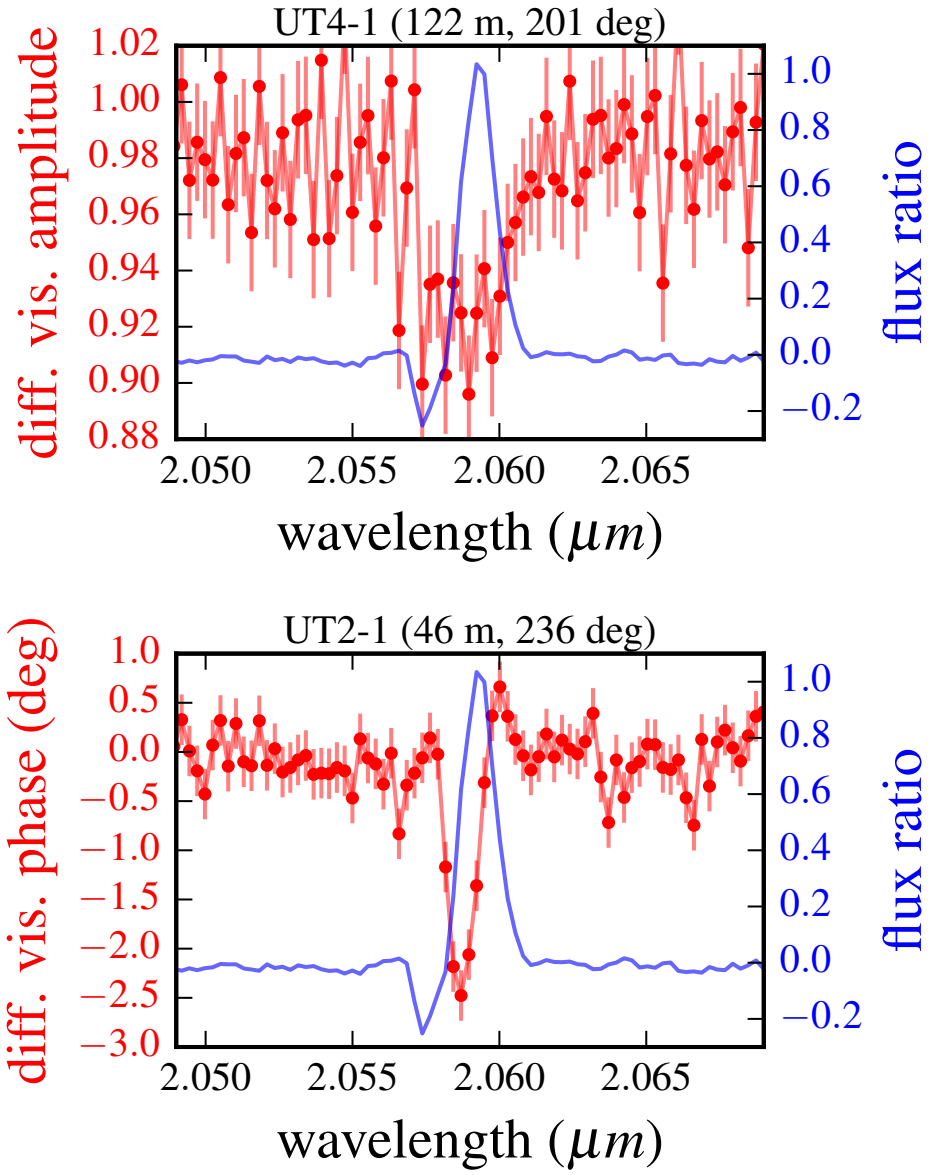

Figure 4.7: Differential visibility amplitudes and phases across the HeI 2.059μm line for some representative baselines. The features agree with those seen in Brγ, but are, in general, noisier due to instrumental and atmospheric effects.

4.5.3 Closure Phases

Closure phases are sums of visibility phases formed in a closed triangle of baselines which are independent of telescope errors. For this reason they are robust probes of asymmetry. As mentioned above, the closure phases across the continuum are zero to within the noise on all four baseline triangles (only three are independent). In theory, *differential* closure phases are not independent measurements from what has already been presented since they are derived from linear combinations of differential phases.

Figure 4.18 (and Figure 4.8 for a closer look at the Brγ line) shows that the differential closure phases across the emission lines vanish to within the noise level. Even though the differential closure phases are naturally noisier than the individual baseline differential visibility phases by $\approx \sqrt{3}$ (RMS$= 0.4°$), the fact that they vanish might be puzzling at first since the differential visibility phases are nonzero and therefore indicate the presence of asymmetry. This will be clarified in the following section.

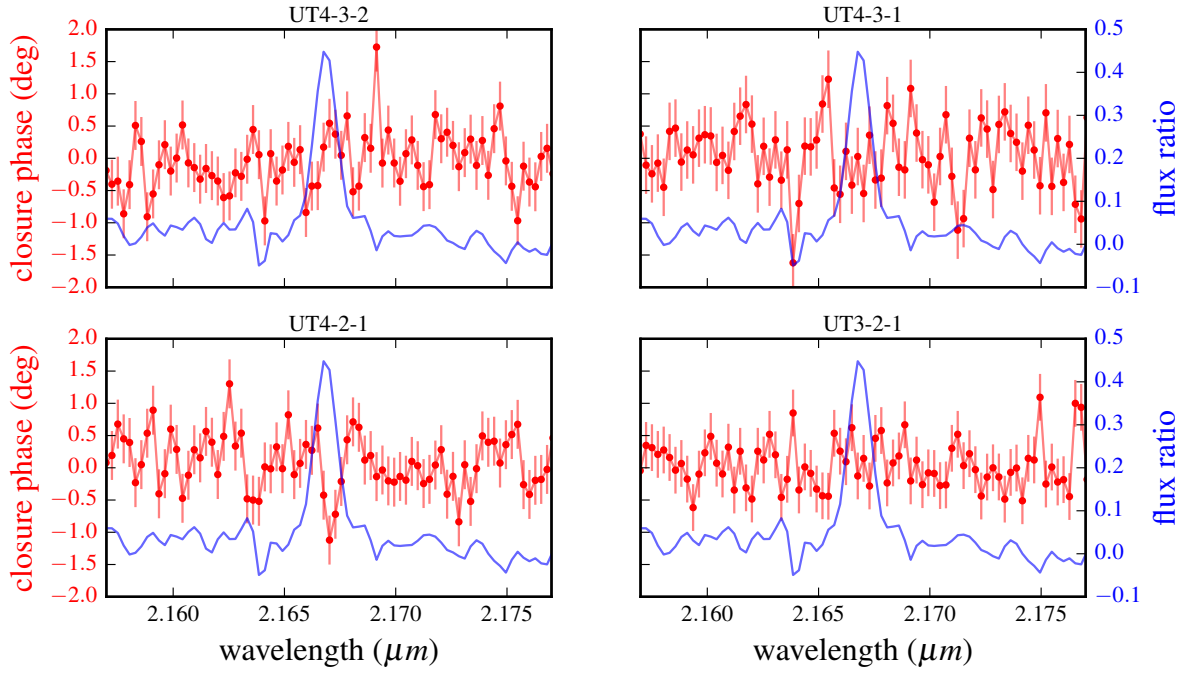

Figure 4.8: Differential closure phases across Brγ line (red) and normalized photospheric-corrected flux ratio (blue). In contrast to the differential visibility phases, there is no clearly distinguishable feature within the noise.

4.6 Discussion

4.6.1 Continuum

The photospheric radius $R(\tau_{Ross} = 2/3) = 70R_{\odot}$ and the distance 3 kpc to Wray 977 (Kaper et al., 2006) imply a photosphere angular diameter $\theta \approx 0.2$ mas. Our continuum size measurements are therefore consistent with a size $\lesssim 2\times$ the photosphere diameter, using our conservative upper limit referenced above. For hot stars with strong winds, the observed continuum emission in the infrared is a combination of blackbody thermal emission around the photosphere region as well as bound-free and free-free emission in the optically thin wind. Kaper et al. (2006) compares the SED of Wray 977 with a Kurucz model with the same temperature and finds a strong infrared excess, associated with emission from the wind. However, at the maximum wavelength probed by GRAVITY, $\sim 2.5\mu$m, the wind contribution is still relatively small, $\sim 20\%$ of the flux. Therefore, it is expected that the continuum in the K band is still dominated by the photosphere rather than the wind. This is consistent with the interferometric results presented here. Furthermore, the lack of a resolved structure in the near-infrared continuum also argues against the presence of a circumstellar disk, which is often seen in Be stars as extended continuum emission in the K band with FWHM $\gtrsim 2D_*$ (Meilland et al., 2012).

4.6.2 Differential Visibilities

The main advantage of using spectral differential visibility measurements is that they are much less susceptible to systematic errors that can affect the absolute visibility quantities. The errors in fringe contrast and phase are, in general, monotonic functions of the phase difference caused by spurious OPDs between baselines, $\Delta\phi = \frac{2\pi}{\lambda}OPD$. The error in the differential quantities will then have the form $f(d\Delta\Phi) \approx f(-2\pi\frac{OPD}{\lambda}\frac{d\lambda}{\lambda})$, which is greatly reduced with respect to the non-differential error when $\frac{d\lambda}{\lambda} \ll 1$, which is the case, for example, when using the wavelength of a narrow line compared to the continuum around it. On top of that, the differential quantities are not affected by wavelength-independent errors and are robust to low-order spurious effects along the spectrum given the narrowness of the spectral lines.

Model-independent Analysis in the Marginally Resolved Limit

The downside of spectral differential quantities is that, when imaging is not possible, their ultimate interpretation relies on knowing the spectral decomposition of the line, in case there is more than one emission component. Given the likely complex nature of the source in question and the many possible components in the system (hypergiant photosphere, wind, pulsar, gas stream, accretion disk etc), it would be useful to derive model-independent properties about the image that any model would have to reproduce. In general, this is not possible without image reconstruction, which requires a much more dense u-v sampling than we have available here.

However, when the interferometric signatures are small, such as is the case here, spectral differential quantities nicely fit into the special framework of the marginally resolved limit in interferometry. Lachaume (2003) lays out the formalism of this limit, showing that the visibility signals can be related to the moments of the flux distribution in a model-independent way. This technique has been applied extensively in the interpretation of spectral differential visibility phases as photocenter displacements (Monnier and Allen, 2013). Because here we also want to use the visibility amplitudes to estimate the second-order moments, we review the basic idea of the method and extend it to spectral differential visibilities.

From the Van Cittert-Zernike theorem,

$$F(\boldsymbol{u}) = \iint I(\boldsymbol{\sigma}) e^{-2\pi i \boldsymbol{\sigma}\cdot\boldsymbol{u}} dl dm \tag{4.6.1}$$

where F is the coherent flux, I is the source intensity distribution, $\boldsymbol{\sigma} = (l, m)$ are the object coordinates on sky and $\boldsymbol{u} = \frac{\boldsymbol{B}}{\lambda} = (u, v)$ is the baseline vector. In the following, it will be useful to define the moments of the intensity distribution about the origin as

$$\mu_{pq} = \iint I(\boldsymbol{\sigma}) l^p m^q dl dm \tag{4.6.2}$$

so that, for example, the zero-order moment μ_{00} is the total intensity and the normalized first-order moments $l_1 = \frac{\mu_{10}}{\mu_{00}}$ and $m_1 = \frac{\mu_{01}}{\mu_{00}}$ are the centroid positions along the l- and m-axes respectively. We can expand the complex exponential term in the integral of Eq. (4.6.1) in a Taylor series

$$e^{-2\pi i \boldsymbol{\sigma}\cdot\boldsymbol{u}} = 1 - 2\pi i(\boldsymbol{\sigma}\cdot\boldsymbol{u}) - 2\pi^2(\boldsymbol{\sigma}\cdot\boldsymbol{u})^2 + \frac{4\pi^3 i}{3}(\boldsymbol{\sigma}\cdot\boldsymbol{u})^3 + \mathcal{O}((\boldsymbol{\sigma}\cdot\boldsymbol{u})^4) \tag{4.6.3}$$

which allows the use of approximations when

$$|\boldsymbol{\sigma}\cdot\boldsymbol{u}| \ll 1 \Leftarrow |\boldsymbol{\sigma}| \ll \frac{\lambda}{|\boldsymbol{B}|} \tag{4.6.4}$$

i.e. when the source is sufficiently unresolved for a given baseline vector. Using the standard definition of the complex visibility

$$V(\boldsymbol{u}) = \frac{F(\boldsymbol{u})}{F(\boldsymbol{0})} = \frac{F(\boldsymbol{u})}{\mu_{00}} \tag{4.6.5}$$

it follows that

$$V(\boldsymbol{u}) \approx 1 - 2\pi i w_1 - 2\pi^2 w_2 + \frac{4\pi^3 i}{3} w_3 \tag{4.6.6}$$

where

$$w_i = \frac{1}{\mu_{00}} \int I(\boldsymbol{\sigma})(\boldsymbol{\sigma}\cdot\boldsymbol{u})^i dl dm \tag{4.6.7}$$

To first order in $\boldsymbol{\sigma} \cdot \boldsymbol{u}$, the phase of the visibility is

$$arg(V(\boldsymbol{u})) \approx \arctan\left(\frac{-2\pi w_1}{1}\right) \approx -2\pi w_1 \tag{4.6.8}$$

since $w_1 \ll 1$. Calling $\boldsymbol{x} = (l_1, m_1)$ the centroid positions for the given intensity distribution,

$$arg(V(\boldsymbol{u})) \approx -2\pi \boldsymbol{u} \cdot \boldsymbol{x} \tag{4.6.9}$$

For given two images a and b at the same spatial frequency $\boldsymbol{u}$, the differential phase

$$\begin{aligned} \Delta\phi_{ba} &= arg(V_b) - arg(V_a) \\ &\approx -2\pi(w_{1,b} - w_{1,a}) \\ &\approx -2\pi \boldsymbol{u} \cdot (\boldsymbol{x}_b - \boldsymbol{x}_a) \end{aligned} \tag{4.6.10}$$

Eq. (4.6.10) shows that *differential visibility phases give model-independent centroid displacements along the baseline direction for close to unresolved sources*. If two or more baselines are available, this allows to solve or fit for the centroid displacement $\boldsymbol{\Delta x}_{ab}$. Note that the differential phase is proportional to the baseline length. Therefore, for this approximation method to work in practice as a robust, model-independent estimation, we must have sufficiently small differential phase errors so that a signal can be measured even with a small enough baseline so that the sources remain very close to unresolved. Fortunately, this is exactly the case in spectral differential phase measurements, for which the error is much smaller then the absolute phase errors plagued by systematics.

We can go one order further by using differential visibility amplitudes. To second-order in $\boldsymbol{\sigma} \cdot \boldsymbol{u}$,

$$|V(\boldsymbol{u})| \approx ((1 - 2\pi^2 w_2)^2 + (2\pi w_1)^2)^{1/2} \tag{4.6.11}$$

$$\approx 1 + 2\pi^2 w_1^2 - 2\pi^2 w_2 + 2\pi^4 w_2^2 \tag{4.6.12}$$

$$\approx 1 + 2\pi^2(w_1^2 - w_2) \tag{4.6.13}$$

since $w_1, w_2 \ll 1$ and where we must expand to second order since the first-order term alone would result in $|V| > 1$. Note that in this expression the visibility amplitude depends on w_1 i.e. on the centroid of the image and therefore on the absolute phase, which is not available from single-axis interferometry. Even the differential visibility amplitude between two images a and b with this expression would depend on $w_{1,b}^2 - w_{1,a}^2$, whereas only $w_{1,b} - w_{1,a}$ is available from the differential visibility phase as shown above. In order to circumvent this, it is useful to define the moments of the image with respect to the centroid $\boldsymbol{x} = (l_1, m_1)$

$$\tilde{\mu}_{pq} = \iint I(\boldsymbol{\sigma})(l - l_1)^p (m - m_1)^q dl dm \tag{4.6.14}$$

so that, for example, the normalized second-order moments $\tilde{l}_2 = \frac{\tilde{\mu}_{20}}{\mu_{00}}$ and $\tilde{m}_2 = \frac{\tilde{\mu}_{02}}{\mu_{00}}$ are the variances about the centroid position along the l- and m-axes respectively, and $\frac{\tilde{\mu}_{11}}{\mu_{00}}$ is the

covariance. Analogously, we define

$$\tilde{w_i} = \frac{1}{\mu_{00}} \int I(\boldsymbol{\sigma})((\boldsymbol{\sigma} - \boldsymbol{x}) \cdot \boldsymbol{u})^i dl dm \tag{4.6.15}$$

It is straightforward to show directly from the definitions that $\tilde{w_2} = w_2 - w_1^2$, so that

$$|V| \approx 1 - 2\pi^2 \tilde{w_2} \tag{4.6.16}$$

where by Eq.(4.6.15), for a given baseline $\boldsymbol{u} = (u, v)$

$$\tilde{w_2} = u^2 \frac{\tilde{\mu}_{20}}{\mu_{00}} + v^2 \frac{\tilde{\mu}_{02}}{\mu_{00}} + 2uv \frac{\tilde{\mu}_{11}}{\mu_{00}} \tag{4.6.17}$$

Note that this is a better definition since these moments are about the image centroid rather than an arbitrary phase center. Given two images a and b, for example at the continuum and at a spectral line, the differential visibility amplitude is therefore

$$\Delta|V|_{ba} = |V|_b - |V|_a \approx -2\pi^2 (\tilde{w_{2,b}} - \tilde{w_{2,a}}) \tag{4.6.18}$$

If three or more baselines are available, it is possible to solve for the difference in variances and covariance about the centroid between the continuum and the spectral line images. If a model for the continuum is available, *differential visibility amplitudes allow obtaining robust estimates of the size and asymmetry of the image in the spectral line.*

Note that Eq.(4.6.9) implies that, for any baseline triangle $\boldsymbol{u_1} + \boldsymbol{u_2} + \boldsymbol{u_3} = 0$, the closure phase

$$arg(V(\boldsymbol{u_1})) + arg(V(\boldsymbol{u_2})) + arg(V(\boldsymbol{u_3})) \tag{4.6.19}$$

$$= -2\pi(\boldsymbol{u_1} + \boldsymbol{u_2} + \boldsymbol{u_3}) \cdot \boldsymbol{x} = 0 \tag{4.6.20}$$

Therefore, the marginally resolved limit must be compatible with very small closure phases for all baselines. Lachaume (2003) shows that the closure phases are related to the third-order moments of the image distribution, and are therefore expected to be much smaller than the visibility phases themselves in the marginally resolved limit.

The marginally resolved limit is applicable when $|\boldsymbol{\sigma} \cdot \boldsymbol{u}| \ll 1$. The translation of this condition into a minimum $|V|$, and the error incurred in the approximation, are baseline- and model- dependent. Lachaume (2003) compared the exact versus the approximated visibilities for different simple models (binary, ring, gaussian disc) and found that the approximation holds up to $|V| \gtrsim 0.9$ (see their Figure 4).

The validity of the marginally resolved limit for our dataset is supported by the large visibility amplitudes $|V| > 90\%$, small ($< 3^\circ$) differential visibility phases and vanishing closure phases (or closure phases that are much smaller than the individual visibility phases). Using the above formalism, we fit for the difference in centroid between the image at the continuum and the image at the spectral line (which includes emission from both the continuum and the line) using the differential visibility phases of the six baselines, per

spectral channel (therefore, there are six measurements and two parameters). The best fit model (and corresponding χ^2_{red}) are shown in Figure 4.6 (black line). For this and all subsequent model fits, we use a Markov Chain Monte Carlo technique as implemented in the publicly available EMCEE code (Foreman-Mackey et al., 2013) using uniform priors. We only fit the spectral channels in which there is emission line flux above the continuum noise level.

The consistency between the six baselines is further confirmation that the marginally resolved limit is valid. The resulting centroids on the sky plane for each wavelength across the emission line are shown in Figure 4.9. The errorbars shown correspond to the 16% and 84% marginalized quantiles. The red part of the line must have a smaller ($\sim 10\mu$as) centroid shift with respect to the continuum image than the blue part of the line ($\sim 30\mu$as). This statement is model-independent. Because the image at the line contains both a line as well as a continuum contribution, we can estimate the barycenter of the line emission with respect to the continuum (at (0,0)) by scaling the model-independent centroids by $\frac{1+f}{f}$, where f is the flux ratio between continuum and line emission (see Appendix B). This, however, must be interpreted carefully since the line emission could have more than one component. The result is also shown in Figure 4.9. The resulting centroid positions suggest line emission offset from the continuum by less than the size of the binary orbit, with a spatial gradient across wavelengths and the bluest channels consistent with one of the possible positions of the pulsar on the sky plane.

Analogously, we fit for the difference in the second-order moments (variance and covariance) between the image in the continuum and the image along the emission line. In this case, there are six measurements and three parameters. The results are shown in Figure 4.5 (black line). Again, a consistency between baselines confirms the validity of the marginally resolved limit. The resulting variance difference is both RA and DEC as a function of wavelength is shown in Figure 4.10. Clearly, a higher variance is required on the blue side of the line, implying that this part of the emission must come from larger scales. Also, the fact that the variances are not symmetrical in RA and DEC suggests an asymmetric emission structure.

The differential amplitude signatures are larger than expected from the differential phases. For example, for a binary model with compact components and flux ratio given by the spectrum, the binary separation as implied by the differential phases is one order of magnitude smaller than the one that would be necessary to produce the differential visibility amplitudes. This is illustrated in Figure 4.11, where we plot the visibility amplitude vs phase for a 1D binary model as the binary separation is changed. We choose a flux ratio $f = 0.3$ and a u-coordinate 0.2 mas^{-1}, which are representative to our data. We can clearly see that visibility amplitudes $\sim 95\%$ are not compatible with visibility phases $\sim 1 - 2^\circ$. This statement is robust and not dependent on the chosen f and u.

Simple Geometric Models

The model-independent analysis in the context of the marginally resolved limit presented above allows to derive properties that any interferometric model has to satisfy in order to

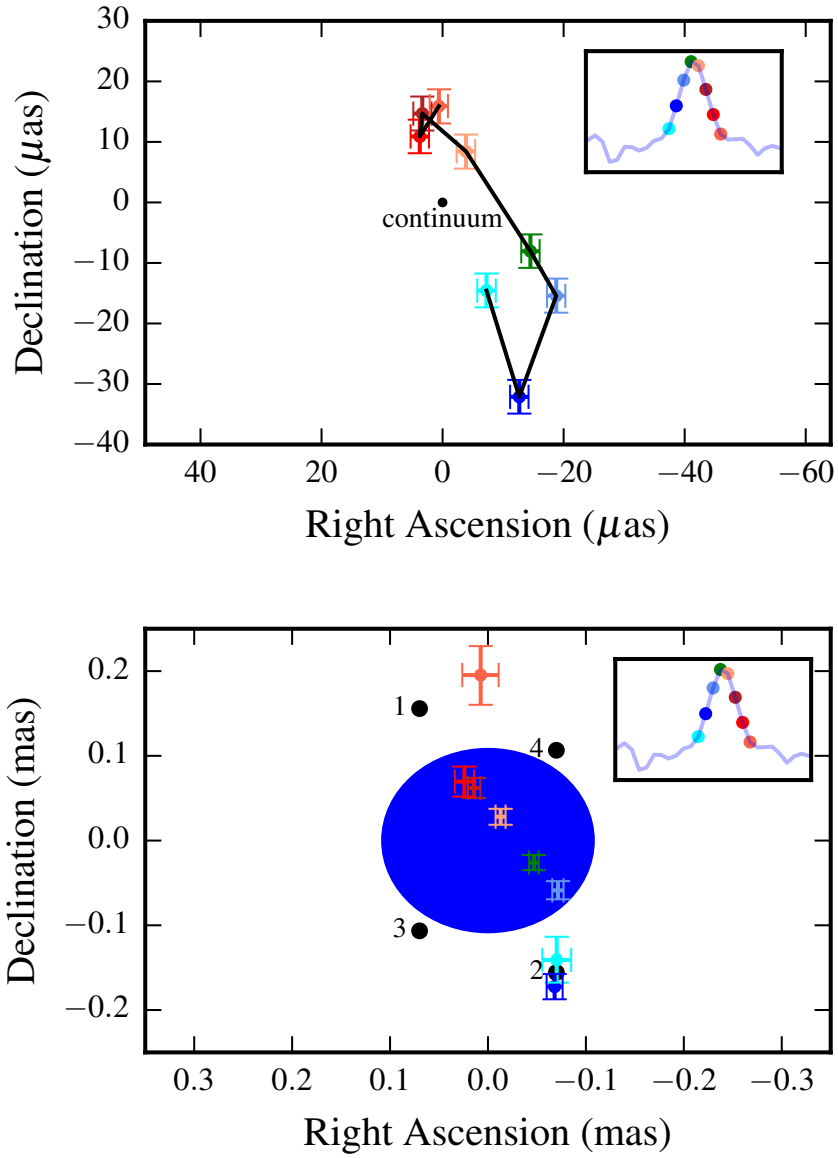

Figure 4.9: **Top.** Model-independent centroid positions for each wavelength across the Brγ line (continuum is at (0,0)). The image on the blue side of the line has a larger centroid shift as compared to the image on the red side. **Bottom.** Same as above, but using the flux ratio to derive the barycenter of the line emission. The hypergiant and the predicted four possible pulsar positions are also shown.

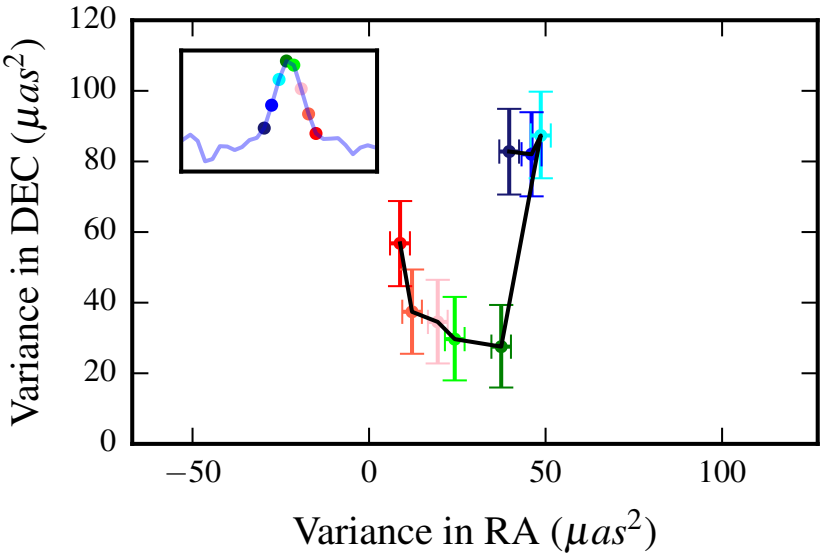

Figure 4.10: Model-independent variances of the image as a function of wavelength across the Brγ line. The blue part of the line has higher values, which suggests that the emission must be coming from larger scales.

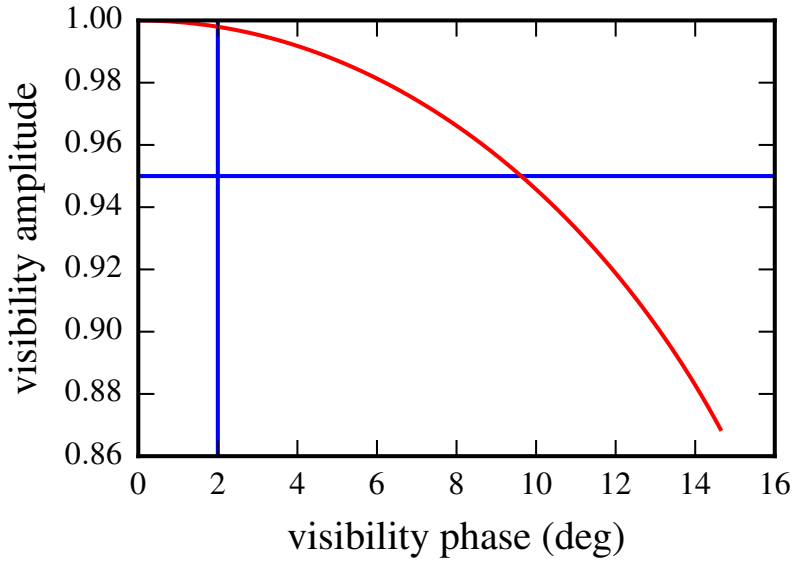

Figure 4.11: Visibility amplitude vs phase as the separation is changed for a 1D binary model with flux ratio $f = 0.3$ and u coordinate 0.2 mas^{-1}. The measured visibility amplitudes $\sim 95\%$ and phases $\sim 1 - 2^\circ$ are not compatible with this simple model.

explain the data. In summary:

1. the image centroid must have a spatial gradient across the spectrum, with larger centroid deviations from the continuum at the blue side of the line, and in the opposite direction at the red side;

2. the image variance must also show such a gradient, with larger spatial extension also at the blue side of the line; and

3. small centroid displacements must coexist with large scale structure.

Fitting the data with complex hydrodynamic models which produce Brγ emissivity maps is beyond the scope of this paper. Instead we restrict ourselves to the use of physically motivated, geometric models. We note that any interferometric model must deal with flux ratios, which are often degenerate with the spatial parameters. Whereas the simplest assumption is to use the spectrum to set the flux ratio, this only works if there is only one emission component. Since determining a complex spectral decomposition from interferometric data at moderate resolution is not possible, we limit ourselves to the simplest assumptions in the following models.

Model A: Extended and Distorted Wind

In this model, we assume that the Brγ emission is completely dominated by the hypergiant stellar wind. A spherically symmetric wind centered on the star would not be able to produce differential visibility phases with respect to the continuum; therefore, we allow the wind, which is modeled as a Gaussian, to be displaced from the center. For each wavelength channel across the Brγ, we therefore model the complex visibility as

$$V(\boldsymbol{u}) = \frac{V_{cont}(\boldsymbol{u}) + f e^{-\pi^2 |\boldsymbol{u}|^2 \frac{\theta_d^2}{4 \log 2}} e^{-2\pi i \boldsymbol{\sigma_0} \cdot \boldsymbol{u}}}{1+f} \tag{4.6.21}$$

where $V_{cont}(\boldsymbol{u})$ is the continuum visibility, f is the photospheric-corrected flux ratio between wind emission and continuum set by the spectrum, and the fit parameters are θ_d, the FWHM of the wind, and $\boldsymbol{\sigma_0}$, the centroid position of the wind.

This model is fit to both visibility amplitudes ($\chi^2_{red} = 2.67$) and differential visibility phases ($\chi^2_{red} = 1.36$). Because the (differential) closure phases can be derived from the visibility phases, they are not included in the fit; in other words, a good fit with respect to differential visibility phases should automatically be consistent with differential closure phases. The resulting centroid fits are identical to those shown in Figure 4.9 (bottom), as they should, since we are likewise assuming here that only one (spherically symmetric) structure contributes to the emission. The resulting wind sizes, as a function of wavelength, are shown in Figure 4.12.

The resulting wind FWHM (from ~ 0.8 mas on the red part of the wind up to ~ 1.5 mas on the blue part) would imply that there is substantial emission in Brγ up to $\sim 4-7 \times R_*$.

On the other hand, the non-Lyman H lines in hot stars are usually recombination lines, which means that their source function is roughly Planckian and stays approximately constant throughout a wind that is at radiative equilibrium. At the same time, their opacity $\kappa \propto \rho^2$ is a very sensitive function of density, and for an accelerating wind with a fast-decaying density profile ($\rho \propto \frac{1}{r^2 v(r)}$), only the innermost ($\sim 1 - 1.5 R_*$) regions of the wind would have a substantial contribution to the emission (Kudritzki and Puls, 2000). A varying temperature profile and the dependence of optical depth with velocity gradient ($\tau \propto \frac{dv}{dr}$) might smooth the density decay, but it is unlikely to resolve the discrepancy in the case of Wray 977, where the CAK wind law (Castor et al., 1975) predicts a density at $4R_*$ that is already $\sim \frac{1}{1000}$ of the value at R_*. A radiative transfer calculation to determine the emission region of Brγ in the wind is beyond the scope of this work; nonetheless, preliminary results (F. Martins, private communication) show that a dense wind could indeed bring Brγ into emission, but the emission region would be sharply peaked between $\sim 1.3 - 3 R_*$, therefore unable to account for such extended emission. Mid-infrared observations of BP Cru have detected the presence of dust and the possibility that the binary system is enshrouded by a disk-like circumstellar envelope ~ 2 mas (Servillat et al., 2014). Even though (i) the optical spectrum shows no evidence for a circumstellar disk (ii) the interferometric signatures are not typical of a symmetric disk and (iii) the near-infrared continuum is unresolved, there could be a connection between the very extended wind emission seen in these data and the reported dusty CS structure in the mid-infrared.

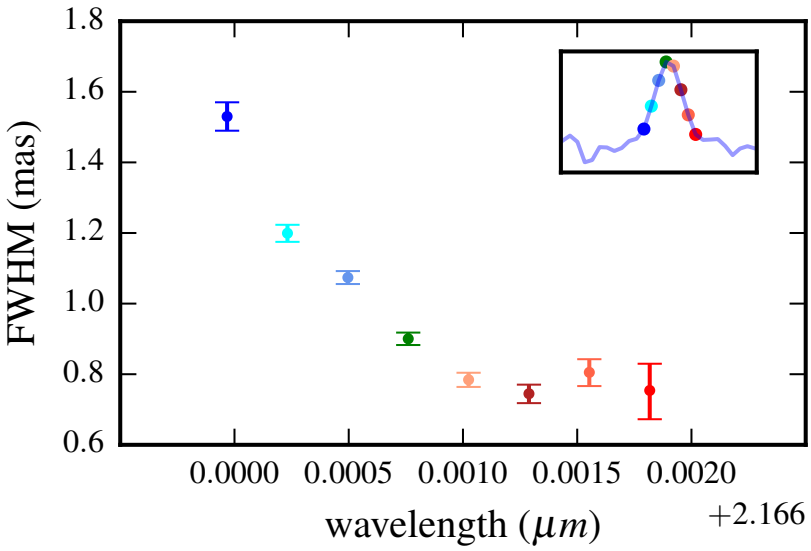

Figure 4.12: Wind size (FWHM) as a function of wavelength for a model in which the Brγ emission is dominated by the wind. Such a model predicts that there is still substantial wind emission at $4 - 7 \times R_*$, and that the blue (approaching) part of the wind is up to $\sim 2\times$ more extended than the red (receding) part.

Another feature of the wind model is that the blue (approaching) side of the wind would have to be $\sim 1.5 - 2\times$ more extended than the red (receding) part, where the pulsar is predicted to be at the time of the observation. This could be due to the X-ray illumination of the red part of the wind that hinders the radiative acceleration of the wind by photoionization.

The centroid shifts of the wind with respect to the continuum, necessary to explain the differential visibility phases, are small with respect to the size of the wind, $|\boldsymbol{\sigma_0}|/\theta_d \sim 10\%$. Because a Gaussian image has no intrinsic phase, the small centroid shifts in the model might be indicative of asymmetric wind structure. Such asymmetries could arise from a clumpy wind, or, more generally, from density fluctuations in the wind, which could be caused by the influence of the gravitational or radiation fields of the compact object. Although Kaper et al. (2006) found no evidence for wind clumping in Wray 977 from optical spectrum modeling, X-ray light curves and column density measurements often show fluctuations potentially attributed to clumps in the stellar wind (Leahy and Kostka, 2008).

We also recall that the interferometric data on Vela X-1 (Choquet et al., 2014), whose supergiant also possesses a strong wind, did not find any differential visibility signatures at the spectral lines above the noise level. GRAVITY commissioning data on this same target also had the same conclusion, even though the SNR was comparable to the one here (RMS in differential visibility amplitudes and phases in the continuum around the Brγ line were 1.2% and 0.7°, respectively). However, the donor star in Vela X-1 is $\sim 2\times$ smaller and has a $\sim 5\times$ smaller mass loss rate than Wray 977, and the spectral lines in K band are in absorption or very weak emission.

Model B: Extended Wind + Gas Stream

Here we consider the possibility that a gas stream of enhanced density also contributes to the Brγ emission. The manifestation of a gas stream of enhanced density in the hydrogen emission lines of HMXBs is not completely unfamiliar. Yan et al. (2008) for e.g. studied the double-peaked Hα emission lines in Cyg X-1, which can be explained by a P-Cygni shaped wind profile that follows the orbit of the supergiant as well as emission from a focused stellar wind that has an approximately anti-phase orbital motion to the supergiant. The relevance of the focused wind in Brγ could be even higher than in Hα given that the former line requires much higher densities to be brought into emission.

As alluded above, a gas stream is predicted to be present in this system from both optical and especially X-ray data. Because of its compactness, a gas stream could also be more efficient than a stellar wind in bringing higher density regions to the outer parts of the system. The simplest stream model would therefore be a binary model consisting of the continuum region at the center and an extra unresolved component. However, it was already shown that a binary model cannot explain the discrepancy between the very small differential visibility phases and the larger differential visibility amplitudes. This is confirmed in a formal binary fit to the data, which is completely unsatisfactory in reproducing both visibility amplitudes and phases simultaneously.

Motivated by this discrepancy, we consider here the possibility that the Brγ line has two emission components: a gas stream of enhanced density, with size on the order of the orbit scale and which accounts for the asymmetric differential visibility phase signatures, and an extended wind, which is symmetric relative to the continuum and accounts for most of the differential visibility amplitude signatures. Because of the lack of higher spectral resolution, it is not possible to perform a spectral decomposition to fix the flux ratios for each component. Because the flux ratios are highly degenerate with the spatial parameters, we fix them to be equal for the stream and wind components. This is motivated by comparing the HeI 2.059μm line in Figure 4.3 for BP Cru and ζ^1 Sco: they have similar stellar parameters, so if the extra emission is due to a stream, it would account for roughly 50% of the line emission. We caution that Brγ and HeI 2.059μm have very different behavior, and the goal of this section is not to provide best fit parameters, but rather to assess the possibility of a combined wind+gas stream model. Furthermore, we assume that the Brγ emissivity is constant along the stream, which might not be the case. The complex visibility at each spectral channel is therefore modeled as

$$V(\boldsymbol{u}) = \frac{V_{cont}(\boldsymbol{u}) + \frac{f}{2} e^{-\pi^2 |\boldsymbol{u}|^2 \frac{\theta_d^2}{4 \log 2}} + \frac{f}{2} e^{-2\pi i \boldsymbol{\sigma_1} \cdot \boldsymbol{u}}}{1+f} \tag{4.6.22}$$

where all parameters are as in Model A and $\boldsymbol{\sigma_1}$ is the position of the stream. Figure 4.13 (top) shows the positions of the stream for each wavelength from the best fit to the visibility amplitudes ($\chi^2_{red} = 2.32$) and differential visibility phases ($\chi^2_{red} = 1.44$). For convenience, we also show the hypergiant and the possible four predicted positions of the pulsar. Figure 4.14 shows the resulting size of the extended wind component for each wavelength. The asymmetry in the wind size across wavelength still remains, as in the wind-only model. The wind sizes are slightly increased due to the smaller flux in the wind. The differential phases, on the other hand, are explained by having a compact extra component represented by the gas stream.

For comparison, we also show in Figure 4.13 (bottom) a stream model in the sky plane. The model follows Leahy and Kostka (2008), and assumes that at each time some mass is ejected from the hypergiant star's surface that intersects the line-of-centers of the binary. The stream is then formed by propagating each mass element, assuming that the radial velocity follows the CAK wind velocity law and the angular velocity is given by conservation of angular momentum (the hypergiant is rotating). For the model shown, we simply assumed the relevant parameters from Table4.1, and that the pulsar is located at position "1" ($i = 60°; \Omega = 0°$) at the time of observation. The calculation is performed in the binary plane and then projected to the sky plane, with the colors along the stream representing the radial velocity. The stream shape is very sensitive to the assumed parameters, but it could be an explanation for asymmetric differential visibility phases along the emission line.

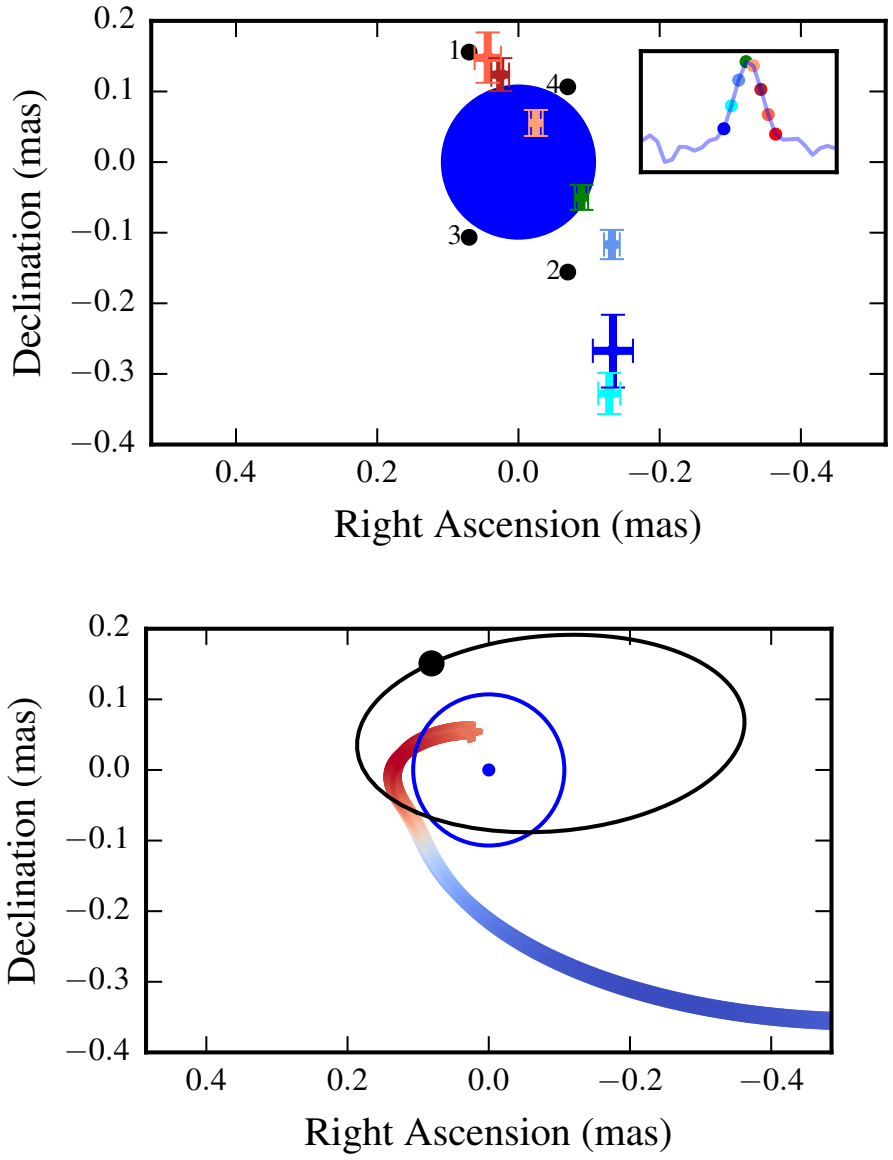

Figure 4.13: **Top:** Best fit positions on sky plane for a gas stream in the combined wind+stream model. Also shown are the hypergiant and the predicted four possible positions of the pulsar. **Bottom:** Example of a gas stream model (Leahy and Kostka, 2008) in the sky plane. The colors refer to radial velocities. A gas stream could be an explanation for asymmetric differential visibility phases across the wavelength.

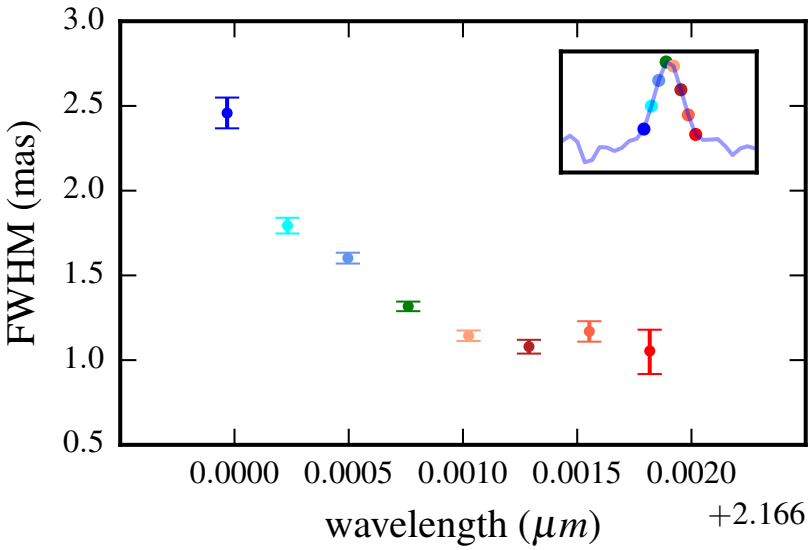

Figure 4.14: Wind Size (FWHM) as a function of wavelength for a combined wind+stream model. The asymmetry in extension across wavelength remains, as in the wind-only model.

4.7 Additional Data and Future Work

Here, we present additional spectral data that hint at the next steps in the study of BP Cru with optical interferometry.

As alluded above, the emission lines in BP Cru may be formed from multiple, distinct components which are either not apparent at the moderate spectral resolution of GRAVITY ($R \sim 4,000$) or are modulated by the pulsar's radial velocity curve ($v \sim 218$ km/s), such as for an accretion disk or possibly a gas stream. This would complicate our model fitting from the previous section.

For these reasons, we have compared the GRAVITY K band spectrum with that measured by XSHOOTER, using archival data[2] reduced with the publicly available ESO XSHOOTER pipeline. It has a substantially higher spectral resolution ($R \sim 11,500$) than GRAVITY.

Figure 4.15 shows the orbit of the pulsar in the binary plane, as well as the positions of the pulsar at the time of the GRAVITY and XSHOOTER observations. The radial velocities of the pulsar are also indicated.

Figure 4.16 shows the spectra at the HeI 2.059μm and Brγ emission lines for the two instruments. The higher resolution XSHOOTER spectra shows substructure that suggests a more complex line emission, possibly with multiple components. It could therefore be that the line emission has both a contribution from the normal hypergiant wind as well as

[2]based on observations with ESO Telescopes at the La Silla Paranal Observatory under programme ID 095.C-0446(A)

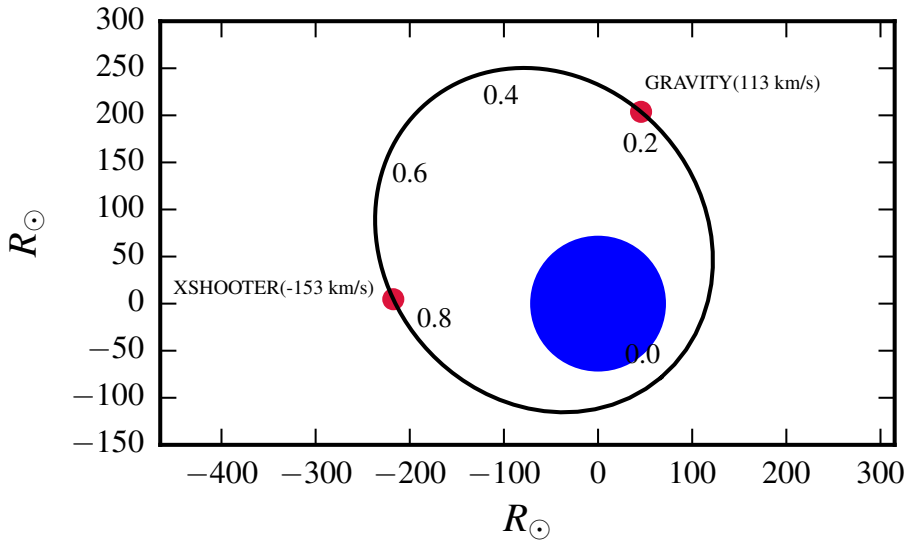

Figure 4.15: Orbit of the pulsar in the binary plane. Orbital phases are indicated, as well as the positions at the time of observations and the corresponding radial velocity. The donor star is shown in blue with the photospheric radius $\sim 70 R_\odot$.

from a dense gas stream, as is the case for the Hα line in Cygnus X-1 (Yan et al., 2008). We note, in particular, what appears to be a blueshifted (~ -130 km/s) emission component with $\sim$ 15% of the main line strength, when the predicted pulsar radial velocity at the XSHOOTER orbital phase is -150 km/s. If they indeed trail the pulsar, such components would be redshifted at the time of the GRAVITY UT interferometric observation and could potentially be related to the interferometric signatures in the red part of the line.

Additional high-resolution spectra at different orbital phases could confirm the presence of such emission components. When coupled with interferometric data, they would also be highly beneficial in testing the different models. Just to mention a few, a comparison between apastron and periastron epochs would help to assess X-ray effects, a comparison between superior and inferior conjunctions could probe the effects of the pulsar at different parts (red versus blue) of the wind and the wavelength at which the interferometric signatures peak could indicate, with the help of high resolution spectroscopy, the line emission component that is responsible for the interferometric signatures. All of these could help, for instance, in differentiating between an extended and distorted wind model from a gas stream model or possibly show the need for a combined model.

Finally, we note that the possibility that the differential signatures reported here could be related to the intrinsic variability of the stellar wind of the hypergiant cannot be absolutely excluded with the present data. Differential visibility amplitude and phase signatures have been observed previously in the Hα and Brγ lines of Rigel, a late-B supergiant (Chesneau et al., 2010, 2014). In this case, however, the lines are in absorption and the extension of the wind emission in Brγ is found to originate close to the photosphere ($\sim 1.25 R_*$), in

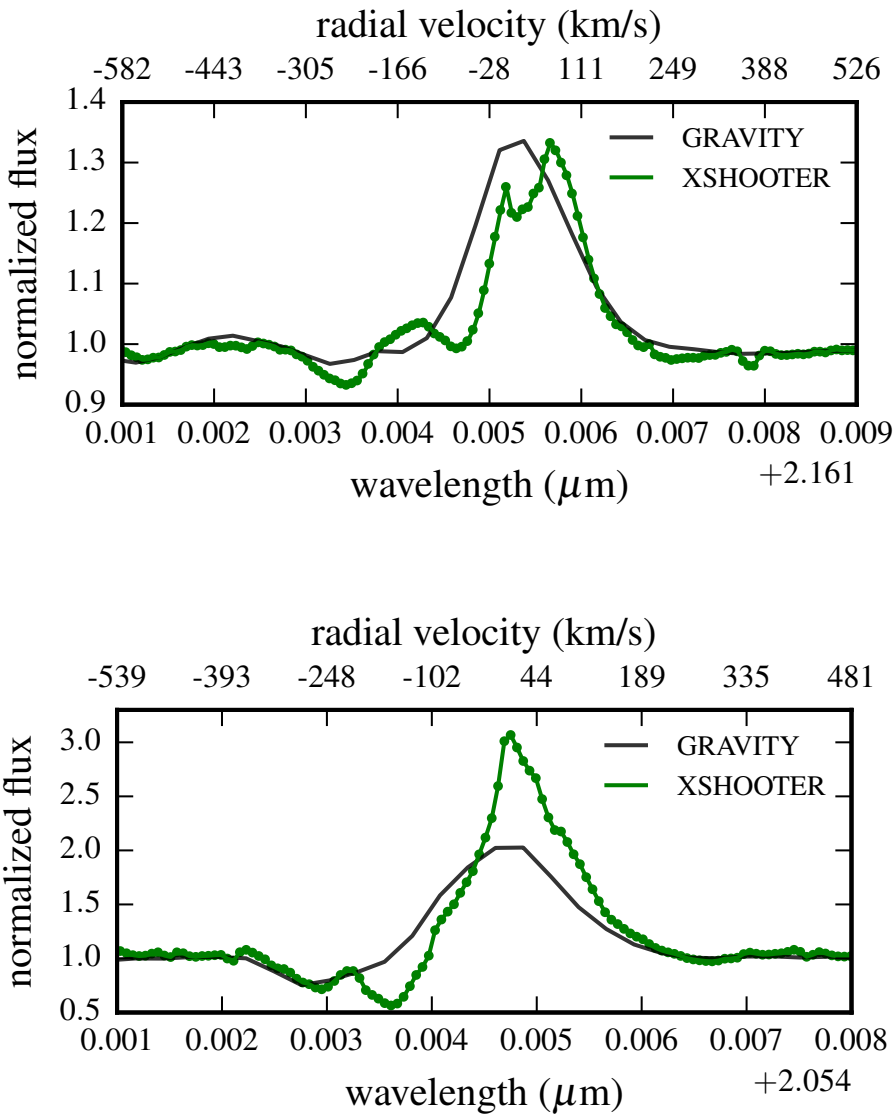

Figure 4.16: Brγ and HeI 2.059μm lines as seen with GRAVITY UT and XSHOOTER at different orbital phases. The latter has a higher spectral resolution than the former ($R \sim 11,500$ vs $4,000$) and shows substructure indicative of multiple line emission components.

contrast to the case of BP Cru. Nevertheless, optical spectroscopy monitoring of the isolated early-B hypergiants mentioned in Section 4.4 has detected variability in the P Cygni-type profiles of wind-sensitive lines, in the form of discrete absorption components that could be associated with non-spherical density perturbations (Rivinius et al., 1997). High spectral resolution interferometric observations of such stars would help to assess whether such variability could cause differential signatures of the same scale as what is seen in BP Cru, or whether the gravitational and radiation fields of the X-ray pulsar are indeed determinant.

4.8 Summary

We have shown a first analysis of near-infrared interferometric data of the HMXB BP Cru obtained with VLTI/GRAVITY:

1. The spectrum shows unusual Brγ emission for a star of its spectral type; the higher mass-loss rate may be related to an intrinsically denser wind or, as has been proposed from the X-ray data on this source, to a gas stream of enhanced density;

2. The continuum visibilities suggest a size $\sim 1R_*$, compatible with the still low infrared excess due to the wind in the K band;

3. Spectral differential interferometry shows differential visibility amplitudes and phases across the Brγ and HeI 2.059μm emission lines;

4. Any model for the emission lines must produce asymmetric, extended structure and a smooth spatial centroid gradient with radial velocity;

5. Examples of physically motivated, geometrical models satisfying these constraints include scenarios where the Brγ is dominated by an extended ($R \simeq 4-7R_*$), distorted wind or by a combination of extended wind and high density gas stream;

6. Further orbital phase resolved high resolution spectroscopy and interferometric observations could help to distinguish between models.

To our knowledge, this is the first dataset probing HMXB spatial structure on such small microarcsecond scales, in which the interaction between the donor star and the pulsar is expected to occur. Follow up studies may offer the possibility of testing the accretion mechanism and, more generally, the gravitational and radiation effects of the compact object on the stellar environment in these exotic systems.

Acknowledgements

Based on observations made with ESO Telescopes at the La Silla Paranal Observatory under program ID 60.A-9102. We thank the technical, administrative and scientific staff of

the participating institutes and the ESO Paranal observatory for their extraordinary support during the development, installation and commissioning of GRAVITY. This research has made use of the Jean-Marie Mariotti Center `Aspro`, `OIFits Explorer` and `SearchCal services`, and of CDS Astronomical Databases `SIMBAD` and `VIZIER`.

Appendix

A. Pulsar positions on the Sky Plane

Here we estimate the predicted pulsar positions in the sky plane (centered on the donor star) at the time of observation based on what is currently known about the system. In addition to the orbital parameters determined from the pulsar's radial velocity curve (Koh et al., 1997), the following parameters are in theory needed:

1. The binary inclination i;
2. The mass ratio q;
3. The longitude of the ascending node Ω;

In practice q is not important because the donor star is much more massive than the pulsar.

We adopt the inclination $i = 60^\circ$ or $120^\circ \pm 10^\circ$ from Kaper et al. (2006), which is estimated based on the upper limit on the neutron star mass and the absence of X-ray eclipsing. This allows to estimate $a_X \approx 0.28$ mas from $a_X \sin i$ known from the pulsar's radial velocity amplitude. From the mass ratio $q = \frac{M_X}{M_{opt}} \approx 0.046$ estimated in Kaper et al. (2006) from Wray 977's radial velocity curve, we estimate $a_{opt} = qa_X \approx 0.01$ mas, and therefore the semi-major of the relative orbit $a_{rel} = a_X + a_{opt} \approx 0.29$,mas $\approx 192 R_\odot$. The only remaining parameter to determine is Ω, of which radial velocity measurements are completely independent. However, we may constrain Ω from X-ray and column density measurements. Kaper et al. (2006) claims that the pulsar is behind Wray 977 in the orbital phase interval $0.18 \lesssim \phi \lesssim 0.34$ based on the decrease in X-ray flux after periastron passage due to absorption by the dense stellar wind, as well as an increase in column density. This allows to estimate Ω by setting x, the pulsar position in the sky plane, to zero when $\phi \approx 0.26$:

$$x \propto \cos\Omega \cos(\omega + \nu) - \sin\Omega \sin(\omega + \nu) \cos i \tag{4.8.1}$$

where ν is the true anomaly, which depends on ϕ and e only. Plugging in the appropriate values, we get

$$\tan\Omega \sim \cot(7.85) \cos i \Rightarrow \Omega \sim 0^\circ \tag{4.8.2}$$

Therefore, there are four solutions for the pulsar position, corresponding to $(i, \Omega) \sim (60°, 0°)$, $(60°, 180°)$, $(120°, 0°)$, $(120°, 180°)$. They all have the same radial velocity solution and the same orbital phase at superior conjunction, and therefore cannot be distinguished with what is currently known about the system.

Figure 4.2 shows the four possible positions of the pulsar on the sky plane (centered on Wray 977), along with the six baseline directions.

B. Correcting for the Photospheric Spectrum

Figure 4.17 shows the visibility amplitude on top of the flux ratio along the Brγ region for baseline UT4-2, with the flux ratio taken directly from the spectrum by assuming a flat continuum (i.e. continuum = 1 in the normalized spectrum). Especially on the blue side of the line, it is clear that interferometric signatures occur at regions where the flux ratio is near zero, which is confusing at first. However, one must remember that the unresolved part of the flux (i.e. the "continuum") includes photospheric absorption lines, which get filled by the emission component(s) in the combined spectrum. This is especially clear from the spectra of the comparison stars in Figure4.3, which actually show absorption in Brγ, likely due to their $\sim 5 - 10\times$ smaller mass-loss rate.

Therefore, in order to obtain a more correct value for the flux ratio between the emission component(s) and the unresolved continuum, we must estimate the purely photospheric spectrum of Wray 977. One possibility would be to use stellar atmosphere model codes and set an artificially lower mass-loss rate. Since this is beyond the scope of this paper, we take a simpler approach and use the spectrum of an isolated blue supergiant star of the same spectral type to estimate the photospheric spectrum. Contrary to the H-band Brackett lines, the Brγ line depth is not very sensitive to the star's luminosity/gravity (Hanson et al., 1996); therefore, the spectrum of a smaller star, with a lower luminosity and much weaker wind, should be a good approximation to the spectrum of Wray's photosphere, at least at the Brγ line.

With this in mind, we chose the star HD 148688 (B1Ia), with K band spectrum available from Hanson et al. (2005). After degrading the original resolution ($R \sim 12,000$) to GRAVITY's, we divide the GRAVITY spectrum by it, resulting in $1 + f$, where f is the flux ratio between emission and photosphere. This "photospheric corrected" flux ratio is also shown in Figure 4.17.

C. Spectrum and Interferometry Full View

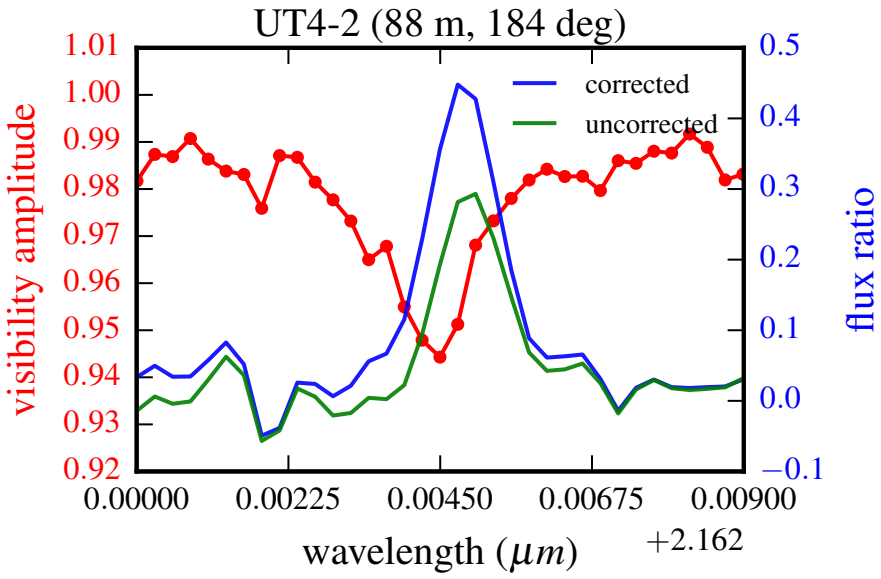

Figure 4.17: Differential visibility amplitude (red) across the Brγ line for one baseline (red), together with the flux ratio obtained from the spectrum assuming a flat continuum (green) and a continuum that contains a photospheric line (blue). The latter yields a flux ratio $\sim$ 50% larger, as well as an increase in the blue portion of the line, in which the interferometric signatures are largest.

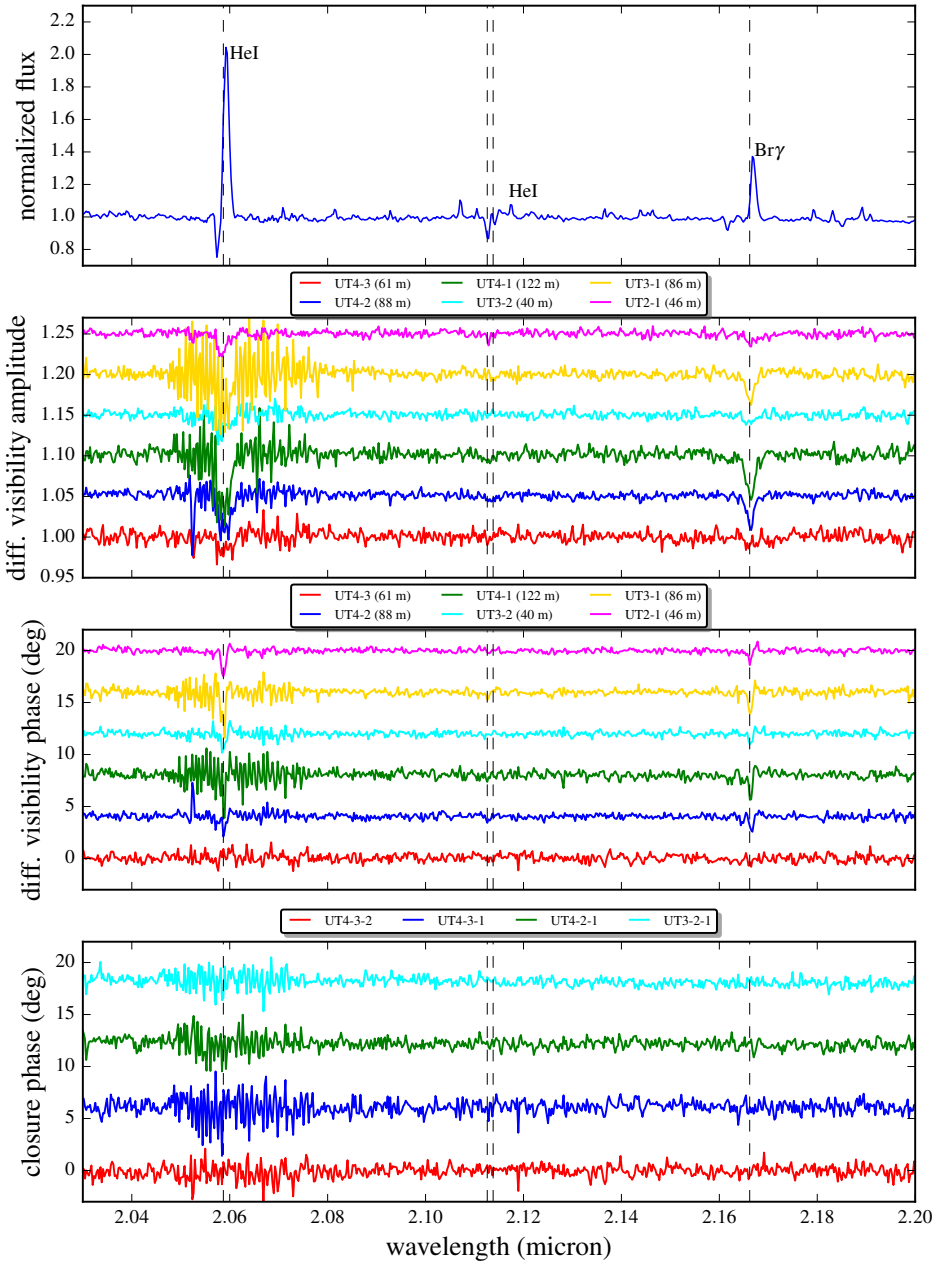

Figure 4.18: K band spectrum at the original resolution and interferometric quantities. The differential visibility amplitudes, phases and closure phases have been shifted by 0.05, 4° and 6° per baseline for plotting. The data has been neither binned nor smoothed. Note the strong systematics near the HeI 2.059μm line; analyzing those data will be considered in future work.

Chapter 5

Super-Keplerian equatorial outflows in SS 433. Centrifugal ejection of the circumbinary disk

Original publication: I. Waisberg, J. Dexter, P. Olivier-Petrucci, G. Dubus & K. Perraut, 2019, A&A, 623, 47, *Super-Keplerian equatorial outflows in SS 433. Centrifugal ejection of the circumbinary disk*, DOI: 10.1051/0004-6361/201834746

Abstract: *Context:* The microquasar SS 433 is the only known steady supercritical accretor in the Galaxy. It is well-known for its relativistic baryonic jets, but the system also drives equatorial outflows. These have been routinely detected in radio images, and components associated with a circumbinary disk have also been suggested in optical emission lines.
Aims: We aim to spatially resolve the regions producing the stationary emission lines of SS 433 to shed light on its circumbinary structure and outflows. With an estimated binary orbit size of $\lesssim 0.1$ mas, this requires optical interferometry.
Methods: We use the optical interferometer VLTI+GRAVITY to spatially resolve SS 433 in the near-infrared K band at high spectral resolution ($R \approx 4000$) on three nights in July 2017. This is the second such observation, after the first one in July 2016.
Results: The stationary Brγ line in the 2017 observation is clearly dominated by an extended ~ 1 mas ~ 5 AU circumbinary structure perpendicular to the jets with a strong rotation component. The rotation direction is retrograde relative to the jet precession, in accordance with the slaved disk precession model. The structure has a very high specific angular momentum and is too extended to be a stable circumbinary disk in Keplerian rotation; interpreting it as such leads to a very high enclosed mass $M \gtrsim 400 M_\odot$. We instead interpret it as the centrifugal ejection of the circumbinary disk, with the implication that there must be an efficient transfer of specific angular momentum from the binary to the disk. We suggest that the equatorial outflows sometimes seen in radio images result from similar episodes of circumbinary disk centrifugal ejection. In addition to the equatorial

structure, we find a very extended ~ 6 mas ~ 30 AU spherical wind component to the Brγ line: the entire binary is engulfed in an optically thin spherical line emission envelope.

5.1 Introduction

The extreme emission-line object SS 433 (Stephenson and Sanduleak, 1977; Clark and Murdin, 1978) was the first microquasar discovered, from its broad, red/blueshifted hydrogen and helium emission lines moving across its optical spectrum (Margon et al., 1979) and produced by relativistic, precessing baryonic jets moving at $0.26c$ (Fabian and Rees, 1979; Margon, 1984). The jets are also seen in emission lines of highly ionized metals in X-rays (e.g., Marshall et al., 2013) and as moving knots (e.g., Vermeulen et al., 1993) and a large-scale corkscrew structure in radio (e.g., Blundell and Bowler, 2004). SS 433 is the only known Galactic manifestation of a steady super-Eddington accretion disk, which outshines its donor star at all wavelengths and drives powerful outflows, manifested not only in the jets but also in strong, broad, and complex "stationary" (in wavelength) emission lines. The estimated mass outflow $\dot{M} \sim 10^{-4} M_\odot$/yr (Shklovskii, 1981; Fuchs et al., 2006) establishes SS 433 as an outflow-regulated supercritically accreting system ($\dot{M} \sim 500 \dot{M}_{Eddington}$ for a $10 M_\odot$ black hole). For a review of the fascinating properties of SS 433, see Fabrika (2004).

Although famous for its jets, one of the more exotic aspects of SS 433 is its equatorial outflows. The presence of an equatorial excretion flow from the accretion disk was proposed to explain the photometric and eclipsing behavior of SS 433 by Zwitter et al. (1991), possibly fed from the Lagrangian point behind the compact object (Fabrika, 1993). The equatorial outflows were later detected in high-resolution radio images as outflowing emission knots at anomalous position angles, almost perpendicular to the jets (Paragi et al., 1999). Blundell et al. (2001) later detected a smooth, extended (~ 40 mas) equatorial structure in radio images, calling it the "radio ruff". A collection of further observations (Paragi et al., 2002; Mioduszewski et al., 2004) showed that the orientation of the equatorial outflows is roughly perpendicular to the precessing jets but spans a larger angle range of $\sim 70^\circ$ (compared to 40° for the jets; Doolin and Blundell, 2009).

On the other hand, the presence of equatorial, circumbinary material has also been inferred from the double-peaked shapes that often appear in the optical emission lines. Filippenko et al. (1988) ascribed the double peaks with half-separation ≈ 150 km/s in the high-order Paschen lines to an accretion disk (deriving a rather low mass for the compact object, suggestive of a neutron star), but also recognized that the structure may instead arise in a circumbinary disk that, if in Keplerian rotation, would imply a much larger $\gtrsim 40 M_\odot$ enclosed mass. Robinson et al. (2017) presents a similar analysis of the higher-order Brackett lines, assigning them to an accretion disk and favoring a neutron star as the compact object. On the other hand, based on decomposition of the line profiles with several different Gaussian components, Blundell et al. (2008) concluded that the Hα

emission line arises from a combination of a disk wind and a circumbinary disk, the latter manifesting itself as stable Gaussian components with half-separation $\gtrsim$ 200 km/s. This velocity was interpreted as evidence that the total system mass must be large ($\gtrsim 40M_{\odot}$) and the compact object must be a massive $\gtrsim 16M_{\odot}$ black hole. Gaussian components arising from a circumbinary disk have also been suggested in the Brγ and He I emission lines (Perez M. and Blundell, 2009; Bowler, 2010). Cherepashchuk et al. (2018) argues that the double-peaked structure must indeed arise from extended material because the wings of the line are not eclipsed (as would be expected for an accretion disk; SS 433 is an eclipsing binary). On the other hand, radial-velocity measurements, notably extremely challenging in SS 433 due to the complexity of the emission lines and lack of clear stellar signatures, tend to favor lower masses of $2-5M_{\odot}$ for the compact object (Hillwig and Gies, 2008; Kubota et al., 2010). The relation between the circumbinary structure detected in optical emission lines and the equatorial outflows seen in radio is not clear. It has been suggested that the former might feed the latter (Blundell et al., 2008; Doolin and Blundell, 2009).

With an orbital period of $P_{orb} = 13.1$ days (Goranskij, 2011) and a distance of $d = 5.5$ kpc (Blundell and Bowler, 2004), the semi-major axis of SS 433 is $a_{orb} = \left(\frac{M}{40M_{\odot}}\right)^{1/3} \times 0.07$ mas, where M is the total binary mass. Spatially resolving the optical emission requires sub-milliarcsecond resolution. This is beyond the capabilities of even future extremely large telescopes, but is achievable through spectro-differential optical interferometry. In Gravity Collaboration et al. (2017) (Paper I) we presented the first such observations taken during the commissioning of the GRAVITY instrument (Gravity Collaboration et al., 2017) in July 2016 at the Very Large Telescope Interferometer (VLTI), which works in the near-infrared K band. These observations spatially resolved the near-infrared continuum as well as the stationary double-peaked Brγ line. The interferometric signature across the latter showed a complex structure dominated by emission in the jet direction, suggestive of a bipolar outflow.

Here we report on a second set of observations of SS 433 with GRAVITY in July 2017, which clearly revealed equatorial emission with a strong rotation component. In Section 5.2, we summarize the observations and data reduction. The analysis of the K-band near-infrared continuum is presented in Section 5.3, whereas Section 5.4 describes the results on the stationary Brγ line. Finally, Section 5.5 presents the conclusions.

We often quote the results in milliarcseconds, as that is the measured unit. For convenience, we quote 1 mas $\leftrightarrow 8.2 \times 10^{13}$ cm $= 1180R_{\odot} = 5.5$ AU, assuming a distance $d = 5.5(\pm 0.2)$ kpc derived from radio images using the aberration induced by the light travel-time effect between the two jets (Blundell and Bowler, 2004). The GAIA DR2 distance of 4.6 ± 1.3 kpc (Luri et al., 2018) is consistent with this value.

5.2 Observations and data reduction

SS 433 ($K \approx 8$) was observed with GRAVITY (Gravity Collaboration et al., 2017) with the Unit Telescopes (UT) on VLTI on three nights over a period of four days in July 2017. Half of the K band light of SS 433 itself was directed to the fringe tracker (FT), which operates at > 1000 Hz to stabilize the fringes in the science channel (SC), allowing coherent integration over detector integration times of 10s in high spectral resolution ($R \approx 4000$). The FT operates in low resolution ($R \approx 20$) with five channels over the K band. The data were obtained in split polarization mode. The adaptive optics (AO) was performed at visual wavelength using SS 433 itself as the AO guide star ($V \approx 14$).

Table 5.1 summarizes the observations. The precessional phase was ≈ 0.9, when the disk inclination is close to its minimum value ($i \approx 60°$). The orbital phases varied from $\sim 0.25 - 0.5$, meaning that the accretion disk is not eclipsed. Figure 5.1 shows the *uv*-coverage for the second epoch, with the jet precessional axis and cone as seen in radio observations (e.g., Stirling et al., 2002). The *uv* coverage for the other epochs is similar, but shorter in the third observation. The imaging resolution is ≈ 3 mas; however, we can resolve structures at sub-milliarcsecond resolution through spectral differential visibilities.

Table 5.1: Summary of observations

Date Time(UTC)	Total integration time (min)	Seeing (")	Coherence time @ 500 nm (ms)	Calibrator[a] spectral type diameter (mas)	Jet precessional phase[c]	Orbital phase[d]
2017-07-07 6:25-8:10 Epoch 1	70	0.4-0.6	4-6	HD 183518 A3V 0.157 ± 0.002	0.895	0.252
2017-07-09 6:35-8:10 Epoch 2	60	0.5-0.7	8-13	HD 185440 A2/3V[b] 0.218 ± 0.002	0.907	0.405
2017-07-10 6:25-6:55 Epoch 3	20	0.4-0.5	7-9	HD 188107 B9V 0.173 ± 0.002	0.913	0.480

[a] Based on Chelli et al. (2016).
[b] This calibrator is probably misclassified as it has strong CO bands in its spectrum.
[c] Based on the kinematic parameters in Eikenberry et al. (2001). Phase zero is when the eastern/western jet is maximally blue/redshifted.
[d] Based on the orbital parameters in Goranskij (2011). Phase zero corresponds to the eclipse center of the accretion disk.

The data were reduced with the standard GRAVITY pipeline (version 1.0.7, Lapeyrere et al., 2014). The interferometric calibrators used are listed in Table 5.1. They were also used as telluric line calibrators. We detected no significant difference in the interferometric quantities between the two polarizations in any of the three nights, either in the continuum FT or differential SC visibilities, and therefore we averaged the two polarizations. The data are also averaged in time for each of the three epochs because we do not see clear

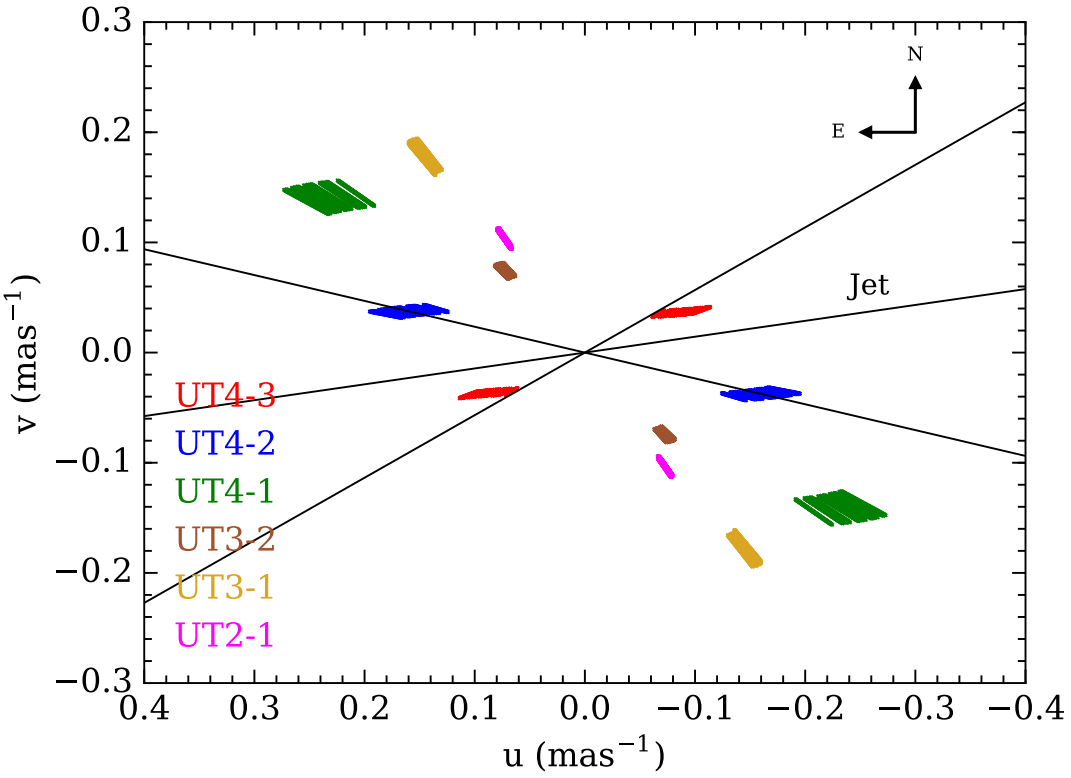

Figure 5.1: The *uv*-coverage for Epoch 2 of the GRAVITY 2017 observations. The colors represent the six different baselines, and the coverage in the radial direction corresponds to the different wavelength channels across the K band ($2 - 2.5\mu$m). We also show the precessional axis of the jet and its precession cone as seen on sky. The projected baselines are sensitive to both the jet and the orthogonal directions.

variability during each observation. We use the low-resolution FT data to study the K band continuum, and the high-resolution SC data to study the emission lines through differential visibility amplitudes and phases. Our limited *uv*-coverage resulting from the rather short observations did not allow for model-independent image reconstruction; therefore, we have to rely on model-independent quantities and model fitting.

5.3 The near-infrared K band continuum

SS 433 is known to have strong infrared excess (e.g., Allen, 1979; Fuchs et al., 2006) from extended outflows. At NIR wavelengths, we expect a flux contribution from both the accretion disk and donor star (< 0.1mas) and from more extended emission. In all observations, the continuum closure phases are very small $\lesssim 2°$, pointing to symmetric structures within the spatial resolution of ≈ 3 mas.

In Paper I we reported a phenomenological model for the K band continuum consisting of a partially resolved source (FWHM $\lesssim$ 1mas) embedded in a completely resolved background with $\approx 10\%$ of its flux. Here we construct a slightly more involved model in face of the strong evidence for an equatorial structure in the 2017 observations. The model consists of two components: an unresolved point source representing the binary (accretion disk + donor star) and a two-dimensional elliptical Gaussian which could represent an extended disk/wind. The model parameters are:

1. the flux ratio f between the Gaussian and the point source components;
2. the FWHM θ_g of the Gaussian component along the major axis;
3. the disk inclination i, which gives the aspect ratio of the Gaussian $\cos(i)$;
4. the position angle (PA) of the Gaussian axis.

The model visibility is therefore:

$$V(\boldsymbol{u}) = \frac{1 + f \times V_{gaussian}(\boldsymbol{u})}{1 + f}, \tag{5.3.1}$$

where $V_{gaussian}$ is the visibility of the elliptical Gaussian and $\boldsymbol{u} = \dfrac{\boldsymbol{B}}{\lambda}$ with $\boldsymbol{B}$ the baseline vector.

Table 5.2 and Figure 5.2 show the results for the model fits to the continuum squared visibilities for the 2016 observation and Epoch 2 of the 2017 observations (the other epochs look similar). Because the measurement errors are dominated by systematic errors from imperfect calibration of the visibilities (which leads to large $\frac{\chi^2}{\mathrm{dof}}$), we estimate the parameter errors from bootstrapping over the different baselines. We also note that spectral channels with strong emission lines were not used, to avoid the biasing of continuum visibilities by the differential visibilities.

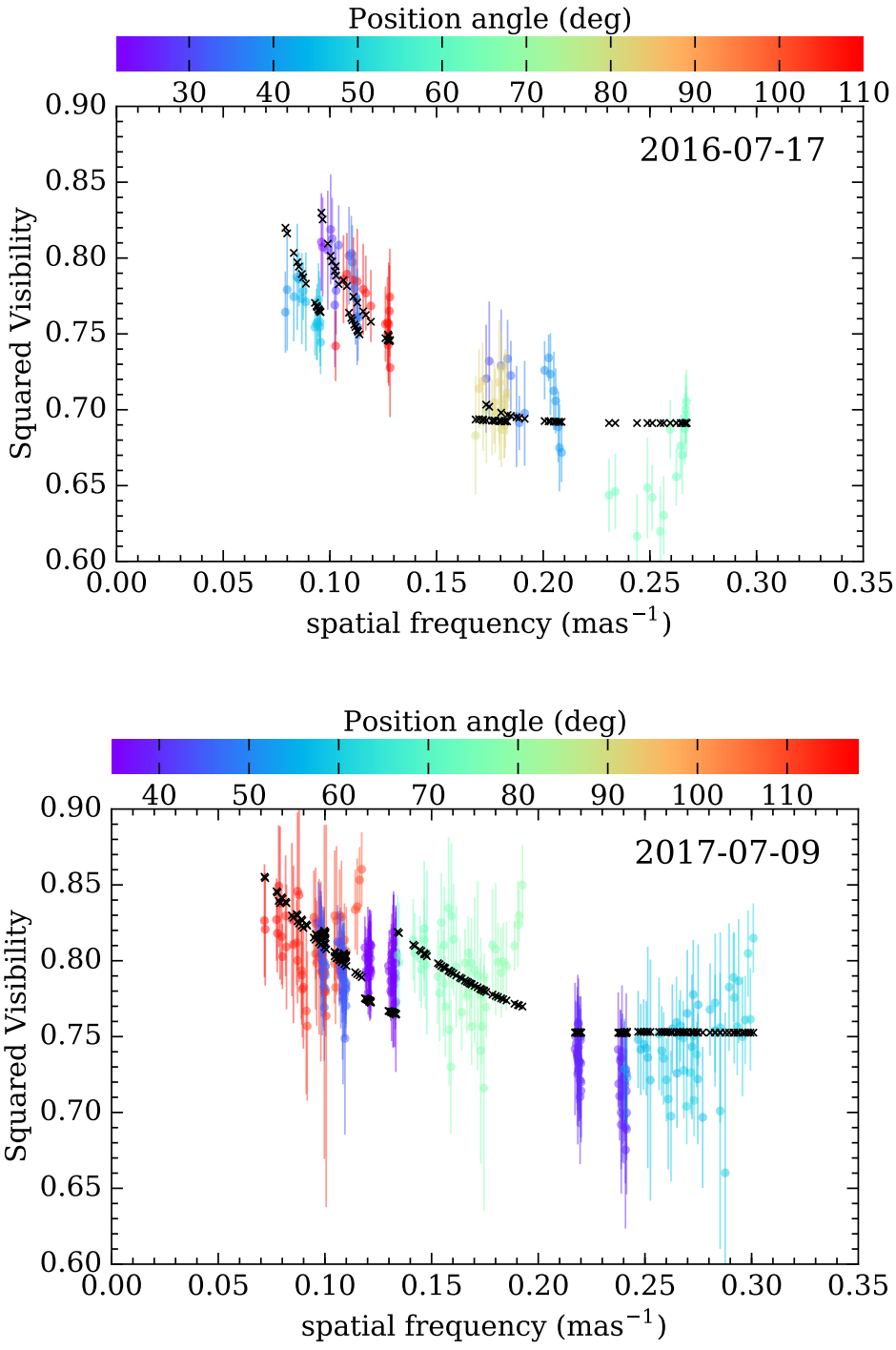

Figure 5.2: K band continuum squared visibilities of SS 433 from the GRAVITY fringe tracker for the 2016 observation (**top**) and Epoch 2 of the 2017 observation (**bottom**). The continuum is modeled by the combination of an unresolved point source representing the binary (accretion disk + donor star) and a two-dimensional elliptical Gaussian which could represent an extended disk/wind. The data is shown in color and the best fit model is shown in black.

Table 5.2: K band continuum model fit results

Parameter	unit	2016-07-17	2017-07-07 Epoch1	2017-07-09 Epoch2	2017-07-10 Epoch3
f	-	0.20 ± 0.01	0.10 ± 0.01	0.15 ± 0.01	0.28 ± 0.01
θ_g	mas	7 ± 1	7 ± 1	9 ± 2	7 ± 1
i	deg	90 ± 27	48 ± 16	60 ± 13	90 ± 14
PA	deg	22 ± 58	98 ± 39	103 ± 43	12 ± 63
$\frac{\chi^2}{dof}$		60	102	42	127

The model fits point to an extended structure with a FWHM $\sim$ 7 mas containing $10 - 30\%$ of the flux of the central point source. The PAs are very not well-constrained, but the inclinations do not favor a symmetric Gaussian. The extended continuum structure could therefore correspond to a disk, with some possible contribution from an extended wind (both of which are seen in the Brγ line, see below). The inclination and position angle of the jets are $i_{jet} \approx 90°$, $PA_{jet} \approx 75°$ in the 2016 observation (Paper I) and $i_{jet} \approx 60°$, $PA_{jet} \approx 88°$ for the 2017 observations (see companion paper on the jets; Waisberg et al., 2018).

5.4 The stationary Brγ line

The K band spectrum

The K band spectrum of SS 433 contains both stationary emission lines (Brγ, He I 2.06 μm, He I 2.112 μm and high-order (upper levels 19-24) Pfund lines) as well as emission lines from the baryonic jets. By far the strongest stationary line is the Brγ line, which is the focus of this paper. It is a broad line with FWHM $\sim$ 1000 km/s and often shows a double-peaked structure. We note that the Brγ stationary line in our observations is partially blended with Paα emission lines from the receding jet. Figure 5.4 shows the relevant part of the K band spectrum for Epoch 2, with velocities centered on the Brγ line. For the complete K band spectra, we refer to the companion paper on the jets (Waisberg et al., 2018).

Model-independent results

As mentioned previously, the stationary emission lines in SS 433 have been ascribed to multiple components, including an accretion disk, extended accretion disk wind/outflow, and a circumbinary ring. Our interferometric data spatially resolve the Brγ line emission

for the first time. The differential phases on most baselines show a remarkable "S-shape", which is a typical signature of a spatial velocity gradient (Figure 5.4). A comparison of the differential phases between the jet lines and the Brγ line reveals that in 2017 the latter is perpendicular to the jets, rather than along their direction as was the case in the 2016 observation (Paper I). This can be clearly visualized in a model-independent way by converting the differential phases $\Delta\phi$ to centroid offsets $\Delta\boldsymbol{x}$ between the line and the continuum, since in the marginally resolved limit (e.g., Monnier and Allen, 2013; Waisberg et al., 2017)

$$\Delta\phi = -2\pi\boldsymbol{u}\cdot\Delta\boldsymbol{x}\left(\frac{f-1}{f}\right), \tag{5.4.1}$$

where $\boldsymbol{u} = \dfrac{\boldsymbol{B}}{\lambda}$ and f is the line flux in continuum-normalized units. Figure 5.3 shows the centroid of emission across the Brγ line for the 2016 observation (Paper I) and Epoch 2 of the 2017 observations, along with the centroid of the jet emission lines. The emission is dominated by a bipolar (jet-like) structure in the 2016 observation, as reported in Paper I (although with a substantial scatter and an apparent offset ≈ 0.2 mas between the jet PA and the stationary line PA), and by a clear equatorial structure in the 2017 observation.

Figure 4 shows the interferometric data of Epoch 2 of the 2017 observations on two representative baselines (one close to perpendicular to the jets, the other close to parallel to the jets). We note the following important findings:

1. From Figure 3, the higher-velocity part of the line is more compact than the lower-velocity part, which points to a significant rotation component rather than a radially accelerating outflow.

2. Figure 4 shows that the differential phase peaks, which are much stronger in baselines closer to perpendicular to the jets, have a half-separation of ~ 250 km/s, and extend to $\gtrsim 1000$ km/s. The jet inclination in SS 433 is $\gtrsim 60°$, so that any disk-like component is likely to be very close to edge-on, meaning that this velocity should be close to the deprojected velocity.

3. From Figure 3, the centroid displacement near the line peak (where the differential phase peaks occur) is $\gtrsim 0.4$ mas. This is a lower limit to the size of the region associated with that intrinsic velocity because, in a disk, projection effects cause inner material to also contribute to that velocity. We also note that, if the emission line has additional components, meaning that the true f in Equation (2) is reduced, the centroid displacement necessary to produce the same differential phase will be larger. Therefore, 0.4 mas is a lower limit to the size of the region where the velocity is ~ 250 km/s.

This clearly shows that the rotating structure is too extended to be an accretion disk, since $a_{orb} < 0.07$ mas for a total binary mass $M < 40M_{\odot}$. The phase peaks ~ 250 km/s are close in velocity to the Gaussian components that have been associated with a circumbinary ring in previous spectral decompositions (Blundell et al., 2008; Bowler, 2010); however, the

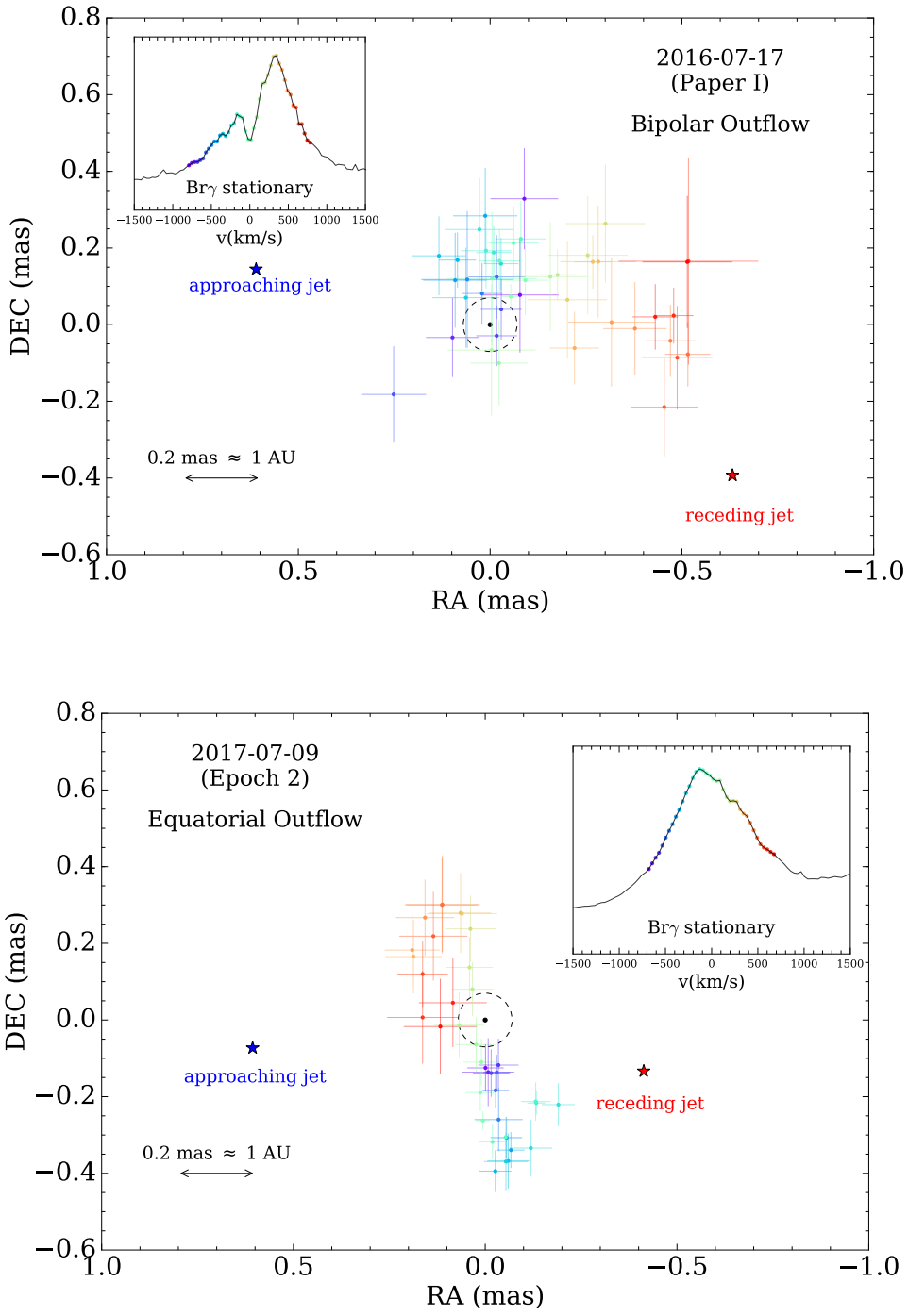

Figure 5.3: Model-independent centroid shifts across the Brγ stationary line for the 2016 observation and Epoch 2 of the 2017 observations. The dashed circle shows the binary size $a \approx 0.07$ mas for a total mass $M = 40 M_{\odot}$. The insets show the Brγ line spectrum with the color corresponding to the different wavelength/velocity channels.

interferometric data show that these structures are too extended to correspond to the inner edge of a circumbinary ring at $\approx 2a_{orb}$. We note that the Keplerian velocity $v_{\rm Kep} = \sqrt{\frac{GM}{r}}$ at 0.4 mas for $M < 40M_{\odot}$ is $\approx$ 130 km/s, meaning that if in Keplerian rotation, the structure would imply a very high enclosed mass $\gtrsim 150M_{\odot}$. Alternatively, the structure may be an equatorial rotating outflow (see below).

Models

We model the equatorial structure emitting in Brγ as a geometrically and optically thin disk-like structure, which can be either stationary in Keplerian rotation or expanding. The parameters are as follows:

1. The outer radius is R_{out} (mas), beyond which Brγ emission ceases.

2. The ratio of outer to inner radius, the latter demarcating the radius at which Brγ emission begins, is $\dfrac{R_{out}}{R_{in}}$.

3. The radial emission profile in Brγ, parametrized by $I(r) \propto r^{-\alpha}$.

4. The deprojected rotational velocity at the outer radius, $v_{\phi}(R_{out})$. The rotational velocity is given by

$$v_{\phi}(r) = v_{\phi}(R_{out}) \left(\frac{R_{out}}{r} \right)^{\beta}, \tag{5.4.2}$$

   where $\beta = 0.5$ for Keplerian rotation and $\beta = 1$ for an expanding outflow from conservation of angular momentum.

5. The outflow velocity v_r for the case $\beta = 1$. This is assumed to be constant, that is, the outflow has reached its terminal velocity by the time Brγ emission starts.

6. The inclination i of the disk.

7. The position angle PA of the disk.

8. The systematic velocity of the disk, v_{sys}, which could include orbital motion, for example.

9. The turbulence velocity fraction, given by $\sigma = \frac{v_{turb}}{v_{\phi}}$. This parameter makes the double-peaked profile, typical of disks, less pronounced.

In addition, there is a need for an extended component, which also creates the high-velocity ($\gtrsim$ 1000 km/s) wings of the line profile. This is because the differential visibility amplitudes decrease across the line, pointing to a net structure that is more extended than the continuum, whereas the disk alone would cause an increase in visibility amplitude if no other component were present (Figure 5.4). The presence of a broad wind component has been inferred from previous spectroscopic decompositions of the stationary lines (e.g., Blundell et al., 2008; Perez M. and Blundell, 2009). We model it as a spherically symmetric component, assumed to produce a Gaussian emission line in the spectrum and a symmetric 2D Gaussian in the image. Since it is spherically symmetric, this component does not induce differential visibility phase shifts. Its model parameters are the strength and FWHM (km/s) of the wind line in the spectrum, FWHM_{wind}, and the size (FWHM) of the wind image (mas), θ_{wind}. The systemic velocity is assumed to be the same as for the equatorial structure.

The errors for the science channel are estimated from the scatter in line-free regions. We fit for the spectrum and the differential visibilities simultaneously; however, because the former is sensitive to telluric correction and has very small statistical error bars, we increase the flux error bars by a factor of two. We found that this scaling led to a comparable reduced χ^2 between flux and visibilities in all observations. Moreover, because of the blending with Paα emission lines from the receding jet, which also produces differential visibility signatures, it is necessary to perform simultaneous fits for the Brγ line and the jets. For the model and results for the jets we refer to the companion paper (Waisberg et al., 2018).

For the velocity-resolved interferometric model for the equatorial disk detailed above, we construct a spatial grid with velocities and fluxes determined by the model parameters, and the visibilities are then computed through a numerical 2D Fourier transform. The total differential visibility at a given spectral channel is then

$$V_{\mathrm{diff}}(\boldsymbol{u}) = \frac{V(\boldsymbol{u})}{V_c(\boldsymbol{u})} = \frac{1 + \sum\limits_i \frac{V_i(\boldsymbol{u})}{V_c(\boldsymbol{u})} f_i}{1 + \sum\limits_i f_i}, \tag{5.4.3}$$

where V_c is the continuum visibility (taken from the best fit continuum model, Section 3), and f_i and V_i are the flux ratios relative to the continuum and visibilities for each component i (equatorial disk/outflow, extended wind and jets).

The fits are done through nonlinear least-squares minimization with the Levenberg-Marquardt method through the `python` package LMFIT [1]. The quoted errors correspond to the 1-σ errors from the least squares fit, i.e., the estimated derivatives around the optimal solution (scaled by $\sqrt{\chi^2_{red}}$). We caution, however, that true uncertainties are dominated by degeneracies between the many parameters, which create a complicated multi-dimensional χ^2 map; systematic errors from the continuum model; and the assumptions of our simple "geometric" models, which cannot capture all the complexities likely involved. A more realistic assessment of the errors can probably be grasped from the comparison between

[1] https://lmfit.github.io/lmfit-py/

the results of the three different epochs (barring fast variability). We note, however, that in Epoch 1 there is very severe spectral blending of the different components, meaning that its results are less robust.

Model results

Table 5.3 shows the model fit results for both the disk and outflow models. Figure 5.4 shows the data and best fit for the "outflow" model in Epoch 2 for two representative baselines. All the data and best fits for the three epochs for the "outflow" model are shown in the Appendix.

The PA of the equatorial structure is almost (although not exactly) perpendicular to the jets (the fit jet PA is 88°; Waisberg et al., 2018), confirming the results from the model-independent analysis. The inclination of the outflow is also close to the jet inclination during the observations (60°). Interestingly, the rotation direction of the equatorial outflow is retrograde relative to the jet precession (known from radio and optical observations), in agreement with the slaved disk precession model, according to which the precession is driven by gravitational torques from the compact object on the donor star with a spin axis misaligned with the binary plane (Roberts, 1974; van den Heuvel et al., 1980). Modeling of the eclipses in the X-ray and optical light curves at different precessional phases had shown evidence of retrograde precession (e.g., Brinkmann et al., 1989; Leibowitz, 1984); our results clearly confirm that the jets precess in a retrograde manner relative to the binary.

The "disk" and "outflow" models look very similar and cannot be distinguished from one another based on the χ^2. However, we disfavor the "disk" model based on the following arguments. The resulting enclosed mass is very high , that is, $\sim 400 M_\odot$, which follows from the fact that the disk is too extended ($R_{out} \approx 1$ mas) for its velocity ($v_\phi(R_{out}) \approx 260$ km/s). It would entail that SS 433 harbors an intermediate-mass black hole, which is strongly disfavored by all that is known about the object, such as the radial-velocity curves and eclipse behavior (Fabrika, 2004). Even more problematic is the fact that the "disk" model is not self-consistent: for such a high mass, $a_{orb} \approx 0.15$ mas, which is larger than the resulting inner radius of the disk $\lesssim 0.1$ mas, implying instability (e.g. Artymowicz and Lubow, 1994).

Instead, we favor the "outflow" model. In this case, the extended equatorial structure we detect would correspond to an outflow moving out at $v_r \sim 240$ km/s but with a very significant rotation component. The inner edge of the outflow at ~ 0.1 mas has a rotational velocity of ~ 1500 km/s and the outer edge at ~ 0.7 mas rotates at ~ 220km/s. This corresponds to a very high specific angular momentum, which is $\gtrsim 10$ times larger than the specific orbital angular momentum of the compact object l_X for a total mass of $M < 40 M_\odot$, assuming a radial-velocity amplitude of $K_X = 175$ km/s as derived from the HeII 4686$\mathring{A}$ line (Fabrika and Bychkova, 1990) and a binary inclination of $i = 78°$ (Eikenberry et al., 2001),

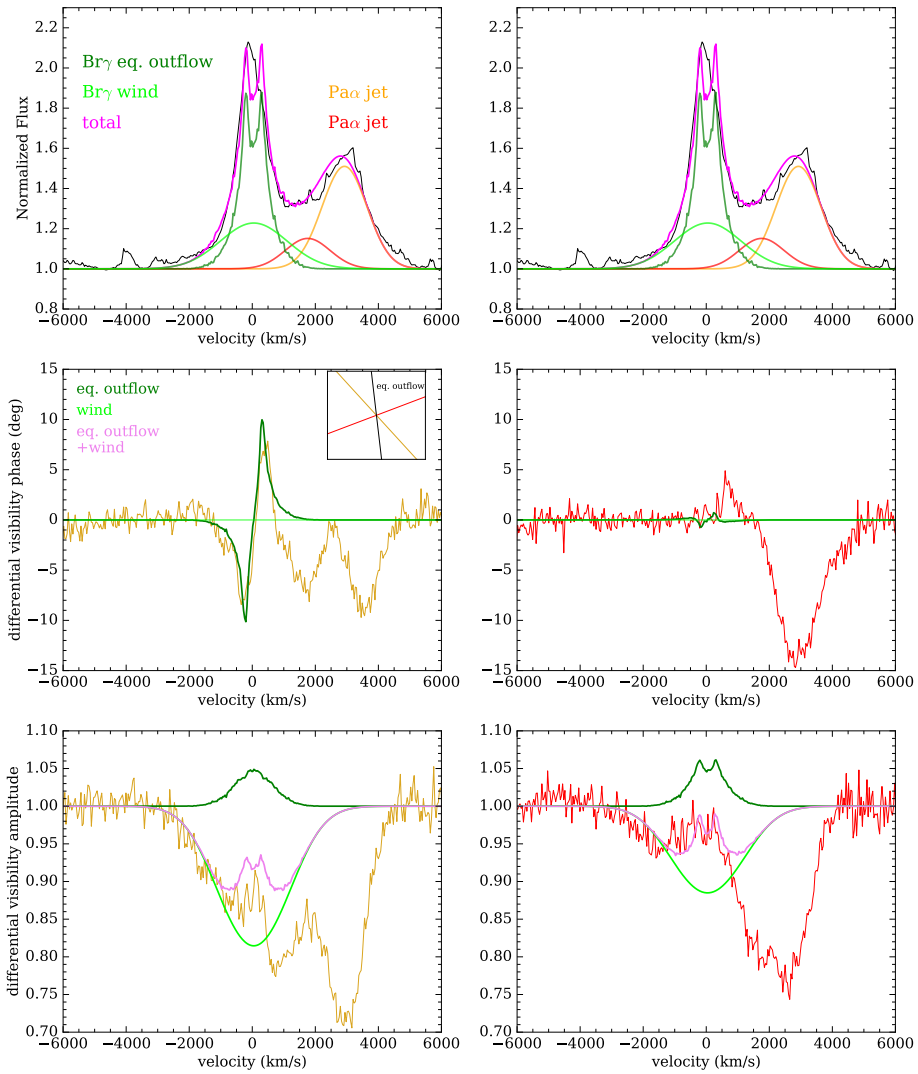

Figure 5.4: This figure illustrates the main features of the data and model. We show two representative baselines (UT3-1, yellow, and UT4-3, red – see Figure 5.1) for Epoch 2 and the outflow model fit. The **top** row shows the spectrum centered on the Brγ stationary line. The latter is decomposed into an equatorial outflow (dark green) and a spherical wind (lime). The former is responsible for the S-shape signatures in the differential visibility phases (**middle** row) for baselines which are close to perpendicular to the jet (left), and show almost no signature on baselines more aligned with the jet (right). The inset shows the position angle of the outflow from the fit as well as the baseline directions on the sky plane. The **bottom** row shows the differential visibility amplitudes. The equatorial outflow alone would lead to an increase in visibility amplitude across the Brγ line. The extended wind component can explain both the high-velocity ($\gtrsim$ 1000 km/s) wings in the spectrum and the net decrease in visibility amplitude across the line. We note that there are two Paα emission lines from the receding jet that are blended with the Brγ stationary line on its red side, and also create strong visibility signatures. The model fits were done for all the components simultaneously, but here we show only the visibility model for the stationary line for clarity (full model is shown in the Appendix). For the jet model and results, we refer to the companion paper on the jets (Waisberg et al., 2018).

$$l_X = \frac{K_X}{\sin i} a_X = \frac{K_X}{\sin i} \frac{a_{orb}}{1+q} < \frac{K_X}{\sin i} a_{orb} = \tag{5.4.4}$$

$$178 \text{ km/s} \times 0.07 \text{ mas} \left(\frac{M}{40 M_\odot} \right)^{1/3} \tag{5.4.5}$$

where $q = \frac{M_X}{M_*}$ is the mass ratio. The specific angular momentum of the donor star is even smaller, since $q < 1$ based on radial velocities (Hillwig and Gies, 2008; Kubota et al., 2010) or other estimates of the mass ratio (Cherepashchuk et al., 2018; Bowler, 2018). The extended outflows therefore seem to require a mechanism for transfer of substantial specific angular momentum to the outflowing material, which requires tidal or magnetic torques. We note that the inferred expansion velocity of the outflow of ≈ 240 km/s corresponds to only ~ 0.02 mas/day, which precludes the detection of movement within the different epochs above the uncertainties.

Because the inner radius of the outflow is ≈ 0.1 mas, which is $\approx a_{orb}$, it appears that it is launched from circumbinary material. Alternatively, it could be launched from the outer parts of the accretion disk, but only become visible in Brγ at larger scales. Centrifugal outflows from magnetic torques in the accretion disk itself require geometrically thin disks ($H \ll R$) threaded by vertical magnetic fields which dominate the pressure (Blandford and Payne, 1982). Although such a mechanism is unlikely to operate in the inner parts of the SS 433 accretion disk (which are geometrically thick and dominated by radiation pressure), it could be at work in the outer parts of the disk. In fact, because the inflow timescale in the outer disk must be short (of the order of the binary period) for the jets to nutate (Begelman et al., 2006), an efficient way to remove angular momentum in the outer disk is indeed needed.

A more exotic possibility would be extraction of angular momentum from a neutron star through a magnetic propeller effect, in which transfer of angular momentum from the spinning neutron star to the flow can happen if the magnetospheric radius R_m is larger than the co-rotation radius R_{co}, leading the flow to be centrifugally ejected (Illarionov and Sunyaev, 1975). Although the currently favored model for SS 433 is based on accretion-powered outflows from a massive stellar-mass black hole (Fabrika, 2004; Cherepashchuk et al., 2018; Bowler, 2018), neutron star models for SS 433 have been considered in the past (e.g., Begelman et al., 1980; Begelman and Rees, 1984), including the idea that it could be a supercritical propeller (Mineshige et al., 1991). In the latter scenario, R_m is smaller than the spherization radius R_{sp} meaning that a thick disk could still form (R_{sp} is the radius within which the disk becomes geometrically thick from radiation pressure, determined from $L(R > R_{sp}) = L_{Eddington}$; Shakura and Sunyaev, 1973). Our equatorial outflow model would require a launch radius $\gtrsim 4 \times 10^{10}$ cm for its speed not to exceed c, which is comparable to $R_{sp} \approx 10^{10} \text{ cm} \frac{\dot{M}}{10^{-4} M_\odot/\text{yr}}$ in SS 433. However, for such a large magnetospheric radius to be inside the light cylinder of a neutron star would require a spin period $P \gtrsim 10$ s, deeming a propeller mechanism very unlikely (in addition, it would require very large, i.e., $\gg 10^{15}$ G, surface magnetic fields).

We instead favor a scenario where the outflow is driven from a circumbinary disk. There is strong evidence for such a disk from optical spectroscopy (Blundell et al., 2008; Bowler, 2010), which appears to be in Keplerian rotation at $\sim 1.5a_{orb}$ with a speed of ~ 250 km/s (Bowler, 2018). It is probably fed by excretion through the Lagrangian points behind the compact object, donor star, or both. We note that the specific angular momentum of such a disk is a few times higher than that available in either binary component, meaning that its formation must also involve transfer of specific angular momentum. Nevertheless, there is strong evidence that this circumbinary disk is not stable: we see no evidence for substantial equatorial material in the 2016 GRAVITY observation, where the asymmetric double-peaked Brγ line is instead mostly aligned in the jet direction. We suggest that the equatorial structure we detected in optical interferometry traces the inner part of a centrifugally ejected disk, which implies there must be an efficient transfer of specific angular momentum from the binary to the disk, making it super-Keplerian by a factor of $\lesssim 10$, probably through tidal torques (e.g., Chen and Zeng, 2009). It is then tempting to associate the enigmatic equatorial outflows sometimes detected in radio images to similar episodes of centrifugal ejection of the circumbinary disk. Interestingly, Goranskij (2017) reports on episodes of disappearance and reappearance of the eclipses and jets in SS 433, which they associate with the formation and ejection of a common envelope, and which could in turn be related to the formation and/or ejection of the circumbinary disk.

The feeding of the circumbinary disk removes angular momentum from the binary, and Cherepashchuk et al. (2018) recently used the stability of the orbital period reported in Goranskij (2011) to constrain the mass ratio $q \gtrsim 0.6$. The ejection of the circumbinary disk we suggest here could also have important implications on the binary evolution. However, because it is most probably a transient structure, more observations are needed to understand its cadence and behavior, and that of the outflows in SS 433 in general. The two optical interferometric observations with GRAVITY so far have revealed extremely variable spatial structure to the line emission.

Finally, we note that the spherical wind component, with FWHM ~ 2000 km/s, surrounds the entire binary with a FWHM size of $\sim 5-6$ mas (the fit size of the wind is much smaller for Epoch 1; however, this epoch suffers from severe blending with jet emission lines, meaning that its parameters are much more degenerate and difficult to constrain). The entire SS 433 system appears to be engulfed in an optically thin line-emission envelope.

5.5 Conclusions

Here we present a second set of optical interferometry observations of the unique microquasar SS 433 with VLTI/GRAVITY. We have focused on the analysis of the near-infrared continuum and the Brγ stationary line. Our results can be summarized as follows.

1. The K band continuum is composed of an unresolved point source (accretion disk+donor star) and an extended structure of FWHM $\sim$ 7 mas. The latter is consistent with being an equatorial disk, but could also have a contribution from an extended spherical wind, both of which are seen in the Brγ stationary line.

Table 5.3: Stationary Brγ model fit results

Parameter	unit	Model	2017-07-07 Epoch 1	2017-07-09 Epoch 2	2017-07-10 Epoch 3
			Equatorial structure parameters		
R_{out}	mas	disk	1.31 ± 0.07	1.00 ± 0.06	1.15 ± 0.07
		outflow	0.93 ± 0.04	0.71 ± 0.04	0.65 ± 0.03
$\frac{R_{out}}{R_{in}}$	-	disk	9.5 ± 0.2	12.7 ± 0.2	12.6 ± 0.2
		outflow	10.9 ± 0.3	7.0 ± 0.1	7.3 ± 0.1
α	-	disk	2.32 ± 0.07	2.38 ± 0.05	2.77 ± 0.04
		outflow	0.6 ± 0.1	2.19 ± 0.05	2.45 ± 0.04
$v_\phi(R_{out})$	km/s	disk	277 ± 2	258 ± 2	243 ± 2
		outflow	284 ± 2	215 ± 2	216 ± 1
v_r	km/s	disk	-	-	-
		outflow	240 ± 2	236 ± 2	232 ± 2
i	deg	disk	72 ± 1	72.0 ± 0.6	64.8 ± 0.4
		outflow	69 ± 1	56.7 ± 0.4	52.2 ± 0.2
PA	deg	disk	97 ± 2	104 ± 4	106 ± 4
		outflow	86 ± 2	96 ± 5	107 ± 5
σ	-	disk	0.349 ± 0.002	0.375 ± 0.001	0.356 ± 0.002
		outflow	0.395 ± 0.001	0.346 ± 0.002	0.368 ± 0.001
M^a_{enc}	$M_\odot$	disk	621 ± 34	416 ± 27	420 ± 23
		outflow	-	-	-
			Spherical wind parameters		
FWHM_{wind}	km/s	disk	2975 ± 100	2810 ± 65	1952 ± 40
		outflow	2582 ± 112	2494 ± 56	1809 ± 38
θ_{wind}	mas	disk	0.7 ± 0.1	5.3 ± 0.2	5.9 ± 0.2
		outflow	0.7 ± 0.1	5.9 ± 0.2	6.3 ± 0.3
			Common parameters		
v_{sys}	km/s	disk	97 ± 1	29.7 ± 0.5	31.9 ± 0.3
		outflow	66.1 ± 0.5	47.1 ± 0.5	31.2 ± 0.3
$\frac{\chi^2}{\text{dof}}$	-	disk	2.7	1.5	1.0
		outflow	2.7	1.6	1.0

[a] The enclosed mass is computed from R_{out} and $v_\phi(R_{out})$ for the case of a Keplerian disk.

2. The model-independent emission centroids across the Brγ line clearly point to it being dominated by an equatorial (perpendicular to the jets) structure in the 2017 observations, whereas in the previous GRAVITY observation in 2016 the emission was rather more aligned with the jets, suggestive of a bipolar outflow. The rotation direction of the outflow is retrograde relative to the jet precession, in accordance with the slaved disk precession model.

3. The equatorial structure is very extended and carries a specific angular momentum that is greater than or approximately equal to ten times that of either binary component. If interpreted as a disk in Keplerian rotation, this would imply an implausibly high enclosed mass of $\sim 400 M_{\odot}$. We suggest instead that it traces an outflow corresponding to the centrifugal ejection of a circumbinary disk, the existence of which has been inferred from optical spectroscopy. The nondetection of an equatorial structure in the 2016 observation suggests that such a disk can disappear. We suggest that the equatorial outflows typically seen in high-resolution radio images correspond to similar episodes of circumbinary disk ejection. The mechanism driving the specific angular momentum transfer necessary to make the disk super-Keplerian and centrifugally eject it is unclear, but is possibly associated with tidal torques from the binary components.

4. The formation and ejection of the circumbinary disk could have an important effect on the binary evolution of SS 433 depending on their cadence. Future optical and radio interferometric observations capable of spatially resolving the outflows are needed to further study them.

5. In addition to the equatorial structure, the data also suggest a line component from a symmetric and extended spherical wind ~ 6 mas responsible for the high-velocity wings $\gtrsim 1000$ km/s of the line. The binary appears therefore to be engulfed in an optically thin and extended emission line envelope.

Acknowledgements

We thank the GRAVITY Co-Is, the GRAVITY Consortium, and ESO for developing and operating the GRAVITY instrument. In particular, I.W. and J.D. thank the MPE GRAVITY team, in particular F. Eisenhauer, R. Genzel, S.Gillessen, T. Ott, O. Pfhul and E. Sturm. We also thank the GRAVITY team members (W. Brandner, F. Einsenhauer, S. Hippler, M. Horrobin, T. Ott, T. Paumard, O. Pfhul, O. Straub, E. Wieprecht) and ESO staff who were on the mountain during the observations. We also thank P. Kervella for comments on the paper. POP acknowledges financial support from the CNRS High Energy National Program (PNHE). POP and GD acknowledge financial support from the CNES. This research has made use of the Jean-Marie Mariotti Center `SearchCal` service [2] co-developped by LAGRANGE and IPAG, CDS Astronomical Databases SIMBAD

[2]Available at http://www.jmmc.fr/searchcal

and VIZIER [3], NASA's Astrophysics Data System Bibliographic Services, NumPy (Van Der Walt et al., 2011) and matplotlib, a Python library for publication quality graphics (Hunter, 2007).

Appendix

Full data and model fits

Here we show the data (spectrum, differential visibility phases, and amplitudes) and best fits for the "outflow" model for the three epochs of the 2017 observations and for all baselines. The solid lines show the models without the blended jet emission lines, whereas the dashed lines show the full combined model (as the fits are done). For the jet models and results, we refer to the companion paper on the jets (Waisberg et al., 2018). The projected length and position angle of each baseline is indicated.

[3]Available at http://cdsweb.u-strasbg.fr/

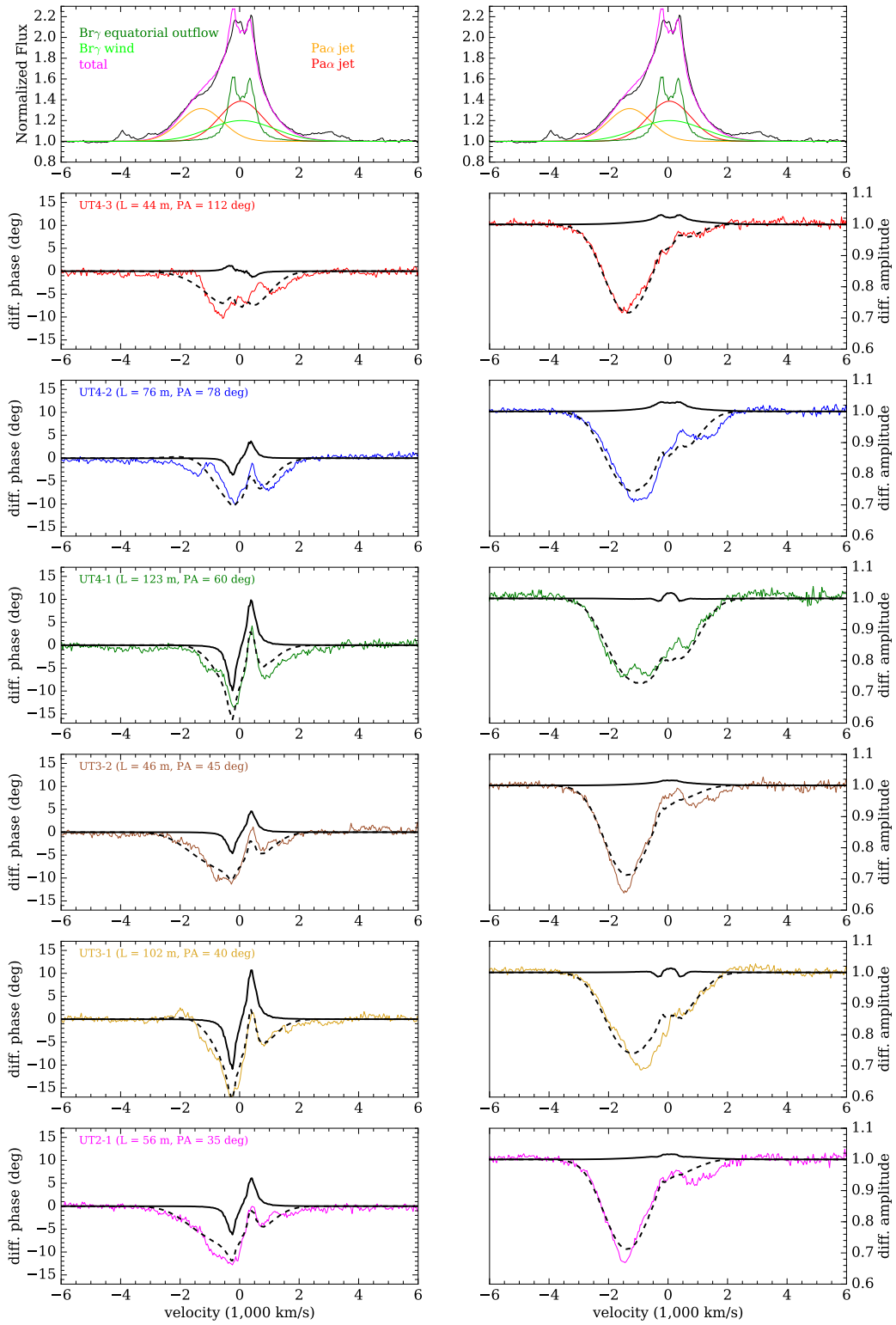

Figure 5.5: Data and best fit "outflow" model for Epoch 1.

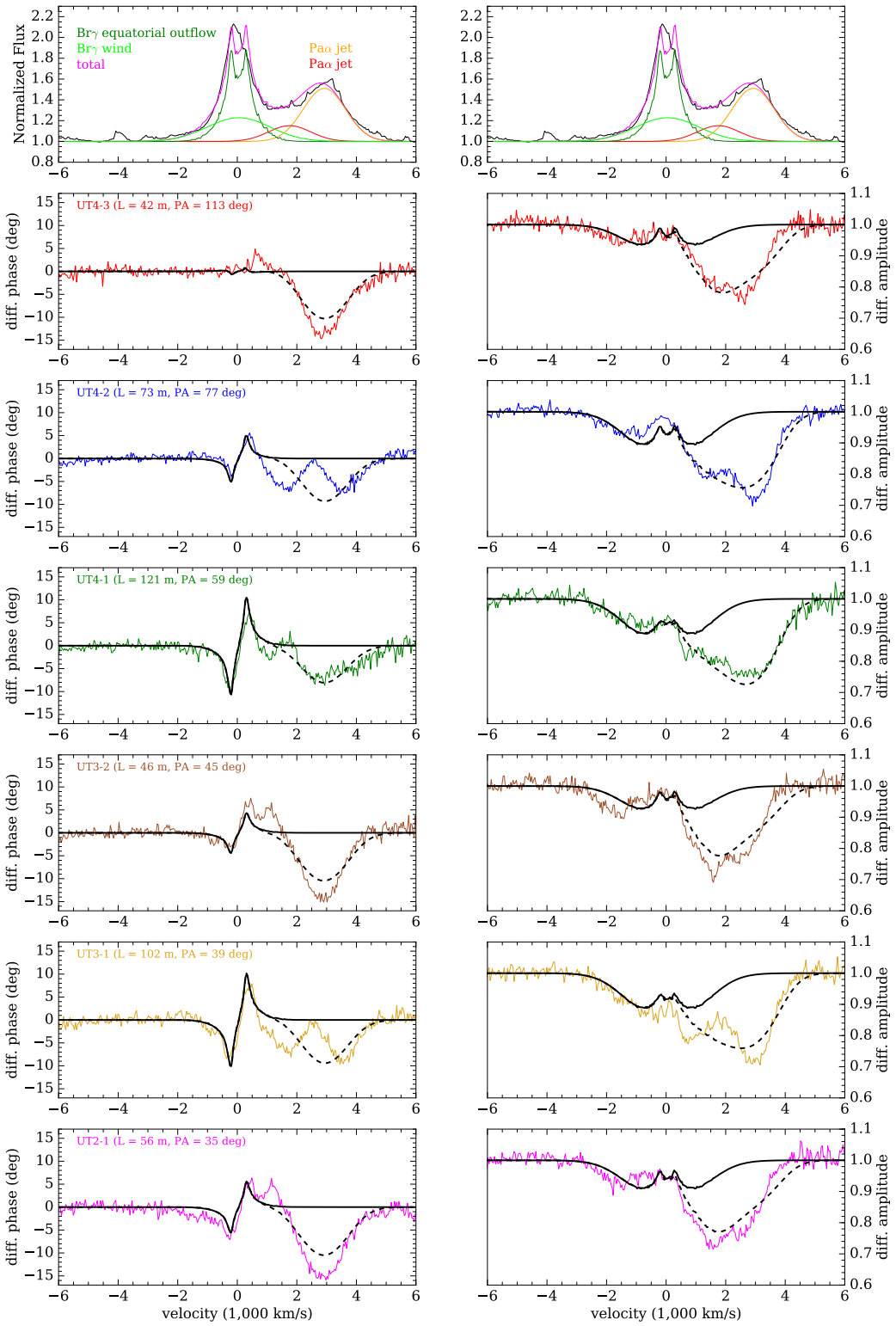

Figure 5.6: Data and best fit "outflow" model for Epoch 2.

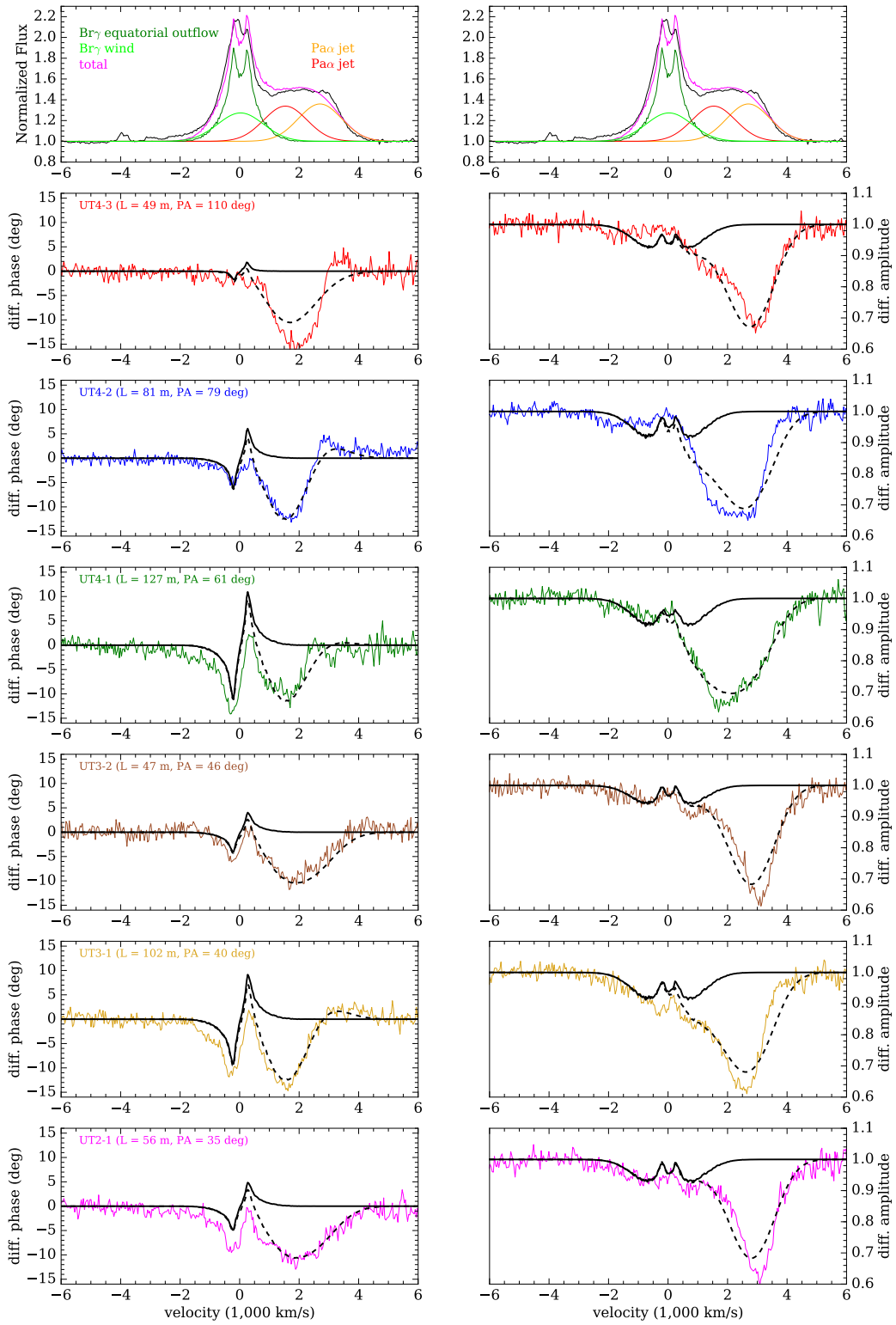

Figure 5.7: Data and best fit "outflow" model for Epoch 3.

Chapter 6

Collimated radiation in SS 433. Constraints from spatially resolved optical jets and `Cloudy` modeling of the optical bullets

Original publication: I. Waisberg, J. Dexter, P. Olivier-Petrucci, G. Dubus & K. Perraut, 2019, A&A, 623, 47, *Collimated radiation in SS 433. Constraints from spatially resolved optical jets and* ***`Cloudy`*** *modeling of the optical bullets*, DOI: 10.1051/0004-6361/201834747

Abstract: *Context:* The microquasar SS 433 is well known for its precessing, relativistic, and highly collimated baryonic jets, which manifest in its optical spectrum as pairs of hydrogen and helium emission lines moving with large Doppler shifts. Depending on their heating mechanism, the optical jet bullets may serve as a probe of the collimated radiation coming from the inner region close to the compact object, and which is not directly visible to observers on Earth.
Aims: We aim to better understand the baryonic jet phenomenon in SS 433, in particular the properties of the optical bullets and their interaction with the ionizing collimated radiation.
Methods: The optical interferometer VLTI/GRAVITY has allowed us to spatially resolve the optical jets in SS 433 for the first time. We present here the second such observation taken over three nights in July 2017. In addition, we used the XSHOOTER spectrograph at VLT to study the optical bullets in SS 433 in detail. Over the full wavelength range $0.3 - 2.5\mu$m, we identified up to twenty pairs of jet lines observed simultaneously, which we modeled with the spectral synthesis code `Cloudy`.
Results: GRAVITY reveals elongated exponential-like radial spatial profiles for the optical jets on scales $\lesssim 1 - 10$ mas, suggestive of a heating mechanism acting throughout a long portion of the jet and naturally explained by photoionization by the collimated radiation.

We also spatially resolve the movement of the optical bullets for the first time, detecting more extended jet components corresponding to previous ejections. Cloudy photoionization models can explain the spatial intensity profiles measured with GRAVITY and the emission line ratios from XSHOOTER, and constrain the properties of the optical bullets and the ionizing radiation. We find that the latter must peak in the UV with an isotropic luminosity (as inferred by a face-on observer) $\sim 10^{41}$ erg/s. Provided that the X-ray spectral energy distribution (SED) is sufficiently hard, the collimated X-ray luminosity could still be high enough so that the face-on observer would see SS 433 as ultraluminous X-ray Source (ULX) and it would still be compatible with the H/He/He+ ionization balance of the optical bullets. The kinetic power in the optical jets is constrained to $2 - 20 \times 10^{38}$ erg/s, and the extinction in the optical jets to $A_V = 6.7 \pm 0.1$. We suggest there may be substantial $A_V \gtrsim 1$ and structured circumstellar extinction in SS 433, likely arising from dust formed in equatorial outflows.

6.1 INTRODUCTION

More than forty years after its discovery, SS 433 (Stephenson and Sanduleak, 1977; Clark and Murdin, 1978) remains a unique object primarily due to its relativistic, precessing baryonic jets. They were first discovered through broad emission lines of hydrogen and helium moving across its optical spectrum with extreme Doppler shifts (Margon et al., 1979). Their blueshifts and redshifts follow a kinematic precession model (Fabian and Rees, 1979; Margon, 1984), according to which the jets precess over a period ≈ 163 days, following a cone of half opening angle $\approx 21^\circ$ and a precessional axis that is inclined $\approx 78^\circ$ relative to the line of sight, with jet material moving at a very stable speed of $\approx 0.26c$ along radial ballistic trajectories (Eikenberry et al., 2001). From the width of the emission lines and assuming a conical geometry, the optical jets are very collimated, with a half opening angle $\theta \lesssim 1^\circ$ (Borisov and Fabrika, 1987). The jet precession is thought to be driven by gravitational torques by the compact object on the donor star (slaved disk model: Roberts, 1974; van den Heuvel et al., 1980), whose spin axis is misaligned with the orbital plane presumably due to the supernova explosion that gave rise to the compact object $\lesssim 10^5$ years ago (Zealey et al., 1980; Lockman et al., 2007), and whose remnant W50 is still observable today (e.g., Dubner et al., 1998). SS 433 is also an eclipsing binary, and the behavior of the X-ray and optical eclipses together with radial velocities of the emission lines reveal that the supercritical disk and its outflows dominate the continuum and line radiation at all wavelengths (for a review of the properties of SS 433 see, e.g., Fabrika, 2004).

The jets in SS 433 were soon also detected in radio (Hjellming and Johnston, 1981), confirming the kinematic precession model derived from the optical lines and establishing the position angle of the precessional axis on sky 98.2° (Stirling et al., 2002). Very Long Baseline Interferometry (VLBI) radio observations have regularly imaged the movement

of individual jet knots (e.g., Vermeulen et al., 1993; Paragi et al., 1999), and larger scale images of the corkscrew structure created by the precessing jets have established a precise distance of $d = 5.5 \pm 0.2$ kpc from the aberration induced by the light travel time effect between the two jets (Blundell and Bowler, 2004). Later the jets were detected in X-rays (Watson et al., 1986), where they are seen as emission lines from highly ionized metals (e.g., Fe, Ni, S, Si) that follow the same kinematic precession model as the optical jets and have a similarly small opening angle (e.g., Kotani et al., 1996; Marshall et al., 2002). They have been modeled with multi-temperature, optically thin collisional ionization models to estimate properties such as temperature, density, and kinetic power. Because the X-ray jets are continuous, emission-line diagnostics depend on the assumptions on the geometry of the outflow, usually taken to be a radially outflowing cone, and may also be affected by photoionization from putative collimated radiation (Brinkmann and Kawai, 2000). The behavior of the X-ray jets during eclipse constrains their length to $\gtrsim 10^{12}$ cm (Marshall et al., 2013).

Because of its edge-on orientation, little is known about the radiation in the beam containing the optical jets, nor about the radiation from the inner parts of the accretion flow in general. The supercritical, geometrically and optically thick disk is thought to reprocess the latter to a large radius ($\sim R_{sp}$, the spherization radius within which radiation pressure leads to a thick disk, Shakura and Sunyaev, 1973), thermally downgrading it to the observed blackbody temperature $T \sim 30,000 - 100,000$ K (Fabrika, 2004). As a result, SS 433 is a relatively faint X-ray source, $L_X \sim 10^{35} - 10^{36}$ erg/s to observers on Earth, with most of the received X-ray flux below 10 keV originating from thermal Bremststrahlung from the X-ray jets, without any apparent X-ray accretion disk (Watson et al., 1986). It has been proposed that, if viewed face on so that the inner portions of the accretion disk/jet funnel were directly visible, SS 433 would appear as an extremely bright X-ray source such as an ultraluminous X-ray source (ULX; Fabrika, 2004; Begelman et al., 2006). Recent optical spectroscopy of ULX counterparts have shown strong emission lines akin to those seen in SS 433 and likely associated with supercritical disks (Fabrika et al., 2015), as well as the discovery of an ultraluminous supersoft source (ULS) containing a baryonic relativistic jet seen in a moving Hα line (Liu et al., 2015), so far the only other known object to show such a feature. Recently, Middleton et al. (2018) showed through time-resolved X-ray spectroscopy that the hard part of the X-ray spectrum in SS 433 is a reflection component of the wind-cone, and estimated an intrinsic X-ray luminosity of $\sim 10^{38}$ erg/s. The corresponding face-on luminosity, $L_X \gtrsim 10^{39}$ erg/s, suggests that SS 433 could be interpreted as an ULX for an observer with a favorable view towards the jets.

The optical bullets that make up the optical jets are thought to form from the collapse of gas from the continuous X-ray jet through a thermal instability as the jet expands and cools (Davidson and McCray, 1980; Brinkmann et al., 1988). If the optical bullets are heated mainly by photoionization by collimated radiation (Bodo et al., 1985; Fabrika and Borisov, 1987; Panferov and Fabrika, 1993), they can serve as a probe of the latter. On the other hand, their heating has generally been ascribed to external processes related to interaction with the ambient gas, either by direct collisions (Davidson and McCray, 1980; Brown et al., 1991) or through photoionization by extreme ultraviolet and X-ray photons produced

in shocks and subsequent collisional ionization and excitation by suprathermal electrons (Begelman et al., 1980). Spatially resolving the optical jets could reveal the dominant heating process; however, they have been associated with scales $\sim 10^{14} - 10^{15}$ cm $\leftrightarrow$ $1 - 10$ mas (e.g. Borisov and Fabrika, 1987; Marshall et al., 2013), beyond the reach of current diffraction-limited large telescopes.

The only way to spatially resolve the optical jets of SS 433 is through interferometry. In Gravity Collaboration et al. (2017) (Paper I) we presented the first such observations taken during commissioning of the GRAVITY instrument (Gravity Collaboration et al., 2017) in July 2016 at the Very Large Telescope Interferometer (VLTI), which works in the near-infrared K band. These observations revealed that the optical jets peak very close to the binary and follow an extended exponential radial emission profile with decay constant ≈ 2 mas, suggestive of a continuous heating process throughout the jet. Here, we present a second set of three GRAVITY observations of SS 433 taken over four nights in July 2017 in which we could observe the change in spatial emission profiles of the jets as the emission lines brighten and fade. We also present the first XSHOOTER observations of SS 433, where we use up to twenty pairs of jet lines to constrain the properties of the bullets and the ionizing collimated radiation under the assumption of heating by photoionization suggested by the GRAVITY data.

This paper is organized as follows. In Sect. 6.2, we summarize the observations and data reduction. The GRAVITY and XSHOOTER data analysis are presented in Sects. 6.3 and 6.4, respectively. Finally, Sect. 6.5 contains the conclusions.

We often quote the results in mas since that is the actual measured unit in interferometry. For convenience, we quote 1 mas $\leftrightarrow 8.2 \times 10^{13}$ cm $= 1180 R_\odot = 5.5$ AU, assuming a distance $d = 5.5(\pm 0.2)$ kpc (Blundell and Bowler, 2004). The GAIA DR2 distance $3.8^{5.0}_{3.1}$ kpc (68% limits; Luri et al., 2018; Bailer-Jones et al., 2018) is roughly consistent with this value but significantly more uncertain.

6.2 Observations and data reduction

GRAVITY

The microquasar SS 433 ($K \approx 8$) was observed with GRAVITY (Gravity Collaboration et al., 2017) with the Unit Telescopes (UT) on VLTI on three nights over a period of four days in July 2017. Half of the K band light of SS 433 itself was directed to the fringe tracker (FT), which operates at > 1000 Hz to stabilize the fringes in the science channel (SC), allowing coherent integration over detector integration times of 10s in high spectral resolution ($R \approx 4000$). The FT operates in low resolution ($R \approx 20$) with five channels over the K band. The data were obtained in split polarization mode. The adaptive optics (AO) was performed at visual wavelength using SS 433 itself as the AO guide star ($V \approx 14$).

Table 6.1 shows the precessional ϕ_{prec} and orbital ϕ_{orb} phases of each observation based on the ephemerides in Eikenberry et al. (2001) and Goranskij (2011), respectively. For more details on the observations and data reduction, including the uv coverage of the

observations, we refer to the companion paper on the equatorial outflows (Waisberg et al., 2018). In light of a slightly improved jet model, we also reanalyze the 2016 observation (Paper I), which is included in Table 6.1.

Table 6.1: Summary of observations.

Date	Instrument	ϕ^a_{prec}	ϕ^b_{orb}
2016-07-17 (Paper I)	GRAVITY	0.71	0.11
2017-05-21 Epoch X1	XSHOOTER	0.61	0.67
2017-05-28 Epoch X2	XSHOOTER	0.65	0.21
2017-06-20 Epoch X3	XSHOOTER	0.79	0.97
2017-06-30 Epoch X4	XSHOOTER	0.85	0.72
2017-07-07 Epoch 1	GRAVITY	0.895	0.25
2017-07-09 Epoch 2	GRAVITY	0.907	0.40
2017-07-10 Epoch 3	GRAVITY	0.913	0.48
2017-07-15 Epoch X5	XSHOOTER	0.94	0.87

[a] Based on the kinematic parameters in Eikenberry et al. (2001). Phase zero is when the eastern and western jets are maximally blueshifted and redshifted.

[b] Based on the orbital parameters in Goranskij (2011). Phase zero corresponds to the eclipse center of the accretion disk.

XSHOOTER

SS 433 was observed five times between May and July of 2017 with the XSHOOTER échelle spectrograph (Vernet et al., 2011) mounted on the Very Large Telescope (VLT). The exposure times per epoch were 1240s, 1260s, and 1248s for the UVB ($0.3 - 0.55\mu$m), VIS ($0.55 - 1.0\mu$m) and NIR ($1.0 - 2.5\mu$m) arms. The slit dimensions were 1.3"×11", 0.9"×11", and 0.4"×11" for each arm, corresponding to spectral resolutions $R = \frac{\lambda}{\Delta\lambda}$ of

4100, 8900, and 11600. The observations were made in nodding pattern for sky subtraction. Table 6.1 shows the precessional ϕ_{prec} and orbital ϕ_{orb} phases of each observation.

The data were reduced with the standard ESO XSHOOTER pipeline (version 2.9.0), which includes de-biasing, flat-fielding, wavelength calibration, sky subtraction, order merging, and flux calibration, the latter based on nightly response curves from flux standard stars. The line-modeling software `Molecfit` (Smette et al., 2015; Kausch et al., 2015) was used to correct for telluric absorption in the VIS and NIR arms. The performance of `Molecfit` was found to be at least as good as using a telluric calibrator star, with the additional benefit that manual removal of the many H I, He I, and additional lines of a telluric calibrator is not needed.

Although our observations were not designed for precise flux calibration, the latter has to be taken into account when comparing emission line strengths across a large wavelength range since SS 433 has a complex and variable continuum. Because the slit widths used are smaller than the seeing, it is necessary to correct for the wavelength-dependent slit losses. We have done this by assuming the typical wavelength dependence for seeing $s \propto \lambda^{-0.2}$, and using the overlapping regions between the spectral arms to fit for the average seeing, which is in good agreement with the estimated seeing value from the acquisition image at the start of each observation.

6.3 GRAVITY data analysis

K band Spectrum

Figure 6.1 shows the GRAVITY spectra of SS 433 for the 2017 observations. There are stationary emission lines (Brγ, He I 2.06 μm, He I 2.11 μm, and high order (upper levels 19-24) Pfund lines) as well as emission lines from the baryonic jets. For the analysis of the stationary Brγ line, we refer to the companion paper on the equatorial outflows (Waisberg et al., 2018). In this paper, we focus on the jets. In the 2016 observation (Paper I), the precessional phase was such ($\phi_{prec} \approx 0.7$) that jet lines from Brγ, Brδ, and He I 2.06 μm fell into the K band spectrum (see Fig. A.1). In the 2017 observations presented here, the precessional phase was significantly different ($\phi_{prec} \approx 0.9$) so that other jet lines were observed: Brβ from the approaching jet and Paα from the receding jet (as well as very weak Brδ and Brϵ lines from the receding jet). Another difference in the latter observations is that there are often two components (knots) to the jet lines. The set of three observations over four nights allows us to follow the spatial evolution of the jets; while the knots in Epoch 1 had faded by Epoch 2, the knots in Epochs 2 and 3 partially overlap. The jet redshifts were such that the Paα jets are partially blended with the Brγ stationary line and the Brβ jets with stationary Pfund lines.

Figure 6.2 shows the measured jet redshifts along with the kinematic precession model using the parameters from Eikenberry et al. (2001). They agree within the perturbations caused by nutational motion and random jitter (Fabrika, 2004).

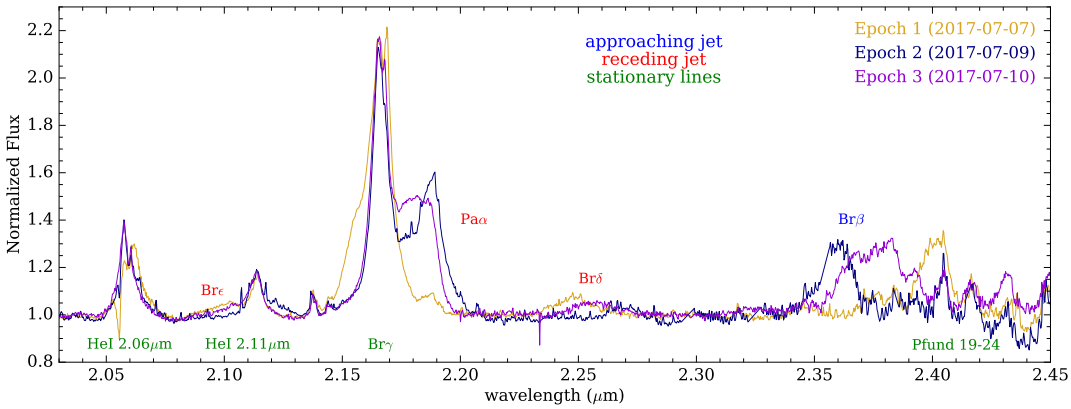

Figure 6.1: K band spectra for the three GRAVITY observations in 2017. The strongest jet emission lines are Paα and Brβ for the receding and approaching jets, respectively (the former is blended with the Brγ stationary line, the latter with stationary Pfund lines). The brightening and fading of different jet knots are visible over the three observations. Stationary emission lines are labeled in green, but are not the subject of this paper.

Optical jet interferometric model

The van-Cittert-Zernike theorem relates the spatial structure of the image on the sky plane $I(\boldsymbol{x})$ to the coherent flux $F(\boldsymbol{u})$ measured by an interferometer (e.g., Glindemann, 2011),

$$F(\boldsymbol{u}) = \int I(\boldsymbol{x}) e^{-2\pi i \boldsymbol{x}\cdot\boldsymbol{u}} d\boldsymbol{x} \tag{6.3.1}$$

where $\boldsymbol{u} = \dfrac{\boldsymbol{B}}{\lambda}$ is the uv coordinate and $\boldsymbol{B}$ is the projected baseline on sky. GRAVITY measures the complex visibility $V(\boldsymbol{u}) := \frac{F(\boldsymbol{u})}{F(\boldsymbol{0})}$ (i.e., normalized coherent flux) for a given set of uv coordinates. In single-field mode (i.e., without a phase-reference source), GRAVITY provides visibility amplitudes $|V(\boldsymbol{u})|$ and closure phases (i.e., the sum of the visibility phases across closed triangles of telescopes), because the individual visibility phases are corrupted by the atmosphere. If enough uv coverage is obtained, an inverse image reconstruction process can be performed to obtain $I(\boldsymbol{x})$; otherwise, model fitting to the available Fourier transform samples has to be done. The imaging resolution of the interferometric array is $\theta_{res} \sim \dfrac{\lambda}{|\boldsymbol{B}|_{max}}$, which for GRAVITY ($\lambda \sim 2\mu$m; $|\boldsymbol{B}|_{max} \sim 100$ m) corresponds to ~ 3 mas.

In addition, in the case of spectrally resolved interferometric observations, the differential complex visibility between the continuum and a spectral line are obtained as

$$V_{diff}(\boldsymbol{u}) = \frac{V(\boldsymbol{u})}{V_c(\boldsymbol{u})} = \frac{|V(\boldsymbol{u})|}{|V_c(\boldsymbol{u})|} e^{-2\pi i(arg(V(\boldsymbol{u}))-arg(V_c(\boldsymbol{u})))} = |V_{diff}(\boldsymbol{u})| e^{-2\pi i \phi_{diff}(\boldsymbol{u})}, \tag{6.3.2}$$

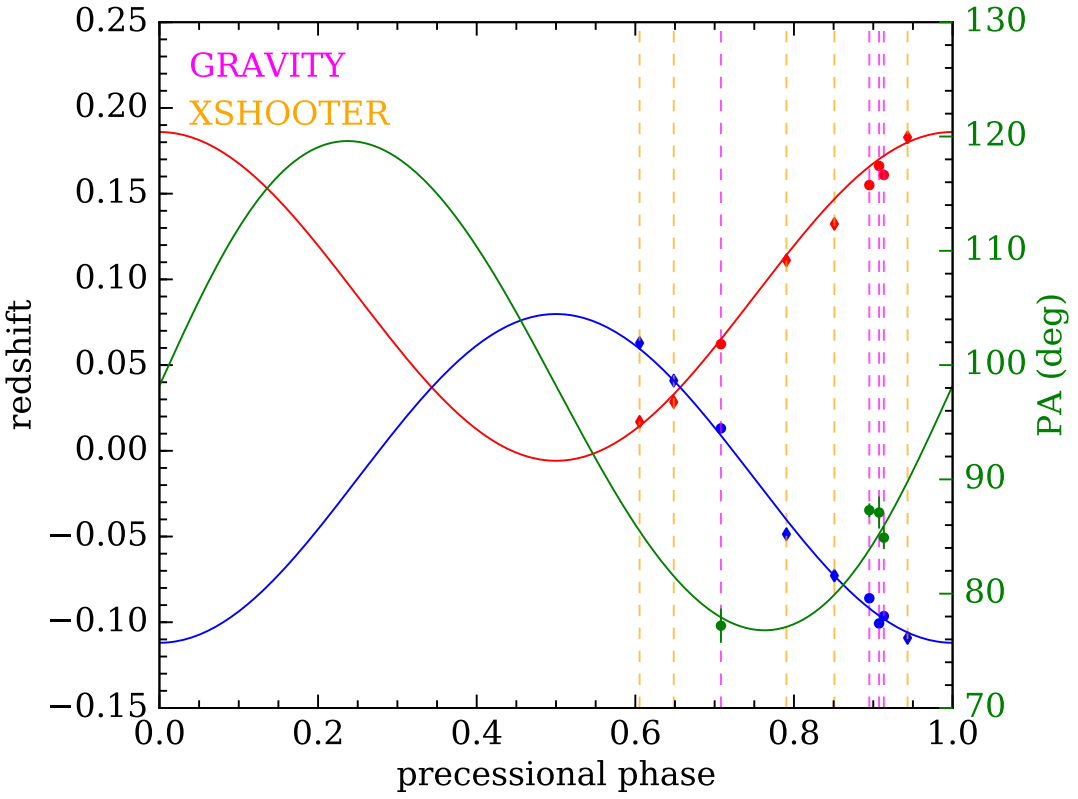

Figure 6.2: Jet redshifts (mostly approaching (eastern) jet in blue; mostly receding (western) jet in red) and position angle on sky (green) of the optical jets for each observation as a function of precessional phase. The curves were made using the kinematic model parameters in Eikenberry et al. (2001) and the precessional axis position angle in Stirling et al. (2002). The PA of the optical jets as derived from the GRAVITY data agrees well with the prediction from the radio jets. We plot both the 2016 ($\phi_{prec} \approx 0.7$) as well as the 2017 ($\phi_{prec} \approx 0.9$) GRAVITY observations.

where $V_c(\boldsymbol{u})$ is the continuum visibility, $|V_{diff}(\boldsymbol{u})|$ is the differential visibility amplitude, and $\phi_{diff}(\boldsymbol{u})$ the differential visibility phase. Because of their differential nature, these quantities are very robust and precise, allowing us to obtain spatial information on scales much smaller than the formal resolution of the telescope (i.e., sub-milliarcsecond or even microarcsecond). Additionally, in the marginally resolved limit (i.e., when the sizes of the structures are $\lesssim \theta_{res}$), the differential phases ϕ_{diff} can be converted to centroid offsets $\Delta\boldsymbol{x}$ between the line and the continuum (e.g., Waisberg et al., 2017):

$$\phi_{diff}(\boldsymbol{u}) = -2\pi\boldsymbol{u}\cdot\Delta\boldsymbol{x}\left(\frac{f-1}{f}\right), \tag{6.3.3}$$

where f is the line flux in continuum-normalized units. Therefore, the differential phases give information on the location of the line-emitting structure relative to the continuum. The differential visibility amplitudes, on the other hand, give information on the size of the line-emitting region relative to the continuum: in the marginally resolved limit, decaying or rising differential visibility amplitudes across a spectral line indicate that the line-emitting region is more or less extended than the continuum-emitting region, respectively.

Figure 6.3 shows the differential visibility amplitudes and phases for Epoch 3 of the 2017 observations. The only strong jet lines present in the GRAVITY spectrum are Paα for the receding jet and Brβ for the approaching jet. As in Paper I, the jets' line emitting regions are more extended than the region emitting the near-infrared continuum as shown by the decrease of the differential visibility amplitude across the lines. In addition, the receding and approaching jets have differential visibility phases of opposite sign, which according to Eq. 3 means that they are located on opposite sides relative to the continuum, as expected for a jet.

We fit the spectrum and differential visibilities simultaneously. For the spectrum, we fit the jet knots as Gaussians. The model parameters are:

1. The jet inclination i, which determines the redshift via

$$z = \gamma(1 \pm \beta\cos(i)), \tag{6.3.4}$$

   where $\beta = 0.26$ is the jet speed in units of c and $\gamma = \dfrac{1}{\sqrt{1-\beta^2}}$. Because we can measure the redshift very precisely for each jet line, we allow for different inclinations of the receding and approaching jets, as well as for the different components. We assume a constant velocity since it is very stable (Eikenberry et al., 2001), and the possible small variations in velocity are absorbed in the inclination.

2. The FWHM in kilometers per second, which is assumed to be the same for all the jet lines for all components;

3. The strength of each jet line relative to the normalized continuum.

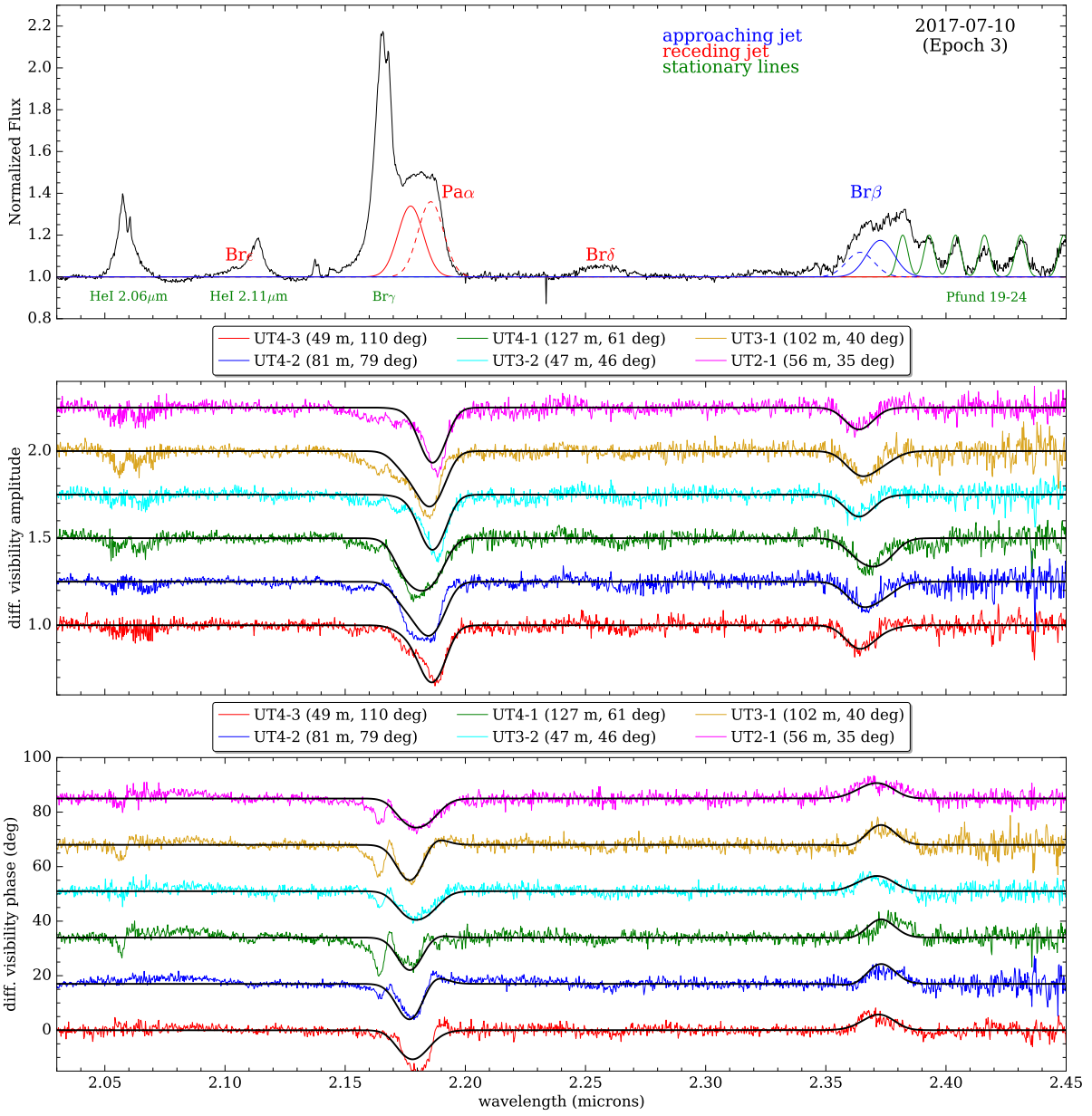

Figure 6.3: Data and best-fit jet model for the 2017 Epoch 3 GRAVITY observation. Compact (recent) and extended (older) jet knots are shown in the spectrum as full and dashed lines, respectively. Stationary lines are labeled in green. There is substantial blending of the Paα lines from the receding jet with the stationary Brγ line, which also has differential visibility signatures across it. The fits are done to all lines simultaneously, but we plot only the model for jet lines for clarity. The baseline projected lengths and position angles on sky are indicated in the labels.

To fit the visibilities, we model the jets as a 1D structure with a radial emission profile, since they are very collimated (opening angle $\lesssim 1^\circ$) from the width of the optical emission lines (Borisov and Fabrika, 1987). The model parameters are:

1. The position angle (PA) of the jet on the sky plane. It is assumed to be the same for all the jet components in a given epoch because it cannot be measured nearly as precisely as the inclination (the typical error is a few degrees);

2. The radial emission profile is controlled by the three parameters θ, α, and r_0,

$$I(r) = \begin{cases} r^{\alpha-1} e^{-r/\theta} & r \geq r_0 \\ 0 & r < r_0 \end{cases} \tag{6.3.5}$$

   where r is the distance from the center. This model is similar to the one used in Paper I, except for the additional parameter α, which allows for more general shapes besides an exponential ($\alpha = 1$), from Gaussian-like ($\alpha > 1$) to steeper profiles ($\alpha < 1$). The parameters θ (which together with α control the shape of the profile) and r_0 (the inner edge where the emission starts) are also debiased from the projection effect, that is, they are already divided by $\sin(i)$.

Figure 6.4 shows representative jet radial emission profiles that can be produced with the model detailed above, and the corresponding differential visibility amplitudes and phases as a function of projected baselines in the direction of the jet. The continuum is modeled as an unresolved point source, the flux ratio between the jet and continuum is 0.5, and the wavelength is 2μm. At the spatial scales probed by GRAVITY, more compact profiles (red) have smoother visibility curves, whereas more extended profiles (blue) have significant substructure that is not present in the data (e.g., different signs of differential visibility phases for different baselines). The profiles show that the expected longitudinal scale for the jet emission is $\sim 1 - 10$ mas.

The errors are estimated from the scatter in line-free regions. We fit for the spectrum and the differential visibilities simultaneously; however, because the former is sensitive to telluric correction and has very small statistical errorbars, we increase the flux errorbars by a factor of two. We found that this scaling led to a comparable reduced χ^2 between flux and visibilities in all observations. Moreover, because of the blending with the Brγ stationary emission line, which also produces differential visibility signatures, it is necessary to perform simultaneous fits for the Brγ line and the jets. For the model and results for the Brγ stationary line we refer to the companion paper on the equatorial outflows (Waisberg et al., 2018). The results presented here correspond to the "outflow" model in the companion paper (which we favor over the "disk" model).

The differential visibilities are computed with respect to the best-fit continuum model (also determined in the companion paper; Waisberg et al., 2018). The total differential

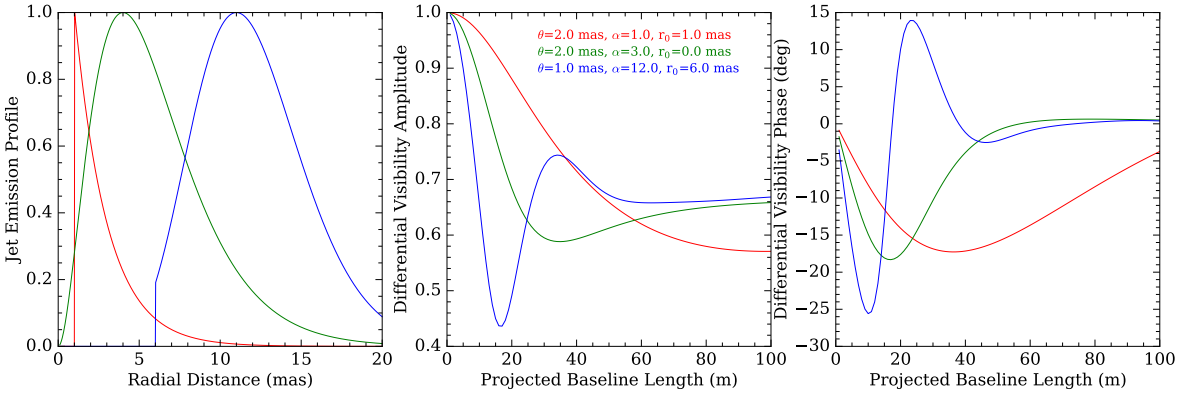

Figure 6.4: Example jet radial emission profiles (**left**) that can be created by the model, and corresponding differential visibility amplitudes and phases (**middle**,**right**) as a function of projected baseline length in the jet direction. The continuum is modeled as an unresolved point source, the flux ratio between the jet and the continuum is 0.5, and the wavelength is 2μm. At the spatial scales probed by GRAVITY, more compact profiles (red) have smoother visibility curves, whereas more extended profiles (blue) show more significant substructure in the visibilities.

visibility at a given spectral channel is then

$$V_{diff}(\boldsymbol{u}) = \frac{V(\boldsymbol{u})}{V_c(\boldsymbol{u})} = \frac{1 + \sum_i \frac{V_i(\boldsymbol{u})}{V_c(\boldsymbol{u})} f_i}{1 + \sum_i f_i}, \tag{6.3.6}$$

where V_c is the continuum visibility, and f_i and V_i are the flux ratios relative to the continuum and visibilities for each component i (different jet knots, Brγ stationary line).

The fits are done through non-linear least squares minimization with the Levenberg-Marquardt method through the `python` package LMFIT. [1] The quoted errors correspond to the 1-σ errors from the least squares fit, that is, the estimated derivatives around the optimal solution (scaled by $\sqrt{\chi^2_{red}}$). We caution, however, that true uncertainties are dominated by (i) degeneracies between the many parameters, which create a complicated multidimensional χ^2 map ; (ii) systematic errors from the continuum model; (iii) the assumption of our simple "geometric" models, which cannot capture all the complexities involved in this object. We note, in addition, that in Epoch 1 there is very severe spectral blending of the Paα jet lines with the stationary Brγ line, so that its results are less robust.

[1] https://lmfit.github.io/lmfit-py/.

Results

Table 6.2 shows the model fit results for the jet emission lines in all epochs. The data and best fits are shown in Fig. 6.3 for Epoch 3 of the 2017 observations and in Appendix A for all other observations. The measured position angle of the jets agrees well with that expected from the kinematic model and radio observations (Fig. 6.2). The results for the 2016 observation are mostly in agreement with Paper I, but the more general model emission profile allows us to better constrain $r_0 = 0.16 \pm 0.02$ mas. Because of the multiple jet components, the blending with stationary lines, and the smaller number of jet lines, the observations in 2017 are not nearly as constraining as the 2016 observation, and often only an upper limit on r_0 can be estimated.

Table 6.2: GRAVITY jets model fit results

Parameter	unit	Jet Knot	2016-07-17	2017-07-09 Epoch 1	2017-07-09 Epoch 2	2017-07-10 Epoch 3
i_{red}	deg	Compact	84.324 ± 0.006	63.67 ± 0.01	61.0 ± 0.1	62.30 ± 0.01
		Extended		64.88 ± 0.01	62.09 ± 0.03	61.21 ± 0.02
i_{blue}	deg	Compact	85.201 ± 0.006	63.11 ± 0.01	59.78 ± 0.01	60.64 ± 0.02
		Extended				59.85 ± 0.02
FWHM	km/s	All	1230 ± 13	1700 ± 13	1661 ± 21	1705 ± 20
PA	deg	All	77.2 ± 1.5	87.3 ± 0.6	87.1 ± 1.4	84.9 ± 1.0
θ	mas	Compact	3.7 ± 0.5	1.2 ± 0.2	3.7 ± 0.3	0.7 ± 0.1
		Extended		1.9 ± 0.1	1.8 ± 0.3	19.9 ± 17.4
α	mas	Compact	0.2 ± 0.1	1.0 ± 0.3	0.7 ± 0.1	1.9 ± 0.4
		Extended		3.6 ± 0.2	4.8 ± 0.5	0.1 ± 0.4
r_0	mas	Compact	0.16 ± 0.02	0.5 ± 0.1	$\lesssim 0.5$	$\lesssim 0.5$
		Extended		$\lesssim 3$	$\lesssim 8$	3.1 ± 0.1
μ^a	mas	Compact	1.7 ± 0.4	1.7 ± 0.3	$\approx 2 - 4$	1.5 ± 0.5
		Extended		$\approx 6 - 8$	$\approx 6.5 - 13$	12 ± 8
$\frac{\chi^2}{\text{dof}}$	-	-	1.4	2.7	1.6	1.0

[a] Centroid of the jet emission profile.

As noted before, there are often two components ("knots") in the jet lines in the 2017 observations. The need for two components in 2017 is clear from:

1. the spectrum, as two Gaussian components are needed for an acceptable fit;

2. the interferometric quantities, as the peaks of the differential visibility amplitudes and phases are often not aligned with the peak flux of the line in the spectrum, which points to substructure within the line, that is, different components with different spatial structure.

In contrast, in the 2016 observation (Paper I), only one jet component is needed as the emission lines are well fit by a single Gaussian and the spectrum and interferometric quantities are perfectly aligned (see Fig. 6.5 in the Appendix).

Two components are clearly distinguishable in all epochs for the Paα line from the receding jet but only on Epoch 3 for the Brβ line from the approaching jet. One of the components is compact (emission centroid $\lesssim 2$ mas), with an emission profile similar to the one in the 2016 observation, and associated with the most recent or current jet ejection. The other component is significantly more extended (emission centroid $\gtrsim 6$ mas), associated with a previous jet ejection. This interpretation agrees with the corresponding redshifts from the precession model in Epochs 1 and 2. Figure 6.5 shows the collection of radial emission profiles of the optical jets for all observations. The compact knots have an exponential-like profile, whereas the extended knots have more rotund shapes. We note that the plotted best-fit emission profiles are only approximate, in particular for the extended components, for which only an upper limit on r_0 can usually be determined (we have used such an upper limit in the plots). Much more robust are the centroids of the emission profiles (last row in Table 6.2), which show a clear difference between compact and extended components, that is, a significant spatial structure to the combined emission.

The emission profiles of the compact components, extending to approximately a few mas, suggest that each individual knot is composed of bullets emitted over $\lesssim 1$ day (their speed of 0.26c corresponds to ≈ 8 mas/day), with their emission decaying with distance from the compact object. As in Paper I, we attempted to fit the jets with more localized emission profiles (such as a point source or Gaussian), but they are inconsistent with the data: an elongated structure for the jets is strongly preferred. We also note that, for the more compact components, the emission peaks substantially close $\lesssim 0.5$ mas to the binary system, and is more compact than previous estimates from optical spectroscopy monitoring; for example Borisov and Fabrika (1987) derived an exponential decay of the jet emission with fall-off distance 6.7×10^{14} cm ≈ 8.2 mas for the Hα jet line. The elongated emission profiles that we measure are strongly suggestive of a continuous heating mechanism along the entire jet, which is naturally accomplished by photoionization by the collimated radiation from the inner regions close to the compact object. The reduced emission with distance could then explained by the decaying intensity of the ionizing radiation, shadowing of the radiation by closer-in bullets in the case of large area covering factor, changing bullet properties with distance, or a combination of such effects.

Furthermore, the 2017 observations allow us to probe the spatial evolution of the jet profiles from night to night. The jet lines in Epoch 1 have clearly disappeared by Epoch 2 two nights later (Fig. 6.1). However, the jets lines in Epochs 2 and 3 (which are separated by one night only) partly overlap. The extended component in Epoch 3 could correspond to the compact component in Epoch 2 after it has travelled ≈ 8 mas/day $\times 1$ day , whereas

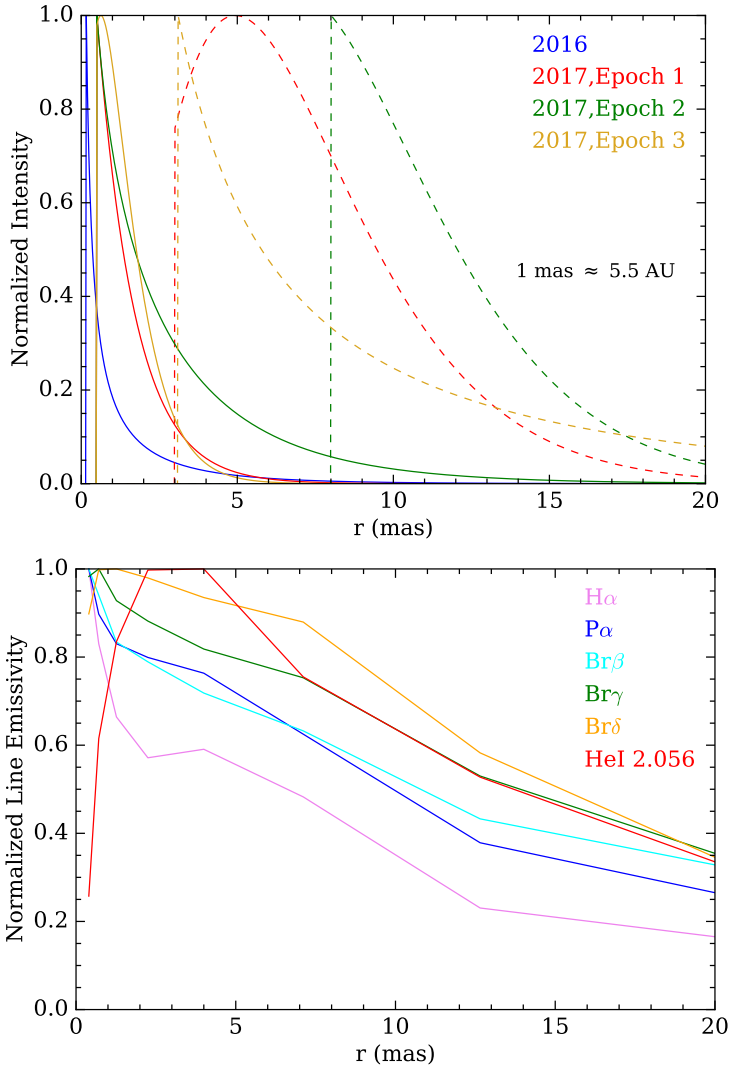

Figure 6.5: **Top:** Collection of optical jet radial emission profiles for all GRAVITY observations. These were derived from the available jet emission lines in the K band spectrum (Brγ, Brδ, and He I 2.06 μm in the 2016 observation, and Paα and Brβ in the 2017 observations). There are two classes of profiles: compact (solid lines), associated with recent or current knots and which peak close to the central binary, and extended (dashed lines), associated with older knots.
Bottom: Emission profiles for selected emission lines calculated from a `Cloudy` photoionization model using the best-fit parameters to the emission line fluxes from Epoch X1 of the XSHOOTER observations. The elongated profiles resolved by GRAVITY suggest photoionization by the collimated radiation as the heating mechanism. The steeper profiles measured by GRAVITY relative to the `Cloudy` model could be explained by screening effects due to the large area covering factor of the bullets in the jets.

a new compact component in Epoch 3 clearly appeared at the same redshift where the extended component in Epoch 2 was located. This is the first time the movement of the optical bullets has been spatially resolved, although longer observations during a single night would be needed to trace the motion of an individual component unambiguously. We note that spectroscopic monitoring of the Hα jet lines consistently shows four or more spectroscopically resolved knots in both jets with a scatter of speeds $\sim$ 3000 km/s (Blundell et al., 2007), so that the presence of multiple knots is in fact expected in the strongest jet lines such as Paα.

6.4 XSHOOTER data analysis

We fit the jet lines with Gaussian or Lorentzian profiles (the jet lines are usually better fit by a Gaussian, but sometimes a Lorentzian profile is clearly preferred) to estimate their central wavelength, FWHM, and total intensity. All line fits were performed with the task `splot` in `IRAF`[2] (Tody, 1986, 1993). Whenever jet lines were blended with other jet or stationary lines, deblending was used. For all line identifications and adopted wavelengths, the "Atomic Line List v2.05b21" (van Hoof, P.) was used. The noise for the spectral fits was estimated from the scatter in continuum regions near each line. A particularly important constraint for photoionization models of the optical bullets is the absence of ionized helium in the jets due to the lack of the He II 4686$\AA$ line. We estimate upper limits on its flux from the known location of where the line would appear based on the measured redshifts and the FWHM from the other jet lines.

Figure 6.6 shows the spectrum for the first XSHOOTER observation of SS 433 (Epoch X1), which contains the largest number of jet lines of all epochs. Emission lines from the jet are shown in blue and red for the eastern and western jets, respectively (at this epoch, the eastern jet, which is approaching most of the time, is receding). Throughout all observations we identify up to twenty pairs of lines: Hα through Hϵ; Paα through Pa9; Brβ through Br12; and five lines of He I (5875$\AA$, 6678$\AA$, 7065$\AA$, 1.083 μm, 2.056μm). The strongest hydrogen lines (Hα, Hβ, Paα, Brβ) and He I 1.083μm often show one or two additional components (shown in cyan and orange in Fig. 6.6), with redshift corresponding to previous ejections according to the precession model (and which we associate with older jet knots), whereas most emission lines show only one component from the most recent or current ejection (this behavior matches what is seen in the GRAVITY observations). The average redshift for the more recent jet knots in each epoch is shown in Fig. 6.2 and agrees with the kinematic precession model within the nutational motion and random jitter. The strength and number of jet emission lines varies significantly between the five XSHOOTER epochs.

[2]IRAF is distributed by the National Optical Astronomy Observatories, which are operated by the Association of Universities for Research in Astronomy, Inc., under cooperative agreement with the National Science Foundation.

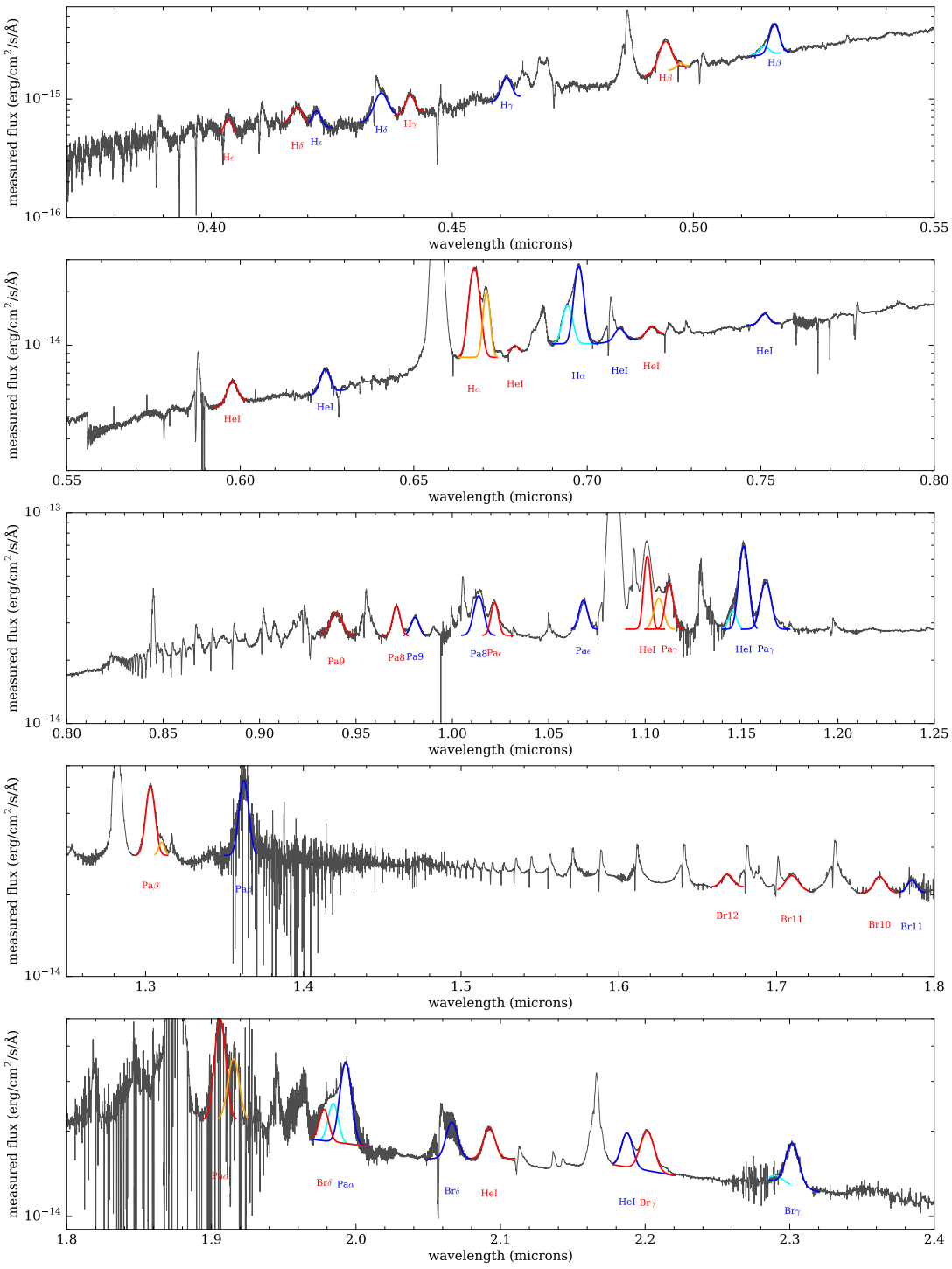

Figure 6.6: First XSHOOTER spectrum of SS 433 (Epoch X1). H I and He I emission lines from the eastern and western optical jets are shown in blue and red, respectively. Older jet ejections (cyan and orange), only present for the strongest line transitions such as Hα (second panel from top) and Paα (bottom panel), are also shown.

Cloudy models for photoionized optical bullets

The spatial emission profiles for the optical jets resolved by GRAVITY are strongly suggestive of photoionization as the main heating mechanism of the optical jets. Therefore, we proceeded to fit the jet emission line fluxes measured from XSHOOTER with photoionization models.

All line emission in SS 433 originates from dense gas; a clear lower limit to the density $n_e \gtrsim 10^7 \mathrm{cm}^{-3}$ follows from the absence of any forbidden lines in the spectrum (Osterbrock and Ferland, 2006, p.60). The true density in the optical bullets is estimated to be $\sim 10^{13} \mathrm{cm}^{-3}$, and the optical jets take the form of dense bullets distributed throughout the jets with a low volume filling factor $\sim 10^{-6}$ (Fabrika, 2004). At such densities, collisional ionization from excited levels and line radiative transfer effects become important, causing strong deviations from Case B recombination; still, such densities are not high enough for local thermodynamic equilibrium (LTE) to apply to all levels, and full collisional radiative models must be used (Ferland et al., 2013, 2017). A clear sign that collisional and radiative transfer effects are important in the optical bullets is the rather flat or even inverted Hα/Hβ jet line ratio (after extinction correction).

We model the jet emission lines with the photoionization code Cloudy (Ferland et al., 2013, 2017) version c17.01. The ionizing radiation is taken to be a single blackbody. We construct a grid in bullet density, bullet size, blackbody temperature, and intensity. In addition, because SS 433 is known to have appreciable extinction, we expand the grid in A_V, assuming an extinction law $\frac{A_\lambda}{A(V)}$ following Cardelli et al. (1989) and $R_V = 3.1$. We attempted to fit for the He abundance, since it is likely that the donor star in SS 433 is at an advanced evolutionary stage, but it was unconstrained in our fits; therefore, we fixed a standard He abundance (0.098 by number). The abundances of other elements are taken as solar. The grid parameters and intervals are shown in Table 6.3. The solutions are iterated until convergence of the line optical depths. Each point in the grid gives a model intensity for each line (erg/s/cm^2). The total number of bullets is then computed to minimize the χ^2 with respect to the measured line intensities. The bullets are assumed to be identical in both jets, but the number of bullets (and therefore the kinetic power) can be different for the receding and approaching jets. We corrected the line intensities in each jet for Doppler boosting $(1+z)^3$ using the average measured redshift.

We use the lines from the most recent jet knots (which contain a much larger number of lines) for the fits. The GRAVITY observations revealed that recent ejections have a typical exponential intensity profile as shown in Fig. 6.5. We integrate our Cloudy models over five radial points covering a factor of 100 in intensity. The reported best-fit intensity is the one at the base of the optical jet.

The statistical line flux errors estimated from the spectral fits are very small. The actual errors are dominated by systematic effects in the flux calibration, telluric correction, contamination by weak lines, line blending, and model uncertainties (such as collisional cross sections and line radiative transfer treatment). We estimate a 25% error in flux for all the lines, which results in $\chi^2_{red} \sim 1$ for the best-fit grid points. The parameter uncertainties are estimated by considering all the models that fall within $\Delta\chi^2 = p$ of the

Table 6.3: `Cloudy` model grid parameters.

Parameter	Symbol	Unit	Minimum	Maximum	Interval
Blackbody Temperature	T	10^4 K	1	10^2	0.1 (Log)
Blackbody Intensity	I	10^{13} erg/s/cm^2	10^{-5}	10^4	0.5 (Log)
Bullet Density	n_H	10^{13} cm^{-3}	10^{-3}	10^2	0.5 (Log)
Bullet Size	R	10^6 cm	10^{-2}	10^2	0.5 (Log)
Extinction	A_V	-	5	8	0.2

best χ^2 (Lampton et al., 1976), where p is the number of model parameters.

From the `Cloudy` model results, we derive further parameters of interest for the jets:

1. The volume filling factor of the optical bullets:

$$V_{\rm ff} = \frac{V_{\rm bullets}}{V_{\rm jet}}, \tag{6.4.1}$$

where $V_{\rm bullets}$ is the total volume in the bullets (calculated from their size and number) and $V_{\rm jet} = \pi\psi_{\rm jet}^2 \frac{l_{\rm jet}^3}{3}$, where $\psi_{\rm jet}$ is the half-opening angle and $l_{\rm jet}$ is the length of the jet;

2. The kinetic power of the optical jets:

$$L_{\rm kin} = 2 \times \frac{1}{2} M v_{\rm jet}^2 \frac{v_{\rm jet}}{l_{\rm jet}}, \tag{6.4.2}$$

where $v_{\rm jet} = 0.26c$, M is the total mass in the bullets (calculated from their density, size, and number).

3. The total line luminosity in the optical bullets $L_{\rm bullets}$. This includes not only the recombination lines within XSHOOTER, but all of the strongest hydrogen and helium lines in the full spectrum output from `Cloudy`.

4. The total ionizing luminosity within the beam containing the optical bullets:

$$L_{\rm beam} = 2 \times I(r_0)\pi\psi_{\rm jet}^2 r_0^2, \tag{6.4.3}$$

where $I(r_0)$ is the intensity at the base of the beam. The total luminosity in the collimated radiation could be higher if it is broader than the beam containing the optical bullets, which is likely the case from the presence of older jet knots that can keep radiating for a few days (Panferov and Fabrika, 1993).

5. The luminosity inferred by an observer (assuming isotropy) whose line of sight is within the collimated beam:

$$L_{\rm face-on} = L_{\rm beam}\frac{4\pi}{\pi(2\psi_{\rm jet})^2} = 2I(r_0)r_0^2. \quad (6.4.4)$$

For these estimates, we assumed $\psi_{\rm jet} = 1^\circ$ and $r_0 = 0.4$ mas and $l_{\rm jet} = 2$ mas from the GRAVITY observations. The length of the jet, l_{jet}, is the region over which the bulk of the optical jet emission arises for the compact knot. It does not affect the intrinsic parameters of the Cloudy model, but only the derived parameters volume filling factor and kinetic power as per Eqs. (7) and (8); for instance, a larger l_{jet} would reduce the estimated kinetic power.

Our model does not take into account screening of radiation by the bullets, which plays a role because the jets are very compact (area covering factors are high). To ensure self-consistency in the energetics, we only accept solutions with enough total luminosity in the beam to power the bullets (i.e., $L_{\rm beam} > L_{\rm bullets}$). We also note that we assume the bullet radiation is isotropic and identical between the two jets (the only difference we allow between the two jets is in the total number of bullets), whereas differences between the luminosity of the two jets with precessional phase have been interpreted in terms of anisotropic radiation (Panferov et al., 1997; Fabrika, 2004).

Results

We note that several related calculations to estimate the properties of the optical jets can be found in previous papers (e.g., Davidson and McCray, 1980; Begelman et al., 1980; Bodo et al., 1985; Borisov and Fabrika, 1987; Fabrika and Borisov, 1987; Brown et al., 1991; Panferov and Fabrika, 1993), primarily based on the Hα luminosity. These calculations have several uncertainties: unknown heating mechanism and emission line emissivity, degeneracy between density and volume filling factor, unknown extinction, optical depth effects, unknown spatial emission profile of the optical jets (e.g., jet size). The calculations presented here are based on the first optical interferometric measurements that have spatially resolved the optical jets, and on a large number of jet line species from XSHOOTER spectra.

Table 6.4 shows the model fit results for the five XSHOOTER epochs. Figure 6.7 shows the measured and model line fluxes for the first XSHOOTER epoch (corresponding plots for the other epochs are shown in Appendix B).

Table 6.4: `Cloudy` photoionization models for the optical jets: Results

Parameter	Unit	Epoch X1	Epoch X2	Epoch X3	Epoch X4	Epoch X5
Number of Jet Lines Fitted (Eastern Jet/ Western Jet)	-	19/17	12/13	4/7	9/9	7/12
Model parameters						
T	10^4 K	$3-4$	$3-4$	$3-4$	3	$3-5$
$I(r_0)$	10^{13} erg/s/cm^2	$1-3$	1	$1-3$	$1-3$	$1-3$
n_H	10^{13} cm^{-3}	$1-3$	$0.3-3$	$0.3-10$	1	$0.3-3$
R	10^6 cm	$1-30$	$1-100$	$1-100$	3	$1-100$
A_V	-	$6.4-6.8$	$6.2-6.8$	$6.6-7.6$	$6.6-7.4$	$6.6-7.6$
$N_{\rm bullets}$ (both jets)	10^{13}	$0.1-300$	$0.02-20$	$0.02-40$	$70-100$	$0.05-450$
$\frac{\chi^2}{\rm dof}$	-	42/29	44/18	8/4	36/11	35/12
Derived parameters						
V_{ff} (average both jets)	10^{-6}	$1-20$	$0.6-100$	$0.5-160$	$8-12$	$1-160$
$L_{\rm kin}$ (both jets)	10^{38} erg/s	$2.5-14$	$1.4-24$	$2-47$	$5-9$	$3-35$
$L_{\rm bullets}$ (both jets)	10^{37} erg/s	$1.2-1.9$	$0.8-1.7$	$1.2-4.0$	$1.6-3.6$	$1.6-3.2$
$L_{\rm beam}$ (both jets)	10^{37} erg/s	$2-6$	2	$2-6$	$2-6$	$2-6$
$L_{\rm face-on}$ (both jets)	10^{40} erg/s	$7-20$	7	$7-20$	$7-20$	$7-20$

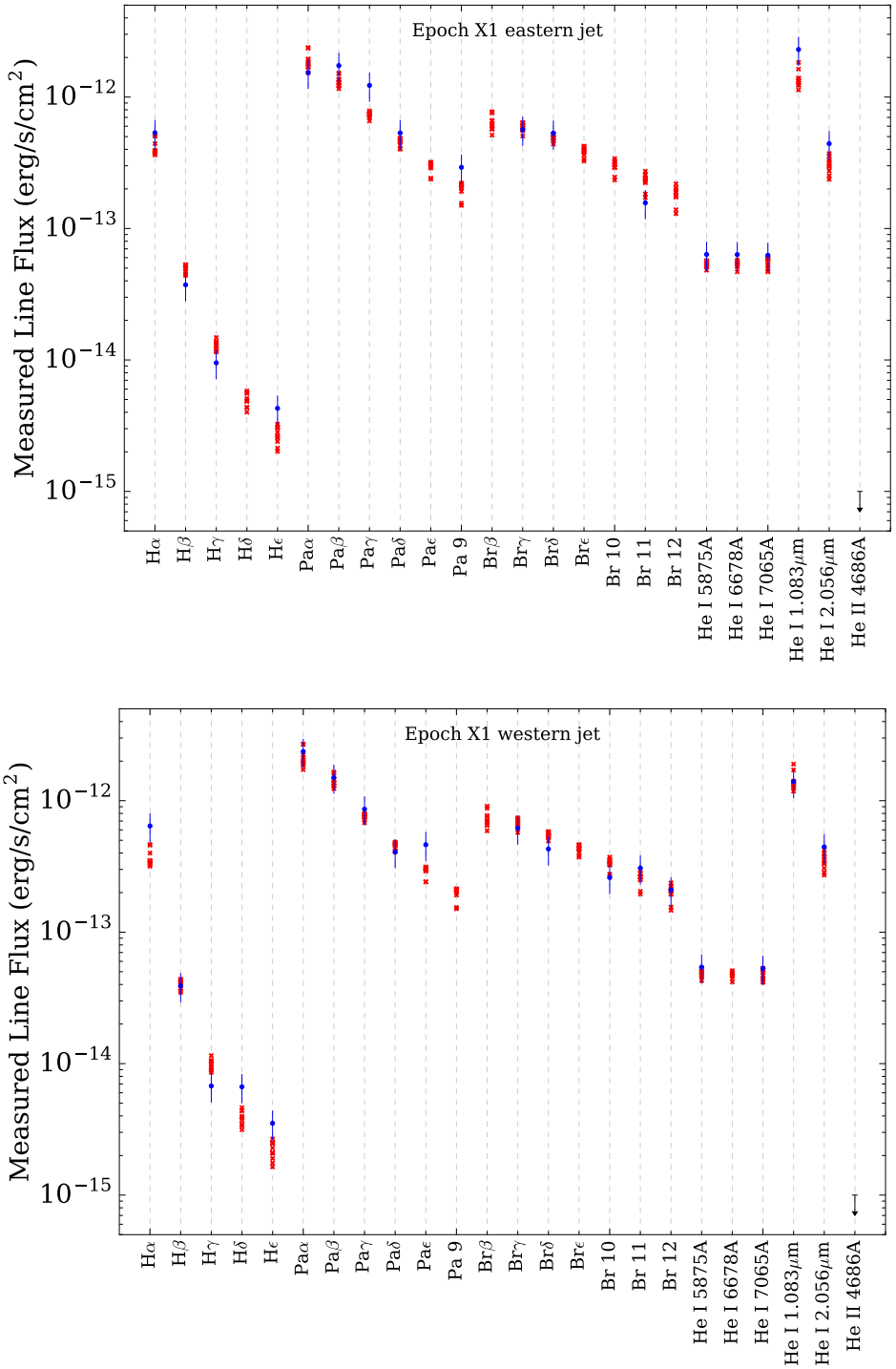

Figure 6.7: Measured line fluxes for the Epoch X1 XSHOOTER observation of SS 433 (blue) and best-fit Cloudy photoionization models (red). The models are shown for all the lines measured in at least one of the five epochs. The He II 4686Å line flux is an upper limit since it was never detected.

Bullet properties

The results confirm that the optical bullets in SS 433 are very dense, $n_H \sim 10^{13}\mathrm{cm}^{-3}$, and have a size $R \approx 10^6 - 10^7$cm. Even though they are optically thin to electron scattering ($\tau_T \sim 0.01$), many emission lines are optically thick. For the best-fit model in Epoch X1, $\tau_{\mathrm{Hff}} \approx \tau_{\mathrm{Pff}} \approx 20$, $\tau_{\mathrm{Hfi}} \approx 4$, $\tau_{\mathrm{Brfl}} \approx 2$, $\tau_{\mathrm{Br10}} \approx 0.3$, $\tau_{\mathrm{HeI6578}} \approx 5$, and $\tau_{\mathrm{HeI1.083}} \approx 0.6$, so that optical depth effects in the line emission indeed have to be taken into account. The cooling in the bullets is dominated by hydrogen and helium recombination lines ($\sim 80\%$), with total line luminosity $\approx 2 \times 10^{37}$ erg/s. Only around 15% of such luminosity is in lines within the XSHOOTER spectrum, with the strongest lines being the Lyman series in the UV. The total number of bullets that compose each knot is $\sim 10^{12} - 10^{15}$, with volume filling factor $\sim 10^{-6} - 10^{-4}$.

Jet kinetic power

We constrain the kinetic power in the optical bullets to $\sim 2 - 20 \times 10^{38}$ erg/s. This agrees with estimates from emission line modeling in the X-rays, which vary from $\sim 3 \times 10^{38}$ to 5×10^{39} erg/s (e.g., Marshall et al., 2002; Brinkmann et al., 2005; Medvedev and Fabrika, 2010). The collapse of the continuous X-ray jets into optical bullets must therefore be an efficient process, both in terms of mass and kinetic energy. Previous estimates from optical spectroscopy give $L_{\mathrm{kin}} \sim 10^{39}$ erg/s (e.g., Panferov and Fabrika, 1997; Fabrika and Borisov, 1987).

Collimated radiation

The results constrain the collimated radiation to be relatively soft, $T \sim 3 - 4 \times 10^4$ K, and the total luminosity in the 1° beam containing the optical bullets to $L_{\mathrm{beam}} \approx 2 - 6 \times 10^{37}$ erg/s. Lower luminosities cannot power the jet emission lines, whereas higher luminosities and temperatures cause too intense heating and ionize helium too much. For an observer looking face-on at the collimated radiation and assuming isotropy, the inferred luminosity would be $\approx 7 - 20 \times 10^{40}$ erg/s, that is, SS 433 would appear as an extremely bright UV source. This luminosity is higher than the $\sim$ few $\times 10^{39}$ erg/s inferred from the SED (Wagner, 1986, although this is a rather uncertain number – see below), suggesting that indeed there is collimated radiation in SS 433 (not only thermal downgrading at low latitudes). The total intrinsic luminosity in collimated radiation depends on its opening angle, and would be $\sim 2 \times 10^{39} - 10^{41}$ erg/s for angles $10° - 50°$. From modeling of the optical filaments in the W50 nebula and assuming photoionization by collimated radiation, Fabrika and Sholukhova (2008) estimated an ionizing luminosity $\sim 10^{40}$ erg/s in an opening angle $\sim 50°$, roughly consistent with our estimates.

Figure 6.5 (bottom) shows the spatial emission profile for selected emission lines for the best-fit `Cloudy` photoionization model to Epoch X1. It assumes the bullets are distributed homogeneously over the jet with constant properties (density, size), and shows the normalized line emissivity as a function of distance r in the jet. It resembles the spatial profiles directly resolved by GRAVITY, and confirms that the different H I and He I lines have

similar emission regions. The elongated, decaying exponential-like profile results from the interplay between the radiation intensity, gas density, and column density, and is a good consistency check for our photoionization models. For a given density and column density, there is an optimal intensity that will maximize the line emission of a given species by ionizing the bullet but not overheating it. Therefore, it is possible to obtain different spatial profiles (rising or decaying) depending on the combination of parameters, so that it is reassuring that the best-fit `Cloudy` models reproduce decaying profiles (albeit less steep than in the GRAVITY data) without an explicit requirement. A caveat of our model is that we do not consider screening of the intensity along the jet by the bullets (which happens in practice due to the large area covering factor), which is possibly the reason for the discrepancy in steepness.

Because of the possibility that SS 433 could be an ULX for an observer looking at it face-on, we attempted to constrain the X-ray luminosity in the beam containing the optical bullets. We did this through a perturbative approach: we selected the best-fit model in Epoch X1 from the analysis above, and added a second X-ray component with varying intensity, and checked at which X-ray intensity the optical emission lines are substantially affected and in clear violation of the data (e.g., by producing a too strong He II 4868 $\mathring{A}$ line). Because the main effect comes from the soft X-ray photons capable of ionizing H, He, and He+, the constraint depends on the relative contribution of soft X-ray photons to the total X-ray luminosity. To this end, we repeated the procedure for two different SEDs: a very soft one corresponding to a supersoft ultraluminous (SSUL) source, in the form of a blackbody $kT = 0.14$ keV, and a harder one corresponding to a hard ultraluminous (HUL) source, in the form of a blackbody $kT = 0.27$ keV plus a strong hard component (Kaaret et al., 2017). The corresponding SEDs and limits are shown in Fig. 6.8.

In the case of the SSUL SED, we constrain the X-ray luminosity to be $\lesssim 10^{-3}$ of the UV component, that is, $\lesssim 5 \times 10^{34}$ erg/s in the 1° beam containing the optical bullets or $\lesssim 10^{38}$ erg/s for a face-on observer. In this case, SS 433 would not be an ULX. For the HUL SED, the X-ray luminosity could be much larger, up to $\lesssim 10^{-1}$ of the UV component, that is, $\lesssim 5 \times 10^{36}$ erg/s in the 1° beam containing the optical bullets or $\lesssim 10^{40}$ erg/s for a face-on observer. We conclude that SS 433 could be an ULX, as long as its X-ray spectrum is dominated by hard X-rays. Just the same, face-on ULXs (with a clear view through the funnel) are generally expected to have dominantly X-ray spectra (Kaaret et al., 2017), whereas our results suggest that SS 433 is UV dominated even in the collimated beam. This might mean that thermal downgrading happens already in the funnel of SS 433 (Begelman et al., 2006). The most promising way to find face-on SS 433-like objects in other galaxies might be to look for very bright and variable (due to jet precession) UV sources.

The X-ray luminosity of SS 433 has also been constrained from a putative reflection component $\sim 10^{35}$ erg/s in the hard X-ray spectrum $\gtrsim 10$ keV of SS 433 (Medvedev and Fabrika, 2010; Middleton et al., 2018). Middleton et al. (2018) estimates that the intrinsic X-ray luminosity is $L_X \gtrsim 10^{38}$ erg/s. This is consistent with our upper limits as long as the X-ray radiation is slightly less collimated ($\gtrsim 5°$) than the beam containing the optical bullets, which is almost certainly the case from the presence of older jet knots that keep radiating for a few days (Panferov and Fabrika, 1993).

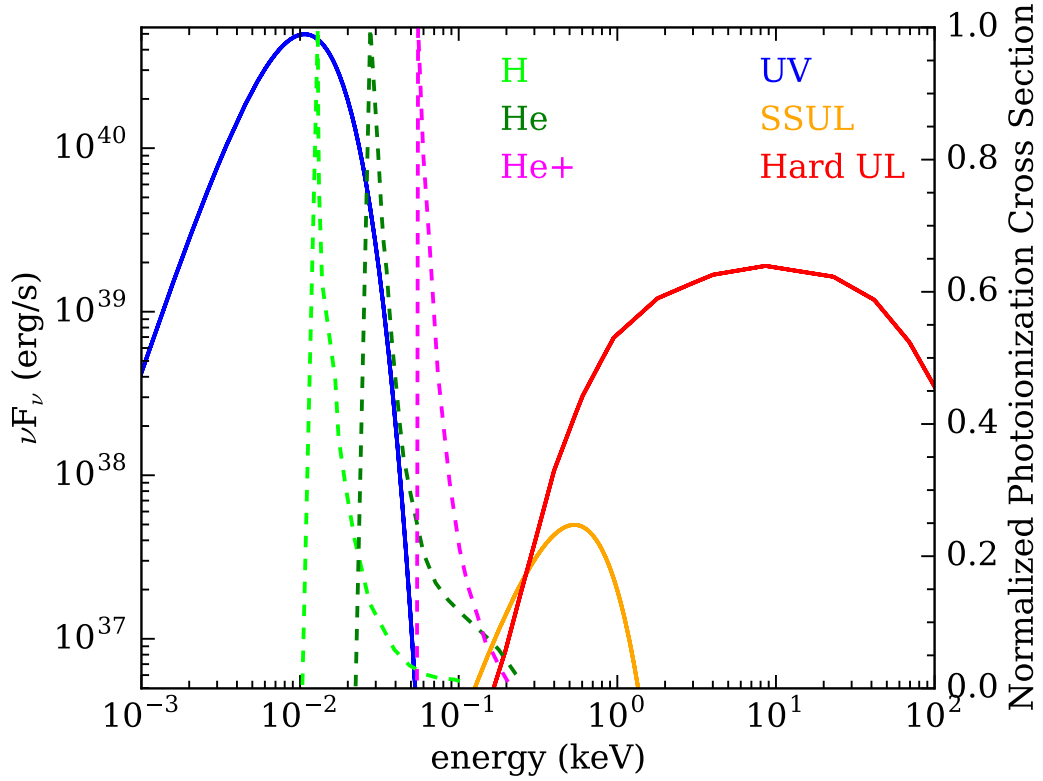

Figure 6.8: Potential SS 433 SED for a face-on observer who sees the beam radiation as the optical bullets see it. The solid blue curve shows the UV component from the best-fit `Cloudy` photoionization model to the line intensities in Epoch X1 of XSHOOTER. The orange and red lines show the upper limit to a possible X-ray component for a supersoft ultraluminous (SSUL) and hard ultraluminous (HUL) type SEDs, respectively. The dashed lines show the ground state photoionization cross sections for H, He, and He+. For SS 433 to look like an ULX for the face-on observer, its X-ray spectrum must be significantly hard, since soft X-ray photons break the H/He/He+ ionization balance in the optical bullets.

Extinction towards SS 433

The extinction towards SS 433 is known to be large from the very red continuum spectrum but its exact value is difficult to assess. Galactic dust extinction maps give $A_V = 7.8$ towards the direction of SS 433 (Schlegel et al., 1998; Perez M. and Blundell, 2010), but that is an upper limit to the total integrated line of sight extinction. More recent 3D dust maps rather give $A_V = 5.7 \pm 0.1$ at $d = 5.5$ kpc towards SS 433 (Green et al., 2018). Strong diffuse interstellar bands (DIBs) are also present in the spectrum of SS 433 (as noted in previous work, e.g., Murdin et al., 1980; Margon, 1984). The strength of DIBs has been shown to be correlated with interstellar extinction (e.g., Herbig, 1975; Friedman et al., 2011; Kos and Zwitter, 2013), although with substantial scatter. We measured the equivalent widths (EW) of several DIBs (5780, 5797, 5850, 6196, 6202, 6270, 6283, 6379, 6613, 6660 $\mathring{A}$) in our XSHOOTER spectra and used the correlations in Friedman et al. (2011) and Kos and Zwitter (2013) to estimate $A_V = 5.1 \pm 1.0$ and $A_V = 5.6 \pm 2.1$, respectively, where the uncertainties are the 1σ scatter between the different DIBs. Therefore, there is evidence that the interstellar extinction towards SS 433 may be $A_V \lesssim 6.0$.

On the other hand, $A_V \gtrsim 7.8 - 8.0$ has also been estimated from fitting the spectral energy distribution with a single reddened blackbody (e.g., Murdin et al., 1980; Wagner, 1986; Dolan et al., 1997). This approach, however, suffers from several problems: (i) in the Rayleigh-Jeans range, the temperature of the blackbody and the extinction are very strongly correlated; (ii) there are numerous and very strong emission lines in SS 433; (iii) it is not clear whether the supercritical disk should look like a single blackbody, for example, the temperature seems to change with precession phase (Wagner, 1986). Our XSHOOTER observations are not optimized for SED continuum fitting, but we confirm the strong degeneracy between blackbody temperature and extinction. A temperature $T \gtrsim 20000$ (a reasonable expectation from the presence of He II 4868 $\mathring{A}$ stationary line) requires $A_V \gtrsim 7.5$.

Our modeling of the jet lines yields $A_V \approx 6.7 \pm 0.1$, which is intermediate between the lower values inferred from 3D dust maps and DIBs and those estimated from the very reddened SED. We suggest that there may be substantial $A_V \gtrsim 1$ and structured circumstellar extinction in SS 433, affecting the equatorial part of the system more than the optical jets. It may be caused by dust forming from the equatorial outflows seen in radio (Paragi et al., 1999; Blundell et al., 2001) and near-infrared stationary emission lines (Waisberg et al., 2018). Mid-infrared observations of SS 433 show evidence of dust from excess emission at $\lambda \gtrsim 20\mu$m (Fuchs et al., 2006). We speculate that mid-infrared interferometric observations with VLTI+MATISSE (Lopez et al., 2014) might resolve an extended dust torus in SS 433.

6.5 Conclusions

We presented a second set of GRAVITY observations of SS 433 after Paper I, as well as the first XSHOOTER observations of this object, focusing on the optical jets. We summarize

our main conclusions from the GRAVITY observations as follows:

1. The optical jets have elongated, exponential-like spatial emission profiles, suggestive of a continuous heating process throughout the entire jet; we argue for photoionization by collimated radiation;

2. We have spatially resolved the movement of the optical bullets for the first time, finding more extended jet knots corresponding to previous jet ejections.

Using the up to twenty simultaneous pairs of measured jet line fluxes in the XSHOOTER observations, we have constrained properties of the optical bullets and the putative ionizing radiation with `Cloudy` photoionization models:

1. The optical bullets are dense, $\sim 10^{13}\mathrm{cm}^{-3}$, and have a size $\sim 10^6 - 10^7$ cm, from which optical depth effects in the jet emission lines are important;

2. The kinetic power of the optical jets is $\sim 2 - 20 \times 10^{38}$ erg/s;

3. The beamed radiation is dominantly UV with a luminosity $\approx 2 - 6 \times 10^{37}$ erg/s in the 1° beam containing the optical bullets. An observer looking directly at the beam would infer an isotropic luminosity $\approx 7 - 20 \times 10^{40}$ erg/s, that is, SS 433 would appear as an extremely bright UV source;

4. In the photoionization picture, SS 433 could still be an ULX with a face-on observer inferring $L_X \lesssim 10^{40}$ erg/s, as long as the X-ray SED is dominantly hard, since soft X-ray photons destroy the H/He/He+ ionization balance in the optical bullets;

5. We constrain the extinction in the optical jets $A_V = 6.7 \pm 0.1$ and suggest there is substantial and structured circumstellar extinction in this object.

Acknowledgements

We thank the GRAVITY Co-Is, the GRAVITY Consortium, and ESO for developing and operating the GRAVITY instrument. In particular, I.W. and J.D. thank the MPE GRAVITY team, in particular F. Eisenhauer, R. Genzel, S.Gillessen, T. Ott, O. Pfhul, and E. Sturm. We also thank the GRAVITY team members (W. Brandner, F. Einsenhauer, S. Hippler, M. Horrobin, T. Ott, T. Paumard, O. Pfhul, O. Straub, E. Wieprecht) and ESO staff who were on the mountain during the observations. We also thank P. Kervella for comments on the paper. I.W. thanks the organizers and participants of the 2018 Cloudy Workshop in Chiang Mai, Thailand, where part of this project was done, in particular Gary Ferland, Christophe Morisset, and Peter van Hoof. POP acknowledges financial support from the CNRS High Energy National Program (PNHE). POP and GD acknowledge financial support from the CNES. This research has made use of the Jean-Marie Mariotti

Center SearchCal service [3] co-developed by LAGRANGE and IPAG, CDS Astronomical Databases SIMBAD and VIZIER [4], NASA's Astrophysics Data System Bibliographic Services, NumPy (Van Der Walt et al., 2011) and matplotlib, a Python library for publication quality graphics (Hunter, 2007).

Appendix

A. GRAVITY: Full data and model fits

Here we show as in Fig. 6.3 the full K band spectrum and interferometric data, as well as the best-fit jet models, for the remaining GRAVITY observations. Compact and extended jet knots are shown in colored solid and dashed lines, respectively. In the 2017 observations, in which there is strong blending between the jets and the Brγ stationary line, a combined fit is done, but we show only the jet model for clarity. For the Brγ stationary line model and results, we refer to the companion paper on the equatorial outflows (Waisberg et al., 2018).

B. XSHOOTER: Full data and model fits

Here we show the data and best-fit models for the remaining XSHOOTER epochs as in Fig. 6.7.

[3] Available at http://www.jmmc.fr/searchcal.
[4] Available at http://cdsweb.u-strasbg.fr/.

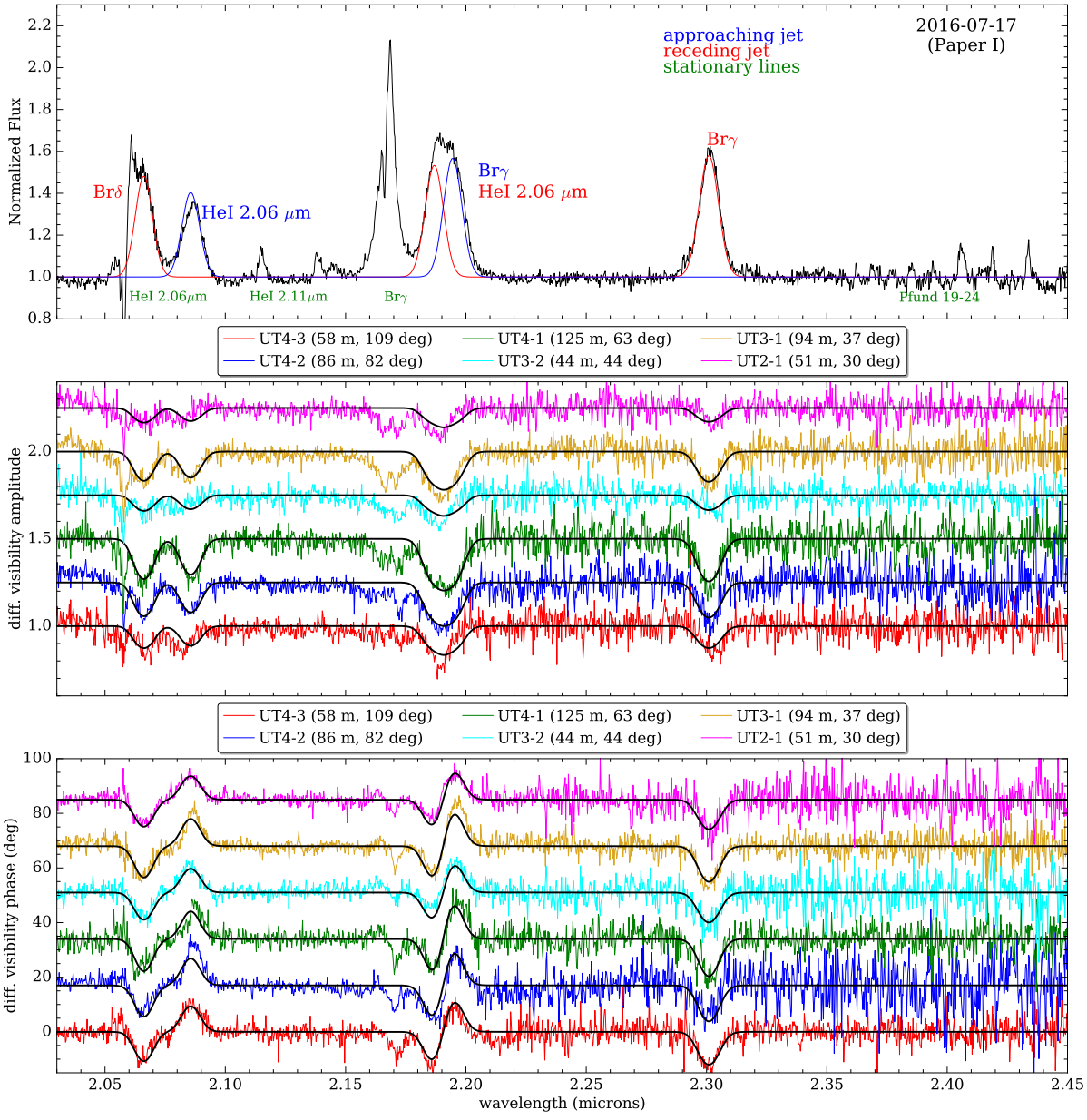

Figure 6.9: Data and best-fit jet model for the 2016 GRAVITY observation.

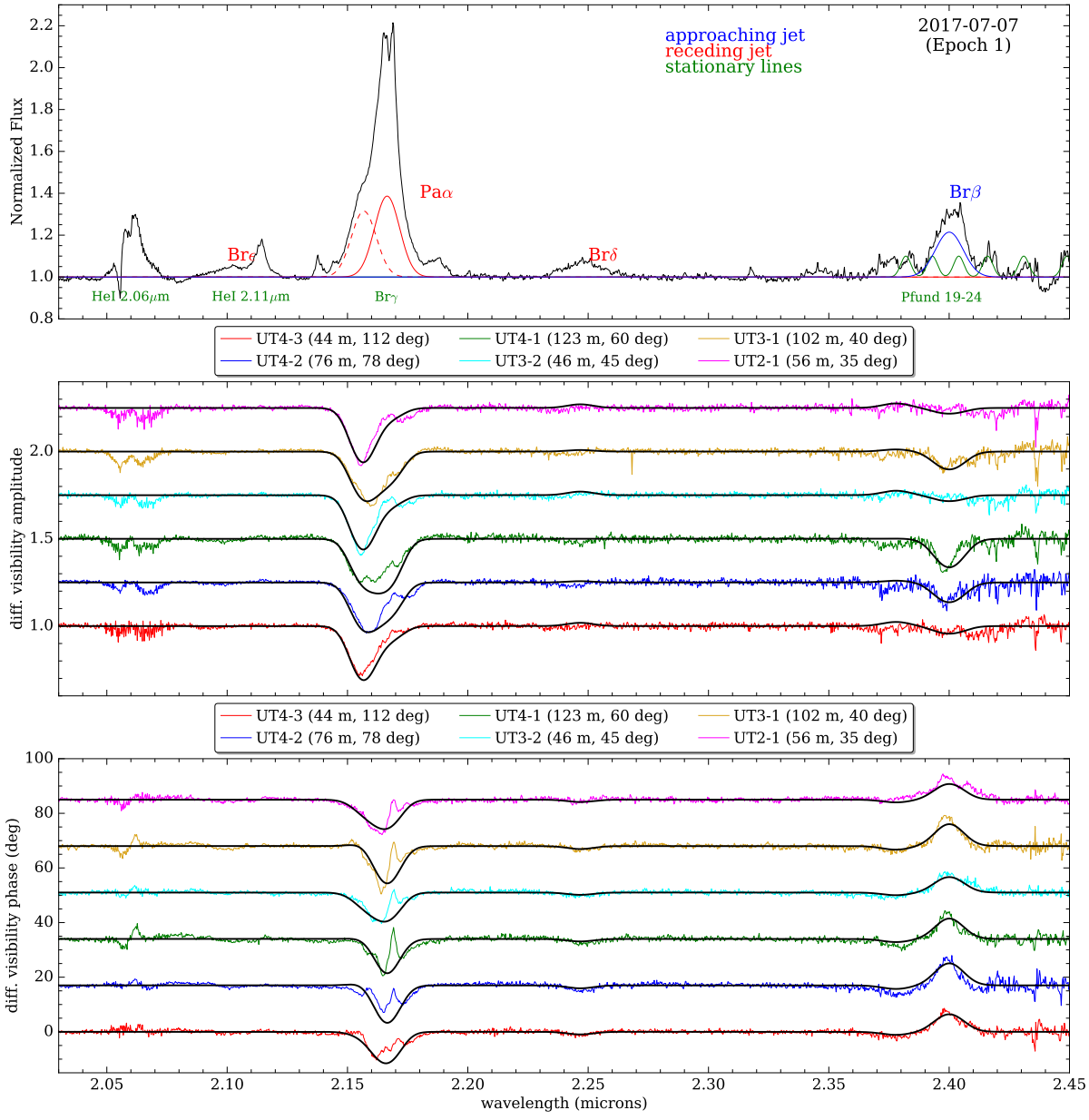

Figure 6.10: Data and best-fit jet model for the 2017 Epoch 1 GRAVITY observation.

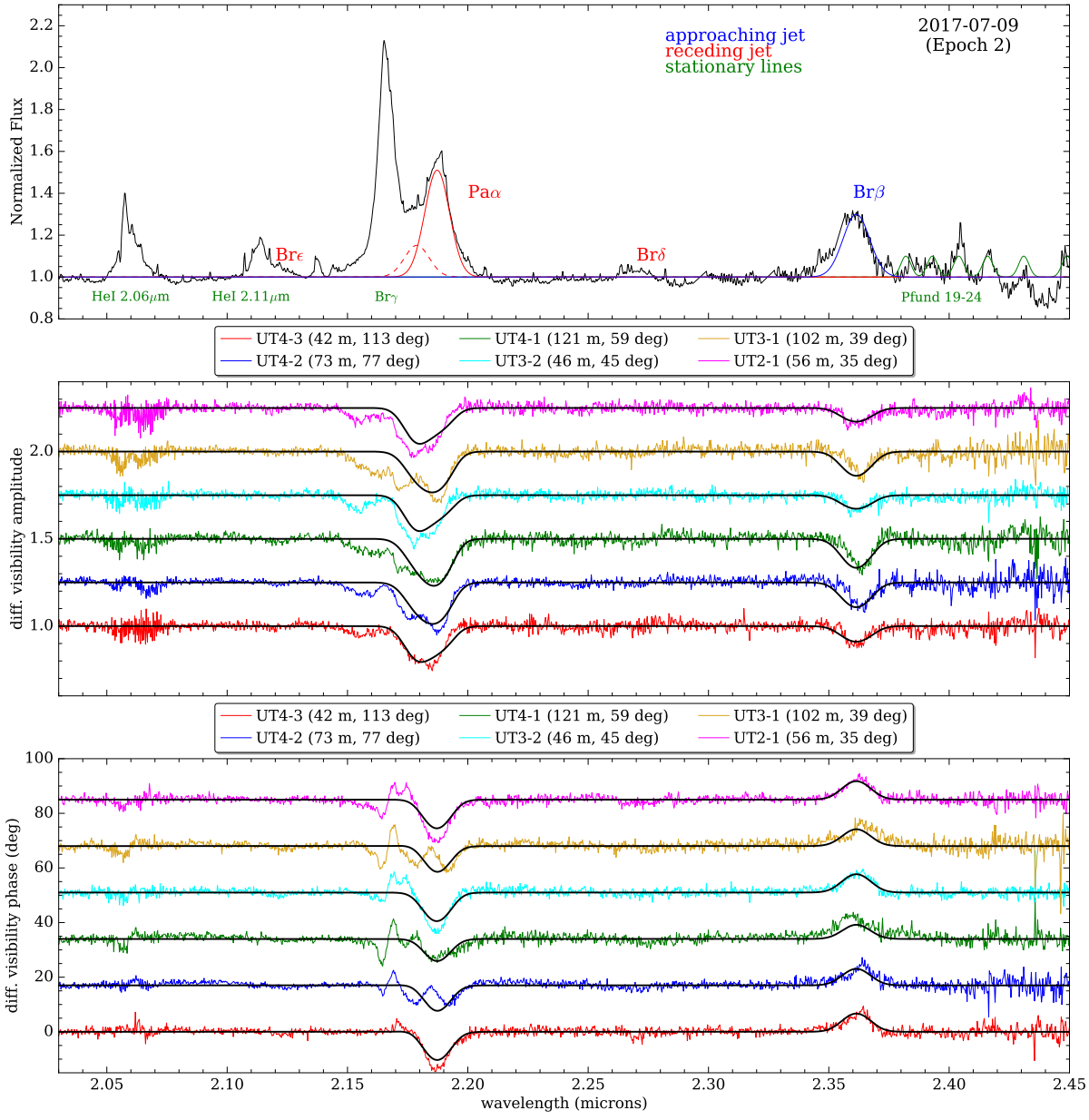

Figure 6.11: Data and best-fit jet model for the 2017 Epoch 2 GRAVITY observation.

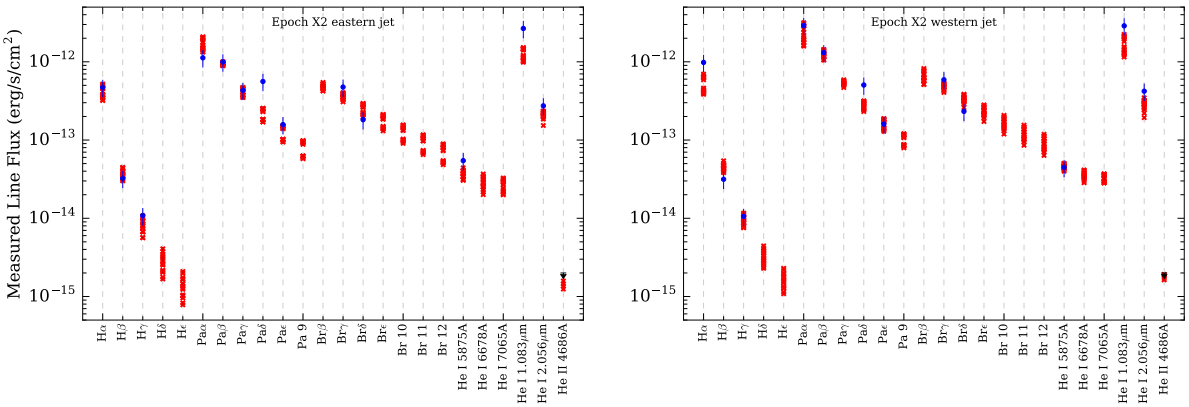

Figure 6.12: Data and best-fit models for Epoch 2 of the XSHOOTER observations.

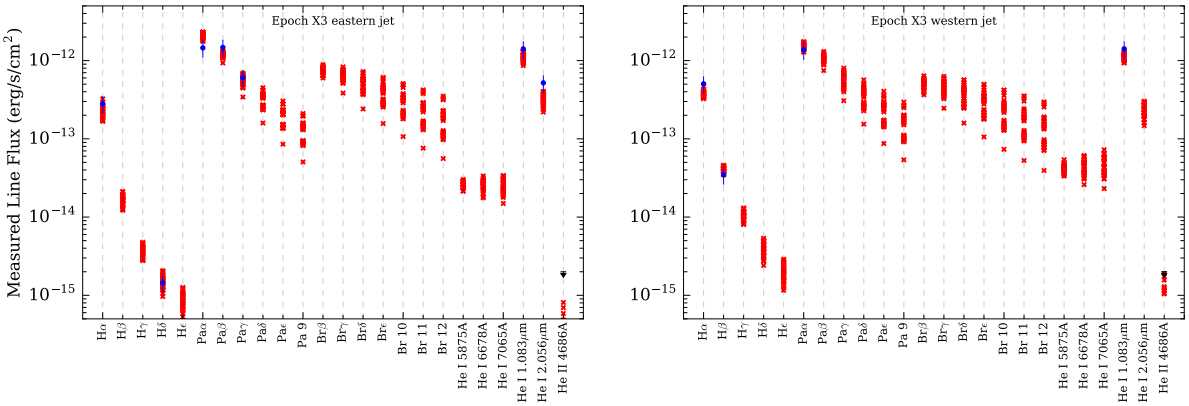

Figure 6.13: Data and best-fit models for Epoch 3 of the XSHOOTER observations.

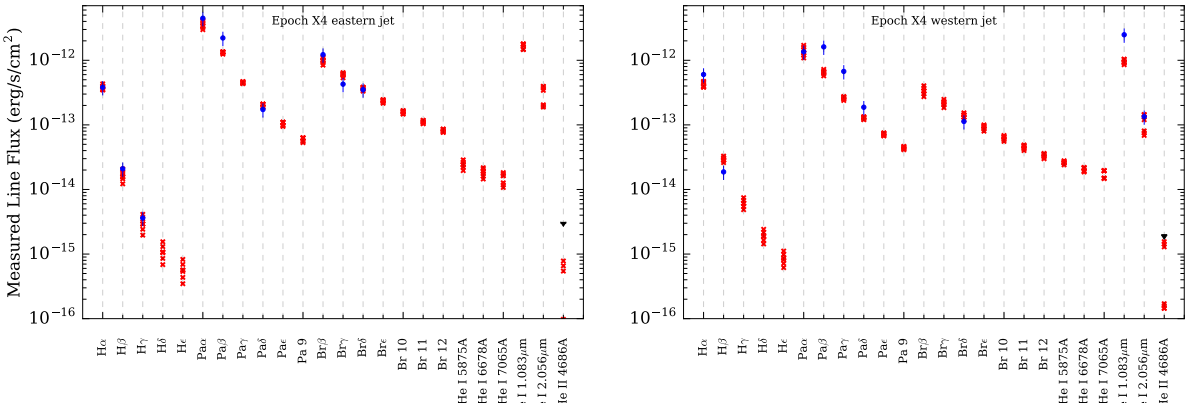

Figure 6.14: Data and best-fit models for Epoch 4 of the XSHOOTER observations.

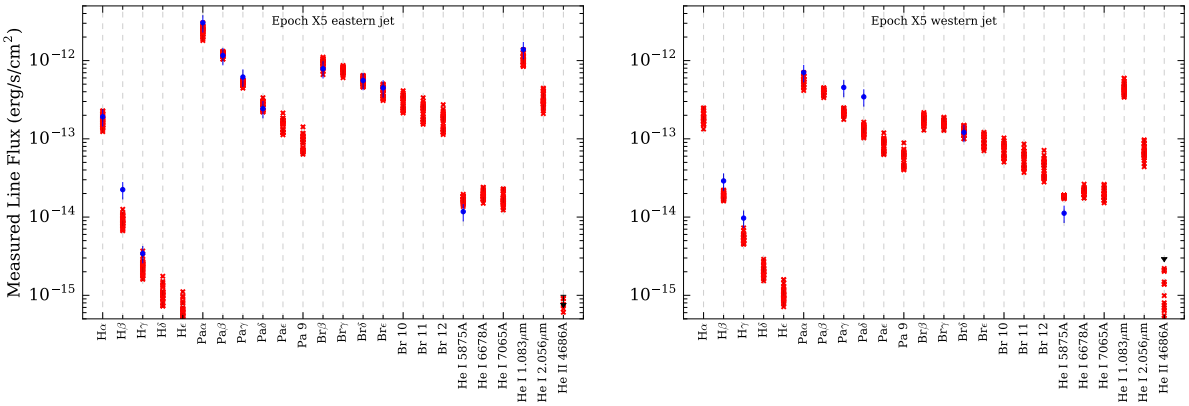

Figure 6.15: Data and best-fit models for Epoch 5 of the XSHOOTER observations.

Chapter 7

Conclusion and Outlook

In this section we provide an outlook for the future work related to the topics in this thesis.

7.1 The Galactic Center

Transitioning to the era of dual-field

Starting in 2019, the separation between S2 and SgrA* has become large enough so that single-field techniques (such as the binary interferometric model presented in Chapter 2) are becoming less applicable. It is then necessary to transition to the envisioned mode of dual-field operation, in which the visibility phases (also referred to as imaging phase) are used obtain the astrometric separation. This mode has the advantage that the model is much simpler (a single point source, so that the phase difference is directly translatable to a separation), but the disadvantage that the visibility phase is more susceptible to systematic errors (such as metrology or fiber dispersion related errors) than the more canonical interferometric quantities of squared visibilities and closure phases used in the single-field approach. Still, the fact that SgrA* is almost always bright enough to be detected (and often flares) means that the dual-field separation between S2 and SgrA* can be computed directly, without referencing to the fringe-tracker star as originally envisioned (and whose structure/motion would have to be included in the model).

Schwarzschild precession with S2

The next relativistic effect expected to be detected in the orbit of S2 is the Schwarzschild precession. Unlike the gravitational redshift (Gravity Collaboration et al., 2018a) which peaks during periastron passage, the astrometric deviation caused by the precession slowly grows and will be maximum during apastron near 2026. However, a significant detection of the effect by GRAVITY is already expected towards the end of 2019. This monitoring should also provide constraints on a potential cluster of compact objects inside of S2's orbit, which would induce Newtonian perturbations that counteract the expected general relativistic effect (e.g. Rubilar and Eckart, 2001; Merritt et al., 2010), or the presence of a

potential intermediate mass black hole, which could induce more localized astrometric and redshift perturbations (e.g. Gualandris et al., 2010).

Finding closer stars

The fact that the separation S2-SgrA* was small enough during the first years of GRAVITY observations has been very advantageous, insofar as allowing very precise astrometry through single-field binary fitting (Chapter 2) during a crucial part of the orbit (periastron passage). However, a side effect of the very bright S2 in the field is that the detection of faint stars is made more difficult, since the visibility signal is completely dominated by the binary S2-SgrA*. Even when S2 was far enough away for its flux to be attenuated, the associated field effects due to bandwidth smearing lead to systematic errors that have limited the faintest object that can be detected. In addition, traditional model-independent image reconstruction is complicated by the fact that SgrA* is very variable, which limits the uv coverage that can be effectively achieved, and which also introduces residuals in the reconstructed images.

The GRAVITY data collected so far have excluded the presence of additional stars in the central ~ 50 mas brighter than $m_K \approx 18$ (Gravity Collaboration et al., 2017, 2018a), but have not been able to probe the limit $18 \lesssim m_K \lesssim 19$ where one star is expected (Chapter 3). As S2 moves away along its orbit, it will become progressively easier to detect such a star, as it would form a binary with SgrA* itself, with a strongerflux ratio when SgrA* is fainter. Depending on the dynamic range that can be achieved by GRAVITY in such conditions, even fainter $m_K \approx 20$ stars might be eventually detected. The stacking of frames required to go deeper would still suffer from a variable SgrA*, so that imaging techniques to overcome that could still be needed.

Measuring spin

If such a faint star on a closer orbit is found, the main goal would be to use it to constrain the black hole spin through Lense-Thirring precession. However, as we show in Chapter 3, even if an astrometric precision of $10 - 100\mu$as is achievable, the probability that such a star would allow a significant detection of spin within a realistic astrometric campaign of duration $\lesssim 10$ years is low ($\sim 10\%$). If radial velocity measurements with precision ~ 50 km/s are available in addition, this probability only doubles. Therefore, barring a significant amount of luck regarding the black hole spin orientation and orbital parameters of such a star, additional data would be needed to measure the black hole spin. A promising option would be to combine the astrometry provided by GRAVITY with extremely precise radial velocity measurements potentially achievable by the next generation of extremely large optical telescopes (ELTs). The required precision in radial velocities to probe the black hole spin with stars on close ($P \sim 1$ year) orbits (rather than only to better constrain the orbital parameters, as used in Chapter 3) is $\sim 1 - 10$ km/s (e.g. Zhang et al., 2015; Yu et al., 2016). Although very challenging, this could be achievable if such faint stars are

of late-type, since they contain a much richer spectrum of narrow absorption lines in the NIR than early-type stars such as S2.

Towards a test of the no-hair theorem

A test of the no-hair theorem in the Galactic Center would require the measurement not only of the spin, but also of the quadrupole moment of SgrA*. The effect of the latter on even very short-period stellar orbits is too small to be detected with current or near-future facilities (e.g. Will, 2008; Merritt et al., 2010). On the other hand, the shape and size of the black hole shadow carry information about the spin and the quadrupole moment of the metric (Johannsen, 2012), but cannot disentangle the two (measuring these quantities from the size of the shadow also requires precise knowledge on $\frac{M}{D}$, which is only available for the Galactic Center from stellar orbits (e.g. Gravity Collaboration et al., 2019)). Therefore, there is still hope for testing the no-hair theorem by combining a spin measurement from stellar orbits (which are practically insensitive to quadrupole moment) with constraints on the size and shape of the black hole shadow, which could potentially be imaged using millimeter wavelength very long baseline interferometry with the Event Horizon Telescope (e.g. Falcke et al., 2000; Psaltis et al., 2016; Event Horizon Telescope Collaboration et al., 2019a).

Flare collection

The astrometric tracking of NIR SgrA* flares with GRAVITY has already revealed orbital-like motion close to the ISCO of the black hole (Gravity Collaboration et al., 2018b), with a consistent spatial scale and clockwise motion direction, and concomitant polarization measurements are promising for probing the magnetic field structure in the inner regions of the accretion flow. Over the years, as more flares are collected and the astrometric precision increases, they will continue to probe the accretion flow and spacetime structure close to the event horizon; they may, for instance, reveal different flavors of flaring mechanisms, or even provide constraints on the black hole spin if orbital motion is seen closer to the black hole than allowed by a zero-spin metric.

7.2 X-ray Binaries

BP Cru

The GRAVITY observations of BP Cru (Chapter 4) have revealed an extended wind emission that is significantly distorted and asymmetric through spectral differential interferometry. While it is natural to attribute the deviations from spherical symmetry to the gravitational and radiation influence of the pulsar, the latter must be disentangled from natural variability in the stellar wind, which is difficult to do with a single observation. This can be done with observations of isolated blue hypergiants with spectral type similar

to that of the donor star in BP Cru. GRAVITY observations of a couple such stars have been obtained with the Auxiliary Telescopes (ATs), and preliminary results indeed show that the level of asymmetry of the wind in BP Cru is higher compared to isolated hypergiants. Another approach is to compare observations at different orbital phases: due to the unusually high eccentricity of the system ($e \approx 0.5$), the distance between the accretor and the donor star varies substantially, which should induce differences in the spatial profile of the wind should it be significantly affected by the pulsar. Although BP Cru is a very special system for spectral differential interferometry because of the very high mass-loss rate of the hypergiant donor star producing strong emission lines, a similar analysis can be applied to other wind-accreting High-mass X-ray binaries, especially as the sensitivity of the instrument improves.

SS 433

The GRAVITY observations have revealed a complex and variable spatial morphology to the emission lines in SS 433. The stationary emission line of Brγ changed from a bipolar-dominated to an equatorial-dominated outflow for observations spaced by one year (Chapter 5). Given the importance of these outflows to the evolution of the binary, it is important to understand the cadence of these changes with more observations. For instance, the mass and angular momentum loss through the outflows can be used, together with the stability of the orbital period, to constrain the mass ratio of the binary (e.g. Cherepashchuk et al., 2019), which is crucial when trying to determine the elusive nature of the compact object. The mechanism driving the super-Keplerian equatorial outflows is also unknown; while we suggest tidal torques between the binary and material lost through the outer Lagrangian points, they could also be driven from the outer parts of the accretion disk through magnetic torques, in which case they can be used to probe the accretion process in a hypercritical disk. Because the outflows can be seen in both the NIR and in radio, this is a rare opportunity for synergetic optical and radio interferometric observations.

Also the optical jets of SS 433 offer opportunity for further studies. The GRAVITY observations presented in Chapter 6 have for the first time shown evidence for spatial changes in the emission profile within consecutive nights, but detecting optical jet motion within a single night, which is necessary to disentangle the motion of individual components from newly ejected ones at a close redshift, has remained elusive because of the shortness ($\lesssim 3$ hrs) of the observations. Longer GRAVITY observations, which could be up to 8 hrs in the most suitable months, would both (i) detect the spatial evolution of the jets throughout a night, and (ii) increase the uv coverage so that model-independent image reconstruction of the jet emission could become possible. As we show in Chapter 6, the optical jets can reveal information about the collimated radiation which is otherwise invisible to observers on Earth, and which in turn is crucial to probe the energetics close to the compact object where the jets are launched and collimated. For instance, one of the most mysterious questions about SS 433 relates to the mechanism that controls the speed of jets to always be near the value $0.26c$. The only mechanism so far proposed that explains this specific

jet velocity, line-locking to hydrogenic ions (Milgrom, 1979; Shapiro et al., 1986), requires very intense collimated radiation in the funnel.

Finally, the XSHOOTER observations also contain an unprecedented wealth of information on the stationary lines of SS 433, which are key to securing the elusive nature of the compact object. To that goal, we have obtained follow-up XSHOOTER observations of SS 433, which are currently under analysis. The behavior of the emission and absorption lines during eclipse is particularly useful to determine their origin (accretion disk, donor star or extended outflows); in particular, the XSHOOTER observations offer for the first time simultaneous monitoring of the He II 4686Å line, the absorption lines and the higher-order Paschen and Brackett lines, which have given conflicting results in the past (e.g. Fabrika and Bychkova, 1990; Blundell et al., 2008; Kubota et al., 2010; Robinson et al., 2017).

Another idea: astrometry

The X-ray binary work in this thesis has focused on single-field observations with the goal of studying the morphology of inflows/outflows on a scale comparable to the binary orbit. Another science case relates to very precise astrometry $\sim 10-100\mu$as to monitor the orbit of the donor star or centroid shifts due to variability in the emission of the compact object. Astrometry would require a nearby bright object that could be used for phase-referencing. The current limit on the separation between the FT and SC objects ($\lesssim 4$"), however, is too small for nearly all X-ray binaries, so a substantial improvement on the allowed separation is needed for this technique to be applied ubiquitously.

On the one hand, for X-ray binaries in which the NIR light is completely dominated by the donor star (e.g. most High-mass X-ray binaries), $10-100\mu$as precision astrometry of the orbit of the donor star could allow measuring the mass of the neutron star companion to precisions $\lesssim 10\%$ (e.g. Tomsick and Muterspaugh, 2010), helping to constrain the NS equation of state (EOS). For Low-mass X-ray binaries, which typically contain a black hole, an astrometric shift in the NIR centroid during state transitions (due to e.g. to the appearance of an NIR jet component in the hard state) could also potentially be detected with optical interferometry (original idea: S. Markoff, D. Russell).

Bibliography

B. P. Abbott, R. Abbott, T. D. Abbott, M. R. Abernathy, F. Acernese, K. Ackley, C. Adams, T. Adams, P. Addesso, R. X. Adhikari, and et al. Observation of Gravitational Waves from a Binary Black Hole Merger. *Physical Review Letters*, 116(6): 061102, February 2016. doi: 10.1103/PhysRevLett.116.061102.

D. K. Aitken, J. Greaves, A. Chrysostomou, T. Jenness, W. Holland, J. H. Hough, D. Pierce-Price, and J. Richer. Detection of Polarized Millimeter and Submillimeter Emission from Sagittarius A*. ApJ, 534:L173–L176, May 2000. doi: 10.1086/312685.

T. Alexander. Stellar processes near the massive black hole in the Galactic center [review article]. Phys. Rep., 419:65–142, November 2005. doi: 10.1016/j.physrep.2005.08.002.

T. Alexander and C. Hopman. Strong Mass Segregation Around a Massive Black Hole. ApJ, 697:1861–1869, June 2009. doi: 10.1088/0004-637X/697/2/1861.

D. A. Allen. Infrared observations of SS433. Nature, 281:284–285, September 1979. doi: 10.1038/281284a0.

P. Amaro-Seoane and M. Preto. The impact of realistic models of mass segregation on the event rate of extreme-mass ratio inspirals and cusp re-growth. *Classical and Quantum Gravity*, 28(9):094017, May 2011. doi: 10.1088/0264-9381/28/9/094017.

A. Amorim, M. Bauböck, J. P. Berger, W. Brandner, Y. Clénet, V. Coudé Du Foresto, P. T. de Zeeuw, J. Dexter, G. Duvert, M. Ebert, A. Eckart, F. Eisenhauer, N. M. Förster Schreiber, P. Garcia, F. Gao, E. Gendron, R. Genzel, S. Gillessen, M. Habibi, X. Haubois, T. Henning, S. Hippler, M. Horrobin, Z. Hubert, A. Jiménez Rosales, L. Jocou, P. Kervella, S. Lacour, V. Lapeyrère, J.-B. Le Bouquin, P. Léna, T. Ott, T. Paumard, K. Perraut, G. Perrin, O. Pfuhl, S. Rabien, G. Rodríguez-Coira, G. Rousset, S. Scheithauer, A. Sternberg, O. Straub, C. Straubmeier, E. Sturm, L. J. Tacconi, F. Vincent, S. von Fellenberg, I. Waisberg, F. Widmann, E. Wieprecht, E. Wiezorrek, S. Yazici, and Gravity Collaboration. Test of the Einstein Equivalence Principle near the Galactic Center Supermassive Black Hole. *Physical Review Letters*, 122(10):101102, March 2019. doi: 10.1103/PhysRevLett.122.101102.

R. Angélil and P. Saha. Relativistic Redshift Effects and the Galactic-Center Stars. ApJ, 711:157–163, March 2010. doi: 10.1088/0004-637X/711/1/157.

R. Angélil, P. Saha, and D. Merritt. Toward Relativistic Orbit Fitting of Galactic Center Stars and Pulsars. ApJ, 720:1303–1310, September 2010. doi: 10.1088/0004-637X/720/2/1303.

N. Anugu, A. Amorim, P. Gordo, F. Eisenhauer, O. Pfuhl, M. Haug, E. Wieprecht, E. Wiezorrek, J. Lima, G. Perrin, W. Brandner, C. Straubmeier, J.-B. Le Bouquin, and P. J. V. Garcia. Methods for multiple-telescope beam imaging and guiding in the near-infrared. MNRAS, 476:459–469, May 2018. doi: 10.1093/mnras/sty223.

P. Artymowicz and S. H. Lubow. Dynamics of binary-disk interaction. 1: Resonances and disk gap sizes. ApJ, 421:651–667, February 1994. doi: 10.1086/173679.

F. K. Baganoff, M. W. Bautz, W. N. Brandt, G. Chartas, E. D. Feigelson, G. P. Garmire, Y. Maeda, M. Morris, G. R. Ricker, L. K. Townsley, and F. Walter. Rapid X-ray flaring from the direction of the supermassive black hole at the Galactic Centre. Nature, 413: 45–48, September 2001. doi: 10.1038/35092510.

C. A. L. Bailer-Jones, J. Rybizki, M. Fouesneau, G. Mantelet, and R. Andrae. Estimating Distance from Parallaxes. IV. Distances to 1.33 Billion Stars in Gaia Data Release 2. AJ, 156:58, August 2018. doi: 10.3847/1538-3881/aacb21.

R. M. Bandyopadhyay, T. Shahbaz, P. A. Charles, and T. Naylor. Infrared spectroscopy of low-mass X-ray binaries - II. MNRAS, 306:417–426, June 1999. doi: 10.1046/j.1365-8711.1999.02547.x.

J. M. Bardeen, W. H. Press, and S. A. Teukolsky. Rotating Black Holes: Locally Nonrotating Frames, Energy Extraction, and Scalar Synchrotron Radiation. ApJ, 178:347–370, December 1972. doi: 10.1086/151796.

H. Bartko, F. Martins, T. K. Fritz, R. Genzel, Y. Levin, H. B. Perets, T. Paumard, S. Nayakshin, O. Gerhard, T. Alexander, K. Dodds-Eden, F. Eisenhauer, S. Gillessen, L. Mascetti, T. Ott, G. Perrin, O. Pfuhl, M. J. Reid, D. Rouan, A. Sternberg, and S. Trippe. Evidence for Warped Disks of Young Stars in the Galactic Center. ApJ, 697: 1741–1763, June 2009. doi: 10.1088/0004-637X/697/2/1741.

H. Bartko, F. Martins, S. Trippe, T. K. Fritz, R. Genzel, T. Ott, F. Eisenhauer, S. Gillessen, T. Paumard, T. Alexander, K. Dodds-Eden, O. Gerhard, Y. Levin, L. Mascetti, S. Nayakshin, H. B. Perets, G. Perrin, O. Pfuhl, M. J. Reid, D. Rouan, M. Zilka, and A. Sternberg. An Extremely Top-Heavy Initial Mass Function in the Galactic Center Stellar Disks. ApJ, 708:834–840, January 2010. doi: 10.1088/0004-637X/708/1/834.

M. C. Begelman and M. J. Rees. The cauldron at the core of SS 433. MNRAS, 206: 209–220, January 1984. doi: 10.1093/mnras/206.1.209.

M. C. Begelman, C. L. Sarazin, S. P. Hatchett, C. F. McKee, and J. Arons. Beam models for SS 433. ApJ, 238:722–730, June 1980. doi: 10.1086/158029.

M. C. Begelman, A. R. King, and J. E. Pringle. The nature of SS433 and the ultraluminous X-ray sources. MNRAS, 370:399–404, July 2006. doi: 10.1111/j.1365-2966.2006.10469.x.

R. D. Blandford and D. G. Payne. Hydromagnetic flows from accretion discs and the production of radio jets. MNRAS, 199:883–903, June 1982. doi: 10.1093/mnras/199.4.883.

R. D. Blandford and R. L. Znajek. Electromagnetic extraction of energy from Kerr black holes. MNRAS, 179:433–456, May 1977. doi: 10.1093/mnras/179.3.433.

J. M. Blondin. The shadow wind in high-mass X-ray binaries. ApJ, 435:756–766, November 1994. doi: 10.1086/174853.

K. M. Blundell and M. G. Bowler. Symmetry in the Changing Jets of SS 433 and Its True Distance from Us. ApJ, 616:L159–L162, December 2004. doi: 10.1086/426542.

K. M. Blundell, A. J. Mioduszewski, T. W. B. Muxlow, P. Podsiadlowski, and M. P. Rupen. Images of an Equatorial Outflow in SS 433. ApJ, 562:L79–L82, November 2001. doi: 10.1086/324573.

K. M. Blundell, M. G. Bowler, and L. Schmidtobreick. Fluctuations and symmetry in the speed and direction of the jets of SS 433 on different timescales. A&A, 474:903–910, November 2007. doi: 10.1051/0004-6361:20077924.

K. M. Blundell, M. G. Bowler, and L. Schmidtobreick. SS 433: Observation of the Circumbinary Disk and Extraction of the System Mass. ApJ, 678:L47, May 2008. doi: 10.1086/588027.

G. Bodo, A. Ferrari, S. Massaglia, and K. Tsinganos. Acceleration and thermal instabilities in the jets of SS 433. A&A, 149:246–252, August 1985.

A. Boehle, A. M. Ghez, R. Schödel, L. Meyer, S. Yelda, S. Albers, G. D. Martinez, E. E. Becklin, T. Do, J. R. Lu, K. Matthews, M. R. Morris, B. Sitarski, and G. Witzel. An Improved Distance and Mass Estimate for Sgr A* from a Multistar Orbit Analysis. ApJ, 830:17, October 2016. doi: 10.3847/0004-637X/830/1/17.

H. Bondi and F. Hoyle. On the mechanism of accretion by stars. MNRAS, 104:273, 1944. doi: 10.1093/mnras/104.5.273.

N. V. Borisov and S. N. Fabrika. SS:433 Jet Parameters Derived from Simulated Moving-Line Profiles. *Soviet Astronomy Letters*, 13:200, May 1987.

G. C. Bower, W. M. Goss, H. Falcke, D. C. Backer, and Y. Lithwick. The Intrinsic Size of Sagittarius A* from 0.35 to 6 cm. ApJ, 648:L127–L130, September 2006. doi: 10.1086/508019.

M. G. Bowler. Interpretation of observations of the circumbinary disk of SS 433. A&A, 521:A81, October 2010. doi: 10.1051/0004-6361/201014711.

M. G. Bowler. SS 433: Two robust determinations fix the mass ratio. A&A, 619:L4, November 2018. doi: 10.1051/0004-6361/201834121.

V. Bozza and L. Mancini. Observing Gravitational Lensing Effects by Sgr A* with GRAVITY. ApJ, 753:56, July 2012. doi: 10.1088/0004-637X/753/1/56.

W. Brinkmann and N. Kawai. The jets of SS 433: second order effects. A&A, 363:640–646, November 2000.

W. Brinkmann, H. H. Fink, S. Massaglia, G. Bodo, and A. Ferrari. The thermal evolution of the jets in SS 433. A&A, 196:313–326, May 1988.

W. Brinkmann, N. Kawai, and M. Matsuoka. SS433 - The puzzle continues. A&A, 218: L13–L16, July 1989.

W. Brinkmann, T. Kotani, and N. Kawai. XMM-Newton observations of SS 433 I. EPIC spectral analysis. A&A, 431:575–586, February 2005. doi: 10.1051/0004-6361:20041768.

A. E. Broderick and A. Loeb. Imaging optically-thin hotspots near the black hole horizon of Sgr A* at radio and near-infrared wavelengths. MNRAS, 367:905–916, April 2006. doi: 10.1111/j.1365-2966.2006.10152.x.

A. E. Broderick, V. L. Fish, S. S. Doeleman, and A. Loeb. Estimating the Parameters of Sagittarius A*'s Accretion Flow Via Millimeter VLBI. ApJ, 697:45–54, May 2009. doi: 10.1088/0004-637X/697/1/45.

J. C. Brown, J. P. Cassinelli, and G. W. Collins, II. Constraints on the physical properties of optical bullets in SS 433. ApJ, 378:307–314, September 1991. doi: 10.1086/170432.

R. M. Buchholz, R. Schödel, and A. Eckart. Composition of the galactic center star cluster. Population analysis from adaptive optics narrow band spectral energy distributions. A&A, 499:483–501, May 2009. doi: 10.1051/0004-6361/200811497.

D. F. Buscher and F. b. M. Longair. *Practical Optical Interferometry*. July 2015.

J. A. Cardelli, G. C. Clayton, and J. S. Mathis. The relationship between infrared, optical, and ultraviolet extinction. ApJ, 345:245–256, October 1989. doi: 10.1086/167900.

B. C. Carlson. A table of elliptic integrals. *Mathematics of Computation*, 59:165–180, July 1992. doi: 10.1090/S0025-5718-1992-1134720-4.

B. Carter. Global Structure of the Kerr Family of Gravitational Fields. *Physical Review*, 174:1559–1571, October 1968. doi: 10.1103/PhysRev.174.1559.

J. I. Castor, D. C. Abbott, and R. I. Klein. Radiation-driven winds in Of stars. ApJ, 195: 157–174, January 1975. doi: 10.1086/153315.

P. A. Charles and M. J. Coe. *Optical, ultraviolet and infrared observations of X-ray binaries*, pages 215–265. April 2006.

S. Chaty. Nature, Formation, and Evolution of High Mass X-Ray Binaries. In L. Schmidtobreick, M. R. Schreiber, and C. Tappert, editors, *Evolution of Compact Binaries*, volume 447 of *Astronomical Society of the Pacific Conference Series*, page 29, September 2011.

A. Chelli, G. Duvert, L. Bourgès, G. Mella, S. Lafrasse, D. Bonneau, and O. Chesneau. Pseudomagnitudes and differential surface brightness: Application to the apparent diameter of stars. A&A, 589:A112, May 2016. doi: 10.1051/0004-6361/201527484.

WenCong Chen and QingGuo Zeng. Circumbinary disk, an efficient medium extracting orbital angular momentum in close binaries. *Chinese Science Bulletin*, 54(5):711–718, Mar 2009. ISSN 1861-9541. doi: 10.1007/s11434-009-0034-5. URL `https://doi.org/10.1007/s11434-009-0034-5`.

A. M. Cherepashchuk, K. A. Postnov, and A. A. Belinski. On masses of the components in SS433. MNRAS, 479:4844–4848, October 2018. doi: 10.1093/mnras/sty1853.

A. M. Cherepashchuk, K. A. Postnov, and A. A. Belinski. Mass ratio in SS433 revisited. MNRAS, 485:2638–2641, May 2019. doi: 10.1093/mnras/stz610.

O. Chesneau, L. Dessart, D. Mourard, P. Bério, C. Buil, D. Bonneau, M. Borges Fernandes, J. M. Clausse, O. Delaa, A. Marcotto, A. Meilland, F. Millour, N. Nardetto, K. Perraut, A. Roussel, A. Spang, P. Stee, I. Tallon-Bosc, H. McAlister, T. ten Brummelaar, J. Sturmann, L. Sturmann, N. Turner, C. Farrington, and P. J. Goldfinger. Time, spatial, and spectral resolution of the Hα line-formation region of Deneb and Rigel with the VEGA/CHARA interferometer. A&A, 521:A5, October 2010. doi: 10.1051/0004-6361/201014509.

O. Chesneau, A. Kaufer, O. Stahl, C. Colvinter, A. Spang, L. Dessart, R. Prinja, and R. Chini. The variable stellar wind of Rigel probed at high spatial and spectral resolution. A&A, 566:A125, June 2014. doi: 10.1051/0004-6361/201322894.

É. Choquet, P. Kervella, J.-B. Le Bouquin, A. Mérand, J.-P. Berger, X. Haubois, G. Perrin, P.-O. Petrucci, B. Lazareff, and J.-U. Pott. The close environment of high-mass X-ray binaries at high angular resolution. I. VLTI/AMBER and VLTI/PIONIER near-infrared interferometric observations of ¡ASTROBJ¿Vela X-1¡/ASTROBJ¿. A&A, 561: A46, January 2014. doi: 10.1051/0004-6361/201321977.

D. H. Clark and P. Murdin. An unusual emission-line star/X-ray source/radio star, possibly associated with an SNR. Nature, 276:44, November 1978. doi: 10.1038/276044a0.

J. S. Clark, P. A. Charles, W. I. Clarkson, and M. J. Coe. Near IR spectroscopy of the X-ray binary ¡ASTROBJ¿Circinus X-1¡/ASTROBJ¿. A&A, 400:655–658, March 2003. doi: 10.1051/0004-6361:20030017.

J. S. Clark, F. Najarro, I. Negueruela, B. W. Ritchie, M. A. Urbaneja, and I. D. Howarth. On the nature of the galactic early-B hypergiants. A&A, 541:A145, May 2012. doi: 10.1051/0004-6361/201117472.

C. T. Cunningham and J. M. Bardeen. The Optical Appearance of a Star Orbiting an Extreme Kerr Black Hole. ApJ, 183:237–264, July 1973. doi: 10.1086/152223.

K. Davidson and R. McCray. SS 433 as a prototype of astrophysical jets. ApJ, 241: 1082–1089, November 1980. doi: 10.1086/158423.

K. Davidson and J. P. Ostriker. Neutron-Star Accretion in a Stellar Wind: Model for a Pulsed X-Ray Source. ApJ, 179:585–598, January 1973. doi: 10.1086/151897.

J. Dexter and E. Agol. A Fast New Public Code for Computing Photon Orbits in a Kerr Spacetime. ApJ, 696:1616–1629, May 2009. doi: 10.1088/0004-637X/696/2/1616.

J. Dexter and R. M. O'Leary. The Peculiar Pulsar Population of the Central Parsec. ApJ, 783:L7, March 2014. doi: 10.1088/2041-8205/783/1/L7.

J. Dexter, E. Agol, and P. C. Fragile. Millimeter Flares and VLBI Visibilities from Relativistic Simulations of Magnetized Accretion Onto the Galactic Center Black Hole. ApJ, 703:L142–L146, October 2009. doi: 10.1088/0004-637X/703/2/L142.

T. Do, A. M. Ghez, M. R. Morris, J. R. Lu, K. Matthews, S. Yelda, and J. Larkin. High Angular Resolution Integral-Field Spectroscopy of the Galaxy's Nuclear Cluster: A Missing Stellar Cusp? ApJ, 703:1323–1337, October 2009. doi: 10.1088/0004-637X/703/2/1323.

T. Do, A. Hees, A. Dehghanfar, A. Ghez, and S. Wright. Measuring the effects of General Relativity at the Galactic Center with Future Extremely Large Telescopes. *ArXiv e-prints*, November 2017.

S. S. Doeleman, J. Weintroub, A. E. E. Rogers, R. Plambeck, R. Freund, R. P. J. Tilanus, P. Friberg, L. M. Ziurys, J. M. Moran, B. Corey, K. H. Young, D. L. Smythe, M. Titus, D. P. Marrone, R. J. Cappallo, D. C.-J. Bock, G. C. Bower, R. Chamberlin, G. R. Davis, T. P. Krichbaum, J. Lamb, H. Maness, A. E. Niell, A. Roy, P. Strittmatter, D. Werthimer, A. R. Whitney, and D. Woody. Event-horizon-scale structure in the supermassive black hole candidate at the Galactic Centre. Nature, 455:78–80, September 2008. doi: 10.1038/nature07245.

S. S. Doeleman, V. L. Fish, A. E. Broderick, A. Loeb, and A. E. E. Rogers. Detecting Flaring Structures in Sagittarius A* with High-Frequency VLBI. ApJ, 695:59–74, April 2009. doi: 10.1088/0004-637X/695/1/59.

J. F. Dolan, P. T. Boyd, S. Fabrika, S. Tapia, V. Bychkov, A. A. Panferov, M. J. Nelson, J. W. Percival, G. W. van Citters, D. C. Taylor, and M. J. Taylor. SS 433 in the ultraviolet. A&A, 327:648–655, November 1997.

S. Doolin and K. M. Blundell. The Precession of SS433's Radio Ruff on Long Timescales. ApJ, 698:L23–L26, June 2009. doi: 10.1088/0004-637X/698/1/L23.

G. M. Dubner, M. Holdaway, W. M. Goss, and I. F. Mirabel. A High-Resolution Radio Study of the W50-SS 433 System and the Surrounding Medium. AJ, 116:1842–1855, October 1998. doi: 10.1086/300537.

A. Eckart and R. Genzel. Observations of stellar proper motions near the Galactic Centre. Nature, 383:415–417, October 1996. doi: 10.1038/383415a0.

S. S. Eikenberry, P. B. Cameron, B. W. Fierce, D. M. Kull, D. H. Dror, J. R. Houck, and B. Margon. Twenty Years of Timing SS 433. ApJ, 561:1027–1033, November 2001. doi: 10.1086/323380.

A. Einstein. Zur allgemeinen Relativitätstheorie. *Sitzungsberichte der Königlich Preußischen Akademie der Wissenschaften (Berlin), Seite 778-786.*, 1915.

F. Eisenhauer, R. Genzel, T. Alexander, R. Abuter, T. Paumard, T. Ott, A. Gilbert, S. Gillessen, M. Horrobin, S. Trippe, H. Bonnet, C. Dumas, N. Hubin, A. Kaufer, M. Kissler-Patig, G. Monnet, S. Ströbele, T. Szeifert, A. Eckart, R. Schödel, and S. Zucker. SINFONI in the Galactic Center: Young Stars and Infrared Flares in the Central Light-Month. ApJ, 628:246–259, July 2005. doi: 10.1086/430667.

F. Eisenhauer, G. Perrin, W. Brandner, C. Straubmeier, K. Perraut, A. Amorim, M. Schöller, S. Gillessen, P. Kervella, M. Benisty, C. Araujo-Hauck, L. Jocou, J. Lima, G. Jakob, M. Haug, Y. Clénet, T. Henning, A. Eckart, J.-P. Berger, P. Garcia, R. Abuter, S. Kellner, T. Paumard, S. Hippler, S. Fischer, T. Moulin, J. Villate, G. Avila, A. Gräter, S. Lacour, A. Huber, M. Wiest, A. Nolot, P. Carvas, R. Dorn, O. Pfuhl, E. Gendron, S. Kendrew, S. Yazici, S. Anton, Y. Jung, M. Thiel, É. Choquet, R. Klein, P. Teixeira, P. Gitton, D. Moch, F. Vincent, N. Kudryavtseva, S. Ströbele, S. Sturm, P. Fédou, R. Lenzen, P. Jolley, C. Kister, V. Lapeyrère, V. Naranjo, C. Lucuix, R. Hofmann, F. Chapron, U. Neumann, L. Mehrgan, O. Hans, G. Rousset, J. Ramos, M. Suarez, R. Lederer, J.-M. Reess, R.-R. Rohloff, P. Haguenauer, H. Bartko, A. Sevin, K. Wagner, J.-L. Lizon, S. Rabien, C. Collin, G. Finger, R. Davies, D. Rouan, M. Wittkowski, K. Dodds-Eden, D. Ziegler, F. Cassaing, H. Bonnet, M. Casali, R. Genzel, and P. Lena. GRAVITY: Observing the Universe in Motion. *The Messenger*, 143:16–24, March 2011.

Y. Evangelista, M. Feroci, E. Costa, E. Del Monte, I. Donnarumma, I. Lapshov, F. Lazzarotto, L. Pacciani, M. Rapisarda, P. Soffitta, A. Argan, G. Barbiellini, F. Boffelli, A. Bulgarelli, P. Caraveo, P. W. Cattaneo, A. Chen, F. D'Ammando, G. Di Cocco, F. Fuschino, M. Galli, F. Gianotti, A. Giuliani, C. Labanti, P. Lipari, F. Longo,

M. Marisaldi, S. Mereghetti, E. Moretti, A. Morselli, A. Pellizzoni, F. Perotti, G. Piano, P. Picozza, M. Pilia, M. Prest, G. Pucella, A. Rappoldi, S. Sabatini, E. Striani, M. Tavani, M. Trifoglio, A. Trois, E. Vallazza, S. Vercellone, V. Vittorini, A. Zambra, L. A. Antonelli, S. Cutini, C. Pittori, B. Preger, P. Santolamazza, F. Verrecchia, P. Giommi, and L. Salotti. Temporal Properties of GX 301-2 Over a Year-long Observation with SuperAGILE. ApJ, 708:1663–1673, January 2010. doi: 10.1088/0004-637X/708/2/1663.

Event Horizon Telescope Collaboration, K. Akiyama, A. Alberdi, W. Alef, K. Asada, R. Azulay, A.-K. Baczko, D. Ball, M. Baloković, J. Barrett, and et al. First M87 Event Horizon Telescope Results. I. The Shadow of the Supermassive Black Hole. ApJ, 875: L1, April 2019a. doi: 10.3847/2041-8213/ab0ec7.

Event Horizon Telescope Collaboration, K. Akiyama, A. Alberdi, W. Alef, K. Asada, R. Azulay, A.-K. Baczko, D. Ball, M. Baloković, J. Barrett, and et al. First M87 Event Horizon Telescope Results. VI. The Shadow and Mass of the Central Black Hole. ApJ, 875:L6, April 2019b. doi: 10.3847/2041-8213/ab1141.

A. C. Fabian and M. J. Rees. SS 433 - A double jet in action. MNRAS, 187:13P–16P, April 1979. doi: 10.1093/mnras/187.1.13P.

A. C. Fabian, M. J. Rees, L. Stella, and N. E. White. X-ray fluorescence from the inner disc in Cygnus X-1. MNRAS, 238:729–736, May 1989. doi: 10.1093/mnras/238.3.729.

S. Fabrika. The jets and supercritical accretion disk in SS433. *Astrophysics and Space Physics Reviews*, 12:1–152, 2004.

S. Fabrika, Y. Ueda, A. Vinokurov, O. Sholukhova, and M. Shidatsu. Supercritical accretion disks in ultraluminous X-ray sources and SS 433. *Nature Physics*, 11:551–553, July 2015. doi: 10.1038/nphys3348.

S. N. Fabrika. An extended disc around SS 433. MNRAS, 261:241–245, March 1993. doi: 10.1093/mnras/261.2.241.

S. N. Fabrika and N. V. Borisov. Parameters of the SS:433 Jets - Interpretation of the Results. *Soviet Astronomy Letters*, 13:279, July 1987.

S. N. Fabrika and L. V. Bychkova. The mass function of SS 433. A&A, 240:L5–L7, December 1990.

S. N. Fabrika and O. Sholukhova. SS433 as ultraluminous UV source. Comparison with ULXs. In *Microquasars and Beyond*, page 52, 2008.

H. Falcke and S. Markoff. The jet model for Sgr A*: Radio and X-ray spectrum. A&A, 362:113–118, October 2000.

H. Falcke, F. Melia, and E. Agol. Viewing the Shadow of the Black Hole at the Galactic Center. ApJ, 528:L13–L16, January 2000. doi: 10.1086/312423.

G. J. Ferland, R. L. Porter, P. A. M. van Hoof, R. J. R. Williams, N. P. Abel, M. L. Lykins, G. Shaw, W. J. Henney, and P. C. Stancil. The 2013 Release of Cloudy. Rev. Mexicana Astron. Astrofis., 49:137–163, April 2013.

G. J. Ferland, M. Chatzikos, F. Guzmán, M. L. Lykins, P. A. M. van Hoof, R. J. R. Williams, N. P. Abel, N. R. Badnell, F. P. Keenan, R. L. Porter, and P. C. Stancil. The 2017 Release Cloudy. Rev. Mexicana Astron. Astrofis., 53:385–438, October 2017.

A. V. Filippenko, R. W. Romani, W. L. W. Sargent, and R. D. Blandford. Possible evidence for disk emission in SS 433. AJ, 96:242–250, July 1988. doi: 10.1086/114806.

V. L. Fish, M. D. Johnson, S. S. Doeleman, A. E. Broderick, D. Psaltis, R.-S. Lu, K. Akiyama, W. Alef, J. C. Algaba, K. Asada, C. Beaudoin, A. Bertarini, L. Blackburn, R. Blundell, G. C. Bower, C. Brinkerink, R. Cappallo, A. A. Chael, R. Chamberlin, C.-K. Chan, G. B. Crew, J. Dexter, M. Dexter, S. A. Dzib, H. Falcke, R. Freund, P. Friberg, C. H. Greer, M. A. Gurwell, P. T. P. Ho, M. Honma, M. Inoue, T. Johannsen, J. Kim, T. P. Krichbaum, J. Lamb, J. León-Tavares, A. Loeb, L. Loinard, D. MacMahon, D. P. Marrone, J. M. Moran, M. Mościbrodzka, G. N. Ortiz-León, T. Oyama, F. Özel, R. L. Plambeck, N. Pradel, R. A. Primiani, A. E. E. Rogers, K. Rosenfeld, H. Rottmann, A. L. Roy, C. Ruszczyk, D. L. Smythe, J. SooHoo, J. Spilker, J. Stone, P. Strittmatter, R. P. J. Tilanus, M. Titus, L. Vertatschitsch, J. Wagner, J. F. C. Wardle, J. Weintroub, D. Woody, M. Wright, P. Yamaguchi, A. Young, K. H. Young, J. A. Zensus, and L. M. Ziurys. Persistent Asymmetric Structure of Sagittarius A* on Event Horizon Scales. ApJ, 820:90, April 2016. doi: 10.3847/0004-637X/820/2/90.

D. Foreman-Mackey, D. W. Hogg, D. Lang, and J. Goodman. emcee: The MCMC Hammer. PASP, 125:306–312, March 2013. doi: 10.1086/670067.

P. C. Fragile and G. J. Mathews. Reconstruction of Stellar Orbits Close to Sagittarius A*: Possibilities for Testing General Relativity. ApJ, 542:328–333, October 2000. doi: 10.1086/309495.

M. Freitag, P. Amaro-Seoane, and V. Kalogera. Stellar Remnants in Galactic Nuclei: Mass Segregation. ApJ, 649:91–117, September 2006. doi: 10.1086/506193.

S. D. Friedman, D. G. York, B. J. McCall, J. Dahlstrom, P. Sonnentrucker, D. E. Welty, M. M. Drosback, L. M. Hobbs, B. L. Rachford, and T. P. Snow. Studies of Diffuse Interstellar Bands V. Pairwise Correlations of Eight Strong DIBs and Neutral Hydrogen, Molecular Hydrogen, and Color Excess. ApJ, 727:33, January 2011. doi: 10.1088/0004-637X/727/1/33.

T. K. Fritz, S. Chatzopoulos, O. Gerhard, S. Gillessen, R. Genzel, O. Pfuhl, S. Tacchella, F. Eisenhauer, and T. Ott. The Nuclear Cluster of the Milky Way: Total Mass and Luminosity. ApJ, 821:44, April 2016. doi: 10.3847/0004-637X/821/1/44.

Y. Fuchs, L. Koch Miramond, and P. Ábrahám. SS 433: a phenomenon imitating a Wolf-Rayet star. A&A, 445:1041–1052, January 2006. doi: 10.1051/0004-6361:20042160.

F. Fuerst, I. Kreykenbohm, P. Kretschmar, R. Ballhausen, and K. Pottschmidt. Detection of highly ionized iron during a giant flare of GX 301-2. *The Astronomer's Telegram*, 8870, March 2016.

E. Gallego-Cano, R. Schödel, H. Dong, F. Nogueras-Lara, A. T. Gallego-Calvente, P. Amaro-Seoane, and H. Baumgardt. The distribution of stars around the Milky Way's central black hole. I. Deep star counts. A&A, 609:A26, January 2018. doi: 10.1051/0004-6361/201730451.

R. Genzel, A. Eckart, T. Ott, and F. Eisenhauer. On the nature of the dark mass in the centre of the Milky Way. MNRAS, 291:219–234, October 1997. doi: 10.1093/mnras/291.1.219.

R. Genzel, R. Schödel, T. Ott, A. Eckart, T. Alexander, F. Lacombe, D. Rouan, and B. Aschenbach. Near-infrared flares from accreting gas around the supermassive black hole at the Galactic Centre. Nature, 425:934–937, October 2003a. doi: 10.1038/nature02065.

R. Genzel, R. Schödel, T. Ott, F. Eisenhauer, R. Hofmann, M. Lehnert, A. Eckart, T. Alexander, A. Sternberg, R. Lenzen, Y. Clénet, F. Lacombe, D. Rouan, A. Renzini, and L. E. Tacconi-Garman. The Stellar Cusp around the Supermassive Black Hole in the Galactic Center. ApJ, 594:812–832, September 2003b. doi: 10.1086/377127.

R. Genzel, F. Eisenhauer, and S. Gillessen. The Galactic Center massive black hole and nuclear star cluster. *Reviews of Modern Physics*, 82:3121–3195, October 2010. doi: 10.1103/RevModPhys.82.3121.

A. M. Ghez, B. L. Klein, M. Morris, and E. E. Becklin. High Proper-Motion Stars in the Vicinity of Sagittarius A*: Evidence for a Supermassive Black Hole at the Center of Our Galaxy. ApJ, 509:678–686, December 1998. doi: 10.1086/306528.

A. M. Ghez, G. Duchêne, K. Matthews, S. D. Hornstein, A. Tanner, J. Larkin, M. Morris, E. E. Becklin, S. Salim, T. Kremenek, D. Thompson, B. T. Soifer, G. Neugebauer, and I. McLean. The First Measurement of Spectral Lines in a Short-Period Star Bound to the Galaxy's Central Black Hole: A Paradox of Youth. ApJ, 586:L127–L131, April 2003. doi: 10.1086/374804.

A. M. Ghez, S. Salim, N. N. Weinberg, J. R. Lu, T. Do, J. K. Dunn, K. Matthews, M. R. Morris, S. Yelda, E. E. Becklin, T. Kremenek, M. Milosavljevic, and J. Naiman. Measuring Distance and Properties of the Milky Way's Central Supermassive Black Hole with Stellar Orbits. ApJ, 689:1044-1062, December 2008. doi: 10.1086/592738.

S. Gillessen, F. Eisenhauer, S. Trippe, T. Alexander, R. Genzel, F. Martins, and T. Ott. Monitoring Stellar Orbits Around the Massive Black Hole in the Galactic Center. ApJ, 692:1075–1109, February 2009. doi: 10.1088/0004-637X/692/2/1075.

S. Gillessen, P. M. Plewa, F. Eisenhauer, R. Sari, I. Waisberg, M. Habibi, O. Pfuhl, E. George, J. Dexter, S. von Fellenberg, T. Ott, and R. Genzel. An Update on Monitoring Stellar Orbits in the Galactic Center. ApJ, 837:30, March 2017. doi: 10.3847/1538-4357/aa5c41.

A. Glindemann. *Principles of Stellar Interferometry*. 2011. doi: 10.1007/978-3-642-15028-9.

V. Goranskij. Photometric Mass Estimate for the Compact Component of SS 433: And Yet It Is a Neutron Star. *Peremennye Zvezdy*, 31, October 2011.

V. P. Goranskij. Evidence of SS 433 Rapid Evolution. In Y. Y. Balega, D. O. Kudryavtsev, I. I. Romanyuk, and I. A. Yakunin, editors, *Stars: From Collapse to Collapse*, volume 510 of *Astronomical Society of the Pacific Conference Series*, page 466, June 2017.

Gravity Collaboration, R. Abuter, M. Accardo, A. Amorim, N. Anugu, G. Ávila, N. Azouaoui, M. Benisty, J. P. Berger, N. Blind, H. Bonnet, P. Bourget, W. Brandner, R. Brast, A. Buron, L. Burtscher, F. Cassaing, F. Chapron, É. Choquet, Y. Clénet, C. Collin, V. Coudé Du Foresto, W. de Wit, P. T. de Zeeuw, C. Deen, F. Delplancke-Ströbele, R. Dembet, F. Derie, J. Dexter, G. Duvert, M. Ebert, A. Eckart, F. Eisenhauer, M. Esselborn, P. Fédou, G. Finger, P. Garcia, C. E. Garcia Dabo, R. Garcia Lopez, E. Gendron, R. Genzel, S. Gillessen, F. Gonte, P. Gordo, M. Grould, U. Grözinger, S. Guieu, P. Haguenauer, O. Hans, X. Haubois, M. Haug, F. Haussmann, T. Henning, S. Hippler, M. Horrobin, A. Huber, Z. Hubert, N. Hubin, C. A. Hummel, G. Jakob, A. Janssen, L. Jochum, L. Jocou, A. Kaufer, S. Kellner, S. Kendrew, L. Kern, P. Kervella, M. Kiekebusch, R. Klein, Y. Kok, J. Kolb, M. Kulas, S. Lacour, V. Lapeyrère, B. Lazareff, J.-B. Le Bouquin, P. Lèna, R. Lenzen, S. Lévêque, M. Lippa, Y. Magnard, L. Mehrgan, M. Mellein, A. Mérand, J. Moreno-Ventas, T. Moulin, E. Müller, F. Müller, U. Neumann, S. Oberti, T. Ott, L. Pallanca, J. Panduro, L. Pasquini, T. Paumard, I. Percheron, K. Perraut, G. Perrin, A. Pflüger, O. Pfuhl, T. Phan Duc, P. M. Plewa, D. Popovic, S. Rabien, A. Ramírez, J. Ramos, C. Rau, M. Riquelme, R.-R. Rohloff, G. Rousset, J. Sanchez-Bermudez, S. Scheithauer, M. Schöller, N. Schuhler, J. Spyromilio, C. Straubmeier, E. Sturm, M. Suarez, K. R. W. Tristram, N. Ventura, F. Vincent, I. Waisberg, I. Wank, J. Weber, E. Wieprecht, M. Wiest, E. Wiezorrek, M. Wittkowski, J. Woillez, B. Wolff, S. Yazici, D. Ziegler, and G. Zins. First light for GRAVITY: Phase referencing optical interferometry for the Very Large Telescope Interferometer. A&A, 602:A94, June 2017. doi: 10.1051/0004-6361/201730838.

GRAVITY Collaboration, R. Abuter, M. Accardo, A. Amorim, N. Anugu, G. Ávila, N. Azouaoui, M. Benisty, J. P. Berger, N. Blind, H. Bonnet, P. Bourget, W. Brandner, R. Brast, A. Buron, L. Burtscher, F. Cassaing, F. Chapron, É. Choquet, Y. Clénet, C. Collin, V. Coudé du Foresto, W. de Wit, P. T. de Zeeuw, C. Deen, F. Delplancke-Ströbele, R. Dembet, F. Derie, J. Dexter, G. Duvert, M. Ebert, A. Eckart, F. Eisenhauer, M. Esselborn, P. Fédou, G. Finger, P. Garcia, C. E. Garcia Dabo, R. Garcia Lopez,

E. Gendron, R. Genzel, S. Gillessen, F. Gonte, P. Gordo, M. Grould, U. Grözinger, S. Guieu, P. Haguenauer, O. Hans, X. Haubois, M. Haug, F. Haussmann, T. Henning, S. Hippler, M. Horrobin, A. Huber, Z. Hubert, N. Hubin, C. A. Hummel, G. Jakob, A. Janssen, L. Jochum, L. Jocou, A. Kaufer, S. Kellner, L. Kern, P. Kervella, M. Kiekebusch, R. Klein, Y. Kok, J. Kolb, M. Kulas, S. Lacour, V. Lapeyrère, B. Lazareff, J.-B. Le Bouquin, P. Lèna, R. Lenzen, S. Lévêque, M. Lippa, Y. Magnard, L. Mehrgan, M. Mellein, A. Mérand, J. Moreno-Ventas, T. Moulin, E. Müller, F. Müller, U. Neumann, S. Oberti, T. Ott, L. Pallanca, J. Panduro, L. Pasquini, T. Paumard, I. Percheron, K. Perraut, G. Perrin, A. Pflüger, O. Pfuhl, T. Phan Duc, P. M. Plewa, D. Popovic, S. Rabien, A. Ramírez, J. Ramos, C. Rau, M. Riquelme, R.-R. Rohloff, G. Rousset, J. Sanchez-Bermudez, S. Scheithauer, M. Schöller, N. Schuhler, J. Spyromilio, C. Straubmeier, E. Sturm, M. Suarez, K. R. W. Tristram, N. Ventura, F. Vincent, I. Waisberg, I. Wank, J. Weber, E. Wieprecht, M. Wiest, E. Wiezorrek, M. Wittkowski, J. Woillez, B. Wolff, S. Yazici, D. Ziegler, and G. Zins. First Light for GRAVITY: Phase Referencing Optical Interferometry for the Very Large Telescope Interferometer. *ArXiv e-prints*, May 2017.

Gravity Collaboration, P.-O. Petrucci, I. Waisberg, J.-B. Le Bouquin, J. Dexter, G. Dubus, K. Perraut, P. Kervella, R. Abuter, A. Amorim, N. Anugu, J. P. Berger, N. Blind, H. Bonnet, W. Brandner, A. Buron, É. Choquet, Y. Clénet, W. de Wit, C. Deen, A. Eckart, F. Eisenhauer, G. Finger, P. Garcia, R. Garcia Lopez, E. Gendron, R. Genzel, S. Gillessen, F. Gonte, X. Haubois, M. Haug, F. Haussmann, T. Henning, S. Hippler, M. Horrobin, Z. Hubert, L. Jochum, L. Jocou, Y. Kok, J. Kolb, M. Kulas, S. Lacour, B. Lazareff, P. Lèna, M. Lippa, A. Mérand, E. Müller, T. Ott, J. Panduro, T. Paumard, G. Perrin, O. Pfuhl, J. Ramos, C. Rau, R.-R. Rohloff, G. Rousset, J. Sanchez-Bermudez, S. Scheithauer, M. Schöller, C. Straubmeier, E. Sturm, F. Vincent, I. Wank, E. Wieprecht, M. Wiest, E. Wiezorrek, M. Wittkowski, J. Woillez, S. Yazici, and G. Zins. Accretion-ejection morphology of the microquasar SS 433 resolved at sub-au scale. A&A, 602:L11, June 2017. doi: 10.1051/0004-6361/201731038.

Gravity Collaboration, R. Abuter, A. Amorim, N. Anugu, M. Bauböck, M. Benisty, J. P. Berger, N. Blind, H. Bonnet, W. Brandner, A. Buron, C. Collin, F. Chapron, Y. Clénet, V. Coudé Du Foresto, P. T. de Zeeuw, C. Deen, F. Delplancke-Ströbele, R. Dembet, J. Dexter, G. Duvert, A. Eckart, F. Eisenhauer, G. Finger, N. M. Förster Schreiber, P. Fédou, P. Garcia, R. Garcia Lopez, F. Gao, E. Gendron, R. Genzel, S. Gillessen, P. Gordo, M. Habibi, X. Haubois, M. Haug, F. Haußmann, T. Henning, S. Hippler, M. Horrobin, Z. Hubert, N. Hubin, A. Jimenez Rosales, L. Jochum, K. Jocou, A. Kaufer, S. Kellner, S. Kendrew, P. Kervella, Y. Kok, M. Kulas, S. Lacour, V. Lapeyrère, B. Lazareff, J.-B. Le Bouquin, P. Léna, M. Lippa, R. Lenzen, A. Mérand, E. Müler, U. Neumann, T. Ott, L. Palanca, T. Paumard, L. Pasquini, K. Perraut, G. Perrin, O. Pfuhl, P. M. Plewa, S. Rabien, A. Ramírez, J. Ramos, C. Rau, G. Rodríguez-Coira, R.-R. Rohloff, G. Rousset, J. Sanchez-Bermudez, S. Scheithauer, M. Schöller, N. Schuler, J. Spyromilio, O. Straub, C. Straubmeier, E. Sturm, L. J. Tacconi, K. R. W. Tris-

tram, F. Vincent, S. von Fellenberg, I. Wank, I. Waisberg, F. Widmann, E. Wieprecht, M. Wiest, E. Wiezorrek, J. Woillez, S. Yazici, D. Ziegler, and G. Zins. Detection of the gravitational redshift in the orbit of the star S2 near the Galactic centre massive black hole. A&A, 615:L15, July 2018a. doi: 10.1051/0004-6361/201833718.

Gravity Collaboration, R. Abuter, A. Amorim, M. Bauböck, J. P. Berger, H. Bonnet, W. Brandner, Y. Clénet, V. Coudé Du Foresto, P. T. de Zeeuw, C. Deen, J. Dexter, G. Duvert, A. Eckart, F. Eisenhauer, N. M. Förster Schreiber, P. Garcia, F. Gao, E. Gendron, R. Genzel, S. Gillessen, P. Guajardo, M. Habibi, X. Haubois, T. Henning, S. Hippler, M. Horrobin, A. Huber, A. Jiménez-Rosales, L. Jocou, P. Kervella, S. Lacour, V. Lapeyrère, B. Lazareff, J.-B. Le Bouquin, P. Léna, M. Lippa, T. Ott, J. Panduro, T. Paumard, K. Perraut, G. Perrin, O. Pfuhl, P. M. Plewa, S. Rabien, G. Rodríguez-Coira, G. Rousset, A. Sternberg, O. Straub, C. Straubmeier, E. Sturm, L. J. Tacconi, F. Vincent, S. von Fellenberg, I. Waisberg, F. Widmann, E. Wieprecht, E. Wiezorrek, J. Woillez, and S. Yazici. Detection of orbital motions near the last stable circular orbit of the massive black hole SgrA*. A&A, 618:L10, October 2018b. doi: 10.1051/0004-6361/201834294.

Gravity Collaboration, E. Sturm, J. Dexter, O. Pfuhl, M. R. Stock, R. I. Davies, D. Lutz, Y. Clénet, A. Eckart, F. Eisenhauer, R. Genzel, D. Gratadour, S. F. Hönig, M. Kishimoto, S. Lacour, F. Millour, H. Netzer, G. Perrin, B. M. Peterson, P. O. Petrucci, D. Rouan, I. Waisberg, J. Woillez, A. Amorim, W. Brandner, N. M. Förster Schreiber, P. J. V. Garcia, S. Gillessen, T. Ott, T. Paumard, K. Perraut, S. Scheithauer, C. Straubmeier, L. J. Tacconi, and F. Widmann. Spatially resolved rotation of the broad-line region of a quasar at sub-parsec scale. Nature, 563:657–660, November 2018c. doi: 10.1038/s41586-018-0731-9.

Gravity Collaboration, R. Abuter, A. Amorim, M. Bauboeck, J. P. Berger, H. Bonnet, W. Brandner, Y. Clenet, V. Coude du Foresto, P. T. de Zeeuw, J. Dexter, G. Duvert, A. Eckart, F. Eisenhauer, N. M. Foerster Schreiber, P. Garcia, F. Gao, E. Gendron, R. Genzel, O. Gerhard, S. Gillessen, M. Habibi, X. Haubois, T. Henning, S. Hippler, M. Horrobin, A. Jimenez-Rosales, L. Jocou, P. Kervella, S. Lacour, V. Lapeyrere, J.-B. Le Bouquin, P. Lena, T. Ott, T. Paumard, K. Perraut, G. Perrin, O. Pfuhl, S. Rabien, G. Rodriguez Coira, G. Rousset, S. Scheithauer, A. Sternberg, O. Straub, C. Straubmeier, E. Sturm, L. J. Tacconi, F. Vincent, S. von Fellenberg, I. Waisberg, F. Widmann, E. Wieprecht, E. Wiezorrek, J. Woillez, and S. Yazici. A geometric distance measurement to the Galactic Center black hole with 0.3% uncertainty. ApJ, April 2019. doi: 10.1038/383415a0.

G. M. Green, E. F. Schlafly, D. Finkbeiner, H.-W. Rix, N. Martin, W. Burgett, P. W. Draper, H. Flewelling, K. Hodapp, N. Kaiser, R.-P. Kudritzki, E. A. Magnier, N. Metcalfe, J. L. Tonry, R. Wainscoat, and C. Waters. Galactic reddening in 3D from stellar photometry - an improved map. MNRAS, 478:651–666, July 2018. doi: 10.1093/mnras/sty1008.

M. Grould, F. H. Vincent, T. Paumard, and G. Perrin. General relativistic effects on the orbit of the S2 star with GRAVITY. *ArXiv e-prints*, September 2017.

A. Gualandris, S. Gillessen, and D. Merritt. The Galactic Centre star S2 as a dynamical probe for intermediate-mass black holes. MNRAS, 409:1146–1154, December 2010. doi: 10.1111/j.1365-2966.2010.17373.x.

F. Haberl. The X-ray properties of GX 301 - 2 (4U 1223 - 62). ApJ, 376:245–255, July 1991. doi: 10.1086/170273.

M. Habibi, S. Gillessen, F. Martins, F. Eisenhauer, P. M. Plewa, O. Pfuhl, E. George, J. Dexter, I. Waisberg, T. Ott, S. von Fellenberg, M. Bauböck, A. Jimenez-Rosales, and R. Genzel. Twelve Years of Spectroscopic Monitoring in the Galactic Center: The Closest Look at S-stars near the Black Hole. ApJ, 847:120, October 2017. doi: 10.3847/1538-4357/aa876f.

M. Habibi, S. Gillessen, O. Pfuhl, F. Eisenhauer, P. M. Plewa, S. von Fellenberg, F. Widmann, T. Ott, F. Gao, I. Waisberg, M. Bauböck, A. Jimenez-Rosales, J. Dexter, P. T. de Zeeuw, and R. Genzel. Spectroscopic Detection of a Cusp of Late-type Stars around the Central Black Hole in the Milky Way. ApJ, 872:L15, February 2019. doi: 10.3847/2041-8213/ab03cf.

N. Hamaus, T. Paumard, T. Müller, S. Gillessen, F. Eisenhauer, S. Trippe, and R. Genzel. Prospects for Testing the Nature of Sgr A*'s Near-Infrared Flares on the Basis of Current Very Large Telescope and Future Very Large Telescope Interferometer Observations. ApJ, 692:902–916, February 2009. doi: 10.1088/0004-637X/692/1/902.

M. M. Hanson, P. S. Conti, and M. J. Rieke. A Spectral Atlas of Hot, Luminous Stars at 2 Microns. ApJS, 107:281, November 1996. doi: 10.1086/192366.

M. M. Hanson, R.-P. Kudritzki, M. A. Kenworthy, J. Puls, and A. T. Tokunaga. A Medium Resolution Near-Infrared Spectral Atlas of O and Early-B Stars. ApJS, 161: 154–170, November 2005. doi: 10.1086/444363.

S. W. Hawking. Black hole explosions? Nature, 248:30–31, March 1974. doi: 10.1038/248030a0.

A. Hees, T. Do, A. M. Ghez, G. D. Martinez, S. Naoz, E. E. Becklin, A. Boehle, S. Chappell, D. Chu, A. Dehghanfar, K. Kosmo, J. R. Lu, K. Matthews, M. R. Morris, S. Sakai, R. Schödel, and G. Witzel. Testing General Relativity with Stellar Orbits around the Supermassive Black Hole in Our Galactic Center. *Physical Review Letters*, 118(21): 211101, May 2017. doi: 10.1103/PhysRevLett.118.211101.

G. H. Herbig. The diffuse interstellar bands. IV - The region 4400-6850 A. ApJ, 196: 129–160, February 1975. doi: 10.1086/153400.

T. C. Hillwig and D. R. Gies. Spectroscopic Observations of the Mass Donor Star in SS 433. ApJ, 676:L37, March 2008. doi: 10.1086/587140.

R. M. Hjellming and K. J. Johnston. An analysis of the proper motions of SS 433 radio jets. ApJ, 246:L141–L145, June 1981. doi: 10.1086/183571.

C. Hopman and T. Alexander. The Effect of Mass Segregation on Gravitational Wave Sources near Massive Black Holes. ApJ, 645:L133–L136, July 2006. doi: 10.1086/506273.

S. D. Hornstein, K. Matthews, A. M. Ghez, J. R. Lu, M. Morris, E. E. Becklin, M. Rafelski, and F. K. Baganoff. A Constant Spectral Index for Sagittarius A* during Infrared/X-Ray Intensity Variations. ApJ, 667:900–910, October 2007. doi: 10.1086/520762.

J. D. Hunter. Matplotlib: A 2d graphics environment. *Computing In Science & Engineering*, 9(3):90–95, 2007.

A. F. Illarionov and R. A. Sunyaev. Why the Number of Galactic X-ray Stars Is so Small? A&A, 39:185, February 1975.

L. Iorio. Perturbed stellar motions around the rotating black hole in Sgr A* for a generic orientation of its spin axis. Phys. Rev. D, 84(12):124001, December 2011. doi: 10.1103/PhysRevD.84.124001.

N. Islam and B. Paul. Orbital phase resolved spectroscopy of GX 301-2 with MAXI. MNRAS, 441:2539–2545, July 2014. doi: 10.1093/mnras/stu756.

N. Ivanova, S. Justham, X. Chen, O. De Marco, C. L. Fryer, E. Gaburov, H. Ge, E. Glebbeek, Z. Han, X.-D. Li, G. Lu, T. Marsh, P. Podsiadlowski, A. Potter, N. Soker, R. Taam, T. M. Tauris, E. P. J. van den Heuvel, and R. F. Webbink. Common envelope evolution: where we stand and how we can move forward. A&A Rev., 21:59, February 2013. doi: 10.1007/s00159-013-0059-2.

M. Jaroszynski. Relativistic Effects in Proper Motions of Stars Surrounding the Galactic Center. Acta Astron., 48:653–665, December 1998.

T. Johannsen. Testing the No-Hair Theorem with Sgr A*. *Advances in Astronomy*, 2012: 486750, 2012. doi: 10.1155/2012/486750.

M. D. Johnson, V. L. Fish, S. S. Doeleman, D. P. Marrone, R. L. Plambeck, J. F. C. Wardle, K. Akiyama, K. Asada, C. Beaudoin, L. Blackburn, R. Blundell, G. C. Bower, C. Brinkerink, A. E. Broderick, R. Cappallo, A. A. Chael, G. B. Crew, J. Dexter, M. Dexter, R. Freund, P. Friberg, R. Gold, M. A. Gurwell, P. T. P. Ho, M. Honma, M. Inoue, M. Kosowsky, T. P. Krichbaum, J. Lamb, A. Loeb, R.-S. Lu, D. MacMahon, J. C. McKinney, J. M. Moran, R. Narayan, R. A. Primiani, D. Psaltis, A. E. E. Rogers, K. Rosenfeld, J. SooHoo, R. P. J. Tilanus, M. Titus, L. Vertatschitsch, J. Weintroub, M. Wright, K. H. Young, J. A. Zensus, and L. M. Ziurys. Resolved magnetic-field

structure and variability near the event horizon of Sagittarius A*. *Science*, 350:1242–1245, December 2015. doi: 10.1126/science.aac7087.

S. Johnston, M. A. Walker, M. H. van Kerkwijk, A. G. Lyne, and N. D'Amico. A 1500-MHz survey for pulsars near the Galactic Centre. MNRAS, 274:L43–L45, May 1995.

P. Kaaret, H. Feng, and T. P. Roberts. Ultraluminous X-Ray Sources. ARA&A, 55: 303–341, August 2017. doi: 10.1146/annurev-astro-091916-055259.

R. Kannan and P. Saha. Frame Dragging and the Kinematics of Galactic-Center Stars. ApJ, 690:1553–1557, January 2009. doi: 10.1088/0004-637X/690/2/1553.

L. Kaper, H. J. G. L. M. Lamers, E. Ruymaekers, E. P. J. van den Heuvel, and E. J. Zuiderwijk. Wray 977 (GX 301-2): a hypergiant with pulsar companion. A&A, 300, August 1995.

L. Kaper, A. van der Meer, and F. Najarro. VLT/UVES spectroscopy of Wray 977, the hypergiant companion to the X-ray pulsar ¡ASTROBJ¿GX301-2¡/ASTROBJ¿. A&A, 457:595–610, October 2006. doi: 10.1051/0004-6361:20065393.

S. Kaspi, P. S. Smith, H. Netzer, D. Maoz, B. T. Jannuzi, and U. Giveon. Reverberation Measurements for 17 Quasars and the Size-Mass-Luminosity Relations in Active Galactic Nuclei. ApJ, 533:631–649, April 2000. doi: 10.1086/308704.

W. Kausch, S. Noll, A. Smette, S. Kimeswenger, M. Barden, C. Szyszka, A. M. Jones, H. Sana, H. Horst, and F. Kerber. Molecfit: A general tool for telluric absorption correction. II. Quantitative evaluation on ESO-VLT/X-Shooterspectra. A&A, 576:A78, April 2015. doi: 10.1051/0004-6361/201423909.

Roy P. Kerr. Gravitational field of a spinning mass as an example of algebraically special metrics. *Phys. Rev. Lett.*, 11:237–238, Sep 1963. doi: 10.1103/PhysRevLett.11.237. URL `https://link.aps.org/doi/10.1103/PhysRevLett.11.237`.

A. R. King and J. E. Pringle. Growing supermassive black holes by chaotic accretion. MNRAS, 373:L90–L92, November 2006. doi: 10.1111/j.1745-3933.2006.00249.x.

D. T. Koh, L. Bildsten, D. Chakrabarty, R. W. Nelson, T. A. Prince, B. A. Vaughan, M. H. Finger, R. B. Wilson, and B. C. Rubin. Rapid Spin-Up Episodes in the Wind-fed Accreting Pulsar GX 301-2. ApJ, 479:933–947, April 1997.

S. Komossa. Tidal disruption of stars by supermassive black holes: Status of observations. *Journal of High Energy Astrophysics*, 7:148–157, September 2015. doi: 10.1016/j.jheap.2015.04.006.

A. Koratkar and O. Blaes. The Ultraviolet and Optical Continuum Emission in Active Galactic Nuclei: The Status of Accretion Disks. PASP, 111:1–30, January 1999. doi: 10.1086/316294.

J. Kormendy and D. Richstone. Inward Bound—The Search For Supermassive Black Holes In Galactic Nuclei. *ARA&A*, 33:581, 1995. doi: 10.1146/annurev.aa.33.090195.003053.

J. Kos and T. Zwitter. Properties of Diffuse Interstellar Bands at Different Physical Conditions of the Interstellar Medium. ApJ, 774:72, September 2013. doi: 10.1088/0004-637X/774/1/72.

T. Kotani, N. Kawai, M. Matsuoka, and W. Brinkmann. Iron-Line Diagnostics of the Jets of SS 433. PASJ, 48:619–629, August 1996. doi: 10.1093/pasj/48.4.619.

G. V. Kraniotis. Periapsis and gravitomagnetic precessions of stellar orbits in Kerr and Kerr de Sitter black hole spacetimes. *Classical and Quantum Gravity*, 24:1775–1808, April 2007. doi: 10.1088/0264-9381/24/7/007.

I. Kreykenbohm, J. Wilms, W. Coburn, M. Kuster, R. E. Rothschild, W. A. Heindl, P. Kretschmar, and R. Staubert. The variable cyclotron line in GX 301-2. A&A, 427: 975–986, December 2004. doi: 10.1051/0004-6361:20035836.

T. P. Krichbaum, D. A. Graham, A. Witzel, A. Greve, J. E. Wink, M. Grewing, F. Colomer, P. de Vicente, J. Gomez-Gonzalez, A. Baudry, and J. A. Zensus. VLBI observations of the galactic center source SGR A* at 86 GHz and 215 GHz. A&A, 335:L106–L110, July 1998.

K. Kubota, Y. Ueda, S. Fabrika, A. Medvedev, E. A. Barsukova, O. Sholukhova, and V. P. Goranskij. Subaru And Gemini Observations Of SS 433: New Constraint On The Mass Of The Compact Object. ApJ, 709:1374–1386, February 2010. doi: 10.1088/0004-637X/709/2/1374.

R.-P. Kudritzki and J. Puls. Winds from Hot Stars. ARA&A, 38:613–666, 2000. doi: 10.1146/annurev.astro.38.1.613.

R. Lachaume. On marginally resolved objects in optical interferometry. A&A, 400:795–803, March 2003. doi: 10.1051/0004-6361:20030072.

S. Lacour, R. Dembet, R. Abuter, P. Fédou, G. Perrin, É. Choquet, O. Pfuhl, F. Eisenhauer, J. Woillez, F. Cassaing, E. Wieprecht, T. Ott, E. Wiezorrek, K. R. W. Tristram, B. Wolff, A. Ramírez, X. Haubois, K. Perraut, C. Straubmeier, W. Brandner, and A. Amorim. The GRAVITY fringe tracker. A&A, 624:A99, April 2019. doi: 10.1051/0004-6361/201834981.

M. Lampton, B. Margon, and S. Bowyer. Parameter estimation in X-ray astronomy. ApJ, 208:177–190, August 1976. doi: 10.1086/154592.

V. Lapeyrere, P. Kervella, S. Lacour, N. Azouaoui, C. E. Garcia-Dabo, G. Perrin, F. Eisenhauer, K. Perraut, C. Straubmeier, A. Amorim, and W. Brandner. GRAVITY data reduction software. In *Optical and Infrared Interferometry IV*, volume 9146 of Proc. SPIE, page 91462D, July 2014. doi: 10.1117/12.2056850.

D. A. Leahy. Evidence for a gas stream in GX301 - 2. MNRAS, 250:310–313, May 1991. doi: 10.1093/mnras/250.2.310.

D. A. Leahy. The RXTE/ASM X-ray light curve of GX301-2. A&A, 391:219–224, August 2002. doi: 10.1051/0004-6361:20020781.

D. A. Leahy and M. Kostka. Stellar wind accretion in GX 301-2: evidence for a high-density stream. MNRAS, 384:747–754, February 2008. doi: 10.1111/j.1365-2966.2007.12754.x.

E. M. Leibowitz. A geometrical model for the SS 433 system. MNRAS, 210:279–301, September 1984. doi: 10.1093/mnras/210.2.279.

M. Lippa, S. Gillessen, N. Blind, Y. Kok, Ş. Yazıcı, J. Weber, O. Pfuhl, M. Haug, S. Kellner, E. Wieprecht, F. Eisenhauer, R. Genzel, O. Hans, F. Haußmann, D. Huber, T. Kratschmann, T. Ott, M. Plattner, C. Rau, E. Sturm, I. Waisberg, E. Wiezorrek, G. Perrin, K. Perraut, W. Brandner, C. Straubmeier, and A. Amorim. The metrology system of the VLTI instrument GRAVITY. In *Optical and Infrared Interferometry and Imaging V*, volume 9907 of Proc. SPIE, page 990722, August 2016. doi: 10.1117/12.2232272.

G. V. Lipunova. Supercritical disk accretion with mass loss. *Astronomy Letters*, 25:508–517, August 1999.

J.-F. Liu, Y. Bai, S. Wang, S. Justham, Y.-J. Lu, W.-M. Gu, Q.-Z. Liu, R. di Stefano, J.-C. Guo, A. Cabrera-Lavers, P. Álvarez, Y. Cao, and S. Kulkarni. Relativistic baryonic jets from an ultraluminous supersoft X-ray source. Nature, 528:108–110, December 2015. doi: 10.1038/nature15751.

K. Liu, N. Wex, M. Kramer, J. M. Cordes, and T. J. W. Lazio. Prospects for Probing the Spacetime of Sgr A* with Pulsars. ApJ, 747:1, March 2012. doi: 10.1088/0004-637X/747/1/1.

Q. Z. Liu, J. van Paradijs, and E. P. J. van den Heuvel. Catalogue of high-mass X-ray binaries in the Galaxy (4th edition). A&A, 455:1165–1168, September 2006. doi: 10.1051/0004-6361:20064987.

F. J. Lockman, K. M. Blundell, and W. M. Goss. The distance to SS433/W50 and its interaction with the interstellar medium. MNRAS, 381:881–893, November 2007. doi: 10.1111/j.1365-2966.2007.12170.x.

B. Lopez, S. Lagarde, W. Jaffe, R. Petrov, M. Schöller, P. Antonelli, U. Beckmann, P. Berio, F. Bettonvil, A. Glindemann, J.-C. Gonzalez, U. Graser, K.-H. Hofmann, F. Millour, S. Robbe-Dubois, L. Venema, S. Wolf, T. Henning, T. Lanz, G. Weigelt, T. Agocs, C. Bailet, Y. Bresson, P. Bristow, M. Dugué, M. Heininger, G. Kroes, W. Laun, M. Lehmitz, U. Neumann, J.-C. Augereau, G. Avila, J. Behrend, G. van Belle, J.-P.

Berger, R. van Boekel, S. Bonhomme, P. Bourget, R. Brast, J.-M. Clausse, C. Connot, R. Conzelmann, P. Cruzalèbes, G. Csepany, W. Danchi, M. Delbo, F. Delplancke, C. Dominik, A. van Duin, E. Elswijk, Y. Fantei, G. Finger, A. Gabasch, J. Gay, P. Girard, V. Girault, P. Gitton, A. Glazenborg, F. Gonté, F. Guitton, S. Guniat, M. De Haan, P. Haguenauer, H. Hanenburg, M. Hogerheijde, R. ter Horst, J. Hron, Y. Hugues, C. Hummel, J. Idserda, D. Ives, G. Jakob, A. Jasko, P. Jolley, S. Kiraly, R. Köhler, J. Kragt, T. Kroener, S. Kuindersma, L. Labadie, C. Leinert, R. Le Poole, J.-L. Lizon, C. Lucuix, A. Marcotto, F. Martinache, G. Martinot-Lagarde, R. Mathar, A. Matter, N. Mauclert, L. Mehrgan, A. Meilland, K. Meisenheimer, J. Meisner, M. Mellein, S. Menardi, J.-L. Menut, A. Merand, S. Morel, L. Mosoni, R. Navarro, E. Nussbaum, S. Ottogalli, R. Palsa, J. Panduro, E. Pantin, T. Parra, I. Percheron, T. P. Duc, J.-U. Pott, E. Pozna, F. Przygodda, Y. Rabbia, A. Richichi, F. Rigal, R. Roelfsema, G. Rupprecht, D. Schertl, C. Schmidt, N. Schuhler, M. Schuil, A. Spang, J. Stegmeier, L. Thiam, N. Tromp, F. Vakili, M. Vannier, K. Wagner, and J. Woillez. An Overview of the MATISSE Instrument: Science, Concept and Current Status. *The Messenger*, 157:5–12, September 2014.

J. R. Lu, A. M. Ghez, S. D. Hornstein, M. R. Morris, E. E. Becklin, and K. Matthews. A Disk of Young Stars at the Galactic Center as Determined by Individual Stellar Orbits. ApJ, 690:1463–1487, January 2009. doi: 10.1088/0004-637X/690/2/1463.

X. Luri, A. G. A. Brown, L. M. Sarro, F. Arenou, C. A. L. Bailer-Jones, A. Castro-Ginard, J. de Bruijne, T. Prusti, C. Babusiaux, and H. E. Delgado. Gaia Data Release 2. Using Gaia parallaxes. A&A, 616:A9, August 2018. doi: 10.1051/0004-6361/201832964.

D. Lynden-Bell. Galactic Nuclei as Collapsed Old Quasars. Nature, 223:690–694, August 1969. doi: 10.1038/223690a0.

J.-P. Macquart, N. Kanekar, D. A. Frail, and S. M. Ransom. A High-frequency Search for Pulsars within the Central Parsec of Sgr A*. ApJ, 715:939–946, June 2010. doi: 10.1088/0004-637X/715/2/939.

B. Margon. Observations of SS 433. ARA&A, 22:507–536, 1984. doi: 10.1146/annurev.aa.22.090184.002451.

B. Margon, H. C. Ford, S. A. Grandi, and R. P. S. Stone. Enormous periodic Doppler shifts in SS 433. ApJ, 233:L63–L68, October 1979. doi: 10.1086/183077.

S. Markoff, H. Falcke, F. Yuan, and P. L. Biermann. The Nature of the 10 kilosecond X-ray flare in Sgr A*. A&A, 379:L13–L16, November 2001. doi: 10.1051/0004-6361:20011346.

H. L. Marshall, C. R. Canizares, and N. S. Schulz. The High-Resolution X-Ray Spectrum of SS 433 Using the Chandra HETGS. ApJ, 564:941–952, January 2002. doi: 10.1086/324398.

H. L. Marshall, C. R. Canizares, T. Hillwig, A. Mioduszewski, M. Rupen, N. S. Schulz, M. Nowak, and S. Heinz. Multiwavelength Observations of the SS 433 Jets. ApJ, 775: 75, September 2013. doi: 10.1088/0004-637X/775/1/75.

S. Martínez-Núñez, P. Kretschmar, E. Bozzo, L. M. Oskinova, J. Puls, L. Sidoli, J. O. Sundqvist, P. Blay, M. Falanga, F. Fürst, A. Gímenez-García, I. Kreykenbohm, M. Kühnel, A. Sander, J. M. Torrejón, and J. Wilms. Towards a Unified View of Inhomogeneous Stellar Winds in Isolated Supergiant Stars and Supergiant High Mass X-Ray Binaries. Space Sci. Rev., March 2017. doi: 10.1007/s11214-017-0340-1.

A. Medvedev and S. Fabrika. Evidence of supercritical disc funnel radiation in X-ray spectra of SS 433. MNRAS, 402:479–491, February 2010. doi: 10.1111/j.1365-2966.2009.15896.x.

A. Meilland, F. Millour, S. Kanaan, P. Stee, R. Petrov, K.-H. Hofmann, A. Natta, and K. Perraut. First spectro-interferometric survey of Be stars. I. Observations and constraints on the disk geometry and kinematics. A&A, 538:A110, February 2012. doi: 10.1051/0004-6361/201117955.

A. Merand, P. Borde, and V. Coudé du Foresto. VizieR Online Data Catalog: Calibrator stars for 200m baseline interferometry (Merand+, 2005). *VizieR Online Data Catalog*, 343, January 2005.

D. Merritt, T. Alexander, S. Mikkola, and C. M. Will. Testing properties of the Galactic center black hole using stellar orbits. Phys. Rev. D, 81(6):062002, March 2010. doi: 10.1103/PhysRevD.81.062002.

A. A. Michelson and F. G. Pease. Measurement of the Diameter of α Orionis with the Interferometer. ApJ, 53, May 1921. doi: 10.1086/142603.

M. J. Middleton, D. J. Walton, W. Alston, T. Dauser, S. Eikenberry, Y. Jiang, A. C. Fabian, F. Fuerst, M. Brightman, H. Marshall, M. Parker, C. Pinto, F. A. Harrison, M. Bachetti, D. Altamirano, A. J. Bird, G. Perez, J. Miller-Jones, P. A. Charles, S. Boggs, F. Christensen, W. Craig, K. Forster, B. Grefenstette, C. Hailey, K. Madsen, D. Stern, and W. Zhang. NuSTAR reveals the hidden nature of SS433. *ArXiv e-prints*, October 2018.

M. Milgrom. SS433 - The acceleration and collimation mechanisms. A&A, 78:L9–L12, September 1979.

J. M. Miller, M. C. Miller, and C. S. Reynolds. The Angular Momenta of Neutron Stars and Black Holes as a Window on Supernovae. ApJ, 731:L5, April 2011. doi: 10.1088/2041-8205/731/1/L5.

S. Mineshige, M. J. Rees, and A. C. Fabian. Flywheels - Rapidly spinning, magnetized neutron stars in spherical accretion. MNRAS, 251:555–563, August 1991. doi: 10.1093/mnras/251.4.555.

A. J. Mioduszewski, M. P. Rupen, R. C. Walker, K. M. Schillemat, and G. B. Taylor. A Summer of SS433: Forty Days of VLBA Imaging. In *AAS/High Energy Astrophysics Division #8*, volume 36 of *Bulletin of the American Astronomical Society*, page 967, August 2004.

I. F. Mirabel and L. F. Rodríguez. Sources of Relativistic Jets in the Galaxy. ARA&A, 37:409–443, 1999. doi: 10.1146/annurev.astro.37.1.409.

J. D. Monnier and R. J. Allen. *Radio and Optical Interferometry: Basic Observing Techniques and Data Analysis*, page 325. 2013. doi: 10.1007/978-94-007-5618-2_7.

T. A. Moore. *A General Relativity Workbook*. University Science Books., 2012.

P. Murdin, D. H. Clark, and P. G. Martin. The optical spectrum of SS 433. MNRAS, 193: 135–151, October 1980. doi: 10.1093/mnras/193.1.135.

R. Narayan, I. Yi, and R. Mahadevan. Explaining the spectrum of Sagittarius A* with a model of an accreting black hole. Nature, 374:623–625, April 1995. doi: 10.1038/374623a0.

J. A. Nelder and R. Mead. A simplex method for function minimization. *The Computer Journal*, 7(4):308–313, 1965. doi: 10.1093/comjnl/7.4.308. URL `+http://dx.doi.org/10.1093/comjnl/7.4.308`.

D. E. Osterbrock and G. J. Ferland. *Astrophysics of gaseous nebulae and active galactic nuclei*. 2006.

F. Özel, D. Psaltis, and R. Narayan. Hybrid Thermal-Nonthermal Synchrotron Emission from Hot Accretion Flows. ApJ, 541:234–249, September 2000. doi: 10.1086/309396.

A. A. Panferov and S. N. Fabrika. Collimated emission from SS 433 - Simulation of moving line profiles. *Astronomy Letters*, 19:41–45, February 1993.

A. A. Panferov and S. N. Fabrika. The optical jets of SS 433: Physical parameters. *Astronomy Reports*, 41:506–515, July 1997.

A. A. Panferov, S. N. Fabrika, and V. Y. Rakhimov. Optical jets of SS 433 - Anisotropy of the emission. AZh, 74:392, June 1997.

Z. Paragi, R. C. Vermeulen, I. Fejes, R. T. Schilizzi, R. E. Spencer, and A. M. Stirling. The inner radio jet region and the complex environment of SS433. A&A, 348:910–916, August 1999.

Z. Paragi, I. Fejes, R. C. Vermeulen, R. T. Schilizzi, R. E. Spencer, and A. M. Stirling. The Equatorial Outflow of SS 433. In E. Ros, R. W. Porcas, A. P. Lobanov, and J. A. Zensus, editors, *Proceedings of the 6th EVN Symposium*, page 263, June 2002.

M. Parsa, A. Eckart, B. Shahzamanian, V. Karas, M. Zajaček, J. A. Zensus, and C. Straubmeier. Investigating the Relativistic Motion of the Stars Near the Supermassive Black Hole in the Galactic Center. ApJ, 845:22, August 2017. doi: 10.3847/1538-4357/aa7bf0.

T. Paumard, R. Genzel, F. Martins, S. Nayakshin, A. M. Beloborodov, Y. Levin, S. Trippe, F. Eisenhauer, T. Ott, S. Gillessen, R. Abuter, J. Cuadra, T. Alexander, and A. Sternberg. The Two Young Star Disks in the Central Parsec of the Galaxy: Properties, Dynamics, and Formation. ApJ, 643:1011–1035, June 2006. doi: 10.1086/503273.

R. Penrose and R. M. Floyd. Extraction of Rotational Energy from a Black Hole. *Nature Physical Science*, 229:177–179, February 1971. doi: 10.1038/physci229177a0.

S. Perez M. and K. M. Blundell. Inflow and outflow from the accretion disc of the microquasar SS433: UKIRT spectroscopy. MNRAS, 397:849–856, August 2009. doi: 10.1111/j.1365-2966.2009.14979.x.

S. Perez M. and K. M. Blundell. SS433's circumbinary ring and accretion disc viewed through its attenuating disc wind. MNRAS, 408:2–8, October 2010. doi: 10.1111/j.1365-2966.2010.16638.x.

K. Perraut, L. Jocou, J. P. Berger, A. Chabli, V. Cardin, G. Chamiot-Maitral, A. Delboulbé, F. Eisenhauer, Y. Gambérini, S. Gillessen, S. Guieu, J. Guerrero, M. Haug, F. Hausmann, F. Joulain, P. Kervella, P. Labeye, S. Lacour, C. Lanthermann, V. Lapras, J. B. Le Bouquin, M. Lippa, Y. Magnard, T. Moulin, P. Noël, A. Nolot, F. Patru, G. Perrin, O. Pfuhl, S. Pocas, S. Poulain, C. Scibetta, E. Stadler, R. Templier, N. Ventura, C. Vizioz, A. Amorim, W. Brandner, and C. Straubmeier. Single-mode waveguides for GRAVITY. I. The cryogenic 4-telescope integrated optics beam combiner. A&A, 614: A70, June 2018. doi: 10.1051/0004-6361/201732544.

M. Pestalozzi, U. Torkelsson, G. Hobbs, and Á. R. López-Sánchez. Radio emission from the high-mass X-ray binary BP Crucis. First detection. A&A, 506:L21–L24, November 2009. doi: 10.1051/0004-6361/200913151.

O. Pfuhl, T. K. Fritz, M. Zilka, H. Maness, F. Eisenhauer, R. Genzel, S. Gillessen, T. Ott, K. Dodds-Eden, and A. Sternberg. The Star Formation History of the Milky Way's Nuclear Star Cluster. ApJ, 741:108, November 2011. doi: 10.1088/0004-637X/741/2/108.

O. Pfuhl, M. Haug, F. Eisenhauer, S. Kellner, F. Haussmann, G. Perrin, S. Gillessen, C. Straubmeier, T. Ott, K. Rousselet-Perraut, A. Amorim, M. Lippa, A. Janssen, W. Brandner, Y. Kok, N. Blind, L. Burtscher, E. Sturm, E. Wieprecht, M. Schoeller, J. Weber, O. Hans, and S. Huber. The fiber coupler and beam stabilization system of the GRAVITY interferometer. In *Optical and Infrared Interferometry IV*, volume 9146 of Proc. SPIE, page 914623, July 2014. doi: 10.1117/12.2055080.

Tsvi Piran. The physics of gamma-ray bursts. *Rev. Mod. Phys.*, 76:1143–1210, Jan 2005. doi: 10.1103/RevModPhys.76.1143. URL `https://link.aps.org/doi/10.1103/RevModPhys.76.1143`.

G. Ponti, E. George, S. Scaringi, S. Zhang, C. Jin, J. Dexter, R. Terrier, M. Clavel, N. Degenaar, F. Eisenhauer, R. Genzel, S. Gillessen, A. Goldwurm, M. Habibi, D. Haggard, C. Hailey, F. Harrison, A. Merloni, K. Mori, K. Nandra, T. Ott, O. Pfuhl, P. M. Plewa, and I. Waisberg. A powerful flare from Sgr A* confirms the synchrotron nature of the X-ray emission. MNRAS, 468:2447–2468, June 2017. doi: 10.1093/mnras/stx596.

S. H. Pravdo, C. S. R. Day, L. Angelini, B. A. Harmon, A. Yoshida, and P. Saraswat. ASCA and GRO Observations of GX 301-2. ApJ, 454:872, December 1995. doi: 10.1086/176540.

M. Preto and P. Amaro-Seoane. On Strong Mass Segregation Around a Massive Black Hole: Implications for Lower-Frequency Gravitational-Wave Astrophysics. ApJ, 708: L42–L46, January 2010. doi: 10.1088/2041-8205/708/1/L42.

D. Psaltis, G. Li, and A. Loeb. Deviation of Stellar Orbits from Test Particle Trajectories around Sgr A* Due to Tides and Winds. ApJ, 777:57, November 2013. doi: 10.1088/0004-637X/777/1/57.

D. Psaltis, N. Wex, and M. Kramer. A Quantitative Test of the No-hair Theorem with Sgr A* Using Stars, Pulsars, and the Event Horizon Telescope. ApJ, 818:121, February 2016. doi: 10.3847/0004-637X/818/2/121.

K. P. Rauch and R. D. Blandford. Optical caustics in a kerr spacetime and the origin of rapid X-ray variability in active galactic nuclei. ApJ, 421:46–68, January 1994. doi: 10.1086/173625.

R. A. Remillard and J. E. McClintock. X-Ray Properties of Black-Hole Binaries. *ARA&A*, 44:49–92, September 2006. doi: 10.1146/annurev.astro.44.051905.092532.

C. S. Reynolds. Observing black holes spin. *Nature Astronomy*, 3:41–47, January 2019. doi: 10.1038/s41550-018-0665-z.

T. Rivinius, O. Stahl, B. Wolf, A. Kaufer, T. Gaeng, C. A. Gummersbach, I. Jankovics, J. Kovacs, H. Mandel, J. Peitz, T. Szeifert, and H. J. G. L. M. Lamers. Variations of the stellar wind in early-B hypergiants. A&A, 318:819–834, February 1997.

W. J. Roberts. A slaved disk model for Hercules X-1. ApJ, 187:575–584, February 1974. doi: 10.1086/152667.

E. L. Robinson, C. S. Froning, D. T. Jaffe, K. F. Kaplan, H. Kim, G. N. Mace, K. R. Sokal, and J.-J. Lee. The Spectrum of SS 433 in the H and K Bands. ApJ, 841:79, June 2017. doi: 10.3847/1538-4357/aa6f0c.

G. F. Rubilar and A. Eckart. Periastron shifts of stellar orbits near the Galactic Center. A&A, 374:95–104, July 2001. doi: 10.1051/0004-6361:20010640.

N. Sabha, A. Eckart, D. Merritt, M. Zamaninasab, G. Witzel, M. García-Marín, B. Jalali, M. Valencia-S., S. Yazici, R. Buchholz, B. Shahzamanian, C. Rauch, M. Horrobin, and C. Straubmeier. The S-star cluster at the center of the Milky Way. On the nature of diffuse NIR emission in the inner tenth of a parsec. A&A, 545:A70, September 2012. doi: 10.1051/0004-6361/201219203.

L. Sadeghian and C. M. Will. Testing the black hole no-hair theorem at the galactic center: perturbing effects of stars in the surrounding cluster. *Classical and Quantum Gravity*, 28(22):225029, November 2011. doi: 10.1088/0264-9381/28/22/225029.

A. Sądowski and R. Narayan. Powerful radiative jets in supercritical accretion discs around non-spinning black holes. MNRAS, 453:3213–3221, November 2015. doi: 10.1093/mnras/stv1802.

S. Scheithauer, W. Brandner, C. Deen, T. Adler, H. Bonnet, P. Bourget, F. Chemla, Y. Clenet, F. Delplancke, M. Ebert, F. Eisenhauer, M. Esselborn, G. Finger, E. Gendron, A. Glauser, F. Gonte, T. Henning, S. Hippler, A. Huber, Z. Hubert, G. Jakob, L. Jochum, L. Jocou, S. Kendrew, R. Klein, J. Kolb, M. Kulas, W. Laun, R. Lenzen, M. Mellein, E. Müller, J. Moreno-Ventas, U. Neumann, S. Oberti, J. Ott, L. Pallanca, J. Panduro, J. Ramos, M. Riquelme, R.-R. Rohloff, G. Rousset, N. Schuhler, M. Suarez, and G. Zins. CIAO: wavefront sensors for GRAVITY. In *Adaptive Optics Systems V*, volume 9909 of Proc. SPIE, page 99092L, July 2016. doi: 10.1117/12.2232997.

D. J. Schlegel, D. P. Finkbeiner, and M. Davis. Maps of Dust Infrared Emission for Use in Estimation of Reddening and Cosmic Microwave Background Radiation Foregrounds. ApJ, 500:525–553, June 1998. doi: 10.1086/305772.

M. Schmidt. 3C 273 : A Star-Like Object with Large Red-Shift. Nature, 197:1040, March 1963. doi: 10.1038/1971040a0.

R. Schödel, T. Ott, R. Genzel, R. Hofmann, M. Lehnert, A. Eckart, N. Mouawad, T. Alexander, M. J. Reid, R. Lenzen, M. Hartung, F. Lacombe, D. Rouan, E. Gendron, G. Rousset, A.-M. Lagrange, W. Brandner, N. Ageorges, C. Lidman, A. F. M. Moorwood, J. Spyromilio, N. Hubin, and K. M. Menten. A star in a 15.2-year orbit around the supermassive black hole at the centre of the Milky Way. Nature, 419:694–696, October 2002. doi: 10.1038/nature01121.

R. Schödel, T. Ott, R. Genzel, A. Eckart, N. Mouawad, and T. Alexander. Stellar Dynamics in the Central Arcsecond of Our Galaxy. ApJ, 596:1015–1034, October 2003. doi: 10.1086/378122.

R. Schödel, A. Eckart, T. Alexander, D. Merritt, R. Genzel, A. Sternberg, L. Meyer, F. Kul, J. Moultaka, T. Ott, and C. Straubmeier. The structure of the nuclear stellar cluster of the Milky Way. A&A, 469:125–146, July 2007. doi: 10.1051/0004-6361:20065089.

R. Schödel, A. Feldmeier, D. Kunneriath, S. Stolovy, N. Neumayer, P. Amaro-Seoane, and S. Nishiyama. Surface brightness profile of the Milky Way's nuclear star cluster. A&A, 566:A47, June 2014. doi: 10.1051/0004-6361/201423481.

R. Schödel, E. Gallego-Cano, H. Dong, F. Nogueras-Lara, A. T. Gallego-Calvente, P. Amaro-Seoane, and H. Baumgardt. The distribution of stars around the Milky Way's central black hole. II. Diffuse light from sub-giants and dwarfs. A&A, 609:A27, January 2018. doi: 10.1051/0004-6361/201730452.

K. Schwarzschild. Über das Gravitationsfeld eines Massenpunktes nach der Einsteinschen Theorie. *Sitzungsberichte der Königlich Preußischen Akademie der Wissenschaften (Berlin), 1916, Seite 189-196*, 1916.

M. Servillat, A. Coleiro, S. Chaty, F. Rahoui, and J. A. Zurita Heras. Herschel Observations of Dust around the High-mass X-Ray Binary GX 301-2. ApJ, 797:114, December 2014. doi: 10.1088/0004-637X/797/2/114.

T. Shahbaz, R. M. Bandyopadhyay, and P. A. Charles. Infrared spectroscopy of V616 Monocerotis (=A0620-00): the accretion disc contamination. A&A, 346:82–86, June 1999.

N. I. Shakura and R. A. Sunyaev. Black holes in binary systems. Observational appearance. A&A, 24:337–355, 1973.

P. R. Shapiro, M. Milgrom, and M. J. Rees. The radiative acceleration of astrophysical jets - Line locking in SS 433. ApJS, 60:393–431, February 1986. doi: 10.1086/191092.

I. S. Shklovskii. Mass Loss by SS433 and its Effect on the X-Ray and Radio Emission. Soviet Ast., 25:315, June 1981.

A. Smette, H. Sana, S. Noll, H. Horst, W. Kausch, S. Kimeswenger, M. Barden, C. Szyszka, A. M. Jones, A. Gallenne, J. Vinther, P. Ballester, and J. Taylor. Molecfit: A general tool for telluric absorption correction. I. Method and application to ESO instruments. A&A, 576:A77, April 2015. doi: 10.1051/0004-6361/201423932.

C. B. Stephenson and N. Sanduleak. New H-alpha emission stars in the Milky Way. ApJS, 33:459–469, April 1977. doi: 10.1086/190437.

I. R. Stevens. An enhanced stellar wind accretion model for binary X-ray transients. MNRAS, 232:199–213, May 1988. doi: 10.1093/mnras/232.1.199.

A. M. Stirling, F. H. Jowett, R. E. Spencer, Z. Paragi, R. N. Ogley, and T. V. Cawthorne. Radio-emitting component kinematics in SS433. MNRAS, 337:657–665, December 2002. doi: 10.1046/j.1365-8711.2002.05944.x.

Y. Tanaka, K. Nandra, A. C. Fabian, H. Inoue, C. Otani, T. Dotani, K. Hayashida, K. Iwasawa, T. Kii, H. Kunieda, F. Makino, and M. Matsuoka. Gravitationally redshifted emission implying an accretion disk and massive black hole in the active galaxy MCG-6-30-15. Nature, 375:659–661, June 1995. doi: 10.1038/375659a0.

E. Tatulli, F. Millour, A. Chelli, G. Duvert, B. Acke, O. Hernandez Utrera, K.-H. Hofmann, S. Kraus, F. Malbet, P. Mège, R. G. Petrov, M. Vannier, G. Zins, P. Antonelli, U. Beckmann, Y. Bresson, M. Dugué, S. Gennari, L. Glück, P. Kern, S. Lagarde, E. Le Coarer, F. Lisi, K. Perraut, P. Puget, F. Rantakyrö, S. Robbe-Dubois, A. Roussel, G. Weigelt, M. Accardo, K. Agabi, E. Altariba, B. Arezki, E. Aristidi, C. Baffa, J. Behrend, T. Blöcker, S. Bonhomme, S. Busoni, F. Cassaing, J.-M. Clausse, J. Colin, C. Connot, A. Delboulbé, A. Domiciano de Souza, T. Driebe, P. Feautrier, D. Ferruzzi, T. Forveille, E. Fossat, R. Foy, D. Fraix-Burnet, A. Gallardo, E. Giani, C. Gil, A. Glentzlin, M. Heiden, M. Heininger, D. Kamm, M. Kiekebusch, D. Le Contel, J.-M. Le Contel, T. Lesourd, B. Lopez, M. Lopez, Y. Magnard, A. Marconi, G. Mars, G. Martinot-Lagarde, P. Mathias, J.-L. Monin, D. Mouillet, D. Mourard, E. Nussbaum, K. Ohnaka, J. Pacheco, C. Perrier, Y. Rabbia, S. Rebattu, F. Reynaud, A. Richichi, A. Robini, M. Sacchettini, D. Schertl, M. Schöller, W. Solscheid, A. Spang, P. Stee, P. Stefanini, M. Tallon, I. Tallon-Bosc, D. Tasso, L. Testi, F. Vakili, O. von der Lühe, J.-C. Valtier, and N. Ventura. Interferometric data reduction with AMBER/VLTI. Principle, estimators, and illustration. A&A, 464:29–42, March 2007. doi: 10.1051/0004-6361:20064799.

A. R. Thompson, J. M. Moran, and G. W. Swenson, Jr. *Interferometry and Synthesis in Radio Astronomy, 3rd Edition*. 2017. doi: 10.1007/978-3-319-44431-4.

N. D. Thureau, J. D. Monnier, W. A. Traub, R. Millan-Gabet, E. Pedretti, J.-P. Berger, M. R. Garcia, F. P. Schloerb, and A.-K. Tannirkulam. Imaging the asymmetric dust shell around CI Cam with long baseline optical interferometry. MNRAS, 398:1309–1316, September 2009. doi: 10.1111/j.1365-2966.2009.14949.x.

D. Tody. The IRAF Data Reduction and Analysis System. In D. L. Crawford, editor, *Instrumentation in astronomy VI*, volume 627 of Proc. SPIE, page 733, January 1986. doi: 10.1117/12.968154.

D. Tody. IRAF in the Nineties. In R. J. Hanisch, R. J. V. Brissenden, and J. Barnes, editors, *Astronomical Data Analysis Software and Systems II*, volume 52 of *Astronomical Society of the Pacific Conference Series*, page 173, January 1993.

J. A. Tomsick and M. W. Muterspaugh. Masses of Neutron Stars in High-mass X-ray Binaries with Optical Astrometry. ApJ, 719:958–965, August 2010. doi: 10.1088/0004-637X/719/1/958.

S. Trippe, T. Paumard, T. Ott, S. Gillessen, F. Eisenhauer, F. Martins, and R. Genzel. A polarized infrared flare from Sagittarius A* and the signatures of orbiting plasma hotspots. MNRAS, 375:764–772, March 2007. doi: 10.1111/j.1365-2966.2006.11338.x.

J. Čechura and P. Hadrava. Stellar wind in state transitions of high-mass X-ray binaries. A&A, 575:A5, March 2015. doi: 10.1051/0004-6361/201424636.

E. P. J. van den Heuvel, J. P. Ostriker, and J. A. Petterson. An early-type binary model for SS433. A&A, 81:L7–L10, January 1980.

Stefan Van Der Walt, S Chris Colbert, and Gael Varoquaux. The numpy array: a structure for efficient numerical computation. *Computing in Science & Engineering*, 13(2):22–30, 2011.

R. C. Vermeulen, P. G. Murdin, E. P. J. van den Heuvel, S. N. Fabrika, B. Wagner, B. Margon, J. B. Hutchings, R. T. Schilizzi, M. H. van Kerkwijk, L. B. van den Hoek, E. Ott, L. P. Angebault, G. K. Miley, S. D'Odorico, and N. Borisov. Monitoring of very rapid changes in the optical spectrum of SS 433 in May/June 1987. A&A, 270:204–222, March 1993.

J. Vernet, H. Dekker, S. D'Odorico, L. Kaper, P. Kjaergaard, F. Hammer, S. Randich, F. Zerbi, P. J. Groot, J. Hjorth, I. Guinouard, R. Navarro, T. Adolfse, P. W. Albers, J.-P. Amans, J. J. Andersen, M. I. Andersen, P. Binetruy, P. Bristow, R. Castillo, F. Chemla, L. Christensen, P. Conconi, R. Conzelmann, J. Dam, V. de Caprio, A. de Ugarte Postigo, B. Delabre, P. di Marcantonio, M. Downing, E. Elswijk, G. Finger, G. Fischer, H. Flores, P. François, P. Goldoni, L. Guglielmi, R. Haigron, H. Hanenburg, I. Hendriks, M. Horrobin, D. Horville, N. C. Jessen, F. Kerber, L. Kern, M. Kiekebusch, P. Kleszcz, J. Klougart, J. Kragt, H. H. Larsen, J.-L. Lizon, C. Lucuix, V. Mainieri, R. Manuputy, C. Martayan, E. Mason, R. Mazzoleni, N. Michaelsen, A. Modigliani, S. Moehler, P. Møller, A. Norup Sørensen, P. Nørregaard, C. Péroux, F. Patat, E. Pena, J. Pragt, C. Reinero, F. Rigal, M. Riva, R. Roelfsema, F. Royer, G. Sacco, P. Santin, T. Schoenmaker, P. Spano, E. Sweers, R. Ter Horst, M. Tintori, N. Tromp, P. van Dael, H. van der Vliet, L. Venema, M. Vidali, J. Vinther, P. Vola, R. Winters, D. Wistisen, G. Wulterkens, and A. Zacchei. X-shooter, the new wide band intermediate resolution spectrograph at the ESO Very Large Telescope. A&A, 536:A105, December 2011. doi: 10.1051/0004-6361/201117752.

F. H. Vincent, T. Paumard, G. Perrin, L. Mugnier, F. Eisenhauer, and S. Gillessen. Performance of astrometric detection of a hotspot orbiting on the innermost stable circular orbit of the Galactic Centre black hole. MNRAS, 412:2653–2664, April 2011. doi: 10.1111/j.1365-2966.2010.18084.x.

M. Volonteri, P. Madau, E. Quataert, and M. J. Rees. The Distribution and Cosmic Evolution of Massive Black Hole Spins. ApJ, 620:69–77, February 2005. doi: 10.1086/426858.

M. Volonteri, J. Silk, and G. Dubus. The Case for Supercritical Accretion onto Massive Black Holes at High Redshift. ApJ, 804:148, May 2015. doi: 10.1088/0004-637X/804/2/148.

R. M. Wagner. The binary system of SS 433. I - Further constraints imposed by observations of the optical continuum spectrum. ApJ, 308:152–160, September 1986. doi: 10.1086/164486.

I. Waisberg, J. Dexter, O. Pfuhl, R. Abuter, A. Amorim, N. Anugu, J. P. Berger, N. Blind, H. Bonnet, W. Brandner, A. Buron, Y. Clénet, W. de Wit, C. Deen, F. Delplancke-Ströbele, R. Dembet, G. Duvert, A. Eckart, F. Eisenhauer, P. Fédou, G. Finger, P. Garcia, R. Garcia Lopez, E. Gendron, R. Genzel, S. Gillessen, X. Haubois, M. Haug, F. Haussmann, T. Henning, S. Hippler, M. Horrobin, Z. Hubert, L. Jochum, L. Jocou, P. Kervella, Y. Kok, M. Kulas, S. Lacour, V. Lapeyrère, J.-B. Le Bouquin, P. Léna, M. Lippa, A. Mérand, E. Müller, T. Ott, L. Pallanca, J. Panduro, T. Paumard, K. Perraut, G. Perrin, S. Rabien, A. Ramírez, J. Ramos, C. Rau, R.-R. Rohloff, G. Rousset, J. Sanchez-Bermudez, S. Scheithauer, M. Schöller, C. Straubmeier, E. Sturm, F. Vincent, I. Wank, E. Wieprecht, M. Wiest, E. Wiezorrek, M. Wittkowski, J. Woillez, S. Yazici, and GRAVITY Collaboration. Submilliarcsecond Optical Interferometry of the High-mass X-Ray Binary BP Cru with VLTI/GRAVITY. ApJ, 844:72, July 2017. doi: 10.3847/1538-4357/aa79f1.

I. Waisberg, J. Dexter, P. Olivier-Petrucci, G. Dubus, and K. Perraut. Super-Keplerian Equatorial Outflows in SS 433. Centrifugal Ejection of the Circumbinary Disk. *arXiv e-prints*, November 2018.

R. Walder, M. Melzani, D. Folini, C. Winisdoerffer, and J. M. Favre. Simulation of Microquasars: The Challenge of Scales. In N. V. Pogorelov, E. Audit, and G. P. Zank, editors, *8th International Conference of Numerical Modeling of Space Plasma Flows (ASTRONUM 2013)*, volume 488 of *Astronomical Society of the Pacific Conference Series*, page 141, September 2014.

L. Wallace and K. Hinkle. Medium-Resolution Spectra of Normal Stars in the K Band. ApJS, 111:445–458, August 1997. doi: 10.1086/313020.

R. Walter, A. A. Lutovinov, E. Bozzo, and S. S. Tsygankov. High-mass X-ray binaries in the Milky Way. A closer look with INTEGRAL. A&A Rev., 23:2, August 2015. doi: 10.1007/s00159-015-0082-6.

M. G. Watson, G. C. Stewart, W. Brinkmann, and A. R. King. Doppler-shifted X-ray line emission from SS433. MNRAS, 222:261–271, September 1986. doi: 10.1093/mnras/222.2.261.

N. N. Weinberg, M. Milosavljević, and A. M. Ghez. Stellar Dynamics at the Galactic Center with an Extremely Large Telescope. ApJ, 622:878–891, April 2005. doi: 10.1086/428079.

R. S. Wharton, S. Chatterjee, J. M. Cordes, J. S. Deneva, and T. J. W. Lazio. Multiwavelength Constraints on Pulsar Populations in the Galactic Center. ApJ, 753:108, July 2012. doi: 10.1088/0004-637X/753/2/108.

C. M. Will. Testing the General Relativistic "No-Hair" Theorems Using the Galactic Center Black Hole Sagittarius A*. ApJ, 674:L25, February 2008. doi: 10.1086/528847.

J. Yan, Q. Liu, and P. Hadrava. Optical Spectroscopic Observations of Cyg X-1 = HDE 226868. AJ, 136:631–640, August 2008. doi: 10.1088/0004-6256/136/2/631.

X. Yang and J. Wang. YNOGK: A New Public Code for Calculating Null Geodesics in the Kerr Spacetime. ApJS, 207:6, July 2013. doi: 10.1088/0067-0049/207/1/6.

X.-L. Yang and J.-C. Wang. ynogkm: A new public code for calculating time-like geodesics in the Kerr-Newman spacetime. A&A, 561:A127, January 2014. doi: 10.1051/0004-6361/201322565.

Q. Yu, F. Zhang, and Y. Lu. Prospects for Constraining the Spin of the Massive Black Hole at the Galactic Center via the Relativistic Motion of a Surrounding Star. ApJ, 827: 114, August 2016. doi: 10.3847/0004-637X/827/2/114.

F. Yuan and R. Narayan. Hot Accretion Flows Around Black Holes. ARA&A, 52:529–588, August 2014. doi: 10.1146/annurev-astro-082812-141003.

F. Yuan, E. Quataert, and R. Narayan. Nonthermal Electrons in Radiatively Inefficient Accretion Flow Models of Sagittarius A*. ApJ, 598:301–312, November 2003. doi: 10.1086/378716.

F. Yuan, E. Quataert, and R. Narayan. On the Nature of the Variable Infrared Emission from Sagittarius A*. ApJ, 606:894–899, May 2004. doi: 10.1086/383117.

W. J. Zealey, M. A. Dopita, and D. F. Malin. The interaction between the relativistic jets of SS433 and the interstellar medium. MNRAS, 192:731–743, September 1980. doi: 10.1093/mnras/192.4.731.

F. Zhang and L. Iorio. On the Newtonian and Spin-induced Perturbations Felt by the Stars Orbiting around the Massive Black Hole in the Galactic Center. ApJ, 834:198, January 2017. doi: 10.3847/1538-4357/834/2/198.

F. Zhang and P. Saha. Probing the Spinning of the Massive Black Hole in the Galactic Center via Pulsar Timing: A Full Relativistic Treatment. ApJ, 849:33, November 2017. doi: 10.3847/1538-4357/aa8f47.

F. Zhang, Y. Lu, and Q. Yu. On Testing the Kerr Metric of the Massive Black Hole in the Galactic Center via Stellar Orbital Motion: Full General Relativistic Treatment. ApJ, 809:127, August 2015. doi: 10.1088/0004-637X/809/2/127.

S. N. Zhang, W. Cui, and W. Chen. Black Hole Spin in X-Ray Binaries: Observational Consequences. ApJ, 482:L155–L158, June 1997. doi: 10.1086/310705.

S. Zucker, T. Alexander, S. Gillessen, F. Eisenhauer, and R. Genzel. Probing Post-Newtonian Physics near the Galactic Black Hole with Stellar Redshift Measurements. ApJ, 639:L21–L24, March 2006. doi: 10.1086/501436.

T. Zwitter, M. Calvani, and S. D'Odorico. Photometry of SS 433 and its implication for the nature of the system. A&A, 251:92–102, November 1991.

Acknowledgments

I thank my supervisor Reinhard Genzel for giving me the opportunity to do my PhD in his group with the unique GRAVITY instrument, for continuing support and also for the freedom to work on a variety of topics that interested me. I thank my advisor Jason Dexter for his support and interest for all my ideas, even in topics he was not primarily interested in, and for his patience and optimism and countless hours of advising, and for often trusting my ability more than I do myself. I also thank the other members of my PhD thesis committee, Frank Eisenhauer and Linda Tacconi, for the help in navigating my PhD thesis.

I thank all member of the Galactic Center and Infrared group for collaboration and interesting discussions. In particular, I thank Frank Eisenhauer, Stefan Gillessen and Oliver Pfuhl for all the help in the steep learning curve of the GRAVITY instrument, and Thomas Ott for continuing work support. I thank the postdocs Michi Bauböck, Feng Gao and Maryam Habibi for discussions and/or collaboration over these years, as well as my more and less senior PhD student colleagues for help with various tasks, in particular Annemieke Janssen, Alejandra Jimenez-Rosales, Ming-Yi Lin, Magdalena Lippa, Phillip Plewa, Hannah Übler, Sebastiano von Fellenberg, Felix Widmann and Senol Yazici.

I thank all members of the GRAVITY consortium for collaboration in this complex project, and for the many nights of joy and struggle on the mountain. In particular, I thank the GRAVITY Co-Is Frank Eisenhauer, Guy Perrin, Karine Perraut, Wolfgang Brandner, Christian Straubmeier, Antonio Amorim, Paulo Garcia and Thibaut Paumard for the continued support. I also thank ESO for the collaboration and hospitality in Paranal.

I thank my Grenoble collaborators, in particular Pierre Olivier-Petrucci, Guillaume Dubus and Karine Perraut, for continued support and interest in my SS 433 work, and for the couple invitations to work together in Grenoble.

Above all I thank my parents for unconditional love and support.